Dynamic Behaviour of Dowel-type Connections Under In-service Vibration

Reynolds, Thomas

Award date:
2013

Awarding institution:
University of Bath

Dynamic Behaviour of Dowel-type Connections Under In-service Vibration

submitted by

Thomas Peter Shillito Reynolds

for the degree of Doctor of Philosophy

of the

University of Bath

Department of Architecture and Civil Engineering

September 2013

Acknowledgements

This research was made possible by funding from the University of Bath and Atelier One structural engineers. The Worshipful Company of Armourers and Braziers, the Institution of Civil Engineers and European Cooperation in Science and Technology contributed funding for the academic missions and conference presentations which shaped this study by allowing me to share my ideas with the leading researchers in timber engineering.

Thanks to my supervisors Richard Harris and Wen-Shao Chang. Richard's positivity and huge knowledge of timber construction complemented Wen-Shao's experimental expertise and inventiveness, and they made sure I never had to wait long to get the bit of guidance which got me back on the right path.

In the laboratory, Will Bazeley helped make my ideas into viable test methods and Neil Price got the machines working. In the wood workshop, Walter Guy and Glen Stewart gave me the benefit of their skill and experience to help me put together some realistic timber structures.

At home, my wonderful wife Abi kept me on course with love, supportive words and regular meals, as well as grammatical expertise. My parents have given me unconditional support, love and gentle guidance which has made me feel free to explore whatever opportunities life has presented me, and that exploration has led me here.

Abstract

This study investigated the vibration serviceability of timber structures with dowel-type connections. It addressed the use of such connections in cutting-edge timber structures such as multi-storey buildings and long-span bridges, in which the light weight and flexibility of the structure make it possible that vibration induced by dynamic forces such as wind or footfall may cause discomfort to occupants or users of the structure, or otherwise impair its intended use.

The nature of the oscillating force imposed on connections by this form of vibration was defined based on literature review and the use of established mathematical models. This allowed the appropriate cyclic load to be applied in experimental work on the most basic component of a dowel-type connection: a steel dowel embedding into a block of timber. A model for the stiffness of the timber in embedment under this cyclic load was developed based on an elastic stress function, which could then be used as the basis of a model for a complete connector. Nonlinear and time-dependent behaviour was also observed in embedment, and a simple rheological model incorporating elastic, viscoelastic and plastic elements was fitted to the measured response to cyclic load. Observations of the embedment response of the timber were then used to explain features of the behaviour of complete single- and multiple-dowel connections under cyclic load representative of in-service vibration.

Complete portal frames and cantilever beams were tested under cyclic load, and a design method was derived for predicting the stiffness of such structures, using analytical equations based on the model for embedment behaviour. In each cyclic load test the energy dissipation in the specimen, which contributes to the damping in a complete structure, was measured. The analytical model was used to predict frictional energy dissipation in embedment, which was shown to make a significant contribution to damping in single-dowel connections.

Based on the experimental results and analysis, several defining aspects of the dynamic response of the complete structures, such as a reduction of natural frequency with increased amplitude of applied load, were related to the observed and modelled embedment behaviour of the connections.

Contents

List of Tables

List of Figures

List of Symbols

α_m, β_m	Coefficients in the stress function for an orthotropic plate, page 120
$\alpha_{1,2}, \beta_{1,2}$	Material properties defined for simplification of the stress function, page 135
δ	Logarithmic decrement of damping $\delta = 2\pi\gamma$, page 53
$\delta_{1,2}, \gamma_{1,2}$	Coefficients in the derivation of the stress function for an orthotropic plate with hole, page 126
η	Viscous damping coefficient, page 10
η_2	Coefficient of quadratic stiffness, page 183
Γ	The gamma function, page 87
γ	Equivalent viscous damping ratio, page 35
γ_M	Material factor according to Eurocode 5 (BSI; 2009a), page 79
μ	Friction coefficient, page 121
μ_0	Mean of a sample for Student's t-test, page 139
μ_3	Cubic stiffness coefficient, page 181
$\mu_{1,2}$	Complex roots of the characteristic equation for an orthotropic plate, page 119
ν	Degrees of freedom for Student's t-test, page 87
ν_{12}	Poisson's ratio
ω	Circular natural frequency
$\overline{d}$	Mean of the numerical difference between two test results for the same specimen, page 87
$\overline{x}_i$	Mean value of a sample for Student's t-test, page 87

$\Phi_{1,2}$ Stress functions for orthotropic plates, page 118

σ_x Direct stress in the x direction

σ_y Direct stress in the y direction

τ_{xy} Shear stress in the y direction on the plane orthogonal to the x direction

$\zeta_{1,2}$ Transformed coordinates in the stress function for an orthotropic plate, page 119

A_k Coefficients of the Fourier series defining the force at the interface between dowel and timber, page 126

c Viscous damping coefficient

c_d Dynamic factor for wind forces, page 53

c_f Force coefficient, page 52

c_s Coefficient for dowel slip, page 121

d Dowel diameter

E_b Elastic modulus of the beam in a beam-on-foundation model, page 21

E_d Energy dissipated, page 147

$E_{1,2}$ Principal elastic moduli

f_n Natural frequency

$f_{e,\alpha}$ Embedment strength at angle α to the grain, page 27

$F_{v,1,2,3}$ Failure loads for the different failure modes of the European Yield Model, page 27

G Shear modulus

g Hysteretic damping coefficient, page 40

H System transfer function, page 30

i The imaginary unit

k Elastic stiffness

k_d Dynamic embedment stiffness, page 162

K_r Rotational stiffness of a connection, page 186

k_t Total embedment stiffness, page 162

k_v Viscoelastic embedment stiffness, page 162

K_{bf} Stiffness of a beam on foundation subject to a point load, page 21

$k_{f,r}$ Foundation stiffness associated with the rigid-insert deformation, page 135

$k_{f,s}$ Foundation stiffness associated with the hole-shape deformation, page 136

k_f Foundation modulus in a beam-on-foundation model, page 21

k_{mod} Modification factor according to Eurocode 5 (BSI; 2009a), page 79

K_{ser} Connection slip modulus according to Eurocode 5 (BSI; 2009a), page 19

N Normal force between dowel and timber, page 125

n_i Number of tests in a sample for Student's t-test, page 87

$p_{1,2}, q_{1,2}$ Complex constants based on the orthotropic elastic properties of an orthotropic plate, page 119

P_{ii} Auto correlation of i, page 178

P_{ij} Cross correlation between i and j, page 178

R (R-ratio) description of the amplitude and offset of an oscillating load, page 65

r Dowel radius

R^2 Coefficient of determination, page 19

R_d Design value of a resistance, page 79

R_h, R_b Aerodynamic admittance functions, page 51

S Power spectral density function, page 30

s Slip between dowel and timber, page 147

s_{ij} Elastic compliances, page 107

s_x, s_d Standard deviation of a sample for Student's t-test, page 87

St Strouhal number, page 55

T	Tangential force between dowel and timber, page 125
u	Displacements in the x direction, page 121
u', v'	Displacements at the hole edge in an orthotropic plate with a hole, page 120
u_0	Dowel displacement, page 121
u_θ	Tangential displacement, page 125
u_r	Radial displacement, page 125
v	Displacement in the y direction, page 121
v_m	Mean wind velocity, page 52
v_{crit}	Critical wind velocity for vortex shedding, page 55
W_i	Elastic work done in a particular element or process, page 152
$z_{1,2}$	Complex coordinates in the stress function for an orthotropic plate, page 119

Chapter 1

Introduction

Timber is one of the most widely used construction materials in the world, and the majority of timber structures rely on some dowel-type connections. The structures that motivated this study are the ones that apply timber in more challenging situations than the one- or two-storey houses and short-span footbridges which account for most of its structural use. Based on its fundamental structural properties, and given the engineered wood products which have been developed to take advantage of those properties, timber has the potential to be far more widely used in the multi-storey buildings and bridges which form the infrastructure of cities around the world. The use of timber in more such structures would have the benefit of increasing the diversity of structural materials in urban environments, so reducing the reliance of the construction industry on a particular material and its means of supply.

Whatever material they work with, the task of structural engineers is to design a structure capable of serving a particular purpose in the most efficient manner. The measures of that efficiency include the cost of materials and of the construction process, the volume and weight of material used, and the time taken in construction. As a result of the continual progress of engineers in achieving greater efficiency, structures have become more lightweight and slender, attributes which contribute to achieving all these measures. In such structures, where the structural material is reduced to a minimum, serviceability considerations such as deflection under load and vibration become important design criteria.

As a result, there have been examples of structures which have produced unacceptable vibration. Multi-storey buildings and bridges have had to be designed or retrofitted with systems to increase mass, stiffness or damping for mitigation of vibration. Examples include the Valladolid Science Museum Footbridge (Casado et al.; 2013), the London Millennium Bridge (Ingólfsson et al.; 2012), Park Tower in Chicago

and Taipei Financial Centre (Irwin and Breukelman; 2001). In order for structural engineers to design such systems, however, they must have a thorough understanding of the dynamic properties of the structure. This must come either from modal analysis of the completed structure, or from an understanding of how all the elements of the structure combine to give the mass, stiffness and damping of the structure as a whole. During the design of the structure, the latter is the only possible method, but there has been little research into the stiffness and damping in connections in timber structures under this small-amplitude vibration. This study therefore aimed to trace and understand the development of stiffness and damping in timber structures, from the interaction of a single connector with the timber that surrounds it to the modal properties of a complete frame. As a result, its contribution to knowledge was to measure and interpret the influence of connections on stiffness and damping under loads representative of in-service vibration.

1.1 Timber as a structural material

Timber is an ancient building material still used in cutting-edge construction. It has gained an advantage over other structural materials as the environmental impact of construction has become an increasingly important measure of efficiency. By this measure, timber has the advantage of being a renewable natural material for which, compared with other widely-used structural materials, a relatively small amount of energy is required to prepare the raw material for structural use. Timber also has the potential to contribute to the management of atmospheric carbon dioxide produced by construction, since the carbon dioxide absorbed by the tree as it grows is stored in the timber until it decays, is burnt or otherwise broken down.

The material properties of timber, especially when considered in proportion to its self-weight, compare favourably with those of the most widely used structural materials: steel and reinforced concrete. Using indicative ranges of density, strength and stiffness presented by Cobb (2009), mechanical properties of two species of timber widely used in construction, Douglas fir and spruce, are compared with those of mild steel and concrete in Figure 1-1.

It can be seen that the two species of timber have a stiffness-to-weight ratio similar to that of steel, and higher than concrete, while the strength-to-weight ratio of Douglas fir is higher than both steel and concrete. The result of this relationship is that a timber structure carrying the same load as an equivalent steel structure could be expected to have a similar self-weight.

This comparison is a simplistic one, since the nature of the structural form, the

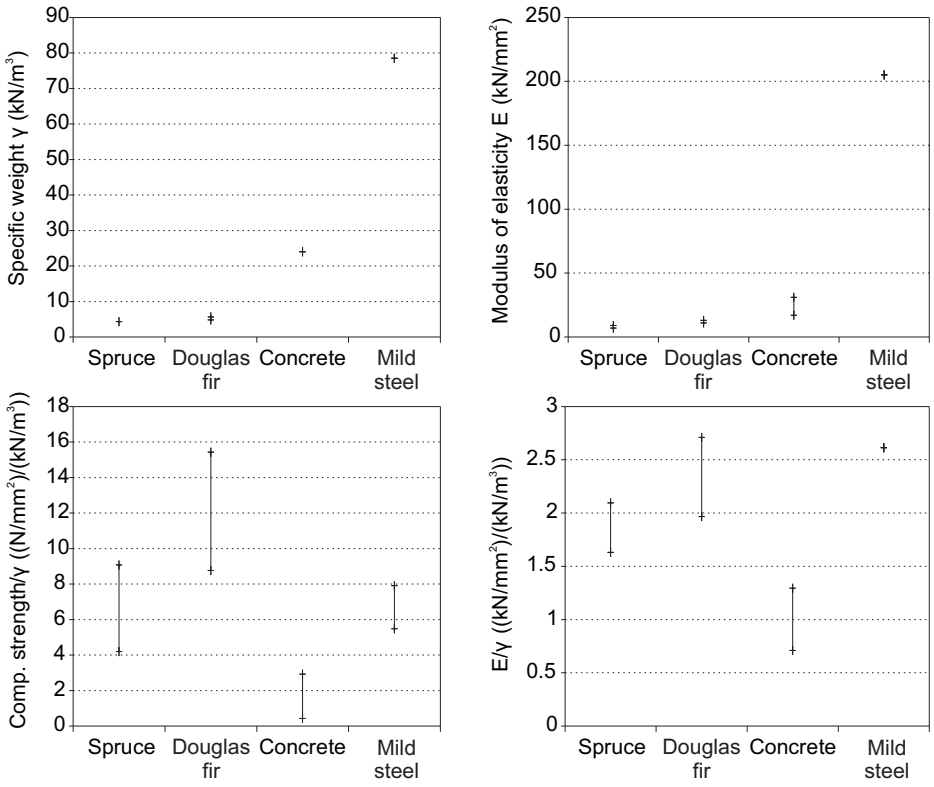

Figure 1-1: Comparison of ranges of compressive strength, elastic modulus and specific gravity of structural materials, using data from Cobb (2009)

material design factors and, of particular significance in timber structures, the connection methods, will influence the volume of material required, and therefore the self-weight, of structures in each material. It does indicate, however, that as, in the future, timber and engineered timber products are used in more efficient structural forms, their dynamic behaviour may become an important design consideration in the same way as is the case for modern lightweight steel structures.

In multi-storey building construction, timber structures have the potential for lower self-weight than conventional construction as a result of the higher strength- and stiffness-to-weight ratio of structural timber compared with reinforced concrete. Even steel-framed buildings generally use steel-concrete composite floors, while timber construction systems can include floor structures constructed entirely of timber, or with a concrete layer thinner than that used in steel-concrete composites. There are, however, many elements in a building which are not part of its primary structure, but contribute to its mass. A reduced mass in the structural material will not, therefore, reduce the mass of the complete building proportionately. In tall buildings and long spans, however, the mass of the structural material represents a large proportion of the total mass. The case study presented in Chapter 4, for example, is a 20-storey building with timber floors, columns and bracing, and the mass of the timber structure represents 43% of the total mass of the completed building which was assumed for dynamic effects.

The resulting lightweight multi-storey timber buildings or bridges have many advantages, such as enabling reduced foundation sizes or even simpler foundation types, and reduced crane loads during construction. A lower structural mass, however, gives lower inertia forces in vibration, resulting in a larger amplitude of acceleration under a given excitation. Higher accelerations are more readily perceived by building occupants, and are more likely to affect any sensitive equipment housed in the building.

Additional mass is not the only way to reduce structural vibration, however, and structural engineers should not be forced to sacrifice all the benefits of lightweight construction to achieve acceptable vibration. Structural vibration is determined by the mass, stiffness and damping of the system, and additional stiffness or damping can also reduce the vibration of a structure, while maintaining a low weight. This study contributes to a more thorough understanding of the mechanisms of stiffness and damping in timber structures, with the aim of allowing more efficient design, whether that is by allowing confidence in inherent damping and stiffness in the structure, or by allowing accurate design of supplementary damping systems or improved connections.

1.2 Dowel-type connections

This study investigates the behaviour of dowel-type connections, in which connectors act in shear across one or more planes between the structural members to be connected. Dowel-type connections are widely used in construction, in timber as well as in steel and fibre-reinforced composites, because of their ease of in-situ installation. In timber construction, dowel-type connectors can take the form of nails, screws, bolts or plain dowels. The connector is normally steel, and steel connectors are used in this study, but non-metallic connectors have also been used successfully, using materials including glass-fibre reinforced plastic, bamboo and hardwood.

The interaction between dowel and timber at their interface produces a stress distribution in the timber which varies with the orientation of the load to the grain and the material properties of the timber in each direction. The nature of this interaction is, therefore, a key area of study in understanding the behaviour of dowel-type connections. Once the dowel-timber interaction in characterized, it can be used to model the behaviour of a complete dowel, a group of dowels and then a complete structure. Connections in timber structures have a strong influence on their strength and stiffness, and since significant deformation occurs in the connections, the energy they dissipate will be an important factor in determining the damping.

By investigating the mechanisms of stiffness and energy dissipation in conventional dowel-type connections, this study contributes to identification of ways in which such connections can be improved, and provides an analytical and experimental framework by which future connection types can be assessed for their behaviour under in-service vibration.

1.3 Summary

Timber structures, due to their low mass, can be expected to be sensitive to in-service vibration in the same way as modern, lightweight steel structures. The benefits of that low mass can be retained, whilst still achieving acceptable vibration, by designing structures with appropriate stiffness and damping properties. A major obstacle to doing so is the lack of knowledge of the stiffness and damping due to connections in timber structures under such vibration.

Dowel-type connections are an important form of connection in timber structures and where used, they make a significant contribution to the stiffness of the complete structure. This study investigates the stiffness and damping due to this form of connection by observing and modelling the response of connections, and the components

which form them, to dynamic loads representative of in-service vibration.

Chapter 2

Literature review

The dynamic response of a dowel-type connection is primarily determined by three processes: the interaction of stress and strain in the timber itself, known as its rheology; the interaction between the dowel and the timber; and the dynamic load applied to the connection in a vibrating structure. This literature review therefore investigated those three areas, with particular emphasis on previously published work which considered dynamic, cyclic and pre-yield behaviour.

Many of the methods used in this project were developed for the study of either creep or seismic response of solid timber and connections. Researchers in these fields were interested in time-dependent effects, plasticity and hysteresis, all of which are also crucial to the response of dowel-type connections to in-service loads. This work is, however, set apart from those fields in that, where creep effects manifest themselves gradually over periods of hours or days, in-service vibration is a much shorter-term effect, and where connections under seismic loads exhibit global plastic deformation, connections under in-service vibration are subject to loads well below their nominal yield load. The extent to which methods used successfully in those other fields can be applied to in-service vibration is, therefore, a focus of this literature review.

2.1 Rheology of timber

Timber can be described as an orthotropic viscoelastic material, which is to say that deformation and strength characteristics vary depending on the orientation of the applied load to its grain and ring structure, and depending on the rate at which the load is applied and removed. These engineering descriptions of timber serve as approximations to its true behaviour, which is affected by natural variations of the material, its cellular structure, and the knots and splits which develop as the tree grows, is felled

and processed to become a structural timber product.

In this study, a range of methods is used to measure, analyse and model the orthotropic elastic and viscoelastic properties of timber in dowel-type connections, particularly under the oscillating load they would experience as part of a timber structure in service. The background to contemporary approaches for assessment of these properties is described in this section.

2.1.1 Orthotropy

The elastic response of a material to the applied loads is represented by Hooke's law, named after Robert Hooke, who asserted that the deformation of a spring was in proportion to the load applied to it (Hooke; 1678). The general form of Hooke's law can be expressed as every stress component being directly proportional to every strain component. The constants of proportionality are called elastic constants and, considering direct and shear stresses and strains in three dimensions, there are 81 of them in total. Compatibility of displacements, equilibrium and thermodynamic arguments (Hearmon; 1961) can be used to show that certain of the elastic constants are equal, leaving 21 independent elastic constants for the general, three-dimensional case.

To say a material is orthotropic is to say that it has different material properties in two or three orthogonal directions. Timber has been classified for engineering design using both two and three orthogonal directions: the European norm for mechanical properties of structural timber EN 338 (BSI; 2009b) gives elastic properties parallel- and perpendicular-to-grain, while the Wood Handbook (Forest Products Laboratory; 2010), a document by the Forest Products Laboratory in the USA bringing together the results of studies on a wide range of wood species, gives the full set of elastic constants for longitudinal, radial and tangential grain directions.

In structural design, it is not normally possible to identify the orientation of the radial and tangential directions in a particular member prior to construction. As a result, members must be designed using orthotropic material properties with two orthogonal directions and conservative perpendicular-to-grain properties. In this study, structural-size specimens were tested, and they were delivered in the form of sawn or glued-laminated timber as they would be to a construction site. The perpendicular-to-grain direction therefore varied between radial and tangential and contributed to the scatter in the measured mechanical properties of the timber and connections.

In the analysis described in Chapter 6, a state of plane stress is assumed, reducing the embedment of the dowel into the timber to the problem of a pin-loaded orthotropic plate. In plane stress, the direct and shear stresses on the faces of the plate are taken to be zero, and the stress state in the plate is fully described by the two in-plane direct

stresses and the in-plane shear. As a result, the number of relevant independent elastic constants is reduced from 21 for the general case to 4: the elastic moduli in each of the two in-plane principal directions, the in-plane shear modulus and the Poisson's ratio. The assumption of plane stress is by no means an obvious simplification in this case, and its implications are discussed in Chapter 6.

Lekhnitskii (1968) developed mathematical models for orthotropic materials, defining general solutions for the stress state in orthotropic plates with a range of geometries and loading conditions, which have formed the basis of engineering models for a wide range of real structures. Lekhnitskii's two-dimensional stress functions are based on that proposed by Airy (1863). The Airy stress function, here denoted by F, can be differentiated with respect to the in-plane coordinates x and y to give the mean stresses across the plate thickness, σ_x, σ_y and τ_{xy}, in the absence of body forces, according to (2.1).

$$\sigma_x = \frac{\partial^2 F}{\partial y^2} \quad \sigma_y = \frac{\partial^2 F}{\partial x^2} \quad \tau_{xy} = -\frac{\partial^2 F}{\partial x \partial y} \tag{2.1}$$

In order to satisfy compatibility of displacements in plane stress, for an orthotropic material, the stress function should satisfy (2.2), where E_1 and E_2 are the elastic moduli in the principal directions, ν_{12} is the Poisson's ratio and G_{12} is the shear modulus (Lekhnitskii; 1968). Principal direction 1 is aligned with the x direction and principal direction 2 with the y direction.

$$\frac{1}{E_2}\frac{\partial^4 F}{\partial x^4} + \left(\frac{1}{G_{12}} - \frac{2\nu_{12}}{E_1}\right)\frac{\partial^4 F}{\partial x^2 \partial y^2} + \frac{1}{E_1}\frac{\partial^4 F}{\partial y^4} = 0 \tag{2.2}$$

This can be simplified to (2.3), where the D_k represent the operation in (2.4), and the μ_k are the four roots of the quadratic equation (2.5).

$$D_1 D_2 D_3 D_4 F = 0 \tag{2.3}$$

$$D_k = \frac{\partial}{\partial y} - \mu_k \frac{\partial}{\partial x} \tag{2.4}$$

$$\frac{\mu^4}{E_1} + \left(\frac{1}{G_{12}} - \frac{2\nu_{12}}{E_1}\right)\mu^2 + \frac{1}{E_2} = 0 \tag{2.5}$$

Any stress function F, which satisfies (2.3) therefore satisfies compatibility of displacements, and all the material properties of the orthotropic material are expressed by the coefficients μ.

Lekhnitskii (1968) then went on to derive stress functions for a variety of geometries

and loading conditions of orthotropic plates, including the plate with a circular hole, which is of particular interest in this study and so is discussed further in Section 2.2.1, and used in Chapter 6.

2.1.2 Viscoelasticity and creep

Timber displays the time-dependency of a viscoelastic material, meaning that its behaviour can be represented by a combination of viscous flow, in which the relationship between stress and strain in a substance depends on time, and elasticity, in which the stress and strain are related by a constant. The concept of viscoelasticity developed from investigations by Thomson (1865) and Maxwell (1868), two researchers who approached viscoelasticity from different backgrounds, one noting elastic properties of substances previously described by viscosity, and one showing the viscous behaviour of a substance previously described by elasticity.

Maxwell (1868) studied fluids, and developed a model to explain the viscous and elastic components of the force exerted by a fluid as a result of a change in strain. He noted that in fluids, a change in strain required a force which decayed with time until the fluid reached a state of rest, and the force was zero. The time for this decay to occur in fluids was very short, but for 'viscous solids', as Maxwell described them, the time might be of the order of hours or days. Maxwell's model can be expressed either by the spring-damper system in Figure 2-1, or by the set of differential equations in (2.6).

$$F = kx = \eta \frac{\mathrm{d}x}{\mathrm{d}t} \tag{2.6}$$

Thomson (1865), who was Baron Kelvin, approached viscoelasticity from the elastic side, noting the dissipation of energy by vibrating aluminium wires and attributing it to viscous behaviour in the metal. This dissipative behaviour was allowed for in a model by Voigt (1892), cited in Bulíĉek et al. (2012), which became known as the Kelvin-Voigt model. The Kelvin-Voigt model can be expressed either by the spring-damper system in Figure 2-1, or by the differential equation in (2.7).

$$F = kx + \eta \frac{\mathrm{d}x}{\mathrm{d}t} \tag{2.7}$$

Burgers (1939) combined the Kelvin-Voigt and Maxwell models in series to create a simple model capable of representing the combination of plastic flow, recoverable creep and elasticity observed in a wide range of materials. Burgers's model, shown in Figure 2-1, has since been applied to materials ranging from plastics to glaciers. The set of differential equations governing the Burgers model is shown in (2.8) and (2.9).

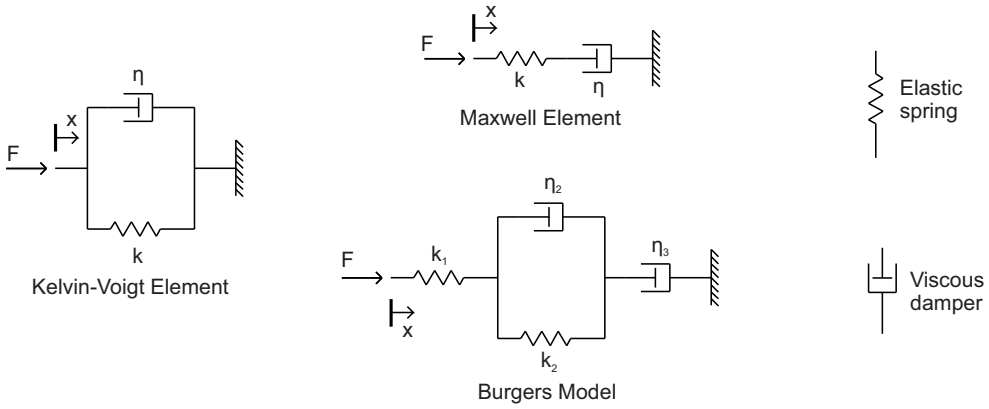

Figure 2-1: Models for viscoelastic behaviour of materials

$$F = k_1 x_1 = k_2 x_2 + \eta_2 \frac{\mathrm{d}x_2}{\mathrm{d}t} = \eta_3 \frac{\mathrm{d}x_3}{\mathrm{d}t} \tag{2.8}$$

$$x = x_1 + x_2 + x_3 \tag{2.9}$$

The Maxwell, Kelvin-Voigt and Burgers models can be compared by considering their response to a step in applied load, and its reversal, plotted in Figure 2-2. The displacement response of the Burgers model to any applied load is the sum of the responses of the Maxwell and Kelvin-Voigt components.

The unit step response of the Maxwell model can be written as in (2.10), that of the Kelvin-Voigt model as in (2.11) and that of the Burger model as in (2.12).

$$x = \frac{1}{k} + \frac{t}{\eta} \tag{2.10}$$

$$x = \frac{1}{k}\left(1 - e^{-\frac{k}{\eta}t}\right) \tag{2.11}$$

$$x = \frac{1}{k_1} + \frac{1}{k_2}\left(1 - e^{-\frac{k_2 t}{\eta_2}}\right) + \frac{t}{\eta_3} \tag{2.12}$$

The Maxwell model gives an instantaneous elastic response followed by a linear increase in displacement with time. The instantaneous response is entirely recovered upon removal of the load, while the time-dependent response is not recovered at all. In the sense that its effect is irreversible, the time-dependent response in the Maxwell model can be described as plastic.

The Kelvin-Voigt model gives no instantaneous deformation, but a gradually increasing displacement which tends asymptotically towards a constant value. Upon re-

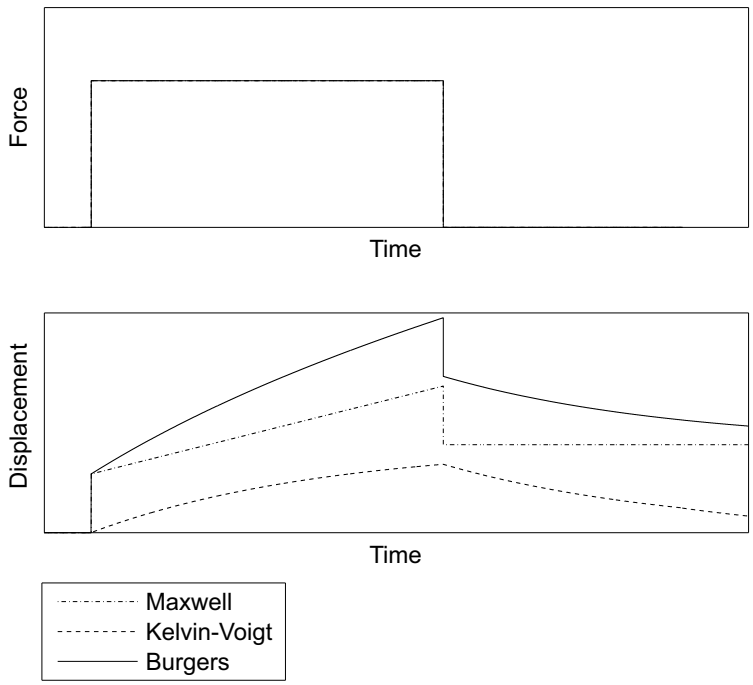

Figure 2-2: Comparison of the step response of the Maxwell, Kelvin-Voigt and Burgers models

moval of the load, the displacement tends asymptotically towards the original position. This behaviour can be described as delayed-elastic.

The Burgers model, therefore, exhibits elastic, plastic and delayed-elastic components. The elastic component responds immediately to the step in applied load, and the displacement then increases with time due to both the plastic and delayed-elastic components. Upon removal of the load, the elastic displacement is immediately recovered, and the delayed elastic component diminishes with time, so the displacement tends towards that of the plastic component. This behaviour has been observed in many materials, which has led to the wide scope of application of the Burgers model.

In timber, viscoelastic models have been primarily used to represent creep, rather than dissipative behaviour, and they therefore aim to model the observed creep or stress relaxation over periods of time which range from a few hours to months and years. The effect of creep in timber on stiffness and strength has long been apparent. Georges-Louis Leclerc, comte de Buffon (Buffon; 1740), most well known as a naturalist, carried out an experimental investigation of the behaviour of timber beams under load, and reported that there were loads that a timber beam could sustain for a few minutes, but which would cause failure after an hour.

...enfin le temps qu'on employe à charger les bois pour les faire rompre, doit

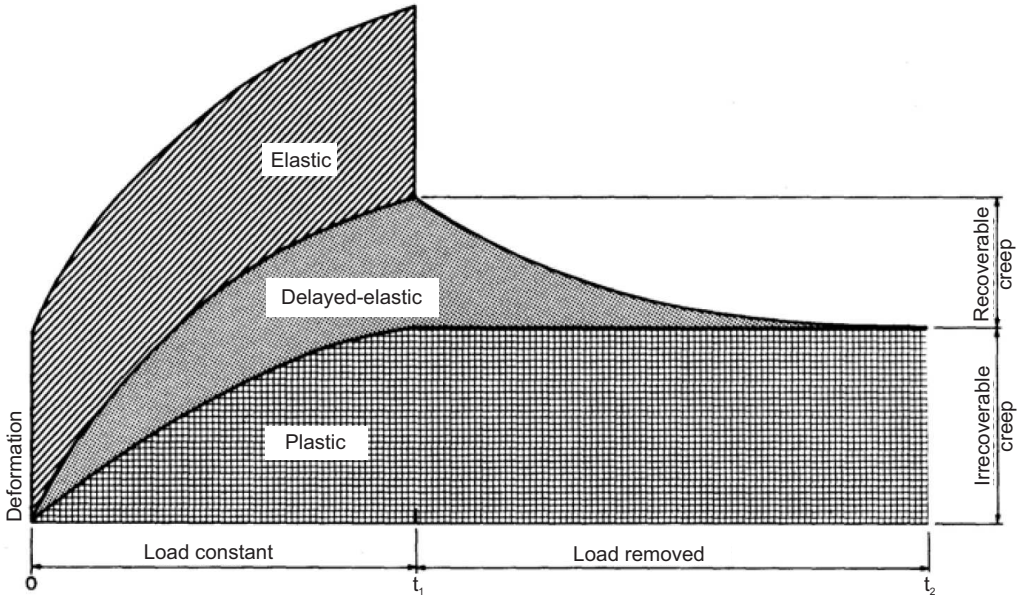

Figure 2-3: Components of creep deformation in timber ©BRE (Dinwoodie; 2000)

> *aussi entrer en considération, parce qu'une pièce qui soûtiendra pendant quelques minutes un certain poids, ne pourra pas soûtenir ce même poids pendant une heure...*

The observed creep deformation of timber under constant load is described by Dinwoodie (2000) using the graph shown in Figure 2-3. The Burgers model (Burgers; 1939), as shown in Figure 2-1, exhibits the main features of the observed creep behaviour of timber. An inaccuracy of the model, in its application to timber, is that it predicts a constant rate of plastic creep under constant load, whereas the observed behaviour, illustrated in Figure 2-3, shows a reduction in the rate of plastic deformation with time. In long-term tests, this can result in a significant difference between measured and modelled behaviour.

It was observed that plotting creep against the logarithm of time resulted in a straight line for many materials, including timber. This behaviour can be modelled by a power law relationship between creep and time, and such a relationship was first applied to timber by Clouser (1959). This relationship has yielded the most success in relating the results of long-term and short-term creep tests (Gressel; 1984; Hunt; 2004), but it only represents the response of the material to a constant applied force, whereas the Burgers model can, at least in theory, predict the response of the material to any time-history of loading. It is reported by Hunt (2004) that the first few hours

of creep do not follow a straight line on a creep versus log time plot, so the power law relationship may not be appropriate to model viscoelastic behaviour in that time scale.

Clouser (1959) took care to maintain his specimens at constant temperature and humidity during the tests. The importance of this aspect of creep testing was highlighted with the publication of work by Armstrong and Kingston (1960), describing what became known as the mechano-sorptive effect in timber, which means that while the relative creep, the ratio of creep deflection to instantaneous deflection, is similar in wood at high and low moisture content, the relative creep is significantly higher if the wood changes from a high moisture content to a low moisture content, or vice versa, during the course of the creep test. Later Hunt (1999) provided experimental evidence to show, by investigating the relationship between strain and strain rate, that the mechano-sorptive effect was an acceleration of the creep caused by time under load, rather than being a separate process. This contribution showed that the strain due to the two effects should not simply be added, therefore, because the mechano-sorptive effect acts to reduce the potential for the timber to creep further under load.

The author is not aware of any published research into the creep deformation of dowel-type connections. Eurocode 5 (BSI; 2009a) allows for creep in connections using the same factor which is used for solid timber, and this assumption appears reasonable, since the only significant creep in a connection will be that due to the timber. The research on solid timber described in this section was therefore used as a basis for a viscoelastic model for embedment, the development of which is described in Chapter 6.

2.1.3 Dissipative behaviour

Under dynamic loads, the plastic and time-dependent behaviour of timber results in energy dissipation, which can be beneficial in a range of situations, not least in a structure where undesirable vibration is to be mitigated. For that purpose, Labonnote et al. (2012) investigated energy dissipation in timber beams under vibrations in the serviceability range using impact tests. They found that timber was most dissipative in shear deformation, so that vibration which included a greater contribution from shear deformation, such as higher modes of vibration and deeper beams, exhibited greater damping.

In a subsequent paper, Labonnote et al. (2013) use complex elastic and shear moduli to represent the hysteretic damping in timber in direct and shear deformation. They fitted this hysteretic damping model to a wide range of experimental results for timber beams with different support conditions and geometry, modelling the energy dissipation and showing the large contribution of damping through shear deformation in the beams

whose geometry means that shear deformation contributes significantly.

Other research into dissipative behaviour in timber has been motivated by its use for shock-absorption in situations including transportation for nuclear waste and mooring of ships (Adalian and Morlier; 2002; Vural and Ravichandran; 2003). The use of timber specifically for its dissipative behaviour suggests that timber structures may have the potential for significant inherent structural damping, but in these applications the timber is normally loaded perpendicular to the grain, so that the crushing of the hollow tracheids and the associated plastic behaviour in the cell walls is assumed to be the primary source of energy dissipation.

2.2 Dowel-timber interaction

The non-linear and time-dependent rheology of timber was described in Section 2.1. In dowel-type connections, the interaction of the dowel and timber leads to further nonlinear behaviour, since the forces are transferred between the dowel and timber by both normal and friction forces at the interface. Previous research into the interaction of dowel and timber can be divided into studies of embedment of the dowel into the timber around it, and whole dowel models, which also consider the bending deformation of the dowel.

2.2.1 Embedment

As in all aspects of structural engineering, finite element modelling has been applied to timber connections, and finite element models have been extensively used to model the deformation in the timber around a dowel (Daudeville et al.; 1999; Kharouf et al.; 2003; Sjödin et al.; 2006; Dorn; 2012). Sjödin et al. (2006) used a full-field measurement technique, digital image correlation, to observe the strain field around a multiple-fastener connection, and compared the measured results with those obtained from a finite-element model. The model treated the timber as orthotropic and elastic, and the interaction between dowel and timber was modelled by frictional contact elements. The results showed a good correlation between the modelled and measured strains, which suggests that, if the interface conditions between the dowel and timber can be modelled accurately, then an orthotropic elastic model of the timber itself may be suitable to calculate deformations.

The stress distribution around the dowel is strongly influenced by the circumferential traction between the dowel and timber. The studies which have shown this influence have focussed on the effect of the nature of the dowel surface on the failure mode of a connection. Rodd and Leijten (2003) tested dowels with three different surfaces: one in

which PTFE tape was used to reduce the traction between the surfaces; one in which the steel dowel was unaltered; and one in which the surface of the dowel was knurled to increase traction. The effect of these variations on the embedment failure mode is shown in Figure 2-4. The PTFE surface resulted in a deformed shape in which the dowel moved through the timber, applying forces to the timber perpendicular to the direction of applied load, whereas the knurled dowel caused compression failure of the timber on the loaded side of the dowel, with little indication of force applied to the timber in any direction other than that of the applied load. The behaviour of the specimens with plain dowels indicated aspects of the behaviour of the other two.

Similarly, Sjödin et al. (2008) tested dowels with two different surface finishes, and observed the effect of the change in surface using digital image correlation to visualize the strain field around the dowels. The interaction of the rougher surface with the timber was seen to reduce the tensile strain perpendicular to the direction of applied force on the loaded side of the dowel. Since failure is caused by splitting due to tensile stresses in this area, the dowel with a rougher surface failed at a higher load.

Dorn (2012) also studied the effect of dowel surface on the behaviour of dowel-type connections. His work is especially relevant to this study, since it concerns the serviceability limit state. Since he tested a complete single-dowel connection, in which the dowel could deform, his work is discussed in Section 2.2.2.

Some of the researchers mentioned above modelled the change in the surface of the dowel by an alteration of the friction coefficient between the steel and timber, showing a Coulomb friction coefficient to be a convenient way to model the relative deflections at the interface between steel and timber. The Coulomb friction model was used in this study, and its application is described in Chapter 6.

Sjödin et al. (2008) stated that it was likely that plastic deformation occurs close to the dowel at higher load levels, and pointed out that the slip between the dowel and the main part of the timber, therefore, may be partly due to plastic shear in the timber. The 'friction coefficient', therefore, represents both the true frictional slip and this plastic shear. The appropriateness of the Coulomb friction approximation is therefore tested as part of this study, as described in Chapter 6.

An alternative to finite element analysis for embedment is the derivation of a stress function which represents the continuous variation of stress and strain throughout the body. The problem of a piece of material with a hole loaded by a circular section is common to various materials and structures, and is generally referred to as a pin-loaded plate. The case in which the pin can be assumed to remain rigidly circular, and the plate can be modelled as orthotropic and elastic is common to the study of timber and fibre-reinforced composite materials.

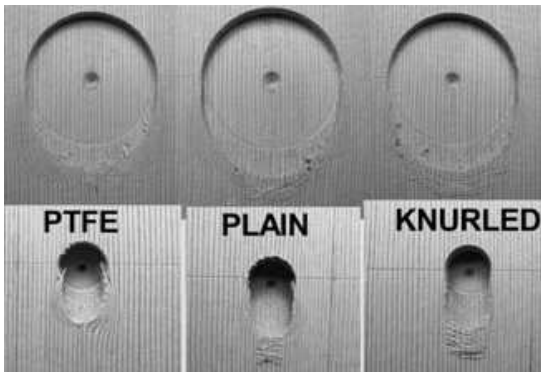

Figure 2-4: Effect of circumferential traction on failure mode of timber around a single dowel (Rodd and Leijten; 2003)

A closed-form solution to this problem can be derived using a complex stress function, and was one of the range of geometries for which the general form of the stress function was derived by Lekhnitskii (1968), as described in Section 2.1.1. This general form of the function was adapted to the particular case in which the load on the edge of the hole is applied by a rigid circular section by De Jong (1977). Different forms of the function have been developed to investigate various phenomena, particularly motivated by the use of composite materials in aircraft. Zhang and Ueng (1984) incorporated the effect of friction at the interface between pin and plate and Hyer and Klang (1985) allowed for deformation of the pin and clearance between the hole and the pin, as well as friction.

There continues to be research interest in the stress function approach, such as the development of a new form of solution by Aluko and Whitworth (2008). One reason for the enduring interest in this approach is the speed of calculation given by a closed-form solution. Derdas and Kostopoulos (2011) use the stress function to determine the loading along the hole edge, and apply that loading to a finite element model, thus reducing the finite element model to a linear elastic one and avoiding the computational cost of carrying out a contact-element analysis.

The potential for application of this method to timber has been clear since Lekhnitskii (1968) used the material properties for plywood in the example calculations in his book, but it was Echavarría et al. (2007) who first noted its potential for application to dowel-type connections in timber structures, and developed a particular form of the stress function for that purpose.

In this study, the stress function models by Zhang and Ueng (1984) and Hyer and Klang (1985) have been investigated in detail, the former for its concise analytical equations and the latter for the generality and accuracy of the solution. The details

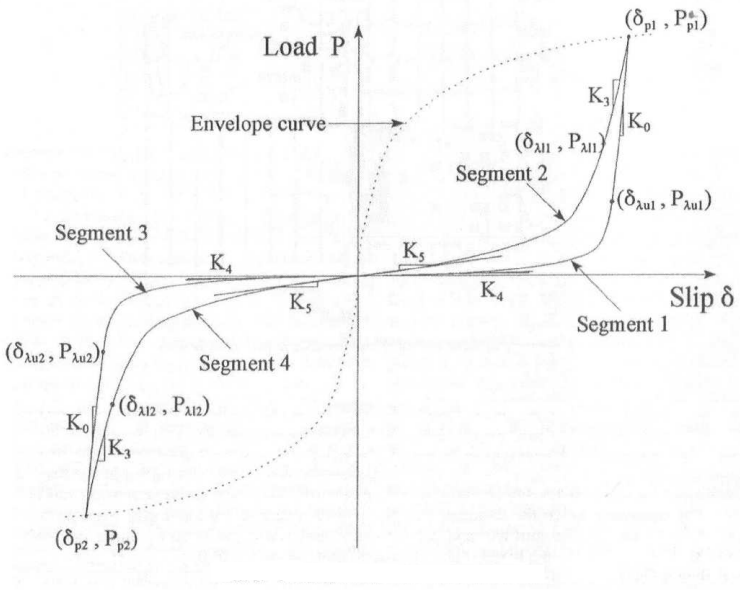

Figure 2-5: Development of hysteresis loops for dowel embedment (Chui and Ni; 1997)

of both approaches and their merits and shortfalls in application to cyclic loading of timber in embedment are discussed in Chapter 6.

The embedment response of timber to cyclic load has not been studied extensively in isolation, most studies incorporating the behaviour of complete connections, as described in Section 2.2.2. One example, however, is by Chui and Ni (1997), who carried out cyclic tests on a connector, and observed the development of hysteresis loops of the shape shown in Figure 2-5. A lower-stiffness region at low load, defined by the stiffnesses K_4 and K_5 in Figure 2-5, was observed to occur as a result of local plastic behaviour around the dowel. This behaviour had been widely noted, but not thoroughly investigated until the doctoral thesis by Dorn (2012), who attributed it to the contact stiffness between the imperfect surface of the timber, and the relatively smooth and hard surface of the steel. Dorn's work also suggested that inelastic behaviour in this contact surface was responsible for other features of the embedment behaviour of a dowel, such as the different force-displacement response under loading and unloading. This behaviour will be further discussed in Section 2.2.2, since Dorn tested and modelled connections in which dowel deformation contributed to the response.

2.2.2 Whole dowels

A model of a complete dowel-type connector must take into account the deformation of the dowel along its length, as well as the embedment described in Section 2.2.1. One

approach is for the embedment and dowel deformation to be represented in a empirical model which allows for both. A simple example is the 'slip modulus' K_{ser} or K_{ult} in Eurocode 5 (BSI; 2009a), which expresses an equivalent elastic stiffness for a connector as a function of the density of the timber and the diameter of the dowel, and is intended to calculate the deformation of a connection under in-service or ultimate limit state static loads. The expression given for K_{ser} for a plain dowel is given in (2.13).

$$K_{ser} = \rho_m^{1.5} d/23 \tag{2.13}$$

Empirically-derived equations such as this are used in design standards globally for prediction of the stiffness of timber connections, however, not all use density as the property with which to characterize the timber. Guidance by the Architectural Institute of Japan, for example, cited by Hwang and Komatsu (2002), uses the elastic modulus of the timber in the relevant direction.

The relationship in Eurocode 5 (BSI; 2009a) was derived by regression analysis of empirical data (Ehlbeck and Larsen; 1993). The coefficient of determination, widely used for evaluation of the accuracy of a model developed by regression analysis, is defined using the standard deviation of the error between a fitted function and the measured results σ_e and the standard deviation of the measured values from their mean value σ_m, as in (2.14).

$$R^2 = 1 - \frac{\sigma_e}{\sigma_m} \tag{2.14}$$

The Eurocode 5 expression in (2.13) uses an empirical relationship between embedment stiffness and density. Embedment tests by Santos et al. (2009), however, suggest that there is not necessarily a reliable correlation between embedment stiffness and density: they stated that the coefficient of determination R^2 for linear regression of the data relating embedment stiffness and density ranged from 0.05 to 0.57 in the four series of tests they carried out. The Wood Handbook (Forest Products Laboratory; 2010) gives mechanical properties for a wide range of wood species, including both density and modulus of elasticity in bending. A comparison of those two properties is shown in Figure 2-6, which shows that there is some correlation between this measure of stiffness and density. A linear relationship was fitted to the collated data using least-squares regression by the *polyfit* function in MATLAB. The resulting line showed that the modulus of elasticity tended to increase with increasing density, with a coefficient of determination R^2 equal to 0.50. Raising density to the power of 1.5, as in (2.13), resulted in the same value of R^2.

Density is a simple property to measure in practice, and shows some correlation with

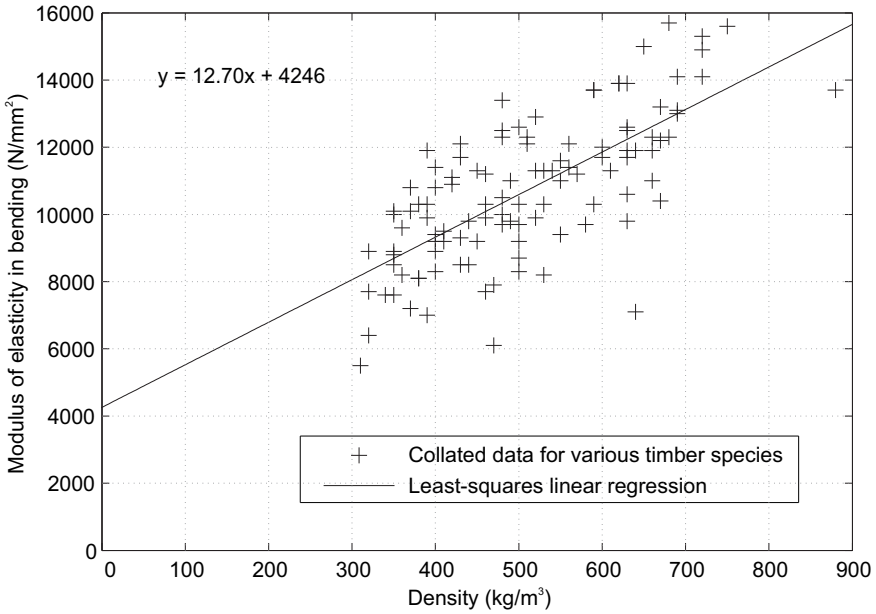

Figure 2-6: Comparison of density and stiffness data, for a range of timber species, taken from the Wood Handbook (Forest Products Laboratory; 2010)

stiffness properties. The orthotropic elastic properties of the timber, however, directly contribute to the stiffness, and were therefore preferred in this study for definition of the stiffness behaviour of connections.

More advanced empirical models have been developed to understand the behaviour of dowel-type connections under earthquake loading. The Bouc Wen Baber Noori (BWBN) model (Baber and Noori; 1986) is an analytical hysteresis model for a single degree of freedom system under forced vibration, which allows for various features of the hysteresis loop observed in force-displacement responses of structural components. An advantage of this model is that its analytical form means that it can be used to calculate the response to a general random loading function. It was modified to suit timber connections by Foliente (1995). The parameters of the model do not relate to any physical properties of the connection, so they must be determined from experimental data for every connection type, such as by Zhang et al. (2002), but once that has been done, the model can be used to efficiently evaluate the response to a range of dynamic loads (Liang et al.; 2011).

Heiduschke (2006a) developed a model which bears a closer relationship to the mechanical processes in the connection, in that it is defined by parameters representing dowel bending, friction and wood embedment. A combination of spring, slider and gap elements were used to build up a model for a bolted connection, and cyclic tests were carried out to fit the model parameters to its hysteretic force-displacement behaviour.

The model does not have the mathematical convenience of the BWBN model, however, so must be modelled in a non-linear time-history analysis (Heiduschke; 2006b), and the model parameters for Heiduschke's model still have to be defined by tests on each connection to be modelled.

A widely-used model which is based on the mechanical properties of timber and connector is the beam-on-foundation model, in which the beam represents the bending behaviour of the dowel, and the foundation represents the resistance in embedment of the surrounding timber. The solution to the problem of a beam on elastic foundation was originally derived by Winkler (1867), as he studied the behaviour of railway sleepers.

Having mentioned beam-on-foundation models, it is pertinent to briefly return to the Eurocode 5 (BSI; 2009a) model for the stiffness of a dowel-type connection, described by (2.13). That model makes no allowance for the length of the dowel or the dimension of the timber along the dowel axis. This observation can perhaps be explained by the fact that, for a beam of circular section on an elastic foundation, the stiffness seen by a central point load K_{bf} tends towards (2.15) as the length of the beam increases, where d is the beam diameter, E_b the elastic modulus of the beam and k_f the foundation modulus.

$$K_{bf} = d\sqrt[4]{\pi E_b k_f^3} \tag{2.15}$$

Therefore for a long dowel, the stiffness is proportional to the diameter of the dowel. This corresponds to the Eurocode 5 model, given in 2.13 so, even if the derivation of that model was entirely empirical, it does follow the same trend as beam-on-elastic-foundation theory. The theory therefore suggests that the Eurocode model may be inaccurate for shorter dowels, and this observation is discussed further in Chapter 7.

The beam-on-foundation model was first applied to timber connections by Kuenzi (1955), and beam on foundation models were later used by Chui et al. (1998), Foschi (2000) and Sawata and Yasumura (2003) to model nailed connections, using non-linear embedment parameters for timber and connector. In this study, for its simplicity and its direct relationship to the material properties of the connection, a beam-on-foundation model is applied to represent the connection stiffness under vibration. The nature of the model required to represent stiffness under vibration is described in Chapter 7.

The stress-strain behaviour of steel can be readily used to evaluate the behaviour of the beam in its elastic and plastic ranges. The foundation modulus, on the other hand, has conventionally been empirically defined. Chui and Ni (1997) and Sawata and Yasumura (2002) used embedment tests in which dowel deformation was considered negligible in order to determine the embedment parameters.

In contrast, Foschi et al. (2000) used tests on a relatively flexible nail to determine foundation properties for the beam-on-foundation model. Since the nail deformed in the test, an assumed deformed shape of the nail was used to calculate the foundation stiffness. Foschi argued that this was the most accurate way to obtain this parameter, since it is not possible to carry out an embedment test with the dowel fully enclosed in the timber in which the dowel does not bend.

If the timber does not fully enclose the dowel, then the dowel can be held rigidly straight as it is loaded. This is the basis of the method given by the American Society for Testing and Methods (ASTM), described in D5764 (ASTM; 1997), in which the dowel rests in a half-hole in the surface of the timber specimen, and is loaded by a flat loading head. Conversely, the European Norm (EN) for dowel embedment, EN383 (BSI; 2007), tests a dowel passing through a complete hole in the timber specimen, and recommends that the results be corrected to allow for deformation of the dowel. The precise test setup to determine this correction is not clear, however, since the text of the standard simply asks that a tight-fitting steel specimen be used.

These two methods were compared through experiment and finite-element modelling by Santos et al. (2010). They tested 24 specimens according to each standard, and found the mean stiffness according to the ASTM method 7.6% higher in the longitudinal grain direction and 1.2% lower in the radial direction, using no correction for dowel deformation. Given the coefficient of variation of measured stiffness of 22% for the ASTM tests and 18% for the EN383 tests, these variations are small in comparison to the natural variation in the material.

The results of the finite-element model by Santos et al. (2010) allowed a more detailed consideration of the nature of the difference between the tests. The finite element model for the EN method required a sensitivity study into the nature of the contact between the loading piece and the dowel: The contact between the two neither provided complete moment restraint to the dowel nor simply supported it. Santos et al. (2010) therefore simulated both conditions. When the timber was loaded in the longitudinal grain direction, the results of the simulation showed an elastic stiffness 9.1% higher than the ASTM model for the clamped condition, and for the simply supported condition the stiffnesses of the two models were within 0.3%. The results therefore again suggested that the effect of the timber on the unloaded face of the dowel on the foundation modulus is small in comparison to the coefficient of variation of the stiffness.

Santos et al. (2010) noted that, in finite-element modelling, contact elements between dowel and timber had to be assigned a finite stiffness, which resulted in seemingly unrealistic penetration of one surface into the other, called overclosure. Dorn (2012)

used that feature of the contact element models to represent an important aspect of the force-displacement behaviour of the connection: the imperfection of the contact surface between dowel and timber. As a result, he was able to model the gradual increase in stiffness in a connection as the load is increased from zero, tending towards a maximum stiffness in a linear section of the force-displacement curve.

Dorn (2012) investigated the conventional dowel-type connection, and studied the force-displacement relationship for loading, unloading and reloading. He investigated the contact behaviour between dowel and timber by testing timber blocks with flat surfaces cut by different methods, resulting in different surface finishes, and loading them with a flat steel plate. Qualitatively similar behaviour to the dowel tests under loading, unloading and reloading was observed in these timber blocks, suggesting that the contact behaviour between the face of the dowel and the timber may be responsible for the nonlinear force-displacement relationship in dowel-type connections at low loads and the difference between the first-loading curve and the unloading-reloading curve.

Dorn (2012) also carried out tests using dowels with different surfaces, described as smooth, roughened and knurled. The influence of the dowel surface on the failure mode of the connections was noted, along with the effect on the stress distribution around the dowel. The purpose of Dorn's work was to investigate serviceability behaviour, however, and the effect of the dowel surface on displacement was found to be small. His model predicted a 15% change in stiffness by increasing the friction coefficient in the model from zero to 0.8. In his tests, the effect of changing dowel surface on stiffness could not be clearly observed.

To the author's knowledge, Dorn (2012) was the first researcher to use empirically-derived contact behaviour to model the force-displacement response of a dowel-type connection. As a result, his model provides a unique insight into the development of stress and strain in the dowel and timber as the applied load increases. The annotated force-displacement diagram produced by his model is shown in Figure 2-7. He modelled both timber and steel as elastic-perfectly-plastic materials, and the figure shows that the onset of first yielding in both steel and timber was predicted to occur before even the development of the peak stiffness, and that yield occurs first in the steel. This suggests that the different force-displacement paths for loading and unloading-reloading may be due not only to the irreversible contact behaviour described in Section 2.2.1, but also to irreversible material behaviour in the steel and the timber beyond the contact area.

Three-dimensional finite element models have been used to model various other aspects of the materials and geometry in timber connections (Santos et al.; 2009; Resch and Kaliske; 2010; Dorn; 2012). They can be particularly useful for detailed one-off studies, such as investigating the behaviour of innovative connection types like the

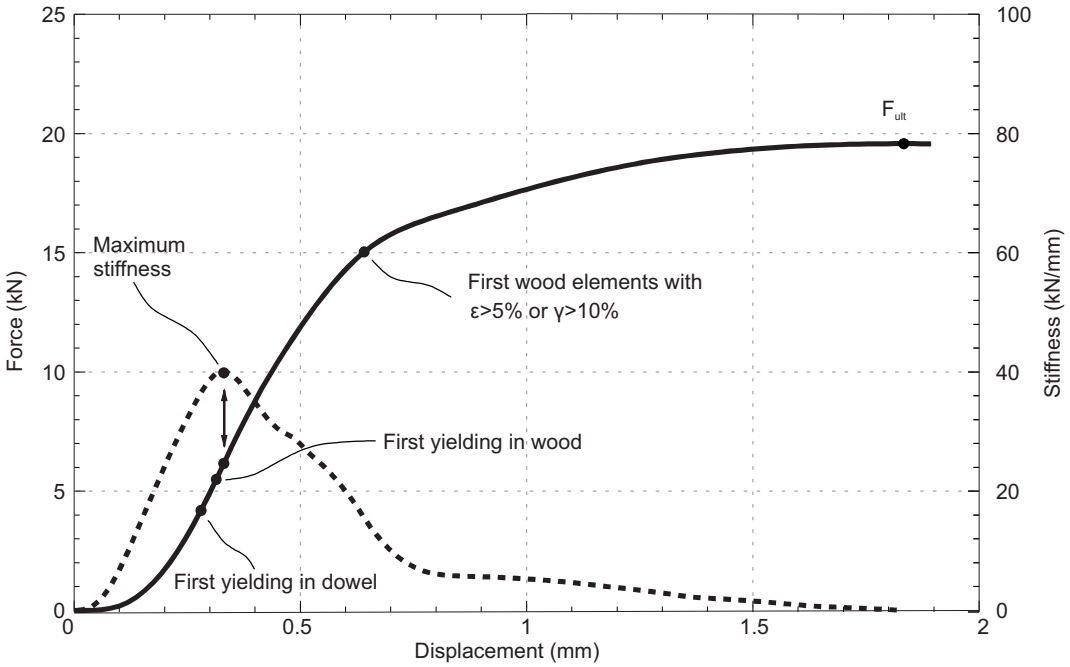

Figure 2-7: Force-displacement response from finite element model of a single dowel-type connection with empirically-derived contact behaviour, replotted from a figure by Dorn (2012)

expanded tube connector by Leijten et al. (2006), or for a detailed investigation of an experimental method, as by Santos et al. (2010). However, the use of finite element models has been limited to academic studies of particular connections, rather than use in practical design, since their construction and alteration is time-consuming, and real structures may contain hundreds of connections, with many different geometries. Given the inherent variation in material properties of timber, and the inaccuracies inevitable in construction, it is considered that the accuracy achieved in finite element models may be unnecessary for application to the engineering of timber structures in general.

2.2.3 Groups of dowels

Single-dowel connections in timber structures are rare, so once the behaviour of a single dowel has been characterized, further analysis must be performed to predict the behaviour of a complete connection.

A connection with n dowels does not, in general, exhibit n times the stiffness of a connection with one dowel. This is because lack of fit of the dowels into the timber and imperfection of the contact surface between dowel and timber means that each connector must move a certain distance before its full stiffness is mobilised, called its

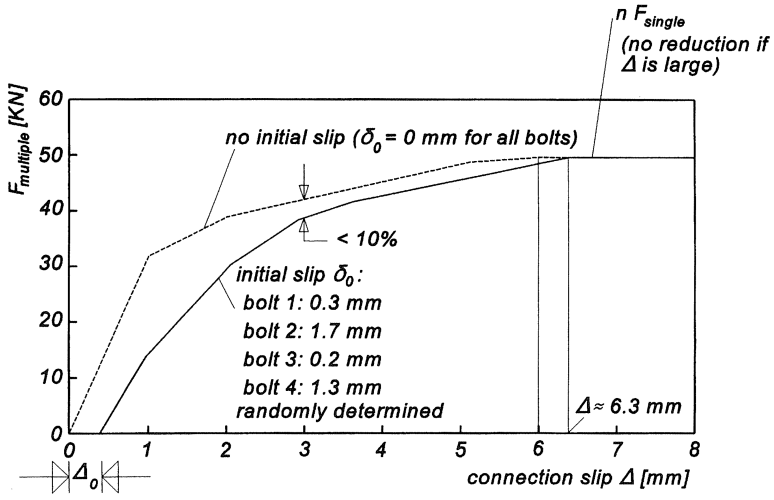

Figure 2-8: Effect of initial slip on overall connection stiffness (Jorissen; 1999)

'initial slip'. This distance will, in general, be different for each connector in a group as a result of tolerances in manufacture, and so the stiffness of the connection will gradually increase as the connection deforms and the stiffness of each dowel is mobilized.

Jorissen (1999) noted this effect and devised a model for a 4-dowel connection loaded axially. The force-displacement diagram for the connection, with randomly-generated initial slip in its 4 dowels, is shown in Figure 2-8. The dowel is assumed to provide no resistance until it reaches its initial slip value, immediately after which it exhibits its maximum stiffness.

In moment connections, conventional design practice assumes that the deformation of each connector is proportional to its distance from the centre of rotation of the connection (Porteous and Kermani; 2007). Chui and Li (2005) used a beam-on-foundation model to represent a moment connection with the same assumption, and noted that the stiffness of the connection was generally over-predicted.

Noguchi and Komatsu (2004) investigated this deformation by considering the transfer of forces across the shear plane in each connector to be equivalent to a plane in torsion. They state that the conventional approach is analogous to Coulomb torsion theory, in which the shear stress and strain in a body subject to torsion is proportional to the distance from its centre of rotation. The assumption that the deformation at each connector is proportional to its distance from the centre of rotation relies on the behaviour closely approximating the conditions described by Goodier (1942), where the deformation occurs in a thin elastic layer between two rigid plates. In reality, in a dowel-type connection, there is deformation in the timber between the centre of rotation and

each connector, and the connectors themselves deform, both of which affect the distribution of forces. Noguchi and Komatsu (2004) presented an alternative representation of the stiffness and strength behaviour of a group of connectors using Saint-Venant torsion theory, which is appropriate for a thick elastic layer between rigid plates. In their experiments, they showed that the conventional approach over-predicted stiffness by as much as two times for asymmetric arrangements of connectors, while Saint-Venant torsion theory gave a more accurate prediction.

Saint-Venant torsion theory was derived to represent torsion in a continuous solid, so its application to a set of discrete connectors requires care, but an analogy can be drawn between the torsional warping in a thick plate and the bending deformation of connectors in a moment connection in timber, and the experimental results presented by Noguchi and Komatsu (2004) justify that analogy.

2.2.4 Prediction of strength

Although this study is concerned with the behaviour of connections in service, rather than their failure, it will be necessary to evaluate the strength of connections to provide a reference value with which to evaluate the likely in-service loads.

The calculations for connection strength in Eurocode 5 (BSI; 2009a) are based on Johansen's equations (Johansen; 1949). Johansen derived equations for connection strength for ductile failure modes in nailed, dowelled and bolted connections based on plasticity theory, and empirically-based methods for avoiding brittle failure modes. The equations were modified for inclusion in Eurocode 5 to allow for the pull-out resistance of the fastener, and to allow strength calculation for joints between timber members with different structural properties. The resulting set of equations is known as the European Yield Model, and is used in Chapters 5 and 7 for strength prediction. The connections tested and analysed in this study all have a central steel plate inserted into a slot at the end of the timber member and attached by steel dowels. The force is therefore transferred between the plate and the timber member across two shear planes, and so the strength of the member in the various failure modes is given by (2.16) to (2.18), and the predicted strength will be the minimum of the values given by those three equations. F_v is the strength of a single connector, f_e is the embedment strength of the timber, t is the width of the loaded part of the timber on each side of the plate and M is the moment capacity of the dowel. F_v is expressed as the minimum of the upper-bound strengths from the three possible failure modes: $F_{v,1}$, $F_{v,2}$ and $F_{v,3}$. The failure modes are illustrated schematically in Figure 2-9, which shows the variation of connection capacity for a 12mm steel dowel in glued-laminated timber of the GL28h grade according to EN 1194 (BSI; 1999).

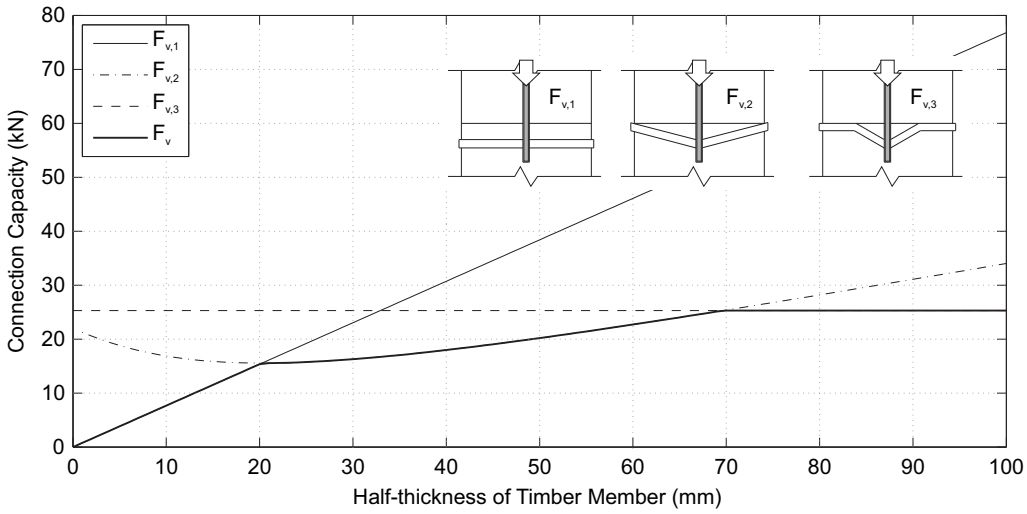

Figure 2-9: Predicted capacity of a connector using the European Yield Model according to (2.16) to (2.18)

$$F_{v,1} = 2f_e td \tag{2.16}$$

$$F_{v,2} = 2f_e td\left(\sqrt{2 + \frac{4M}{f_e dt^2}} - 1\right) \tag{2.17}$$

$$F_{v,3} = 4.6\sqrt{Mf_e d} \tag{2.18}$$

2.2.5 Effect of angle to grain

The effect of angle to the grain on the strength of connections is then allowed for in Eurocode 5 (BSI; 2009a) by (2.19), an empirical equation proposed by Hankinson (1921). α is the angle of the load to the grain direction in degrees.

$$f_{e,\alpha} = \frac{f_{e,0}}{\frac{f_{e,0}}{f_{e,90}}\sin^2\alpha + \cos^2\alpha} \tag{2.19}$$

Schniewind and Barrett (1972) later showed that this transformation equation could be applied to the magnitude of creep at different angles to grain. This result is important in the context of this study, since it suggests the transformation equation applies to a deformation effect, as well as the original application to strength calculations. Eurocode 5 (BSI; 2009a) makes no allowance for the angle of the load to the grain in calculating the slip modulus K_{ser}. Where it is necessary to interpolate the stiffness of a

single connector between the parallel- and perpendicular-to-grain directions in Chapter 7, therefore, the equation developed by Hankinson (1921) is used.

2.3 Structural dynamics

2.3.1 In-service vibration

Most structures are in a constant state of movement. While the majority of the design process is normally concerned with transmitting forces which can be approximated as static loads, such as the self-weight of a building, its cladding, furniture and occupants, there is also a range of dynamic loads applied to a structure throughout its life. This includes the footfall loading as occupants move around a building, the constantly varying pressure applied by turbulent wind, the vibration of machinery housed in the structure, deliberate or accidental impacts, waves in water and seismic actions.

Most vibration goes by unperceived and without detriment to the performance of the structure. However, if the vibration is sufficient in magnitude, it can

- produce higher forces on structural components than the peak static load;
- cause failure of structural components due to fatigue;
- affect the operation of sensitive equipment supported by the structure; or
- lead to discomfort of building occupants and therefore complaints.

Such an occurrence can constitute a failure of the structure either in the ultimate limit state, in the case of the first two items, or in the serviceability limit state, in the case of the latter two. This study focusses on the serviceability limit state, so addresses the potential for vibration to affect the ability of a structure to perform its function under the actions applied to it during its normal service life. Previous research and design methods for in-service vibration are described in this section and in Chapter 4 the methods and data are used to define the magnitude of the forces and displacements under such vibration.

In this study, wind-induced and footfall-induced vibration are investigated to define loads representative of in-service vibration. They were chosen because they are common loads experienced by building and bridge structures. Both have also been extensively researched, which made it possible to estimate the loads they impose on a structure based on reliable methods and experimental results.

2.3.2 Wind-induced vibration

Modern design codes such as Eurocode 1 (BSI; 2005) give guidance on assessment of wind-induced vibration in structures. Wind-induced vibration can be divided into

- processes in which a dynamic pressure is imposed on the structure by the nature of the air flow, causing the structure to vibrate and
- a process in which the air flow and the movement of the structure interact, modifying the dynamic load on the structure and its vibration.

The former will be referred to as dynamic-pressure effects, and the latter aeroelastic effects.

In Eurocode 1 (BSI; 2005), the dynamic effects due to wind load are: along-wind vibration due to turbulence; across-wind vibration due to vortex shedding; wake buffeting; galloping; divergence; and flutter.

2.3.2.1 Along-wind vibration due to turbulence

Along-wind vibration due to turbulence is considered as a dynamic-pressure effect. Wind is a turbulent flow, which means that the force imposed on a structure in the flow varies with time as vortices move around the structure. This varying force has the potential to cause a resonant response in the structure, which is known as along-wind vibration.

The time-history of pressure exerted by the turbulent air flow on a structure cannot be precisely predicted, so is instead represented as a stochastic variable, the magnitude of the frequency components of which are defined. Modern analytical methods are based on a method first proposed by Davenport (1961), in which the wind speed was broken down into a mean and time-varying component. The time-varying component of the wind speed was expressed as a stationary stochastic variable, whose properties were defined by a power spectral density function. This approach was further developed by Simiu and Scanlan (1986), who derived an analysis method based on the structure as a slender, line-like vibrating object.

The power spectral density function (PSD) is central to the method proposed by Davenport (1961). The PSD is the Fourier transform of the autocorrelation function of a variable. It is, therefore, a function in the frequency domain. Here, frequency will be represented by n, and the PSD by $S(n)$. Where a variable in the time domain, say $x(t)$, is represented as its PSD, the variable will be indicated in the subscript, i.e. $S_x(n)$.

The reason that the PSD is used in wind loading analysis is that it has some useful properties when dealing with the dynamics of linear systems. Say a linear system has a transfer function in the frequency domain $H(n)$, so that $X(n) = H(n)F(n)$, where $X(n)$ is the Fourier transform of a displacement variable $x(t)$ and $F(n)$ is the Fourier transform of a force variable $f(t)$. $H(n)$ is a transfer function known as the receptance, and can be obtained based on the mechanical properties of the system. The same transfer function can be used for the PSD, as in (2.20).

$$S_x(n) = H^2(n)S_F(n) \tag{2.20}$$

Once the PSD for displacement is obtained, the mean square value of x, σ_x^2, can be obtained from (2.21).

$$\sigma_x^2 = \int_0^\infty S_x(n)\mathrm{d}n \tag{2.21}$$

Therefore the PSD of the response can be calculated from the PSD function of the applied force, and the mean square value, and therefore the standard deviation, of the response can then be calculated, which can be compared to acceptability criteria, or used to derive an equivalent static load for capacity calculation.

2.3.2.2 Across-wind vibration due to vortex shedding

When the speed of a fluid flow around a bluff body reaches a critical value, it causes vortices to be shed alternately from one side of the body and the other. This effect was originally described by von Karman and Rubach (1912), and the resulting trail of vortices are known as the von Karman vortex street.

The periodicity of this phenomenon means that a periodic variation of force is experienced by the bluff body in a direction perpendicular to the flow direction. In building structural dynamics, the resulting vibration response is known as across-wind vibration. Vibration due to vortex shedding can be primarily a dynamic-load effect or primarily an aeroelastic effect, since the oscillation of the structure can affect the rate of vortex shedding and the magnitude of the pressure exerted on the structure. A particularly dramatic aeroelastic response can occur when the frequency of vortex shedding is equal to the natural frequency of the structure.

2.3.2.3 Other aeroelastic effects

The other aeroelastic effects for which guidance is given in Eurocode 1 (BSI; 2005): wake buffeting, galloping, divergence and flutter, all only have a significant influence on

extremely slender, flexible structures. They have, therefore, been excluded from this study.

2.3.3 Footfall-induced vibration

Renowned Scottish civil engineer Robert Stevenson (1821) described the effect of footfall-induced vibration on a timber bridge.

> The greatest trial, for example, which the timber bridge at Montrose, about 500 feet in extent, has been considered to withstand, is the passing of a regiment of foot, marching in *regular time*.

The vibration which can build up in a structure in resonance with a crowd performing rhythmic activities remains an important design consideration for structural engineers.

Since Stevenson's time, structures have become ever more lightweight due to the development of more efficient structural forms, improved connection methods and, even within the field of timber construction, improved materials. The result is that footfall-induced vibration in floors and bridges has been the cause of many serviceability failures of structures in recent years, and has been a subject of extensive research interest.

Bachmann and Ammann (1987) characterized the force imposed by a person walking on a rigid surface by Fourier decomposition. They identified the coefficients of the first five terms in a Fourier series to represent the force imposed by footfall, and represented them as dynamic load factors (DLFs), where the DLF is the ratio of the Fourier coefficient to the weight of the person walking. Knowledge of these imposed forces was then extended by Rainer et al. (1988), who experimentally derived DLFs for a single person walking, running and jumping at a range of speeds and footfall frequencies.

This representation of the footfall force forms the basis of a method commonly used in practice for assessment of footfall-induced resonant vibration (Willford and Young; 2006; Smith et al.; 2009), in which the maximum response of the structure is taken to occur when one of the frequency components of the footfall force coincides with a natural frequency of the structure. The peak or root mean square acceleration of the floor is then calculated based on the natural frequency, modal mass, DLF and damping.

If none of the frequency components of the footfall force coincides with a natural frequency of the structure, i.e. if the highest frequency component of the footfall force is lower than the fundamental natural frequency of the structure, then the impulse response of the floor is considered (Willford and Young; 2006; Smith et al.; 2009).

An alternative approach to modelling footfall loading was proposed by Eriksson (1994), cited by Živanović et al. (2005), who defined the footfall force as a narrow-band

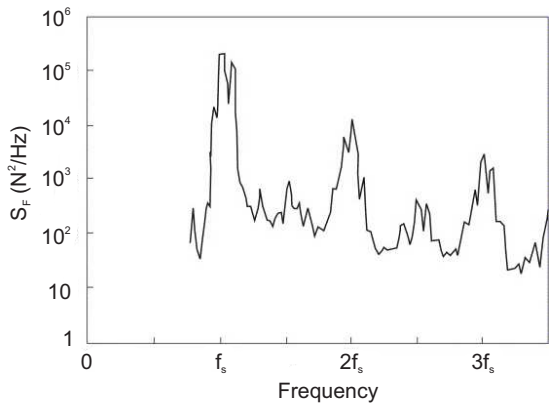

Figure 2-10: Power spectral density function for footfall force, after (Eriksson; 1994)

stochastic process. With this definition of the footfall force, an analysis method similar to that used for along-wind vibration of structures, described in Section 2.3.2.1, can be used to calculate the structural response. As shown in Figure 2-10, however, the power spectral density function is dominated by the force at the step frequency and its multiples, which suggests that the improvement in accuracy of the calculated response may not be sufficient to make this method preferable to the more intuitive approach based on considering each of the frequency components independently.

Bachmann (1992) and Ingólfsson et al. (2012) reported case studies of structures where significant footfall-induced vibration has been noted by engineers, some of which resulted in complaint by users of the structures. A summary of those case studies is shown in Table 2.1. All of the measured and calculated vibrations are due to resonance between one of the frequency components of the footfall force and a mode of vibration of the structure either in the vertical or lateral direction. The lowest frequency of the structure in the relevant direction is tabulated. With the exception of the pop concert, all of the crowd loadings were produced in experiments in which a crowd of volunteers was asked to walk or jump in a particular way, so the measured peak accelerations may represent the worst case of vibration that could occur in service.

Table 2.1 shows that excessive vibrations have been observed in structures in all major structural materials, and particularly in modern, lightweight structural forms. In vertical vibrations, most of the cases addressed by Bachmann (1992) are in buildings in which crowds move rhythmically in unison, and the vibrations which were observed to result from such behaviour were considerable. The 8.6m/s^2 recorded in Sports hall No. 1 would result in at least part of the mass of the structure itself being subject to an inertia force almost as large as the gravity force, i.e. a peak dynamic load nearly twice the static load from the mass of the part of the structure moving with this acceleration.

Figure 2-11: The Lardal footbridge, photograph by Anders Rönnquist

The Lardal footbridge in Norway, shown in Figure 2-11, is worthy of particular consideration, since it is the only structure in Table 2.1 which is made of timber. It was caused to vibrate laterally by footfall excitation, which eventually meant that a steward was employed to ensure that the bridge was not used by too many people at one time. Rönnquist et al. (2006) created a dynamic model of the structure, and made particular reference to the inaccuracy in the model due to the difficulty in estimating the semi-rigid connection stiffness of the screwed dowel-type connections between the steel and timber elements of the bridge. In their model, this stiffness was eventually chosen to fit the model to the observed natural frequencies of the bridge. This shows the challenge currently facing the designers of such structures, in that the behaviour of connections under in-service dynamic load has not been properly researched.

Table 2.1: Case studies of footfall-induced vibration (Bachmann; 1992; Ingólfsson et al.; 2012)

Case study	Main structure	Stage	Test method	Lowest freq. (Hz)	Peak accel. (m/s^2)	Subsequent action
Vertical vibration						
Footbridge No. 1	Post-tensioned concrete	Preliminary	Calculated	2	0.8	redesign
		Constructed	Calculated	2.4	0.4	no complaint
Footbridge No. 2	Steel girder	Constructed	Crowd walking	4		vertical vibration noticed
Gymnasium No. 1	Reinforced concrete beams	Constructed	Crowd jumping	4.9	5.2	retrofit additional stiffness
Gymnasium No. 2	Ribbed concrete slab	Constructed	Crowd jumping	5.15	1.7	retrofit additional stiffness
Sports hall No. 1	Prestressed concrete	Constructed	Crowd jumping	2.4	8.6	design modification and retrofit
Concert hall	Hollow concrete slab	Constructed	Pop concert	6.2	2.7	change of use
Lateral vibration						
London Millennium bridge	Shallow steel suspension	Constructed	Crowd walking	0.48	0.8	retrofit tuned vibration absorbers
Paris pont de Solférino	Steel arch	Constructed	Crowd walking	0.81	0.6	retrofit tuned vibration absorbers
Changi Mezzanine Bridge	Steel arch	Before opening	Crowd walking	0.9	0.17	tuned vibration absorbers installed
Lardal footbridge	Shallow glulam arch	Constructed	Crowd walking	0.81	1	limited number of people on bridge
Weil-am-Rhein footbridge	Steel arch	Before opening	Crowd walking	0.91	1.7	number of people on bridge limited

2.3.4 Seismic vibration

There has been a great deal of research into the dynamic performance of timber structures with dowel-type connections under the forces and displacements associated with seismic loading (Polensek and Schimel; 1991; Folz and Filiatrault; 2001; Filiatrault et al.; 2003; Heiduschke; 2006b; Ceccotti; 2008; Filiatrault et al.; 2010). Heiduschke (2006b) tested a timber frame with bolted connections using a shaking table, and sheathed stud walls were tested by Polensek and Schimel (1991). Both noted the variation of damping coefficient with amplitude of loading.

The variation of damping with amplitude can be understood as a variation in each of the mechanisms contributing to damping. As amplitude increases, for example, the normal force on friction surfaces changes, materials enter their plastic range and so on. This highlights the importance of defining the energy dissipation properties for timber structural systems under the appropriate range of load.

Filiatrault et al. (2003) investigated damping in a sheathed stud-and-rail timber structure, and developed a method for assessing the variation of damping with peak displacement, and the degradation of stiffness with repeated cycles of load. This was done by defining a numerical computer model with hysteretic connections and components, then verifying the model against shake-table tests on full-scale structures. The behaviour of the panel elements was modelled with a non-linear hysteresis model appropriate for the highly non-linear behaviour associated with the seismic response of such a building. The numerical model was then used to predict damping for different drift ratios, where the drift ratio is defined as the horizontal deflection divided by the vertical height. This resulted in the empirical equation (2.22), in which γ is the equivalent viscous damping ratio for the whole system and Δ_b is the drift ratio.

$$\begin{aligned} \gamma &= 50\Delta_b \quad \text{for} \quad 0 \leqslant \Delta_b < 0.36\% \\ \gamma &= 0.18 \quad \text{for} \quad 0.36\% \leqslant \Delta_b \end{aligned} \tag{2.22}$$

In serviceability considerations, the drift of a building is limited to prevent damage to the non-structural elements connected to the structure. Investigations such as that by Charney (1990) into the potential for damage to non-structural elements by lateral deflection in buildings have resulted in design guidance such as that given in the UK National Annexe to Eurocode 3, which gives guidance for the design of steel structures (BSI; 2008b), and recommends a horizontal drift limit of height/300 or 0.33%. Applying (2.22) at this drift level gives a damping ratio of 15%. Such a conclusion must be treated with care, however, since the highly non-linear model used by Filiatrault may not be

appropriate for the smaller drifts associated with wind-induced vibration.

2.3.5 Acceptability of vibration

An overview of studies on assessment of human response to wind-induced vibrations was given by Kwok et al. (2009). He noted that experimental studies on human perception of movement fell into three categories:

- surveys and experimental measurements in wind-excited tall buildings;
- experimental measurements in artificially excited tall buildings; and
- shaking table and motion simulator tests in laboratory environments.

Irwin (1978) gathered the results of earlier tests on human perception of vibration from various sources, and used them to derive a set of acceptability criteria. He noted that perception depended on the frequency of movement, on the nature of the surroundings and activities being undertaken by the person and on the direction of movement relative to the person. Irwin proposed using acceleration as the parameter with which to define the acceptable level of vibration, on the basis that it is the acceleration of a vibrating structure which is most readily measured, and for compatibility with previous guidance for human-induced vibration from other sources.

Acceleration remains the primary way of expressing the magnitude of vibration in current design guidance, either in terms of its peak or root mean square value (ISO; 1984; Willford and Young; 2006; ISO; 2007; Smith et al.; 2009). The likelihood of complaint is also said to be effected by the regularity with which vibration of a particular level occurs, and this is allowed for in BS EN 6742 (BSI; 2008a), in which the vibration dose value, an integral of the magnitude of vibration over time, is defined as a measure of the likelihood of complaint by building occupants. Vibration limits are specified by ISO 10137 (ISO; 2007) for movement in vertical and lateral directions at a range of frequencies.

2.3.6 Modal analysis

Modal analysis investigates modes of vibration, either of real systems through experiment, or of theoretical systems through calculation. The modes of vibration of a linear or near-linear system can be used to predict how it will behave under a general dynamic load, since they form an orthogonal set which completely describes the distribution of its mass, stiffness and damping, encoded in the natural frequencies, modal masses and damping ratios of the modes.

Studies of the dynamic characteristics of multi-storey timber structures are rare, but a dynamic analysis of a 6-storey brick-clad timber frame building was carried out as part of the tests on the Building Research Establishment's Timber Frame 2000 project (Ellis and Bougard; 2001). In that project, lasers were used to measure ambient vibration during construction, to investigate the contribution of the structural elements and cladding to the stiffness and damping of the building. Accelerometer measurements of forced vibration were then used on the completed building. This work highlighted the influence of secondary elements on the dynamic properties of this type of structure: the addition of the brick cladding roughly doubled the natural frequency of the structure in each direction. Similarly, Filiatrault et al. (2010) noted a strong influence of stucco and gypsum boards on the dynamic response of a stud and rail timber structure.

This pronounced effect of non-structural elements is not confined to timber structures, however. Proen and Branco (2005) carried out modal analysis of buildings ranging from 1 to 11 storeys forming the Santa Maria Hospital Complex in Lisbon, and found that the stiffness of the buildings was generally two or three times that predicted by elastic analysis for the bare reinforced concrete frame. They attributed this increase in stiffness to the infill masonry walls, not included in the elastic analysis.

Modal analysis of structures typically approximates the structure as a linear system, with linear-elastic stiffness and linear viscous damping throughout. Given the nonlinearity exhibited by timber connections, the effect of nonlinearity on the modal properties of a system is relevant. Duffing (1918) derived the mobility of a system with stiffness made nonlinear by incorporating a cubic function of displacement into the force-displacement relationship. A set of receptance plots are shown in Figure 2-12, and show that the cubic stiffness causes the resonant peak response to move to the left or right depending on its sign. The peak moves further with an increasing amplitude of applied force, eventually producing a discontinuity.

This effect is considered important given the similarity between the force-displacement behaviour of dowel-type connections at low loads, where stiffness gradually increases with load, to the cubic stiffness model. The measured response of systems with dowel-type connections is discussed in light of this effect in Chapter 7, and the mathematics of Duffing's derivation is examined and slightly extended.

2.3.7 Damping models

The dynamic behaviour of individual degrees of freedom in a structural system can be modelled in a variety of ways, reflecting the shape of the response on a force-displacement plot and the dependence of that response on time, frequency and amplitude. In this section, a range of models for dynamic behaviour is presented.

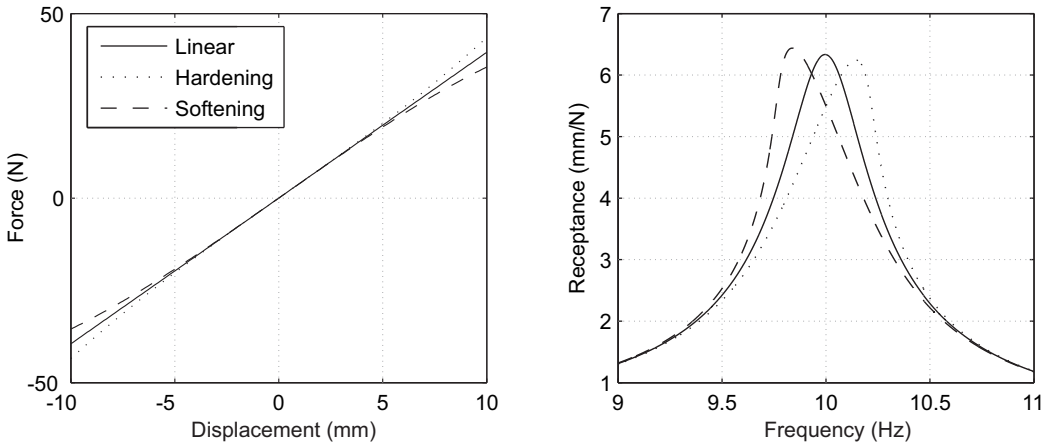

Figure 2-12: Receptance plots for Duffing oscillators with a linear natural frequency of 10Hz, mass of 1kg and a viscous damping ratio of 2%, under an oscillating load with magnitude 1N

A viscous damper applies a resistance force proportional to the rate of change of its extension, and is by far the most commonly used dissipative element, since, when used with an otherwise linear system, it allows a linear transfer function to be written. It is referred to as viscous because viscous fluids are generally observed to exhibit this dependence of resistance force on rate of change of displacement. In an oscillating system, this rate dependence results in an increase in energy dissipation with frequency.

The use of the viscous damping model for structural damping was brought into question when the energy dissipation in many structural materials, including Maple wood and steel, was shown by Kimball and Lovell (1927) to be independent of frequency. No other dissipative element has been found with the mathematical convenience of the viscous damper, however, and so it continues to be used for most structural engineering purposes.

Figure 2-13 shows the force-displacement diagrams for a viscous damper under sinusoidal load at two frequencies. The area inside the hysteresis loop on the force-displacement diagram is significant since it is proportional, as described in Section 5.2.3, to the energy dissipated, and therefore the damping in the system. It can be seen that this area increases with frequency for the viscous damper.

Many engineering material exhibit viscoelastic behaviour, so their response to an applied force consists of a combination of both viscous and elastic components. Various rheological models for viscoelasticity are discussed in Section 2.1.2, consisting of combinations of elastic springs and viscous dampers. As described in that section, those models have generally been used to represent the creep response of timber. Such models also give a response to cyclic loading, and the response of the Kelvin-Voigt ele-

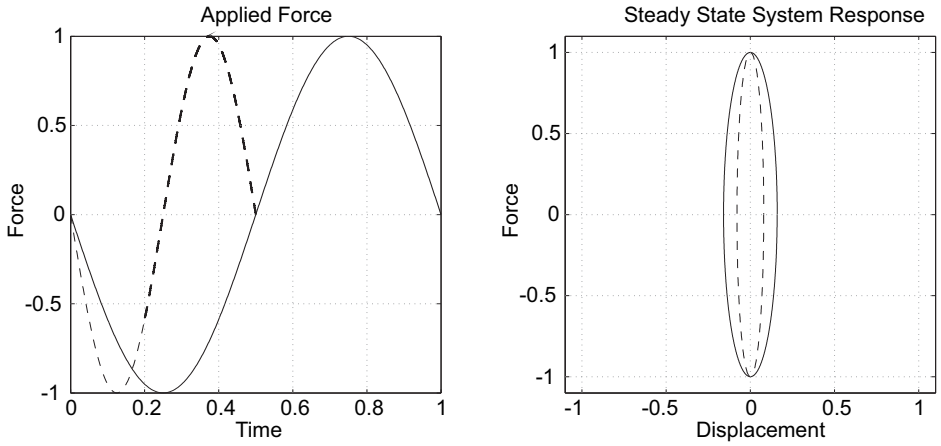

Figure 2-13: Force-displacement diagrams for a viscous damper under sinusoidal load

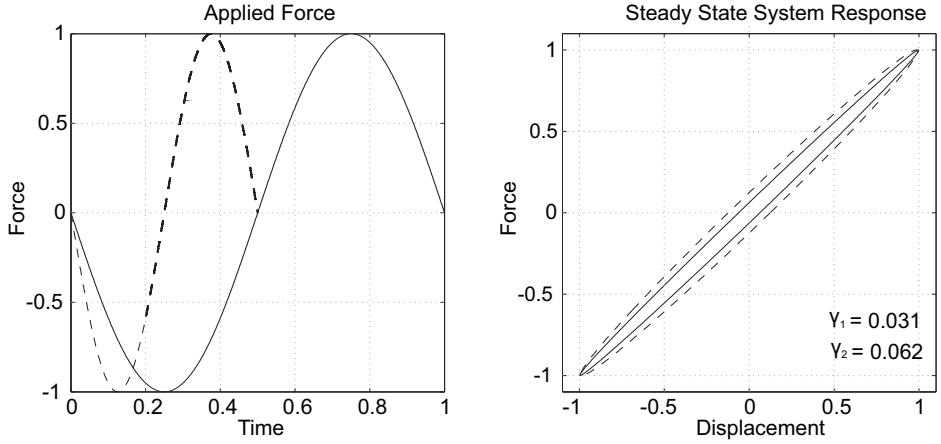

Figure 2-14: Force-displacement diagrams for a spring and viscous damper in parallel under sinusoidal load

ment is shown in Figure 2-14. Again, it can be seen that the magnitude of the energy dissipated varies with frequency.

A rheological model consisting of elastic springs and viscous dampers is used in Section 6.6 to model the response of timber in embedments to a step load with a superimposed oscillating component. Such a model can represent the response to both creep and cyclic load, and so both the transient effects, which are considered to be creep effects, and the steady-state stiffness and damping are captured in the same model.

A damping model in which energy dissipation does not change with frequency is the hysteretic damping model. The term 'hysteretic damping' is slightly misleading, since all damping is the result of hysteresis, but the term is widely accepted as meaning damping for which the energy dissipated is independent of frequency. For this to be

the case, the force exerted must be independent of the rate of change of extension. For the steady-state response to a purely sinusoidal input function, this behaviour can be represented in the frequency domain using complex representation.

If the input force f is purely sinusoidal, it can be expressed as $f = Re(Fe^{i\omega t})$, where F is the magnitude of the force, i is the imaginary unit, ω the circular natural frequency and t time. $Re()$ represents the real part of the complex number in the brackets. The complex number F, therefore, encodes both the magnitude and phase of the input force. The steady-state response can then be assumed to be in the form $x = Re(Xe^{i\omega t})$, where X encodes the magnitude and phase of the displacement x. The equation of motion for a system with viscous damping c, (2.23), can then be simplified by substitution to (2.24), which can be more easily solved for X.

$$m\ddot{x} + c\dot{x} + kx = f \tag{2.23}$$

$$(-\omega^2 m + i\omega c + k)X = F \tag{2.24}$$

The most common way of representing hysteretic damping is to use a complex elastic modulus for the material, replacing the elastic modulus k with $k + ig$, so that the equation of motion of the system is given by (2.25). The damping force is, therefore, proportional to the displacement and independent of $\dot{x}$, but since it is multiplied by i, it represents a force in anti-phase with the displacement.

$$-\omega^2 mX + (k + ig)X = F \tag{2.25}$$

The force-displacement diagram for a hysteretic damper under sinusoidal loading at two different frequencies is shown in Figure 2-15. The response is seen to be identical whatever the frequency of applied force.

The main drawback of the hysteretic damping model is that it is only applicable to the steady-state response of the system to a sinusoidal input force. Crandall (1991) showed that the model gives a non-causal response for other, non-periodic, inputs, which is to say that it gives a response in the time domain before any force has been applied. A more widely applicable hysteretic damping model is proposed by Chen and You (1997), but that model does not have the mathematical simplicity of the complex elastic modulus approach.

Despite this drawback, the complex elastic modulus has been widely used in circumstances in which it is the steady-state dynamic response which is of interest. Dynamic mechanical analysis is one, in which the complex modulus of a material is identified by small-amplitude (of the order of 0.1mm) vibration testing of small specimens (of the

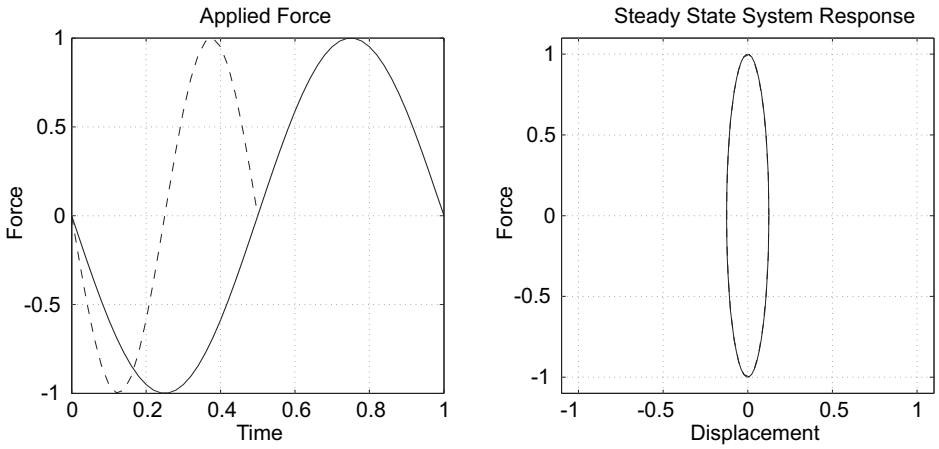

Figure 2-15: Force-displacement diagrams for a hysteretic damper under sinusoidal load

order of 50mm long), which represents the elastic and dissipative properties of the material, typically measured over a range of temperatures or water contents (Birkinshaw et al.; 1986; Sun et al.; 2007; Jiali and Jianxiong; 2009). Labonnote et al. (2013) showed that by representing the elastic properties of timber using a complex elastic modulus and a complex shear modulus, they could model the different energy dissipation in different forms of vibration in timber beams. Since they found that the energy dissipation in shear was greater than that in bending, they could encode that information in the imaginary components of the two moduli, so that modes of vibration in which more work was done in shear exhibited higher energy dissipation than modes in which more work was done in bending.

The damping models described so far all have a similar shape, given by the fact that the energy dissipation is provided by a force in a dissipative element which is a sinusoid in anti-phase with the displacement. Dissipative mechanisms such as plasticity, impact and friction can all give distinctive shapes to the force-displacement diagram. One way of reproducing some of the typical force-displacement behaviour found in structures is the Bouc-Wen model, (Bouc; 1967; Wen; 1976) cited by (Song and Der Kiureghian; 2006). This is a phenomenological model of hysteresis loop, based on fitting experimental data for a particular system. There is no physical derivation for the form of the equations, but the Bouc-Wen model replicates the observed independence of damping ratio from frequency in many structural systems, and has been used to closely define the shape of the hysteresis loop for very non-linear hysteretic behaviour, particularly for seismic loads. Figure 2-16 shows a the response of a very simple form of the Bouc-Wen model to sinusoidal load.

Folz and Filiatrault (2001), for example, applied a Bouc-Wen model to the seismic

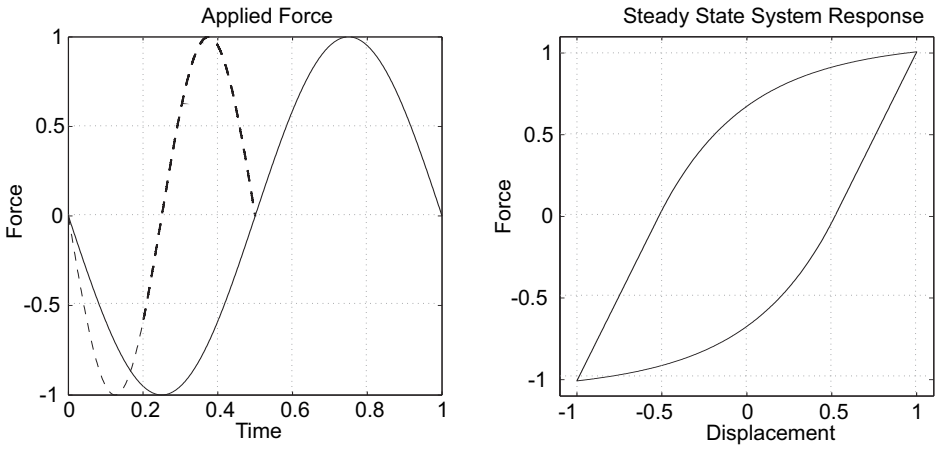

Figure 2-16: Force-displacement diagrams for a Bouc-Wen hysteretic model under sinusoidal load

analysis of sheathed wood-frame walls. Various additions to the model have been made to allow for different features of observed hysteretic behaviour in structural systems, including timber structural systems for which Foliente (1995) added parameters to allow for strength and stiffness degradation and 'pinching', a phenomenon in which the hysteresis loop narrows at low loads and displacements. Models of this form have, therefore, been successfully applied to dowel-type connections in timber and, under seismic loads, they incorporate the extreme nonlinearity which is crucial to the response. In this work, it has been found that the shape of the hysteresis loop under serviceability loads can be adequately represented using other techniques.

A primary source of energy dissipation is friction, and a simple representation of friction was developed by Coulomb (1821) after an extensive programme of testing. Coulomb's laws of friction state that the friction force is independent of the contact area and sliding velocity, and proportional to the normal force.

On this basis, motion will not commence until a force equal to the friction force is applied, and subsequently the frictional resistance force will be constant. It is not possible, therefore, to illustrate the response to a sinusoidal force of a Coulomb frictional damper in isolation, as has been done for the models above. This is due to the fact that, with no other forces acting, the displacement would increase without bound when the applied force exceeds the friction force. A parallel combination of a Coulomb frictional damper and a linear spring is therefore considered, and its response to a sinusoidal applied force is shown in Figure 2-17. In Section 6.5, the energy dissipation due to friction around the dowel is predicted using the Coulomb law.

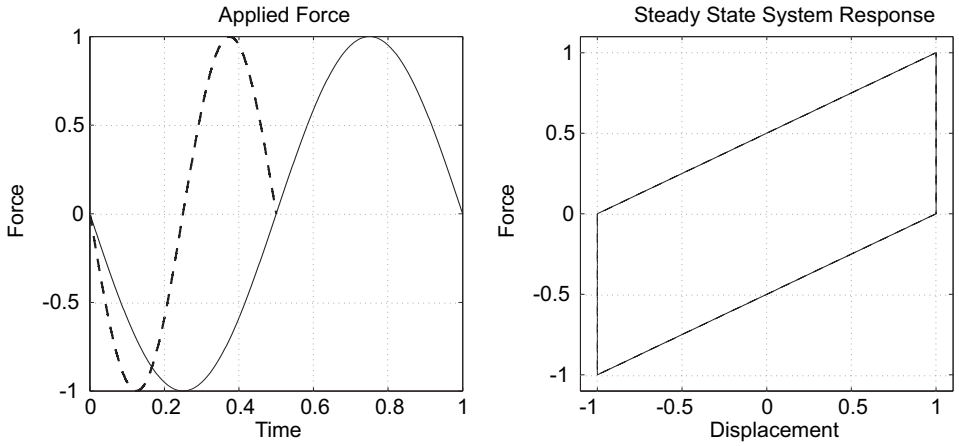

Figure 2-17: Force-displacement diagrams for the parallel combination of a Coulomb friction element and an elastic spring under sinusoidal load

Chapter 3

Methodology

3.1 Background

In dowel-type connections, the load transfer between structural members follows a path which includes bending and shear in the connector and the phenomenon of embedment. Embedment encompasses contact between the connector and timber and the stress concentrations in the timber around the dowel which dissipate as the distance from the dowel increases, until the effect of the stress concentration on the stresses in the member is insignificant. The force-displacement response of the timber in embedment defines a foundation on which the bending and shear, the beam behaviour, of the connector takes place.

This study aimed to provide a basis for prediction of the stiffness and energy dissipation in dowel-type conditions under in-service dynamic loads. Previous research on dynamic behaviour of dowel-type connections under seismic loads has provided insufficient experimental data, and no appropriate predictive model, for stiffness and energy dissipation in the range of dynamic loads which a structure would experience in-service. This research therefore extends the field by considering this important form of loading, and so the focus has been on developing an appropriate series of tests, identifying, extracting and analysing the relevant properties of the behaviour of the specimens, and generating as simple as possible a model to predict that behaviour with reasonable accuracy.

3.2 Objectives

The objectives of the study were:

- to characterize the behaviour of timber under embedment by a relatively rigid

dowel under dynamic loads representative of in-service vibration, and to use that information to interpret the response of complete connections and frames in those conditions;

- to measure the energy dissipation in dowel-type connections and the components which form them, to trace that energy dissipation from individual components to complete frames, and to develop predictive models for one or more sources of that energy dissipation;

- to develop and test a predictive model for stiffness in embedment, and to extend that model to predict the stiffness of connections and frames under loads representative of in-service vibration.

3.3 Outline of research

It was not, in general, possible to study the variety of connections encompassed by the term dowel-type connection. A single, simple structure was therefore chosen, and the main thread of tests, analysis and modelling carried out all refer to that single form of structure and connection. The structure was a portal frame of glued-laminated Norway spruce (Picea abies) with dowel-type moment connections in which each member had a central steel flitch plate with multiple 12mm-diameter steel dowels. In addition to that main thread of experimental research, a study of embedment was carried out using Douglas fir (Pseudotsuga menziesii) and 20mm dowels, and using screws in place of dowels for embedment in Norway spruce, and these results serve to give an indication of the effect of such changes, and inspiration for further study.

An aim of the research was to study the relationship between force and displacement in dowel-type connections under loads representative of in-service vibration. Linear and non-linear components of the response were to be identified to inform the development of a model. Characteristics of the response were to be identified and traced through the experimental work, from the tests on individual components to those on a complete frame.

The stiffness was expected to be largely measurable and predictable, albeit derived from behaviour which is, in part, highly nonlinear. Models were, therefore, developed at each stage of the study from material to structural scale. An attempt was made to generate simplified models which could yield design formulae suitable for use in design guidance and codes. Closed form, analytical solutions were therefore preferred over numerical models.

It was anticipated that energy dissipation could be measured in isolated compo-

nents, by analysis of the force-displacement relationship for that component. In structural systems with imposed mass, it was intended that modal analysis be used to identify the modal damping ratio. It was intended to attempt to identify the primary sources of energy dissipation, and to trace them through the structural system from the embedment tests to the complete structure, to inform future research into connections with high, reliable energy dissipation capacity.

Accurate prediction of energy dissipation and damping was anticipated to be difficult, since the mechanisms through which energy is dissipated are various and occur over a range of scales, from breaking of bonds in the chemical structure of the timber to friction between parts of the complete structure. It was therefore intended to develop predictive models for energy dissipation where possible, to identify one or more significant components of damping in a complete structure.

The main part of the study therefore followed the following path:

- a dynamic loading scheme was derived to be representative of a connection under a typical form of in-service vibration (Chapters 4 and 5);
- the Douglas fir and Norway spruce were characterized by their elastic moduli measured in two directions (Chapter 5);
- the embedment behaviour of the timber under a rigid dowel was measured (Chapter 5);
- the behaviour of a complete single-dowel connection was measured (Chapter 5);
- orthotropic elastic and viscoelastic models were developed for stiffness and energy dissipation in embedment (Chapter 6);
- the stiffness and energy dissipation models for embedment formed the foundation for a beam-on-foundation model of the complete single-dowel connection (Chapter 6);
- the stiffness of the beam-on-foundation model was used, along with consideration of dowel group effects, to predict the stiffness of a complete multiple-dowel connection (Chapter 7);
- the behaviour of an individual multiple-dowel connection subjected to a bending moment, and of a complete portal frame were measured, and modal analysis used to identify their dynamic properties for comparison with predictions (Chapter 7); and finally,

- the connection model was applied to an example building by stiffness matrix analysis (Chapter 8).

Chapter 4

In-service vibration

The majority of the previous work which has studied dowel-timber interaction, described in Section 2.2, was concerned with investigating and modelling either the static failure of dowel-type connections, or their dynamic behaviour under extreme seismic or wind events, in which gross plastic behaviour occurs in the structure, and especially in the connections. What sets this study apart is that it is concerned with the stiffness and energy dissipation exhibited by connections in service conditions, under everyday loads in which the behaviour of an engineered structure must be predictable, reliable and allow the use of a structure to continue unhindered.

The wide variety of dynamic loads which a structure might experience were discussed in Section 2.3.1. This chapter is concerned with identifying the time-history of force that those loads are expected to apply to connections in modern timber structures. It addresses the two major causes of serviceability failure of structures by vibration: wind-induced and footfall-induced vibration. Wind-induced vibration was investigated through a theoretical study of an example structure, while footfall-induced vibration was investigated by reference to published measurements taken of real structures which had been considered to exhibit unacceptable vibration. Based on the results of these studies, an equivalent set of dynamic loads was defined to be used in the experimental work in this study.

4.1 Wind-induced vibration

The dynamic loads applied to a structure should be considered in conjunction with static loads. For the case of dowel-type connections, this point is especially important, since their force-displacement behaviour deviates significantly from linear-elastic, and so the principle of superposition does not necessarily apply.

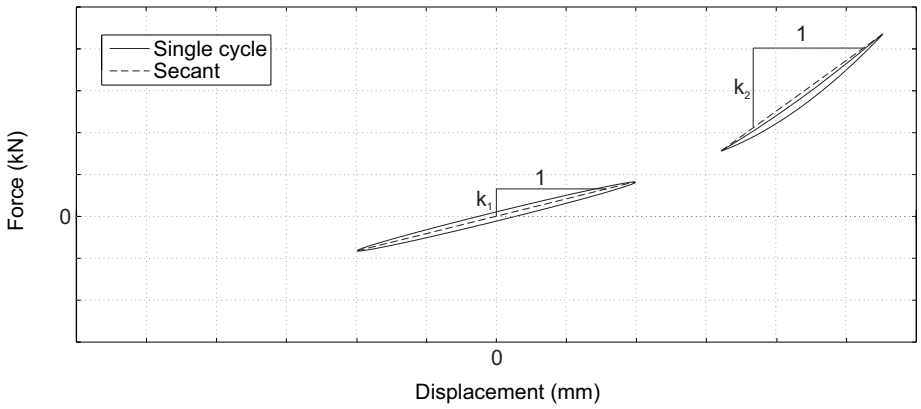

Figure 4-1: Secant stiffness for two possible cycles of force against displacement

It is useful to define here the secant stiffness referred to in this study. It is defined as the slope on the force-displacement diagram between the points of maximum and minimum displacement in a cycle. Figure 4-1 shows the secant stiffnesses k_1 and k_2 for two possible cycles, illustrating that the secant line may pass outside the loop, and that the secant line does not necessarily pass through the origin. It is the secant stiffness which defines the natural frequency of a structure and its amplitude of vibration under a given load.

The secant stiffness exhibited by a connection under oscillating load with zero mean is different to that exhibited by the same connection under an oscillating load with the same amplitude, but a high mean value, such that the load never passes through zero. This is because the connection slips, undergoing some deformation at near-zero load, due to a gap formed by construction tolerance and local irreversible behaviour in the timber.

Every dynamic load must, therefore, be considered with the static mean load which is expected to apply simultaneously. Turbulent wind load, for example, occurs in conjunction with a mean steady wind load, while the oscillating load induced by vortex shedding in the wind is symmetrical around a zero mean.

For the purpose of this study, a theoretical case study was carried out to identify the form of loading expected to occur in vibration of timber structures. The case study structure was a 20-storey building, in which the main vertical structure was formed from glued-laminated timber elements, the floors from cross-laminated timber and lateral loads were resisted by glued-laminated timber bracing. The structural form was based on a structure proposed by structural engineers Sweco for the town of Kirkenes in Norway, as reported by Reid (2009).

An established design method, Eurocode 1 Part 1-4 (BSI; 2005), was used to inves-

tigate the nature of the wind-induced vibration caused in the case study structure, with the aim of assessing the sensitivity of a realistic structure to this form of vibration, and defining the relative magnitude of the mean and oscillating components of the forces in the structure.

4.1.1 Along-wind vibration

The method presented in Eurocode 1 Part 1-4 (BSI; 2005), Annex B for prediction of the along-wind dynamic response of a building to wind load is based on the approach first developed by Davenport (1961), introduced in Section 2.3.2.1. The basis of Davenport's approach was that the dynamic force applied by the wind could be represented as a combination of a steady mean force and a stochastic turbulent component. The stochastic part was treated as a stationary random variable described by a power spectral density function (PSD). As described in Section 2.3.2.1, the displacement PSD S_x is related to the applied force PSD S_F by (4.1), where $|H(n)|$ is the receptance of the system and n is frequency.

$$S_x(n) = |H(n)|^2 S_F(n) \tag{4.1}$$

The pressure at any one point on the face of the structure continually varies, and the peak pressure at one point will not, in general, occur at the same time as the peak pressure at another. To allow for this, the Eurocode applies aerodynamic admittance functions R_h and R_b to allow for the variation in pressure across the surface, as in (4.2).

$$S_x(n) = |H(n)|^2 S_F(n) R_h R_b \tag{4.2}$$

The pressure applied to the face is assumed to be proportional to the velocity of the air flow. This means that the field of fluctuating velocity in the turbulent flow can be used to calculate a field of fluctuating force on the structure. If the force is proportional to the velocity at all frequencies of interest, then the PSD of force is proportional to the PSD of velocity, and the two functions can be related by (4.3), where σ^2 represents the standard deviation.

$$\frac{S_F(n)}{\sigma_F^2} = \frac{S_v(n)}{\sigma_v^2} \tag{4.3}$$

The magnitude of the mean wind load per metre height F_m depends on the shape and size of the structure and the mean wind velocity. It is given by (4.4), where c_f is the force coefficient, which is tabulated and chosen depending on the plan shape of the structure. ρ is the density of the air, b the relevant dimension of the structure and v_m

the mean wind velocity.

$$F_m = c_f \rho b v_m^2 \tag{4.4}$$

The magnitude of the turbulent component of the force is represented by its root mean square value σ_F, and the turbulence intensity l_v is defined to relate σ_F and F_m, by $\sigma_F = l_v^2 F_m$. This relationship can be combined with (4.3) and (4.4) to give (4.5).

$$S_F(n) = \left(c_f \rho b v_m^2 l_v^2\right)^2 \frac{S_v(n)}{\sigma_v^2} \tag{4.5}$$

(4.5) allows the PSD of the force applied to the structure to be calculated from the PSD of the wind velocity. In the Eurocode, the PSD of the wind velocity is provided in the form of a dimensionless PSD function which represents the distribution of frequency components expected in a general wind load. This can then be scaled by the magnitude of the turbulent component of the wind force, represented by σ_v, to be applied to a specific site. The dimensionless PSD function $S_L(n)$ is defined by (4.6).

$$S_L(n) = \frac{n S_v(n)}{\sigma_v^2} \tag{4.6}$$

Rearranging and substituting (4.6) allows (4.5) to be rewritten in terms of this dimensionless PSD, as in (4.7).

$$S_F(n) = \left(c_f \rho b v_m^2 l_v^2\right)^2 \frac{S_L(n)}{n} \tag{4.7}$$

(4.7) provides a way of calculating the properties of the dynamic force imposed on a structure. In order to determine the response of the structure to this applied force, (4.2) is used, so an expression is required for the receptance $H(n)$ of the system. The Eurocode uses the approach first proposed by Simiu and Scanlan (1986), of representing a tall building structure as a slender, line-like vibrating object. The receptance function for such an object for vibration at or near its first mode can be approximated by (4.8), where f_n is the natural frequency of the first mode, m is the equivalent uniform mass per metre height and γ is the damping expressed as the proportion of critical damping. i is the imaginary unit.

$$H(n) = \frac{1 - \left(\frac{n}{f_n}\right)^2 - i\left(2\gamma\left(\frac{n}{f_n}\right)\right)}{m\left(2\pi f_n\right)^2 \left(\left(1 - \left(\frac{n}{f_n}\right)^2\right)^2 + 2\gamma\left(2\gamma\left(\frac{n}{f_n}\right)\right)^2\right)} \tag{4.8}$$

From (4.8), the magnitude of the receptance as a function of frequency can be

determined, and is shown in (4.9).

$$|H(n)| = \frac{1}{m\left(2\pi f_n\right)^2 \sqrt{\left(1 - \left(\frac{n}{f_n}\right)^2\right)^2 + \left(2\gamma\left(\frac{n}{f_n}\right)^2\right)}} \tag{4.9}$$

Using (4.2), (4.7) and (4.9), the along-wind vibration response of the structure can be determined, and expressed as the PSD of displacement S_x. This function can then be used to determine the PSD functions of velocity and acceleration $S_{\dot{x}}$ and $S_{\ddot{x}}$ using $S_{\dot{x}} = (2\pi n)^2 S_x$ and $S_{\ddot{x}} = (2\pi n)^4 S_x$. The PSD functions cannot be directly compared with acceptability criteria, but most of the vibration limits described in Section 2.3.5 are expressed as the root mean square value of acceleration, which can be calculated from the PSD of acceleration $S_{\ddot{x}}$ according to (4.10).

$$\sigma_{\ddot{x}}^2 = \int_0^\infty S_{\ddot{x}}^2 \mathrm{d}n = \int_0^\infty |H(n)|^2 S_F(n) R_h R_b \left(2\pi n\right)^4 \mathrm{d}n \tag{4.10}$$

For small damping, the solution to the integral in (4.10) is dominated by the component at resonance, and is approximately given by (4.11).

$$\sigma_{\ddot{x}}^2 = \frac{\pi f_n}{4\gamma m^2} S_F(f_n) R_h R_b \tag{4.11}$$

This is the approximation used in the derivation of the Eurocode design method. Adding a non-dimensional coefficient K_x, which accounts for the variation in wind force through the height of the structure, a mode shape factor $\Phi(z)$, equal to 1 at the top of the structure, to account for the variation of acceleration with height, and substituting γ with $\delta = 2\pi\gamma$, the logarithmic decrement of damping, gives (4.12), equivalent to Equation B.11 in Eurocode 1 Part 1-4 (BSI; 2005).

$$\sigma_{\ddot{x}}^2 = \frac{\pi^2 f_n}{2\delta m^2} S_F(f_n) R_h R_b K_x \Phi(z) \tag{4.12}$$

The additional forces on the structure due to this vibration are then allowed for using the coefficient c_d, given by (4.13), where the resonance response factor R^2 is defined as in (4.14), B is a size effect factor which allows for non-correlation of pressures over the face of the structure and k_p is the ratio of the peak value of the turbulent component of the wind velocity to the root mean square value which l_v represents.

$$c_d = \frac{1 + 2k_p l_v \sqrt{B^2 + R^2}}{1 + 7 l_v \sqrt{B^2}} \tag{4.13}$$

$$R^2 = \frac{\pi^2}{2\delta} S_L R_h R_b \tag{4.14}$$

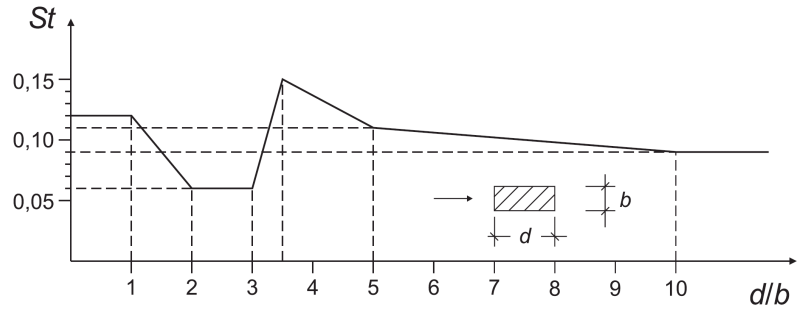

Figure 4-2: Strouhal number for buildings rectangular in plan, taken from Eurocode 1 (BSI; 2005)

The Eurocode therefore provides a method for calculating the forces and accelerations resulting from along-wind vibration due to turbulent wind load. The assumptions inherent in the Eurocode design method are equally valid in their application to timber structures as they are to other structural materials, and it is considered that the method can be used to investigate the effects of changing mass, frequency and damping on the response of a case study structure.

In along-wind vibration, the forces in the structure have a mean value determined by the mean wind velocity and the oscillation caused by turbulence moves around that mean value. The magnitude of the oscillation in comparison to the magnitude of the mean value will be investigated using the example structure in Section 4.1.3, and will be important in determining the stiffness of the connections for that oscillation, given the nonlinearity of the force-displacement behaviour of the connections.

4.1.2 Across-wind vibration

A method is also provided in Eurocode 1 Part 1-4 (BSI; 2005) for the assessment of the across-wind vibration induced by vortex shedding, as described in Section 2.3.2.2. The frequency of vortex shedding is calculated using the Strouhal number St. $St = fL/V$ where f is the frequency of vortex shedding, L is a characteristic dimension of the body, and V is the velocity of the flow.

The Strouhal number for a particular structure depends on its shape in the plane in which the vortices form. It is empirically derived, and for buildings rectangular in plan it varies as shown in Figure 4-2.

For a particular structure, therefore, a critical velocity can be calculated at which the frequency of vortex shedding is equal to the natural frequency of a structure, and it is when this occurs that a severe vibration response can occur. Substituting f_n, the natural frequency of the structure in the relevant direction, for f and using b, the

Figure 4-3: Structure of the Barentshus building ©by Reiulf Ramstad Architects (Reid; 2009)

across-wind breadth of the building, as the characteristic length, the relationship (4.15) is obtained for the critical wind velocity $v_{crit,i}$.

$$v_{crit,i} = \frac{bf_n}{St} \tag{4.15}$$

Across-wind vibration entails a full reversal of the forces in the structure with each oscillation, and can be expected to be completely symmetrical about zero force. Gap-formation in the connections in the lateral-load-resisting system can, therefore, be expected to affect the stiffness of the connections and nonlinear connection behaviour could lead to a variation of stiffness with amplitude of oscillation.

4.1.3 Tall timber building example

The structure which was chosen to illustrate the importance of this form of wind-induced vibration is a conceptual tall timber building. It was based on the 20-storey Barentsus building, proposed for the Norwegian town of Kirkenes. At the time of writing, this project was on hold because of doubts about the demand for space in a development of that size in that area. A preliminary design was carried out by the engineers, Sweco, resulting in the geometry and member sizes described by Reid (2009). The diagram in Figure 4-3, presented by Reid, illustrates the structural form.

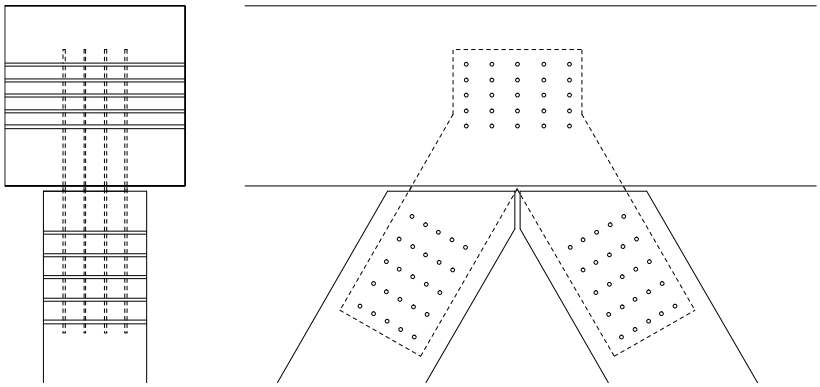

Figure 4-4: Connection detail based on multiple-steel-plate dowel-type connection used for the Rena river bridge (Abrahamsen; 2008)

As well as investigating the global structural behaviour of this structure in response to dynamic wind load, the influence of the connections on that behaviour was also of interest. The information given by Reid (2009) did not address the connections, but the multiple-steel-plate dowel-type connection used by Sweco in the Rena river bridge (Abrahamsen; 2008) provided a realistic connection type for use in this example. That connection was modified, and the form of connection modelled in this study is shown in Figure 4-4.

The stiffness of the structure was assessed using a stiffness-matrix method, for a two-dimensional elastic analysis of the frame structure, including a semi-rigid connection stiffness, which allowed deformation of the connection in the two in-plane directions and rotation. The structure was simplified into an 70m tall frame structure of twenty 3.5m-high storeys, 24m $\times$ 24m in plan. Corner columns and bracing elements form trusses in each face of the building and the floors are 180mm-thick cross-laminated timber panels, which act as a diaphragm, distributing lateral loads to the vertical structure. The lateral load was assumed to be resisted entirely by the trusses in each face of the building, and so the lateral movement was assessed using a two-dimensional model of one of these trusses loaded appropriately.

Two variations of the structure were modelled in order to assess the effect of connection stiffness on its lateral deflection: truss connections fixed and semi-rigid truss connections. The truss structure was broken up into elements 16m long or less, to give approximately realistic member sizes for transportation, and the same connection stiffness was applied between each element.

The flitch plates in the connection were modelled in each case as beam elements, and at each connection between a timber member and the flitch plates, there was an analysis node on the timber member and one on the flitch plates. In the undeformed

Table 4.1: Static deflections under mean wind load for the 20-storey glued-laminated timber structure

Truss connection	Peak displacement (mm)	Mean interstorey drift ratio
Fixed	119	height/670
Semi-rigid	232	height/345

condition, these pairs of nodes had the same coordinates. In the case of the semi-rigid connections, the connection between these nodes was assigned a rotational stiffness, and a translational stiffness in each of the parallel- and perpendicular-to-grain directions. In the fixed connections, the two nodes were constrained to translate and rotate together.

The connection stiffness was determined according to Eurocode 5 (BSI; 2009a), for twenty-five 12mm diameter steel dowels arranged in a rectangular grid, and crossing eight shear planes through the four steel plates slotted into each member. This resulted in a rotational stiffness of 21025kNm/radian and a translational stiffness of 772963kN/m, and the same translational stiffness was applied both parallel and perpendicular to grain, since no effect of grain angle is allowed for in the Eurocode 5 method.

4.1.3.1 Static deflection under wind load

The force on the building due to the mean wind pressure was calculated according to Eurocode 1 Part 1-4 (BSI; 2005), using a mean wind speed at sea level of 25m/s, corrected for an altitude above sea level of 200m. This wind speed and altitude was chosen to be sufficient to allow for all of the major cities in the United Kingdom, and those conditions resulted in a total mean wind force on the building of 3662kN, expected to occur, on average, once every 50 years. This force was distributed evenly around the face of the building, and applied at each storey level.

The resulting deflections in each variation of the structure are shown in Table 4.1, including the interstorey drift ratio, calculated as δ/h, where δ is the horizontal deflection and h the height. Figure 4-5 shows the model used for analysis and the deformed shape.

The interstorey drift ratio is commonly used to assess the acceptability of static deflections, in that it indicates the potential for deflections to cause damage to cladding supported by the structure, and the potential for deflections to be visible to people around the structure. The UK national annex to Eurocode 3 (BSI; 2008b) gives a suggested acceptable interstorey drift ratio for steel structures of height/300. That limit is considered to be a suitable guide for this example structure, since its primary

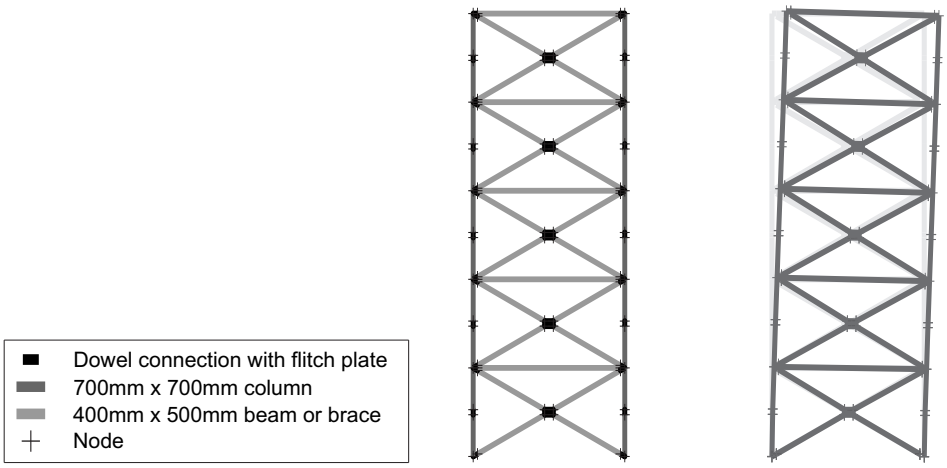

Figure 4-5: Geometry and member dimensions for the stiffness-matrix model of the Barentshus building, and the deformed shape, exaggerated by a factor of 10

structure is a braced frame, a system commonly found in steel construction.

The static deflections under wind load in Table 4.1, therefore, both represent an acceptable interstorey drift. It is notable, however, that the stiffness in the connections strongly influences the deflection of the structure: the stiffness in the structure with semi-rigid connections is 48% lower than in that with fixed connections. Given that the lateral loads are primarily resisted by truss action, this is considered to be mainly due to the translational, rather than rotational, stiffness of the connection.

4.1.3.2 Dynamic along-wind response

The along-wind vibration of the example structure has been assessed using the method described in Section 4.1.1. Modal analysis was carried out on the same model developed for assessment of static deflection under wind load. For this purpose, the mass of the structure, as well as its stiffness, was important. As well as the self-weight of the timber structure, the other loads imposed on the structure were used to calculate its mass. Loads were chosen to be representative of a normal office or residential building, and are shown in Table 4.2. In calculating the mass of the structure, it was assumed that 10% of the variable imposed load was present. This resulted in a total mass of the building for dynamic calculation of 3,770,000kg, or an average mass density inside the building envelope of 81.8kg/m^3.

Since the structure is rotationally symmetrical through 90°, the first two modes of vibration are expected to be translational sway modes with identical natural frequencies. The natural frequencies of the two variations of the structure are shown in Table 4.3.

Table 4.2: Weights of cladding and finishes for calculation of the mass of the example structure

Element	Imposed load (kN/m^2)	Mass per unit area (kg/m^2)
Floor and ceiling services and finishes	1	9.81
External cladding	1	9.81
Variable load due to furniture and occupants	3	29.43

Table 4.3: Natural frequency of the first mode of vibration for the 20-storey glued-laminated timber structure

Truss connection	1st/2nd mode natural frequency (Hz)
Fixed	0.54
Semi-rigid	0.39

Using the natural frequency, dimensions and mass of the structure, the design method from Section 4.1.1 could be applied to determine the amplitude of acceleration and the additional forces imposed on the structure by vibration. The method only considers movement in the first mode of vibration.

There was some uncertainty in these calculated natural frequencies of the structure. This was due to the fact that, as discussed in Section 2.2, the force-displacement behaviour of dowel-type connections is not linear, so the secant stiffness they exhibit depends on the mean and amplitude of the applied force. The stiffness calculated according to Eurocode 5 (BSI; 2009a) is based on regression analysis of experimental work by Ehlbeck and Larsen (1993). Details of the test results used for this regression analysis were not published, but it is considered that they would have been carried out according to the standard procedure at the time, EN 26891 (BSI; 1991), and so the stiffness measured would have been the initial stiffness between the 10% and 40% load levels. This initial stiffness was expected to be different from the secant stiffness under the repeated cycles of load applied by wind-induced vibration, and it was that secant stiffness which would determine the natural frequency.

Another important parameter in the vibration analysis which could not be accurately determined was the modal damping. Eurocode 1 Part 1-4 (BSI; 2005) tabulates damping estimates for various common structural forms, but gives no value for multi-storey timber buildings. For timber bridges, the logarithmic decrement of structural damping is suggested to be between 0.06 and 0.12, which equates to a range of equivalent viscous damping ratio from 0.95% to 1.9%. Given that such damping estimates

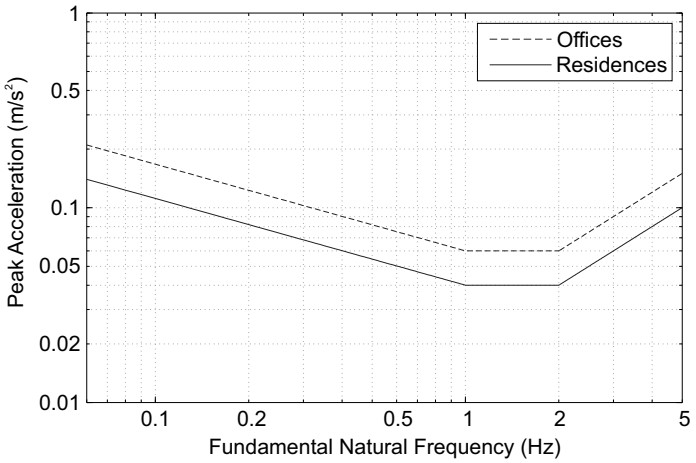

Figure 4-6: Suggested acceptable limits for lateral acceleration in wind-induced vibration with a one-year return period, adapted from ISO 10137 (ISO; 2007)

are purely empirical, this is clearly an area which requires further research, and the development of the energy dissipation which results in damping is considered throughout the experimental and analytical work described in this thesis. For the analysis of this example building, the damping estimates for timber bridges were used.

The uncertainty in natural frequency and damping was allowed for by performing a sensitivity analysis on both. The natural frequency was varied between the values for the semi-rigid and fixed connection conditions, and the damping was varied between the lower and upper estimates given for timber bridges.

The acceptability of vibration was assessed against the ISO 10137 (ISO; 2007) standard, since it provides detailed acceptability criteria specifically for lateral vibration in buildings. The proposed variation of acceptable acceleration with frequency for lateral wind-induced movement from that standard is shown in Figure 4-6. That standard states that, for a wind with a one-year return period, a peak acceleration of up to $55\times10^{-3}\text{m/s}^2$ at a frequency of 0.5Hz is suitable for residential buildings, and that up to $80\times10^{-3}\text{m/s}^2$ is acceptable a general office building at the same frequency.

The parameters given for the wind load in Eurocode 1 Part 1-4 (BSI; 2005) represent a 50-year return period wind event. In order to compare the results of the analysis with the limits given in ISO 10137 (ISO; 2007), equation B.9 from the Eurocode was used to calculate the one-year return period acceleration. With the symbols altered to use the notation in this study, that equation is given in (4.16). $\sigma_{\ddot{x},1}$ is the one-year return period root mean square acceleration, and $\sigma_{\ddot{x},50}$ is that for the 50-year return period. N_g is the number of times the one-year value is expected to be exceeded in the 50-year period, so was taken as 50. The one-year return period peak acceleration was then

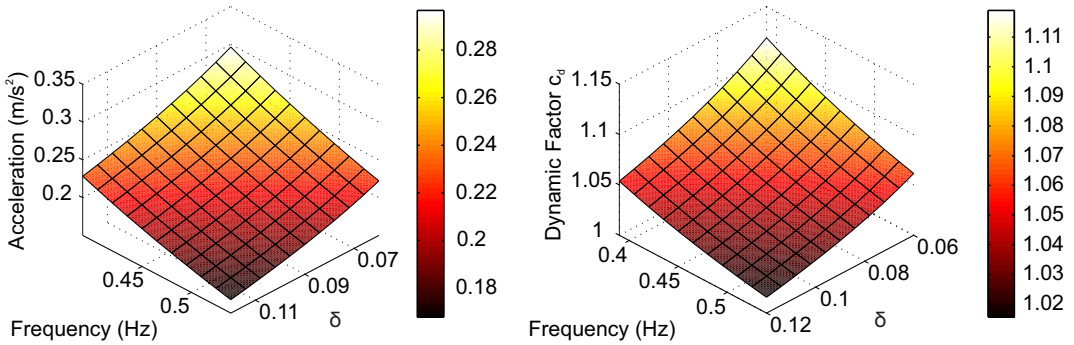

Figure 4-7: Sensitivity analysis for vibration of example structure for frequency and damping, δ - the left hand graph shows the peak acceleration, and the right hand graph the magnification of the static mean force

calculated from the root mean square value using the peak factor given in Eurocode 1 Part 1-4 Annex B.

$$\frac{\sigma^2_{\ddot{x},1}}{\sigma^2_{\ddot{x},50}} = 0.007(\log N_g)^2 - 0.174 \log N_g + 1 \tag{4.16}$$

The variation of peak acceleration and peak force on the structure with natural frequency and damping is shown in Figure 4-7. The additional force on the structure due to vibration had a maximum value of approximately 12%, which can also be expressed by saying the static force was increased by a 'dynamic factor' of 1.12.

Figure 4-7 shows that the acceptable limits of vibration for both residential and office use were exceeded for the entire range of stiffness and damping considered in the sensitivity study. The minimum peak acceleration was 0.168m/s^2.

The results of the sensitivity study showed that for this example structure, which achieved reasonable static deflections under wind load for serviceability, there was potential for levels of wind-induced vibration which would affect its serviceability for either office or residential use.

4.1.3.3 Dynamic across-wind response

The natural frequencies in Table 4.3 can be used to calculate the critical wind velocity, the wind velocity at which vortices are shed at a frequency equal to one of its natural frequencies, for the example structure using (4.15).

The building is 24m $\times$ 24m in plan, which gives a Strouhal number from Figure 4-2 of 0.12. The critical wind velocity for each variation of the connection conditions is shown in Table 4.4. In each case, the critical wind velocity is higher than 78m/s, which can be compared with a 1 in 50 year return-period wind speed of 25m/s. A severe

Table 4.4: Critical wind velocity for vortex shedding for the 20-storey glued-laminated timber structure

Truss connection	1st mode natural frequency (Hz)	Critical wind velocity (m/s)
Fixed	0.54	108
Semi-rigid	0.39	78

across-wind dynamic response therefore appears unlikely for this type of structure. The low weight of the structure is an advantage in this context, since it leads to an increased natural frequency, keeping the natural frequency above the expected frequency of vortex shedding.

4.2 Footfall-induced vibration

The vibration induced by people walking, running, jumping or dancing on a structure, individually or in unison, was discussed in Section 2.3.3. The nature of the oscillating forces imposed by this form of vibration was studied using the case studies from the literature summarized in Table 2.1.

It should be noted that there is some similarity in the distinction between vertical and lateral vibrations due to footfall and the distinction between along-wind and across-wind vibration due to wind load. Vertical vibration in floors or bridges produces an oscillation of force around a mean force provided by the static loads on the structure, while lateral footfall-induced vibration, on the other hand, can be expected to produce an oscillating force around a zero mean force, as in the case of across-wind vibration.

For vertical vibration, the case studies in Table 2.1 show peak accelerations ranging from 0.4m/s^2 to 8.6m/s^2. These accelerations give some indication of the variation of force in the structure, since when the mass of the structure accelerates in the gravity direction, the force in the structure is reduced. Once the mass has an acceleration higher than the acceleration due to gravity, approximately 9.8m/s^2, the force on it reverses. A peak acceleration of 0.4m/s^2, therefore, suggests that the lowest total force on the mass would be 96% of the mean force on that mass, and 8.6m/s^2 suggests a lowest force of 12%. The accelerations at other parts of the structure would have been lower, and so the oscillating forces correspondingly lower, but these values give an indication of the magnitude of the oscillating force on the components in the structure, and show that the force on the structure does not reverse under the vibrations in these case studies.

Table 4.5: Examples of R-ratio calculation, compressive forces are positive

Example	Highest force σ_{max} (kN)	Lowest force σ_{min} (kN)	R-ratio $\sigma_{min}/\sigma_{max}$
1	10	-10	-1
2	-10	-12	1.2
3	12	10	0.8333

Lateral vibration caused a serviceability failure of the Lardal timber and steel footbridge and the dowel-type connections in that structure presented difficulties in accurate prediction of its dynamic behaviour, as described in Section 2.3.3. In general, it is considered reasonable to assume that no constant lateral load would be applied to the structure to produce a mean value of the oscillating forces. Therefore, in the absence of any prestress, the force on each element and connection in the structure resisting the movement caused by lateral footfall-induced vibration would be expected to be symmetrical about a zero mean.

4.3 Equivalent dynamic loads

The investigation of in-service vibration presented in this chapter was used to define the dynamic loads applied in the experimental work in Chapter 5. Sections 4.1 and 4.2 show that in-service vibration can create oscillations of force in the structure which range from a full reversal of load to a small oscillations around a non-zero mean.

To quantify this property of an oscillating load, a term is taken from the study of fatigue: the R-ratio. The R-ratio relates the maximum and minimum values of the oscillating load according to (4.17), where σ_{min} is the numerical minimum stress and σ_{max} is the numerical maximum stress. In this study, the R-ratio is used to describe the oscillating applied force, and a compressive applied force is represented as negative. Table 4.5 has a few examples to clarify the calculation.

$$R = \frac{\sigma_{min}}{\sigma_{max}} \tag{4.17}$$

The highest dynamic force coefficient calculated for the example building in Section 4.1.3 was 1.12, which suggests an R-ratio for a component under compressive load of 1.27. The lowest dynamic force coefficient of 1.002 gives R=1.004. An R-ratio of 1.2 was chosen for the experimental work to be representative of the values calculated in this sensitivity study. The fully-reversed oscillation due to across-wind vibration and

lateral footfall-induced vibration can be represented by an R-ratio of -1.

The problematic in-service vibration which has been described here is due to the resonant response of a structure to a wide variety of dynamic applied forces. Regardless of the nature of the applied force, if the response of the structure is resonant, then its motion, and the forces induced, will be close to sinusoidal. In response to a stochastic applied force such as turbulent wind load, the amplitude of that sinusoid will be continuously varying. For the purpose of the experimental work in this study, it was proposed to simplify the variable-amplitude near-sinusoidal vibration in real structures to a pure sinusoid with constant amplitude.

4.4 Summary

In this chapter, the loads imposed on a structure due to in-service vibration have been investigated. Representative ranges of the amplitude and frequency of these loads have been presented by considering, by calculation and literature review, several forms of wind- and footfall-induced vibration, and a simplified sinusoidal loading profile has been proposed.

The next chapter will take this simplified loading and apply it in experimental work to investigate the embedment of a connector into the timber that surrounds it under dynamic load.

Chapter 5

Dynamic Embedment and Connection Tests

In order to trace the processes responsible for connection stiffness and energy dissipation, and to develop models of those processes, a programme of dynamic testing was developed which started with the basic part of a connection, and ended with a complete frame with connections.

The basic part of the connection was taken to be the interaction between dowel and timber as the circular section of the dowel is pressed into the hole cut in the timber. This process is known as embedment. The experimental investigation of embedment presented in this chapter formed the basis for two peer-reviewed journal papers. The first addressed the elastic component of the embedment stiffness under cyclic load (Reynolds et al.; 2013a), and the second the combination of elastic, viscoelastic and plastic behaviour observed in the embedment tests (Reynolds et al.; 2013b).

In tests investigating the embedment behaviour in isolation, the dowel was held rigidly straight, so that no deformation due to dowel bending occurred. Once the embedment behaviour had been characterized, single-dowel connection specimens were tested in which dowel bending contributed to the deformation, as in a complete connection. The same analysis methods were applied to the results of both tests in order to identify stiffness and energy dissipation, and the instrumentation was similar for both, so they are presented together in this chapter.

5.1 Schedule of tests

Table 5.1 lists every physical test carried out as part of this study. The details of the specimens and methods can be found in the relevant sections of this report. The tests

using servo loading machines are described in this chapter, and those using modal analysis and excitation by electrodynamic shaker or instrumented hammer are presented in Chapter 7.

It can be seen that some specimens were tested only once, while others were used for more than one test, using different load levels or forms of loading. This had consequences for the statistical methods applied to each set of results, in that various tests carried out on the same specimen could be considered as paired, while tests on different specimens were independent.

5.2 Materials and Methods

5.2.1 Embedment test

Two species of timber were tested: Douglas fir and Norway spruce. The Douglas fir was taken from solid timber grown in the south west of England, and the Norway spruce from glulam graded GL28h according to BS EN 1194 (BSI; 1999), produced by Lilleheden in Denmark. The timber was stored after delivery in a controlled environment at 18-22°C, and 60-65% relative humidity. The Norway spruce had been kiln dried before being glue-laminated, and so was assumed to be near equilibrium moisture content on delivery. This assumption was justified by the moisture content measured after testing, given in Section 5.3.1. A piece of Douglas fir was tested for moisture content according to the oven-dry method given by EN 13183 (BSI; 2002b) on delivery, and found to have a moisture content higher than 25%. The timber was therefore stacked with spaces to allow air drying in the controlled environment, and the change in moisture content estimated by monitoring the weight of a 2m-long piece with cross section 60mm × 300mm. The change in moisture content from the delivery date to the start of testing is shown in Figure 5-1. The moisture content estimated this way, at between 14 and 15%, corresponds closely to the moisture content measured by the oven dry method and given in Section 5.3.1.

In the Douglas fir, a 20mm diameter steel dowel was placed in a half-hole in the timber drilled using a 20mm auger drill bit, and in the Norway spruce, a 12mm diameter dowel in a hole drilled using a 12mm auger drill bit. Embedment specimens were also made for screws in Norway spruce, using screws provided by Spax with 7.5mm internal diameter, 12mm external diameter and 6mm pitch. 6mm holes were predrilled for the screws, which were installed between two pieces of timber held together in a vice, as recommended in ASTM D5764 (ASTM; 1997), so that the two pieces could then be separated to leave the screw installed in a half-hole in the timber, as shown in Figure 5-2. In each case, both parallel- and perpendicular-to-grain specimens were tested, and

Table 5.1: Schedule of physical tests

Test	Materials	Grain direction	Specimens	Tests including repetitions
Load applied using a servo loading machine				
Material characterization	Douglas fir	Para.	26	26
		Perp.	26	26
	Norway spruce	Para.	18	18
		Perp.	18	18
Cyclic embedment	Douglas fir and 20mm plain steel dowel	Para.	19	19
		Perp.	18	18
	Norway spruce and 12mm plain steel dowel	Para.	4	16
		Perp.	3	12
	Norway spruce and 12mm steel screw	Para.	3	12
		Perp.	3	12
Single-dowel connection	Norway spruce glulam and 12mm plain steel dowel	Para.	3	12
		Perp.	3	12
Excitation by an electrodynamic shaker or instrumented hammer				
Moment connection	Norway spruce glulam, steel connecting plates and six 12mm plain steel dowels	-	4	8
	Norway spruce glulam, steel connecting plates and two 12mm plain steel dowels	-	2	9
Portal frame	Norway spruce glulam, steel connecting plates and 12mm plain steel dowels	-	2	14

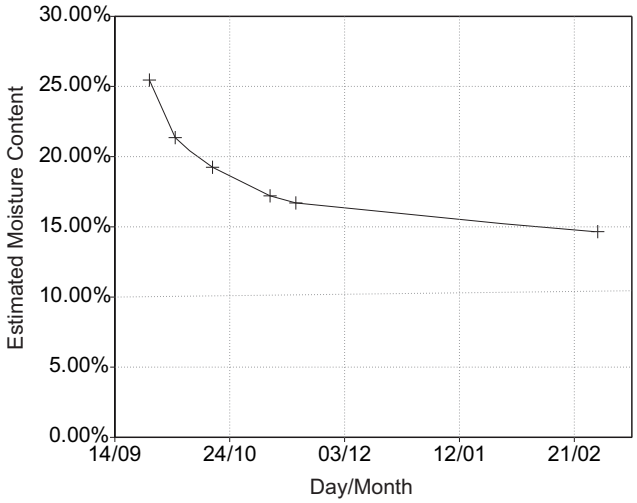

Figure 5-1: Variation in moisture content of Douglas fir stored at 18-22°C, and 60-65% relative humidity

were chosen to be free from knots or splits. The perpendicular-to-grain direction varied between radial and tangential, according to how the plank or laminate had been cut from the log, as would be the case in a real structure.

It was noted that this variation in grain orientation would introduce scatter into the perpendicular-to-grain test results. One approach to reducing this scatter would have been to divide the specimens into sets with different radial-tangential grain orientation, or to classify them by an angle in the radial-tangential plane. Given that the relevant objective of this study was to characterize the embedment behaviour for prediction of the behaviour of complete connections and frames, it was considered that such a study would not make the appropriate contribution. Since the orientation of loading in the radial-tangential plane is not generally known in structural design, and since in glued-laminated timber, a connector would embed into laminates with a variety of such grain angles, it was considered more relevant to measure the perpendicular-to-grain behaviour with a realistic variation of grain angles in the radial-tangential plane.

The full set of embedment test specimens is shown in Table 5.2. Where four repetitions were used rather than three, this was due to an extra test being carried out to replace tests in which an error in measurement or data logging was thought to have occurred, but it was subsequently found that all the results could be used.

A separate Douglas fir specimen was used for every variation of peak force and R-ratio, which resulted in a total of 37 specimens. For the Norway spruce tests, each specimen was tested at the full range of loads and R-ratios, so only 6 specimens were used.

Table 5.2: Cyclic embedment tests

Species	Grain orientation	Peak compressive force	R-ratio	Number of repetitions
Douglas fir and 20mm dowel	Parallel	20%	1.2	3
			10	4
		40%	1.2	3
			10	3
		80%	1.2	3
			10	3
	Perpendicular	20%	1.2	3
			10	3
		40%	1.2	3
			10	3
		80%	1.2	3
			10	3
Norway spruce and 12mm dowel	Parallel	20%	1.2	4
			10	4
		40%	1.2	4
			10	4
	Perpendicular	20%	1.2	3
			10	3
		40%	1.2	3
			10	3
Norway spruce and screw	Parallel	20%	1.2	3
			10	3
		40%	1.2	3
			10	3
	Perpendicular	20%	1.2	3
			10	3
		40%	1.2	3
			10	3

Figure 5-2: Parallel-to-grain screw embedment specimen

As described in Section 2.2.1, embedment tests have been widely used to identify both static and dynamic characteristics of the interaction between dowel and timber. This study required experimental evidence of the stiffness and energy dissipation in embedment under dynamic loads well below the yield load. This meant that the displacement and energy dissipation to be measured were smaller than in the tests reviewed in Section 2.2.1, where gross plastic behaviour generally occurred in the timber.

In defining a suitable test method to measure the small displacements expected in the timber, the magnitude of the displacements to be measured had to be compared both to the resolution of the measurement equipment, and the magnitude of the deflections occurring in the test equipment rather than the specimen.

5.2.1.1 Geometry of specimen and loading apparatus

As has been discussed in Section 2.2.2, there are two widely-used methods for determining embedment properties of timber: the ASTM method (ASTM; 1997), which uses a timber block with a half-hole in its surface, and the EN method (BSI; 2007), which uses a timber block with a full hole through it. The EN method has the clear advantage that it matches the situation in a real connection, and, on that basis, the first pilot tests carried out for this study used the geometry according to the EN method. The test setup is shown in Figure 5-3.

The EN test method requires the displacement readings to be calibrated to account for dowel bending based on the displacement where the timber specimen is replaced by a 'tight-fitting steel piece'. The geometry of the steel piece is not specified.

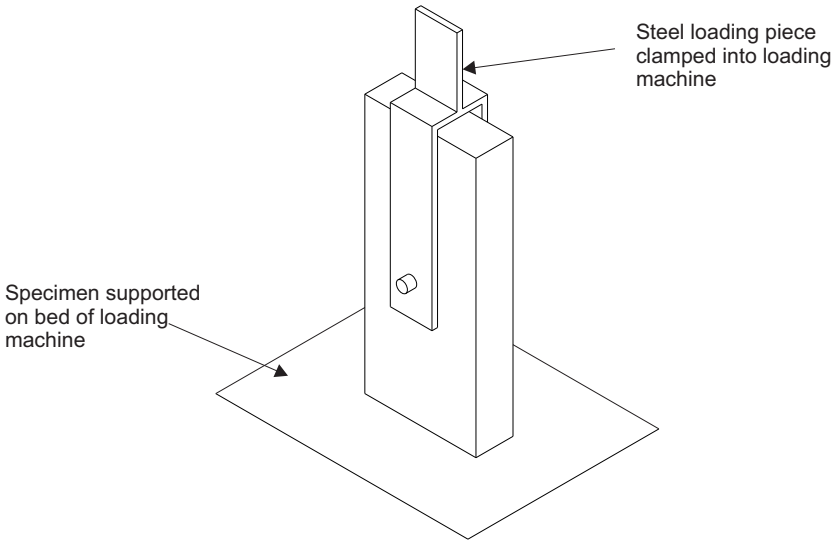

Figure 5-3: EN383 embedment test method used in pilot tests (BSI; 2007)

It is assumed that the calibration method is based on the assumption that the deformation of a steel piece is insignificant in comparison to the deformation of the timber specimen under the same load. There are some inaccuracies inherent in this calibration method, which are prominent particularly when applied to the high embedment stiffness associated with small-amplitude cyclic loading.

As the dowel embeds into the timber during an embedment test, the dowel will assume a deformed shape which depends on the stiffness of the dowel and the resistance of the timber. In contrast, when bearing on the relatively stiff foundation formed by the steel piece, the deformed shape of the dowel will be determined by the much higher stiffness of the steel. A steel piece as wide as the loading fork would prevent deformation of the dowel, and a thin steel piece would allow dowel deformation, but in a very different deformed shape to that caused by the timber specimen. Calibration with a steel piece cannot, therefore, be used to calculate the contribution of dowel deformation to the measured deflection in the test.

In this study a test with a steel piece was used to give an indication of the order of magnitude of the deflection due to deformation in the dowel. The same dynamic load was applied to the steel piece as to the timber. The timber piece was 60mm thick, and a steel piece 50mm thick was used, so as to allow some bending deformation of the dowel. The resulting force-displacement diagrams for the timber specimen and the steel piece are shown in Figure 5-4. While the test with the steel piece does not replicate the deformed shape of the dowel in the EN embedment test, the results in Figure 5-4 suggest that the contribution of the deformation of the loading apparatus

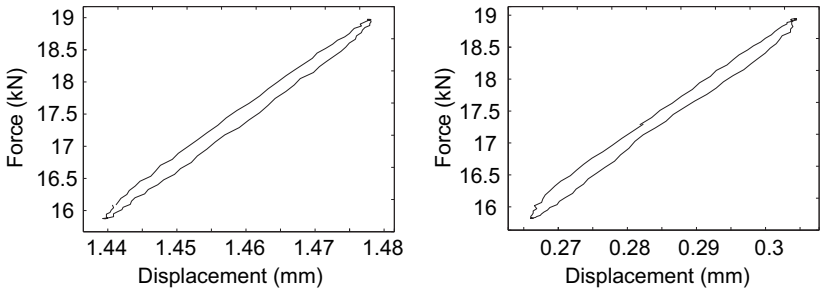

Figure 5-4: Comparison of force-displacement diagrams for a single cycle of applied force at 1Hz for the EN embedment test (left), and a test in which the dowel bears on a steel piece (right)

and dowel to both the secant stiffness and energy dissipation is of a similar magnitude to the stiffness and energy dissipation in the timber itself.

The displacement in the test with the steel specimen is approximately the same as in the test with the timber specimen under the same load, which suggests a significant contribution of dowel deformation to the measured displacement. The energy dissipation, represented by the area inside the force-displacement loop, is similar in the two tests, which suggests a large contribution from dissipative processes in the loading apparatus.

The validity of this part of the study relies on accurate measurement of stiffness and energy dissipation caused solely by the timber and the interaction between dowel and timber at their interface. The test method was therefore altered to eliminate, where possible, the flexibility and energy dissipation in the loading apparatus.

By using the ASTM embedment test method, shown in Figure 5-5, the load could be applied to the dowel by direct contact with the loading head of the test machine, providing the minimum load path through the loading apparatus, and minimizing deformation and energy dissipation from that source. By applying the load this way, the dowel was held rigidly straight by the loading head, ensuring no dowel deformation and an evenly applied displacement over the width of the timber specimen. This method was therefore considered preferable to the EN method for the purpose of these cyclic embedment tests, and was used for all those embedment tests described in this section.

The drawback of the ASTM method is that the specimen does not have the same geometry as the timber subject to embedment by a dowel in a connection, since the timber on the unloaded face of the hole is not present. The effect of this difference is discussed in detail in Section 2.2.2, with reference to the study by Santos et al. (2010). The data from the numerical model presented in that paper suggested a variation in stiffness of approximately 10% resulting from the difference in test method. For the

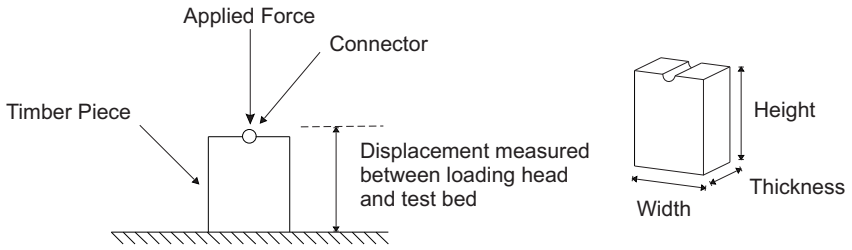

Figure 5-5: Test setup and specimen dimensions for the ASTM embedment test method (ASTM; 1997)

purpose of this study, it is considered that the reliability of measurements of foundation modulus and energy dissipation given by the ASTM method outweigh the benefit of the more accurate geometry in the EN method, in which there would be significant contributions to both measurements by the loading apparatus which could not be readily measured.

The specimen dimensions were chosen to comply both with the requirements of the ASTM method, which specifies minimum dimensions, and, for comparison, with those of the EN method. The specimen dimensions are shown in Table 5.3.

Table 5.3: Specimen dimensions for embedment tests

Dowel/Screw Diameter (mm)	Grain Orientation	Width (mm) (mm)	Height (mm)	Thickness
Norway spruce				
12	Parallel	72	84	40
	Perpendicular	168	50	40
Douglas fir				
20	Parallel	120	140	60
	Perpendicular	280	80	60

5.2.1.2 Measurement of force and displacement

The load applied to the specimen was measured by the load cell integrated with the servo-hydraulic loading machine. The resolution of this measurement was a key consideration in the choice of loading machine for these experiments. In order to identify the noise in readings taken from them, force readings were recorded from the load cells in each of three potential loading machines for the tests, with no load applied. The output force readings could then be inspected, and the noise represented by the standard deviation of the readings, and the resolution by the minimum step between readings. The data for each machine was logged on the same Vishay System 6000 data logger, so

Table 5.4: Noise measurements for servo-hydraulic loading machines

Loading machine	Standard deviation of noise (kN)	Resolution (kN)
Denison Mayes 20t	0.0002819	0.000343
Dartec 10t	0.0024394	0.003052
Instron 10t	0.0063568	<0.00007

the contribution of the data logger to both resolution and noise was the same in each case.

The machines tested were a 20-tonne capacity Denison Mayes, a 10-tonne capacity Dartec and a 10-tonne capacity Instron. The measurement range of the Denison Mayes machine could be adjusted, and the lowest available range of ±20kN was used to provide the minimum amplitude of noise in the force measurement. The resulting standard deviation of force for each machine is shown in Table 5.4. The results show that, although the resolution of the Instron was highest, it showed far more noise under zero load than the Denison Mayes. The Instron and Denison Mayes machines were located in different laboratories, and so it is possible that a difference in electromagnetic activity in each location caused this difference in noise. Because of its lower noise, the Denison Mayes machine was chosen for the tests in this study.

Displacement was measured in the pilot tests using strain-gauge-based displacement transducers in which contact between the transducer and the part to be measured is maintained by the force generated by a spring. The clamp-and-stand support for the transducer, therefore, resisted the reaction from this spring force. Where the displacements to be measured were of the order of tenths of millimetres, the deformation of the clamp-and-stand, assembled with reasonable tightness, could be assumed to be small in comparison to the displacements to be measured.

Given the small deformations to be measured in this study, of the order of microns, it could not be assumed that the support for the transducer would not displace significantly in comparison with the displacements to be measured as a result of the reaction from the spring force. This deformation, and its effect on the measured displacement, were thought to be partly responsible for the very high apparent energy dissipation, shown by a large hysteretic loop, found in some pilot tests.

Further pilot tests were carried out with stiffer supports for the displacement transducers, which yielded a lower measured energy dissipation. Whether the deformation of the support was significant compared with the deformation to be measured, however, remained uncertain. Given this fact, and the need for improved resolution of the displacement measurements for calculation of energy dissipation, it was considered ap-

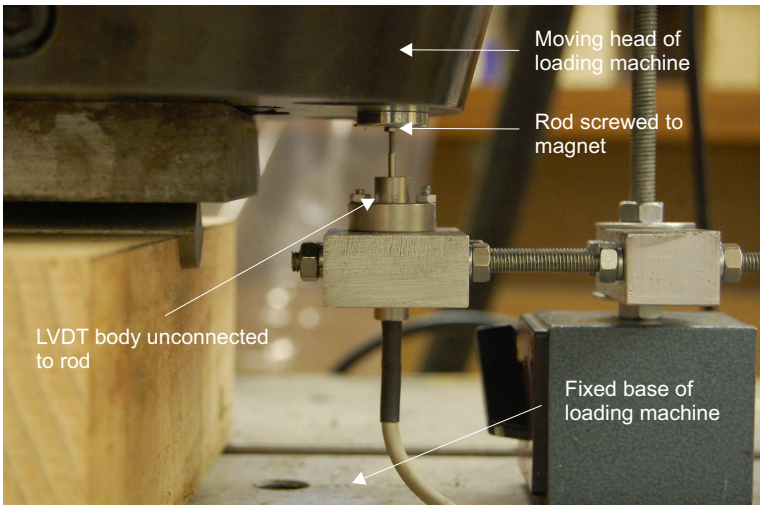

Figure 5-6: Linear variable differential transformer with the rod connected to the loading head by a magnet

propriate to obtain another sensor for these measurements. A non-contact sensor was used to ensure that no force was applied to the support at all, removing the uncertainty in its displacement.

The non-contact sensor which was used was a Micro-Epsilon ±1mm linear variable differential transformer (LVDT), which measures displacement by the differential voltage created by a metallic rod moving through an inductive coil. In the LVDT model chosen, the rod was not connected to the body of the sensor, and so was connected only to the part of the test apparatus to be measured, the head of the loading machine, by a permanent magnet, as shown in Figure 5-6. The rod therefore moved freely relative to the body of the sensor, ensuring no transfer of force between the two, and no variable load to be resisted by the support for the sensor.

5.2.1.3 Definition of loading profiles

Amplitude of cyclic component The types of load which were of interest in this study were discussed in Chapter 4, and the magnitude and form of oscillating load to be applied in this experimental work in Section 4.3. The result was that a sinusoidal variation of force should be applied, the mean and amplitude of which was defined by the R-ratio. R-ratios of 1.2 and -1 were shown to be representative of different forms of in-service vibration.

In the chosen embedment test method, however, only compressive loads could be applied to the half-hole specimen. The R-ratio of 1.2 could therefore be tested, but the R-ratio of -1 was not possible. Instead, an R-ratio of 10 was used, meaning that the

compressive applied load cycled between its maximum value and 10% of that maximum, to investigate the effect of near-removal of the load on that face of the hole. It was not considered safe to use a load of less than 10% of the maximum, in case a slight overshoot led to load reversal and excessive movement of the loading head. It should be noted that, as a result of an overshoot of the lower value of compressive load, the minimum load was often less than 10% of the maximum, so the R-ratio of 10 should be considered a nominal value corresponding to near-removal of the load.

The frequency of the oscillating load was 1Hz in the majority of tests, chosen to be within the range of vertical and lateral structural vibration. Vertical footfall-induced vibration generally occurs at frequencies higher than 1Hz, and the lateral mode natural frequency of tall buildings can be lower, but 1Hz was considered to be a reasonable frequency to investigate the general principles of vibration behaviour in this range.

Magnitude of peak load It was intended that the specimens be tested at loads representative of those they would experience in normal service conditions, such as a turbulent wind load which is expected to occur once per year. To illustrate the relationship between the expected capacity of a structural element and the load on that element expected to occur annually, the following example is given, for a timber connection under wind load, designed according to the Eurocode method. It has been assumed that the element is designed to work to its full efficiency, so that the ultimate limit state load is equal to the ultimate limit state resistance. The relationship is summarized in Figure 5-7.

First, the load carrying capacity, or resistance, was considered: the relationship between the expected resistance of a connection and the design resistance is defined by the statistical properties and partial factors applied by design codes. In design according to Eurocode 5 (BSI; 2009a), either tests or an empirical calculation based on density are used to determine a characteristic value of the embedment strength of the timber, which is exceeded by 95% of specimens. The expected value, the mean embedment strength, is higher than this characteristic value. In the tests by Santos et al. (2010), a standard deviation of 13% for the parallel-to-grain specimens and 18% for perpendicular to grain was recorded. Assuming a normal distribution, the 95th percentile will be approximately 1.64 standard deviations below the mean. Taking the average of the two grain orientations, the 95th percentile would be approximately 75% of the mean value. The design value of a resistance R_d is then obtained from 5.1, in which R_k is the characteristic value of the resistance. The material partial factor γ_M is taken as 1.3 for solid timber, and k_{mod} as 0.9 for a short-term action.

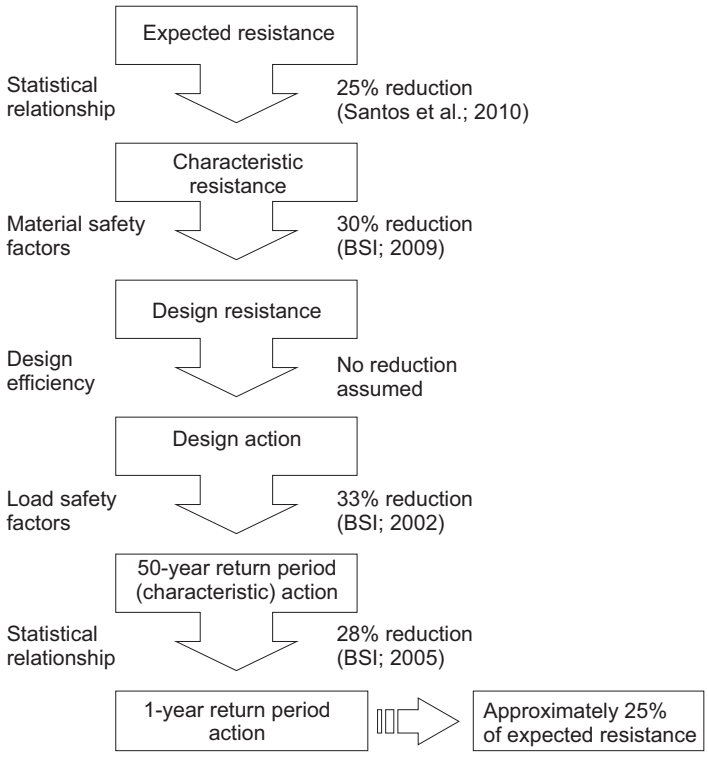

Figure 5-7: Flow diagram for the relationship between the 1-year return period wind load, or action, and the expected resistance of a timber connection

$$R_d = \frac{R_k k_{mod}}{\gamma_M} \tag{5.1}$$

The design value of the resistance is therefore 70% of the characteristic value, and approximately 50% of the mean value.

Next, the applied loads were considered: Eurocode 1 Part 1-4 (BSI; 2005) uses characteristic values of loads that are deemed to be exceeded once in 50 years. The same code also gives an equation to determine the load for different return periods, which is given as (4.16). Using this equation, the 1-year return period load is 72% of the characteristic load. The design value of an applied load is then obtained using factors in Eurocode 0 (BSI; 2002a), which are recommended as 1.35 for a permanent action, and 1.5 for a variable action.

As a result of these statistical relationships and safety factors, for this scenario, the 1-year return period load is 25% of the expected value of the capacity of the connection, or 34% of the characteristic capacity.

For the test programme, peak loads of 20% and 40% of the predicted characteristic capacity were applied, in order to cover the range of loads imposed on a connection in service. The characteristic capacity was predicted using the method given in Eurocode 5 (BSI; 2009a), which determines the embedment strength by an empirical equation based on density at 12% moisture content. The density of each species of timber was therefore measured and adjusted for the measured moisture content. For the Douglas fir, since the specimens were not taken from graded structural timber, two static embedment tests were carried out according to BS EN 383 (BSI; 2007) in each grain direction to check that the predicted embedment strength was reasonable.

Number of cycles The duration of loading was chosen to ensure that any transient effects could be observed and that a single value of either stiffness or energy dissipation could be measured which was representative of the long-term steady-state behaviour. The load was applied for 1000 cycles, which, during the pilot tests, proved sufficient for the stiffness and energy dissipation to reach a representative steady state. There was some evidence of a continued variation in stiffness and energy dissipation up to the end of the 1000-cycle test, which was more prominent in some tests than others, but it was considered that 1000 cycles represented a reasonable compromise between the need to achieve a steady-state response and the available time for testing.

5.2.2 Single-dowel connection test

The single-dowel connection test was intended to investigate the processes which contribute to stiffness and energy dissipation once the dowel is permitted to deform as in a complete connection. As discussed in Chapter 3, the connection tests and analysis in this study were restricted to one type of connection, in which the dowel transmits force from the timber to a steel plate in a central slot. Tensile and compressive loads were applied to each specimen to investigate the effect of the different stress distributions in the timber on stiffness and energy dissipation. In order to keep energy dissipation from sources other than the connection to a minimum, it was decided to avoid the need to anchor the specimen by making it symmetrical, with an identical connection at each end. Only the deformation of the loading head was measured, so the measured deformation represented the sum of the deformations in the two identical connections.

The test specimens were cut from 185mm by 200mm glued laminated timber beams made of Norway spruce, graded GL28h according to BS EN 1194 (BSI; 1999), and supplied by Lilleheden. The beams were made up of five 40mm laminates, and as a result, both the parallel-to-grain and perpendicular-to-grain specimens contained glue lines. Specimens were rejected if they contained a substantial visible defect in the surface of the timber within 25mm of the holes for the connectors. Otherwise, the specimens were used as-delivered, incorporating the defects elsewhere in the timber.

BS EN 383 (BSI; 2007) gives recommended dimensions for a symmetrical tensile test specimen parallel-to-grain, and so these dimensions were used to aid comparisons with work by other researchers. No guidance is given in EN 383 (BSI; 2007) for tensile tests perpendicular-to-grain, so the specimen dimensions were determined to match the compressive tests in that standard. The specimens are shown schematically in Figure 5-8, and a photograph of the tests in each grain orientation is in Figure 5-9. The cyclic loading applied to the single-dowel connection test specimens was the same as for the embedment tests, with the addition of a fully-reversed test with an R-ratio of -1.

The specimens for perpendicular-to-grain loading did not have a sufficiently large cross-section to ensure failure by dowel yield and embedment under tensile loading. The failure mode under tensile loading would instead have been expected to be by tensile failure of the timber between the dowels. The cross-section was, however, large enough to ensure that loads of 20% and 40% of the yield load of the connection could be applied without tensile failure of the timber. This meant that cyclic loading tests could be carried out in both tension and compression on the perpendicular-to-grain specimens up to 40% of the yield load of the connection, but static load tests to failure were only carried out in compression, to avoid brittle failure by splitting.

The single-dowel connection tests were carried out in displacement control, since it

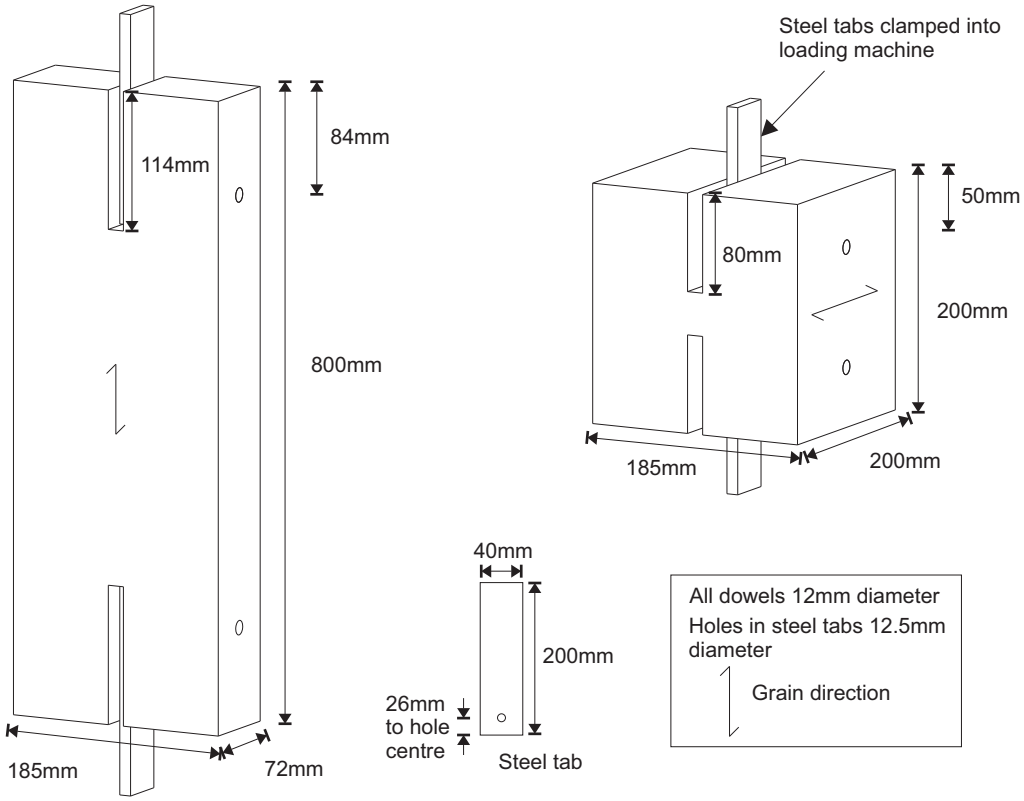

Figure 5-8: Test setup and specimen dimensions for single-dowel connection tests

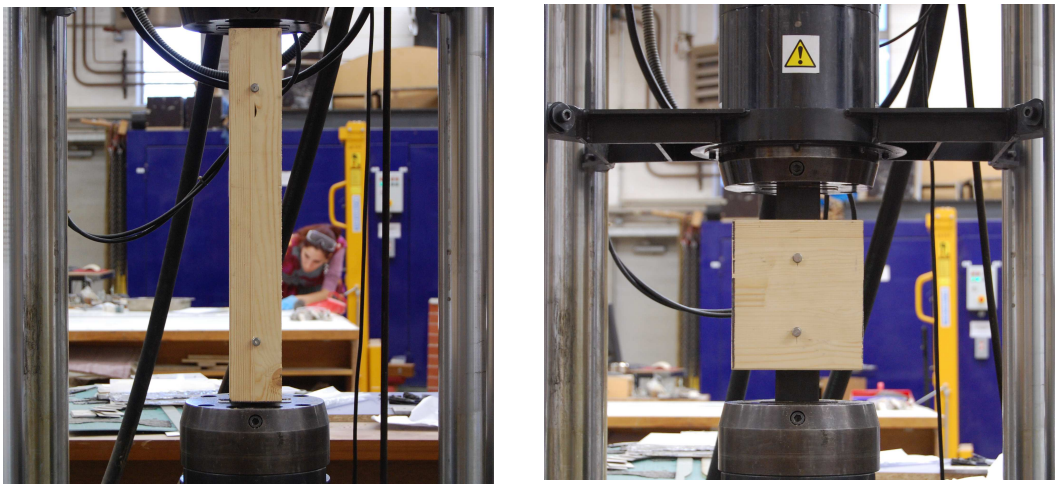

Figure 5-9: Single-dowel connection tests parallel and perpendicular to grain

was found in pilot tests that in load control, the servo-hydraulic loading machine did not reliably achieve the target peak and trough forces, occasionally becoming unstable.

For the small-amplitude oscillating loads, particularly at 20% of the predicted yield force and R=1.2, a noticeable oscillation at a frequency higher than the 1Hz test frequency appeared to be superimposed on the sinusoidal oscillation of the loading head. This was recognized to be a movement of the loading head, rather than a measurement noise, since it was measured by the LVDT and produced a corresponding force in the load cell. It is thought that this small-amplitude movement may be the 'dither' in the servo-hydraulic system: a continuous movement imposed to avoid static friction in the components of the loading machine.

The movement resulted in brief reversals in the force-displacement plot, and so small loops within the overall hysteretic loop. While it was not considered that this behaviour significantly affected the shape of the overall force-displacement response, it was noted that each loop would cause additional energy dissipation not representative of the energy dissipation of the specimen under sinusoidal load. In order to remove the effect of these loops, the energy dissipation was calculated based on the area of a smoothed envelope curve around the measured force-displacement response.

The smoothing was achieved by applying a low-pass filter to both the force and displacement measurements. A 1-pole digital filter was applied using the MATLAB function *filter*. Figure 5-10 shows the effect of applying the filter with cutoff frequencies of 3.2Hz and 6.4Hz. It can be seen that, as well as removing higher-frequency components of the signal, the filter induces a phase lag. The cutoff frequency of 6.4Hz was chosen to achieve adequate smoothing of the signal without excessive phase lag.

5.2.3 Analysis

The aim of this study was to identify the contribution of connections to natural frequency and damping in structures. The natural frequency is determined by the combination of the stiffness of each component of the structure, and the damping by the combination of their energy dissipation. For both the embedment tests and the single-dowel connection tests, the stiffness and energy dissipation were therefore to be determined.

Since the force-displacement response was not perfectly linear-elastic, a range of stiffnesses was exhibited under loading and unloading. The secant stiffness was chosen as the representative stiffness for each cycle of applied load, and was measured for each specimen and each cycle. The secant stiffness was taken as the average gradient on the force-displacement plot between the two extreme values of displacement. For behaviour under cyclic load which was close to linear, as in the left-hand graph in Figure 5-11, the secant stiffness closely followed the lines of loading and unloading

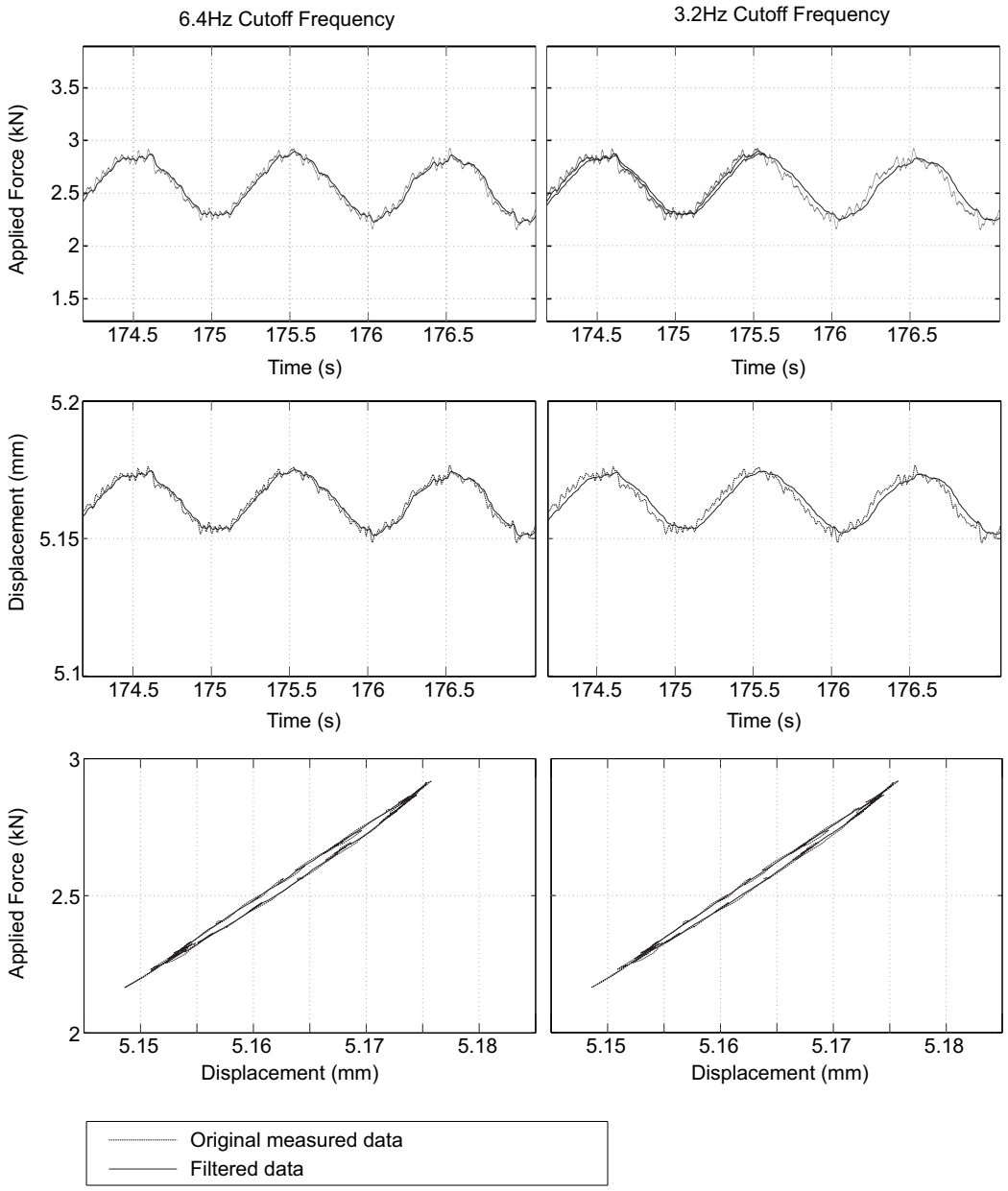

Figure 5-10: Filtering force and displacement measurements: the first row of figures shows the effect of applying a low-pass digital filter to the force measurements, the second row shows the effect on the displacement measurements, and the third the force-displacement loop for the indicated cycle

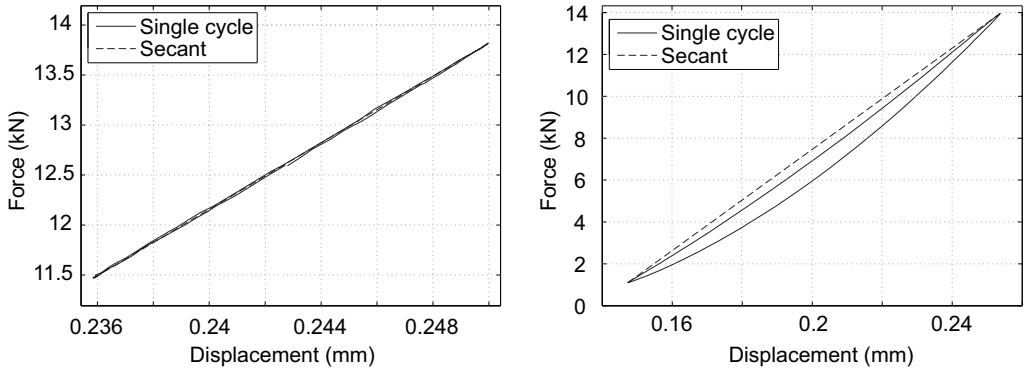

Figure 5-11: Secant stiffness for one-sided vibration with different amplitudes

closely. For non-linear behaviour, as in the right-hand graph in Figure 5-11, the secant line deviated from the lines of loading and unloading. Nonetheless, the secant stiffness was considered to be the appropriate parameter by which to represent the stiffness of each cycle. Whether this linear parameter is a sufficiently accurate representation of the non-linear behaviour is investigated in Chapter 7.

The energy dissipation in each cycle is given by the integral of the work done by the applied force around that cycle, which is equal to the area inside the hysteretic loop on the force-displacement diagram. If the force is expressed in Newtons, and the displacement in metres, then the work done calculated is in Joules. For structural engineering purposes, it is useful, and common, to express energy dissipation in a component as the damping it would generate if it was supporting a vibrating mass. In this study, it is expressed in terms of the viscous damping ratio γ. The relationship between γ and the energy dissipated is derived in various text books, such as by Thorby (2008), but the force-displacement response in these tests differs from the form generally derived, in that the oscillating load is not symmetrical around zero, and the locally linear line of secant stiffness does not necessarily pass through the origin. It is therefore considered useful to derive the relationship for this particular case.

If the stiffness supporting the mass is k, the viscous damping coefficient c and the mass m, then the equation of motion of the system would be as given in (5.2), where x is the displacement of the dowel or connection, and the overdot denotes differentiation with respect to time, t. To allow for the possibility that the force-displacement relationship is only locally linear, the constant A is added, so that the displacement for zero elastic force is not necessarily zero.

$$m\ddot{x} + c\dot{x} + k(x + A) = F \tag{5.2}$$

The natural frequency of the system is usually assessed by looking at the solution

to this equation under zero applied force. In this case, the solution for zero applied force is not of interest, but the solution for oscillation around a non-zero mean force is. In (5.2), for oscillation around a mean force $F = kA$, the equation simplifies to the normal equation of motion for a single-degree-of-freedom system. The system therefore has circular natural frequency ω_n, unaffected by A, where $\omega_n = \sqrt{k/m}$.

In the experimental work in this study, the low mass of the specimen and dowel compared with its stiffness means that the inertial force $m\ddot{x}$ is small compared with the forces due to stiffness and damping. The equation of motion can, therefore, be simplified to $c\dot{x} + k(x + A) = F$.

The energy dissipated in each cycle E, equal to the area inside the hysteretic loop on the force-displacement diagram is given by (5.3), where τ is an arbitrary start time and T is the period of oscillation.

$$E = \oint F \mathrm{d}x = \oint F \frac{\mathrm{d}x}{\mathrm{d}t}\mathrm{d}t = \int_{\tau}^{\tau+T} F\dot{x}\mathrm{d}t \tag{5.3}$$

Suppose the test is being carried out in displacement control, so that $x = X\sin(\omega t) + B$ and $\dot{x} = \omega X\cos(\omega t)$, where X is the half-amplitude of the applied displacement, ω is its circular frequency and B is an arbitrary offset of the displacement from zero. The applied force can then be expressed as $F = k(X\sin(\omega t) + A + B) + c\omega X\cos(\omega t)$, $T = 2\pi/\omega$ and the energy dissipated is given by (5.4).

$$E = \int_{\tau}^{\tau+2\pi/\omega} \left(k(X\sin(\omega t) + A + B) + c\omega X\cos(\omega t)\right) \omega X\cos(\omega t)\mathrm{d}t \tag{5.4}$$

(5.4) can be expanded to give (5.5).

$$E = \int_{\tau}^{\tau+2\pi/\omega} k\omega X^2\sin(\omega t)\cos(\omega t) + k(A+B)\omega X\cos(\omega t) + c\omega^2 X^2\cos^2(\omega t)\mathrm{d}t \tag{5.5}$$

The integrals of both $\cos(\omega t)$ and $\sin(\omega t)\cos(\omega t)$ over a complete period are zero, so (5.5) can be simplified to (5.6).

$$E = c\omega^2 X^2 \int_{\tau}^{\tau+2\pi/\omega} \cos^2(\omega t)\mathrm{d}t = \pi c X^2 \omega \tag{5.6}$$

The viscous damping ratio γ is given by $\gamma = (c\omega_n)/(2k)$. Substituting for c and rearranging gives (5.7).

$$\gamma = \frac{E}{2\pi k X^2 \frac{\omega}{\omega_n}} \tag{5.7}$$

Hence the energy dissipated in a specimen with viscous damping, E, calculated from tests, is related to the viscous damping ratio in an oscillating system with the same stiffness and viscous damping coefficient, γ by (5.7). It can be seen that the offsets in elastic force kA and displacement B have no effect on the calculation, as long as the behaviour is linear between the two extreme values of displacement, so that it can be described by (5.2). The ω/ω_n term in (5.7) arises because, in the viscous damping model, the energy dissipated varies with frequency, so it allows for the general case in which the test frequency ω is not the same as the resonant frequency ω_n.

The viscous damping model does not necessarily apply to dowel-type connections. An alternative damping model, the hysteretic damping model, states that the damping force is proportional to the amplitude of displacement, but in phase with the velocity. This means that, in the hysteretic damping model, the damping force is independent of the magnitude of the velocity, and so independent of the frequency. Thorby (2008) presented the same relationship as (5.7) for the hysteretic damping model. For the same applied displacement and velocity, the force is then given by (5.8), and the integral in (5.3) yields (5.9). Again, applying the offsets A and B, as in (5.4), has no effect. The hysteretic damping coefficient for a specimen can, therefore, be calculated from (5.10).

$$F = kX\sin(\omega t) + gX\cos(\omega t) \tag{5.8}$$

$$E = \pi k X^2 g \tag{5.9}$$

$$g = \frac{E}{\pi k X^2} \tag{5.10}$$

Whether the viscous or hysteretic damping model should be applied to dowel-type timber connections depends on the measured variation of damping with frequency, discussed in Sections 5.3.2 and 5.3.3.

5.2.4 Statistical hypothesis testing

The influence of the magnitude of the peak load on the steady-state secant stiffness measured in the tests was investigated using Student's t-test, attributed to William Sealy Gosset (Student; 1908), who published under the pen name Student at the request of his employers at the Guinness brewery, who did not generally allow their researchers to publish their work. The first paragraph of Gosset's paper introduces the terminology (Student; 1908).

> Any experiment may be regarded as forming an individual of a "population"

of experiments which might be performed under the same conditions. A series of experiments is a sample drawn from this population.

Gosset's work makes it possible to quantify the apparent relationship between two such samples in terms of a probability that a null hypothesis is true. The null hypothesis is that the two sets of test results are samples from populations with the same mean.

If the two samples are independent, then the t-ratio is calculated using their means $\overline{x}_i$, their standard deviations s_{x_i} and n_i, and the number of tests in each sample, according to (5.11).

$$t = \frac{\overline{x}_1 - \overline{x}_2}{\sqrt{\frac{s_{x_1}^2}{n_1} + \frac{s_{x_2}^2}{n_2}}} \tag{5.11}$$

If the samples are two test series on the same specimens, then a paired t-test can be carried out, which uses the mean of the differences between the results of each test on the same specimen $\overline{d}$ and the standard deviation of those differences s_d, according to (5.12).

$$t = \frac{\overline{d}}{\frac{s_d}{\sqrt{n}}} \tag{5.12}$$

The probability is then calculated using Student's t-distribution, which varies according to the degrees of freedom ν in the test. For the paired samples, ν is equal to $n - 1$. For the independent samples, it is calculated according to (5.13).

$$\nu = \frac{\left(\frac{s_{x_1}^2}{n_1} + \frac{s_{x_2}^2}{n_2}\right)^2}{\frac{\left(\frac{s_{x_1}^2}{n_1}\right)^2}{n_1 - 1} + \frac{\left(\frac{s_{x_2}^2}{n_2}\right)^2}{n_2 - 1}} \tag{5.13}$$

The probability density function (PDF) for the t-distribution is given by (5.14), where $\Gamma(n) = (n-1)!$. This can be used to calculate the probability p that the null hypothesis is true, using the calculated value of t.

$$\text{PDF} = \frac{\Gamma\left(\frac{\nu+1}{2}\right)}{\sqrt{\nu\pi}\,\Gamma\left(\frac{\nu}{2}\right)} \left(1 + \frac{t^2}{\nu}\right)^{-\frac{\nu+1}{2}} \tag{5.14}$$

In the experimental work, the t-test was used to quantify the effect of variation of independent variables, such as the peak value of the applied load in cyclic tests, on dependent variables, such as the secant stiffness. In that context, the test returns a probability that the sets of measured stiffness at each load are samples from the same

population of test results. If this null hypothesis were true, then that would imply that, in the case of this example, the peak load has no influence on stiffness.

5.3 Results and discussion

5.3.1 Static embedment tests on Douglas fir

In order to characterize the forces applied to the dynamic test specimens, their embedment strength was predicted according to Eurocode 5 (BSI; 2009a), based on their density. For the Douglas fir, the average density of 27 specimens was measured as 485kg/m^3, and the average moisture content of three preliminary specimens was obtained by the oven dry method according to EN 13183 (BSI; 2002b), and found to be 14.9%. On this basis, the adjusted density for the reference value of 12% moisture content, used in Eurocode 5, was calculated as 453kg/m^3. For the Norway spruce, the density was calculated for a single 0.185m by 0.2m by 2m piece, giving 458kg/m^3.

After the dynamic tests had been carried out, eight of the Douglas fir dynamic test specimens were used for moisture content evaluation. The average moisture content was 14.6%, with a coefficient of variation of 0.065. The preliminary moisture content measurement was, therefore, considered sufficiently accurate for estimation of load capacity. Seven Norway spruce specimens were used for moisture content evaluation, giving an average of 11.9% with a coefficient of variation of 0.050.

The calculated embedment strength is shown in Table 5.5. In the case of the Douglas fir, since the timber had not been graded, four static tests were also carried out, two in each grain orientation, to verify the calculated value. The force displacement plots for those tests is shown in Figure 5-12, and the average of the resulting strengths is shown in Table 5.5 along with the calculated values.

Since it would be the calculated value that would be used to design a connection in practice, the calculated mean embedment strength was used as the reference value for the forces applied in the dynamic tests for each species. It was noted that the mean of the measured strength perpendicular to grain in the Douglas fir was approximately 18% lower than the calculated strength. As a result, the specimens loaded to 20% of their predicted strength might be loaded to 24% of their actual strength. This was considered to be an acceptable level of deviation, but was borne in mind in interpreting the results.

Figure 5-12: Force-displacement plots for static embedment tests on Douglas fir perpendicular (left) and parallel to grain (right)

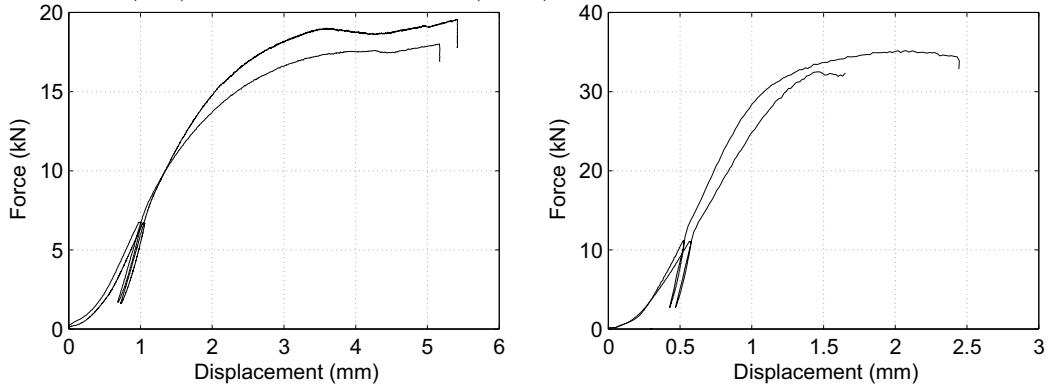

Table 5.5: Static embedment strength of specimens

Grain Orientation	Calculated Strength (kN)	Mean Measured Strength (kN)
Douglas fir		
Parallel	35.7	33.9
Perpendicular	21.6	17.7
Norway spruce		
Parallel	33.1	-
Perpendicular	21.6	-

5.3.2 Cyclic embedment tests

For each of the timber species tested, three parameters were varied: the R-ratio; the peak value of the load; and the orientation of load to the grain. In this section, the effect of each of those parameters on stiffness and energy dissipation is discussed.

The effect of the R-ratio is shown in Figure 5-13, which plots the results of a test in which 200 cycles at $R = 10$ were applied after the 1000-cycle $R = 1.2$ test was completed, so that the changes due to R-ratio could be observed on the same specimen. The specimen was Douglas fir loaded parallel-to-grain by a 20mm dowel with a peak load 40% of its yield force. It can be seen that with $R = 1.2$, the force-displacement curve under loading and unloading is close to linear-elastic. With $R = 10$, the force-displacement curve is non-linear under loading, the stiffness increasing with displacement. The nonlinearity is more pronounced under unloading, resulting in a higher area enclosed in the force-displacement curve for $R = 10$, and therefore a higher energy dissipation. The energy dissipation is measured as the area inside the hysteretic loop, and quantified by the equivalent viscous damping ratio γ.

When the two curves are plotted on the same graph, the force-displacement curve for $R = 1.2$ appears to align more closely to the unloading part of the curve for $R = 10$ than the loading part, but appears to have a slightly higher gradient than both.

As discussed in more detail in Chapter 6, the nonlinearity at low load is thought to be the result of the behaviour of the contact surface between the timber and the dowel. Before loading, the surface of the timber would have been uneven in comparison to that of the dowel; the drilling process would have cut and torn the fibres at this interface, leaving peaks and troughs in the surface. These features are visible in the optical microscope images presented in Section 5.5. As the load is applied, these features of the contact surface are compressed, and this will involve both elastic deformation, and irreversible processes such as buckling of the fibres, or crushing of the hollow trachieds. The irreversible processes were observed in the microscope images in Section 5.5. The movement at the contact surface between dowel and timber acts to reduce the stiffness below that of the solid timber.

As the loading cycles are repeated, the irreversible processes in the contact surface result in a movement of the dowel not recovered upon removal of the load, while the elastic deformation in the contact surface is thought to be responsible for the lower stiffness observed under low loads in each cycle, tending towards the rigid-contact stiffness of the solid timber as the load increases.

Under its first loading, the gradual compression of the contact surface between dowel and timber, as well as viscoelastic behaviour in the timber itself lead to transient variation in both stiffness and energy dissipation. These effects were observed

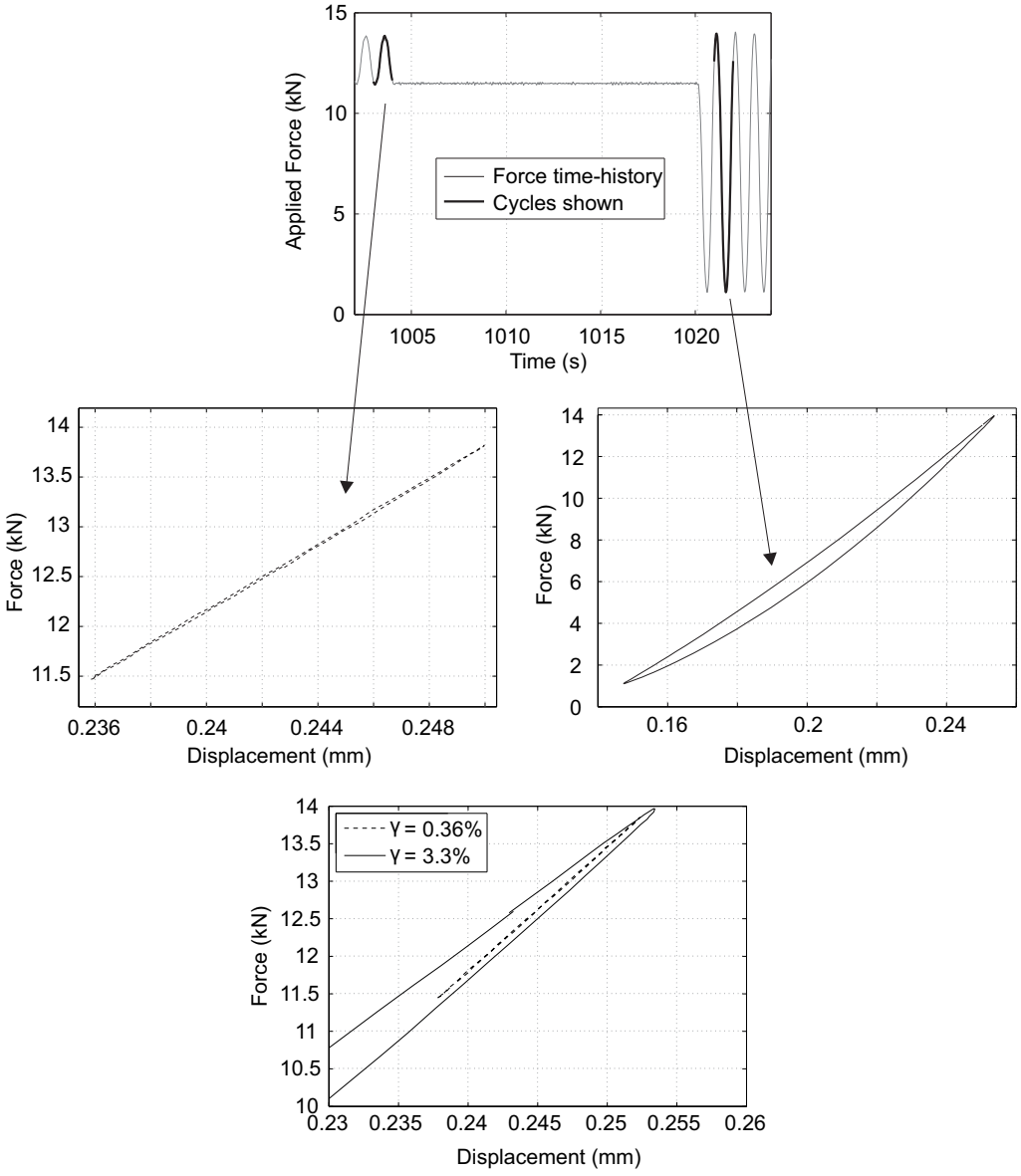

Figure 5-13: Force-displacement plots for two cycles of load on a Douglas fir embedment specimen loaded parallel-to-grain to 40% of its predicted yield load - the cycles, indicated in the top graph, have nominal R-ratios of 1.2 and 10, and γ, the equivalent viscous damping ratio, is shown for each in the bottom graph, which plots the two force-displacement loops on the same scale

by calculating these for every cycle of applied load during the test. The graphs in Figure 5-14 show the variation of stiffness and energy dissipation through a 1000-cycle test on a Norway spruce specimen loaded parallel-to-grain by a 12mm diameter dowel. Both measurements tend towards an approximately constant value during the test, the stiffness increasing and the energy dissipation decreasing. This is consistent with the hypothesis that irreversible behaviour in the contact surface contributes to both: the crushing and buckling of tracheids reducing the secant stiffness and dissipating energy through plastic behaviour, but only for a certain number of cycles until they form a more rigid contact surface.

There is an approximately constant amplitude of scatter in both stiffness and energy dissipation throughout the test. It is considered that this scatter is primarily the effect of measurement noise in the built-in load cell in the loading machine, and in the LVDT. As a result, it is expected that the points are scattered evenly either side of the true measurement.

Both stiffness and energy dissipation in Figure 5-14 reach an approximately constant value after about the 300th cycle. In some of the tests, the stiffness continued to rise, and the energy dissipation to fall, after the 300th cycle, but generally this transient phase was complete by the 700th cycle.

The effect of frequency variation on the stiffness and energy dissipation is shown in Figure 5-15. 200 cycles of load were applied at frequencies of 0.5Hz, 1Hz and 2Hz. The frequencies were not applied in sequential order, to ensure that any gradual change in stiffness or energy dissipation due to the number of cycles applied was not mistaken for a change due to frequency. 200 cycles at 1Hz were applied at both the beginning and end of the test, and showed that no significant change in damping or stiffness could be attributed to the cumulative effect of the number of cycles applied. In general, it was observed that an increase in frequency resulted in an increase in stiffness, and a reduction in energy dissipation. The stiffness can be seen to gradually rise with each rise in frequency, though the change between 0.5Hz and 2Hz is only about 2%. The change in energy dissipation, however, is only noticeable at the frequency of 2Hz, the other two frequencies appearing to give a similar energy dissipation.

This result aligns more closely with the hysteretic damping model, which predicts no change in dissipated energy with frequency. The viscous damping model would predict that the energy dissipated at 2Hz would be four times higher than that at 0.5Hz, whereas the results show a slight reduction in energy dissipation at the higher frequency.

The stiffness and energy dissipation for the dowel embedment tests is plotted in Figure 5-16, and for the screw embedment tests in Figure 5-17. Stiffness and energy

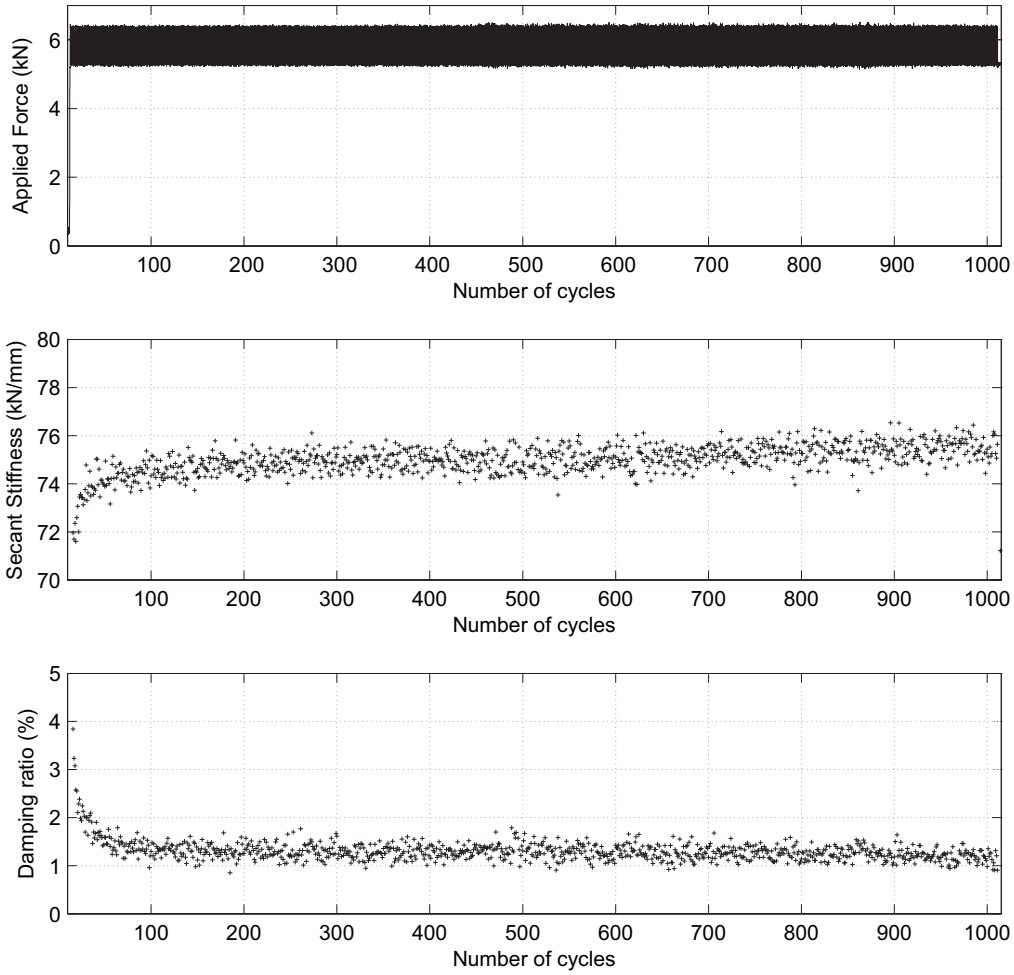

Figure 5-14: Stiffness and energy dissipation in each cycle of load through the test, for a Norway spruce embedment specimen loaded parallel-to-grain to 40% of its predicted yield load, with a nominal R-ratio of 1.2

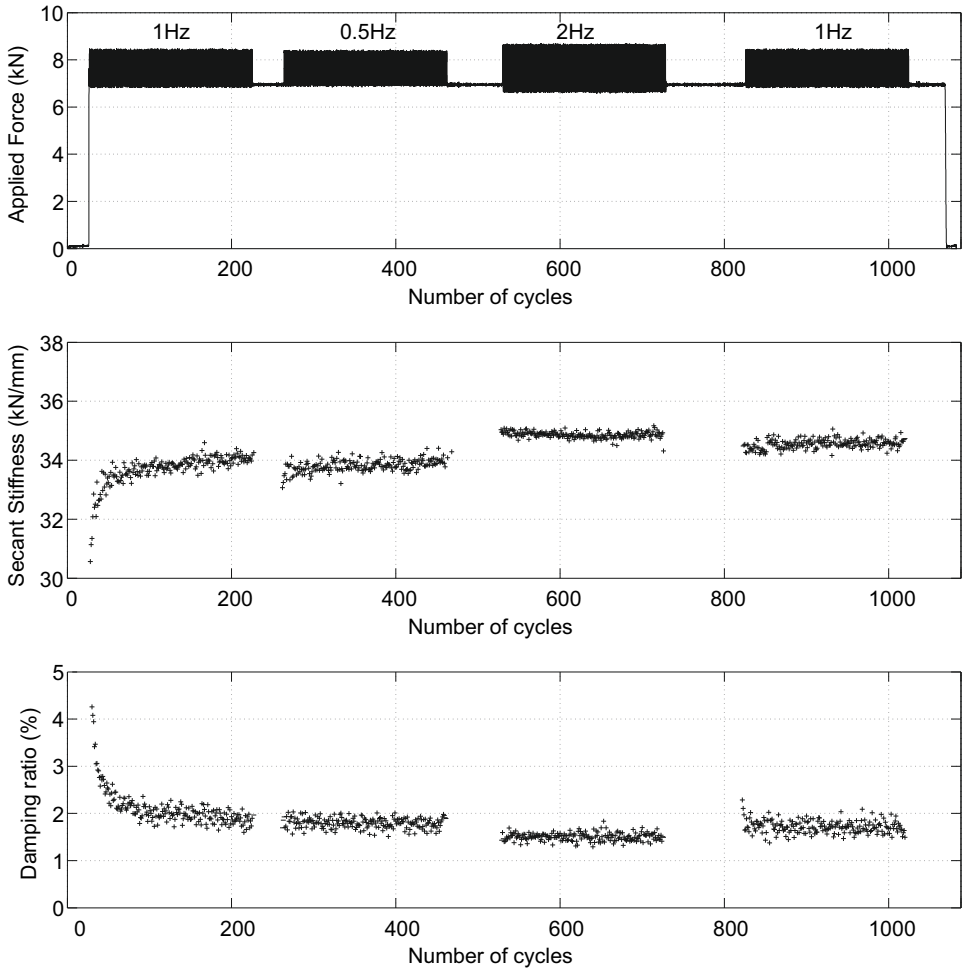

Figure 5-15: Stiffness and energy dissipation in each cycle of load through the test, for a Douglas fir embedment specimen loaded perpendicular-to-grain to 40% of its predicted yield load, with a nominal R-ratio of 1.2 at a range of frequencies

dissipation are expressed as the mean value over the final 300 cycles in the test. This was taken to be a reasonable estimate of the steady-state values, though there were tests in which the stiffness continued to rise, and the energy dissipation to fall, until the end of the test. For those tests, therefore, the plotted stiffness would be expected to be an underestimate of the steady-state value, and the energy dissipation an overestimate.

In each Norway spruce test, the secant stiffness at $R = 10$ was lower than that for $R = 1.2$ for the same specimen. The reduction in stiffness was approximately 20% for the parallel-to-grain dowel specimens at 40% of the predicted yield load and, at the other extreme, approximately 60% for the Douglas fir perpendicular-to-grain at 80%. For the range of peak loads of interest for serviceability conditions, 20% and 40% of the predicted yield load, the reduction from $R = 1.2$ to $R = 10$ falls in the range $30\pm10\%$ for all the dowel tests.

A slight rise in stiffness between the peak load of 20% and 40% is apparent in both Douglas fir and Norway spruce tests, on both screws and dowels, particularly for R=1.2. This may be due to a stiffer contact surface between dowel and timber in the tests with higher mean load, as imperfections in the timber surface are further crushed. Evidence for this working hypothesis is given by the optical microscope images in Section 5.5, which show micro-buckling, in the case of parallel-to-grain loading, or crushing, in the case of perpendicular-to-grain loading, of the tracheids within approximately 1mm of the hole edge.

The R=1.2 tests on both species, and at each load level, yielded similar results, with a consistent damping ratio of approximately 2% for perpendicular-to-grain loading and approximately 1% for parallel-to-grain loading. This pattern was apparent in both dowel and screw tests. In the Norway spruce parallel-to-grain, some scatter of damping was observed, up to 4.5% for the dowel tests and 7.5% for the screw tests. This higher damping may be due to dissipative processes in the contact surface between timber and dowel which may have had a greater influence in the Norway spruce tests because of the smaller connector sizes, which would make imperfections in the contact surface larger in comparison.

The damping in the R=10 tests is far more scattered than the R=1.2 tests, ranging from approximately 2% to 9% in both parallel- and perpendicular-to-grain orientations in all the tests. This suggests that different, more variable, processes are responsible for the increased damping at higher amplitude. The nature of the processes responsible for energy dissipation are discussed with reference to the analytical model in Chapter 6. No change in damping with peak applied load is apparent, except in the case of the perpendicular-to-grain tests with Douglas fir and R=10. These tests show a higher damping with a peak load of 80% of the predicted yield load than at other load levels,

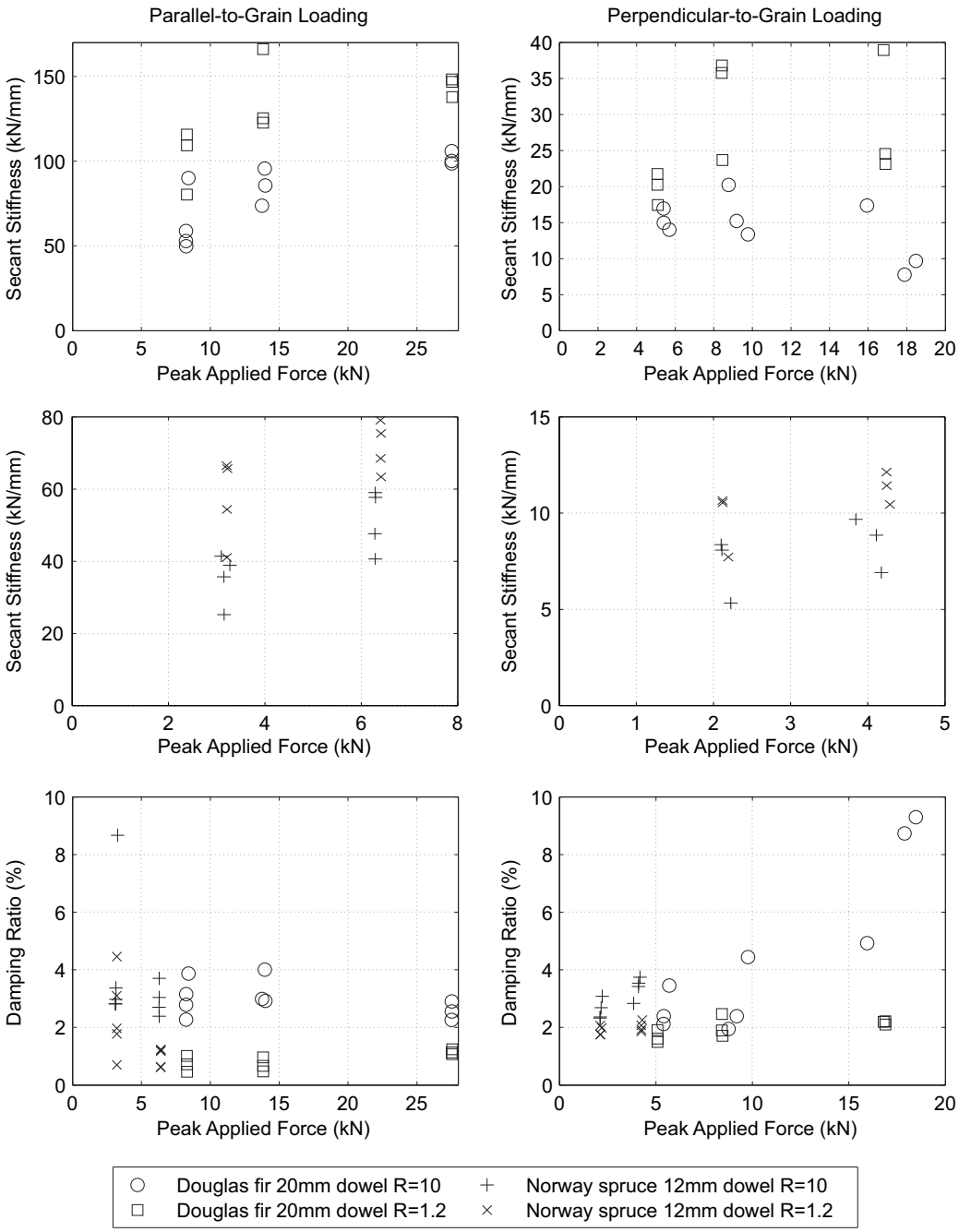

Figure 5-16: Steady-state stiffness and energy dissipation for every dowel embedment test specimen

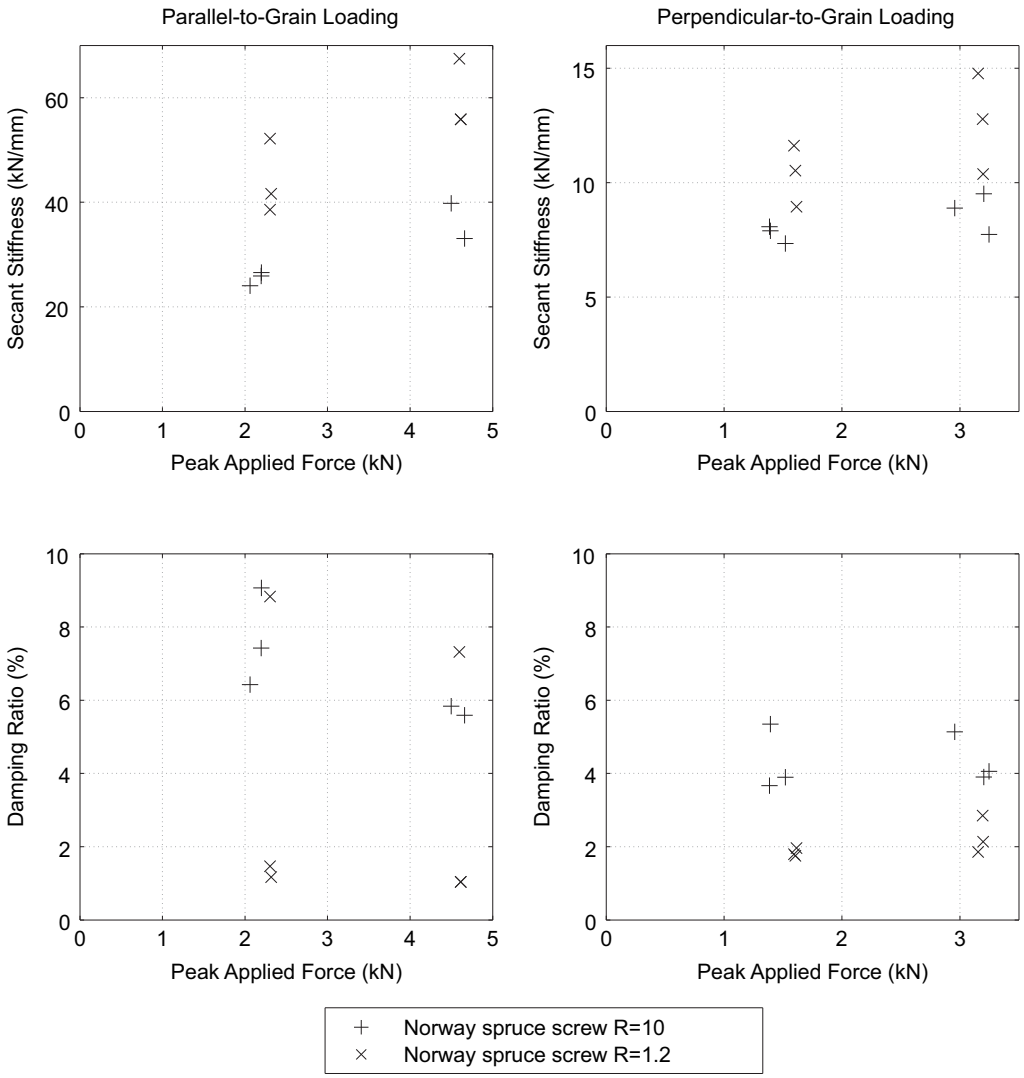

Figure 5-17: Steady-state stiffness and energy dissipation for screw embedment tests

and this is considered to be due to plastic behaviour in the timber at this higher load level, which falls outside of the range of loads expected under in-service vibration.

5.3.2.1 Statistical hypothesis testing

The effect of the peak load on the secant stiffness was investigated by statistical hypothesis testing using Student's t-test. To compare the stiffnesses at a pair of load levels, a two-tailed test was carried out to estimate the probability that the two sets come from a population with the same mean, a rejection of the null hypothesis therefore suggesting an influence of peak load on secant stiffness.

The different test methods applied to each species of timber meant that a different form of the t-test was required for each. In the Douglas fir tests, since a different specimen was used for each peak load, the sets of results for each load level were independent, so an independent-variable t-test was used. For the Norway spruce tests, each specimen was tested at each peak load, so a paired-variable t-test could be used, comparing the results of each pair of tests on a single specimen.

The results of the t-test on the stiffnesses from the Douglas fir embedment tests are shown in Table 5.6. The notation is as defined in Section 5.2.4.

The test was applied to four pairs of samples, comparing the peak loads of 20% and 40% of the predicted yield load and then the 40% and 80% peak loads in each orientation. The results suggest that there is an increase in mean stiffness due to the change of peak load from 20% to 40%, with probabilities p of 0.09 and 0.12 suggesting that there is a difference in the mean values of the populations from which the results were taken. There is not such a clear indication of a change between the peak loads of 40% and 80% of the predicted yield load, so this series of tests suggests that this influence is only at the lower loads and the 40% and 80% tests come from populations with similar mean values.

The results of the t-test for the Norway-spruce embedment stiffness in Table 5.7 suggest a similar trend for both the dowel and screw tests. In this case, only peak loads of 20% and 40% of the predicted yield load were tested, but the fact that the same specimens were tested at each load level meant that a paired-variable t-test could be carried out.

The two-tailed probabilities of 0.09 and 0.01 for the dowel tests and 0.04 and less than 0.005 for the screw tests suggest that the null hypothesis, that the measured stiffnesses at 20% and 40% of the predicted yield load come from the same population, is not likely to be true in either grain orientation. The results therefore suggest an influence of peak load on stiffness.

Table 5.6: Student's t-test applied to the measured stiffness in the Douglas fir embedment tests with R=1.2 to investigate the effect of peak load on secant stiffness

Orientation and load	$\overline{x}$	s_x	n	t	ν	p
Perpendicular 20%	19.8	2.2	3			
				2.79	2.4	0.09
Perpendicular 40%	32.1	7.3	3			
				0.49	3.9	0.65
Perpendicular 80%	28.9	8.8	3			
Parallel 20%	101.7	18.9	3			
				2.02	3.8	0.12
Parallel 40%	137.8	24.5	3			
				0.43	2.2	0.71
Parallel 80%	144.0	5.3				

Table 5.7: Paired-variable Student's t-test applied to the measured stiffness in the Norway spruce embedment tests to investigate the effect of peak load on secant stiffness

	$\overline{d}$	s_x	n	ν	t	p
Dowel						
R=1.2 Perpendicular	1.70	0.95	3	2	3.11	0.09
R=1.2 Parallel	14.69	5.41	4	3	5.43	0.01
Screw						
R=1.2 Perpendicular	2.28	0.86	3	2	4.61	0.04
R=1.2 Parallel	15.60	1.56	3	2	17.34	0.00

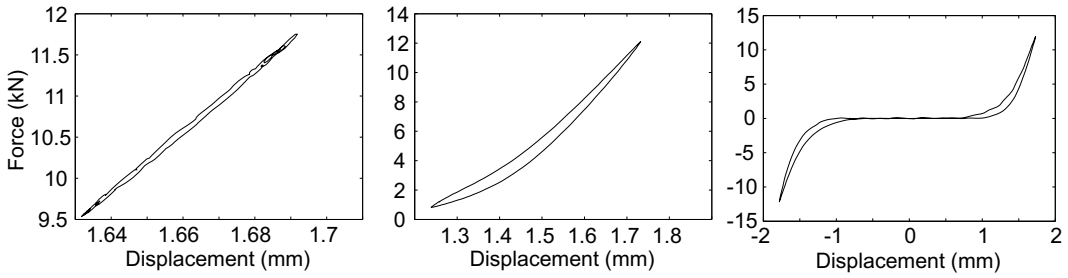

Figure 5-18: Force-displacement plots for single-dowel connection tests with R=1.2, left, R=10, centre, and R=-1, right

5.3.3 Single-dowel connection tests

The single-dowel connection tests show qualitatively the same behaviour as the embedment tests. Again, the tests with R=10 have a significantly non-linear force-displacement response, and have a higher energy dissipation than those with R=1.2. It is thought that the contact surface between dowel and timber in embedment is responsible for the non-linear behaviour at low load which produces these effects.

In contrast to the embedment tests, the single-dowel connection test method allowed a reversed load to be applied, so a test with R=-1 and a load 40% of the predicted yield load was carried out for each specimen. Figure 5-18 shows the force-displacement plots for a single cycle at each of the three R-ratios. These cycles are approximately the 900th in each of the tests, chosen to be representative of the steady-state cyclic behaviour which shows little variation between cycles. The relationship between the embedment stiffness and the single-dowel connection stiffness is discussed further in Chapter 7, with reference to the beam on foundation model to describe the behaviour of the connection.

The slack section in the R=-1 plot, where the loading head moves with very little force applied, is due both to the clearance between the dowel and the holes in the steel plates that load the specimen and the gap formed by irreversible behaviour in the surface of the timber. The dowels, nominally 12mm, were measured as having a diameter of 11.8mm, and the holes in the steel plate were drilled to 12.5mm. The total slack due to this clearance in each of the two dowels was therefore approximately 1.4mm, and so accounts for a large proportion of the displacement at near-zero force shown in R=-1 plot in Figure 5-18.

Figures 5-19 and 5-20 show the stiffness and energy dissipation measured in the single-dowel tests with R=10 and R=1.2. Far more scatter was observed in the perpendicular-to-grain tests than in the parallel-to-grain tests, but both showed similar trends. The magnitude of the energy dissipation, nondimensionalized as the equivalent

viscous damping ratio, was similar to in the equivalent embedment tests. This is considered to be due to the low contribution to energy dissipation from the deformation of the steel dowel, so that most of the energy dissipation comes from the same processes as in the embedment tests.

The most likely cause of any additional energy dissipation in the single-dowel connection is considered to be that, while the connection as a whole is subject to a load 20 or 40% of its predicted yield load, a large proportion of the length of the dowel will transmit a far lower load. In the parallel-to-grain tests illustrated in Figure 5-16, the lower-loaded Norway spruce specimens exhibited higher energy dissipation than those under higher peak loads. The timber under lower load in the single-dowel test may, therefore be responsible for additional energy dissipation.

The additional energy dissipation in the single-dowel tests appeared to be unreliable, however, with some single-dowel tests showing equivalent viscous damping approximately equal to the lowest values in the embedment tests.

In the parallel-to-grain tests, the stiffness, plotted in Figure 5-19, was observed to increase slightly with applied load. As in the case of the embedment tests, it was considered that this effect was due to the higher applied force compressing the surface of the timber and improving the stiffness of the contact between dowel and timber. This suggests that as the contact between the dowel and timber increases in stiffness, the stiffness of the connection tends towards a value which represents a rigid contact surface. This concept is important in considering how the connection is modelled in Chapter 6, since it suggests that, to predict the steady-state stiffness and energy dissipation in the connector, a model with a rigid contact surface may be appropriate.

The perpendicular-to-grain tests in Figure 5-20 do not show the same tendency for an increase in stiffness with the peak value of the applied load. A possible explanation for this is in the plastic deformation in the contact surface observed in microscopy in Section 5.5. The plastic deformation occurs through a different process in each of the two grain directions. The plastic deformation due to crushing of the tracheids in the perpendicular-to-grain direction could, therefore, occur at a different proportion of the yield force of the connection than the equivalent process in the parallel-to-grain direction. If the plastic deformation at the contact surface were largely complete at 20% of the predicted yield force, then that might explain the fact that no further increase in stiffness was observed as the peak load was increased to 40% of the predicted yield force.

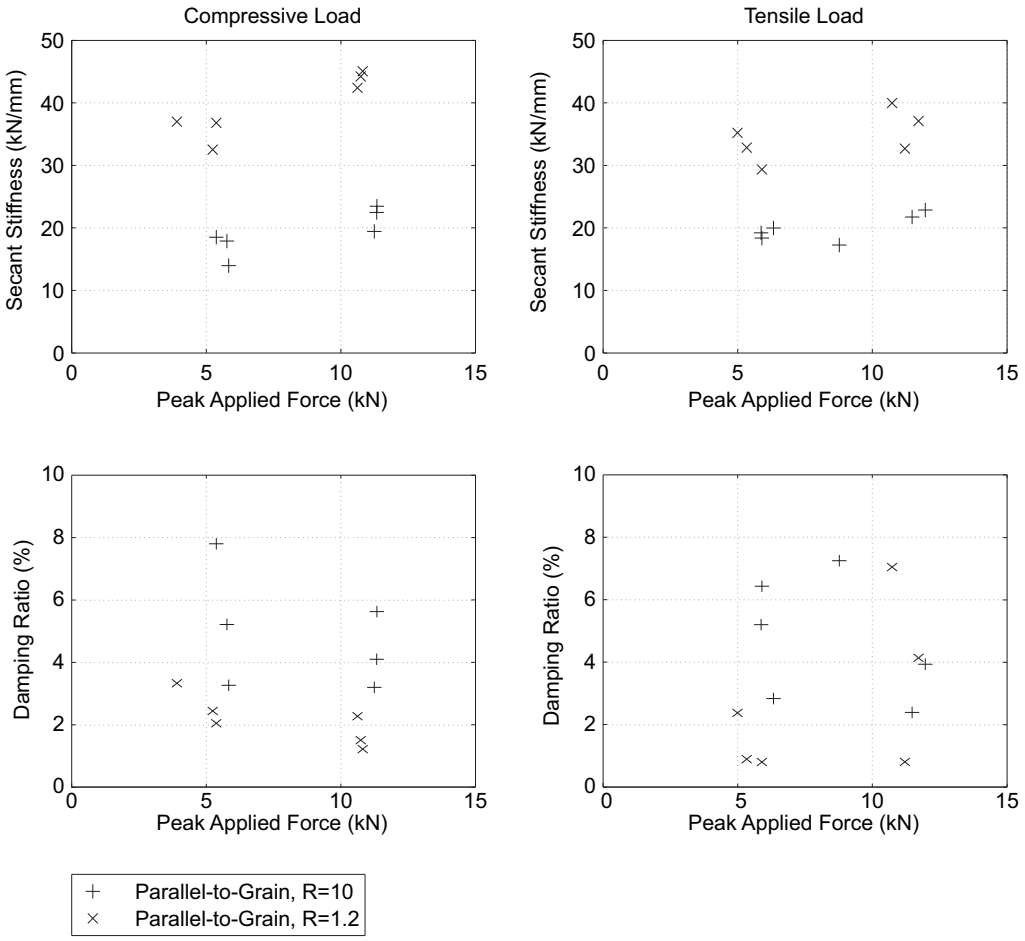

Figure 5-19: Stiffness and energy dissipation for single-dowel connection tests parallel-to-grain

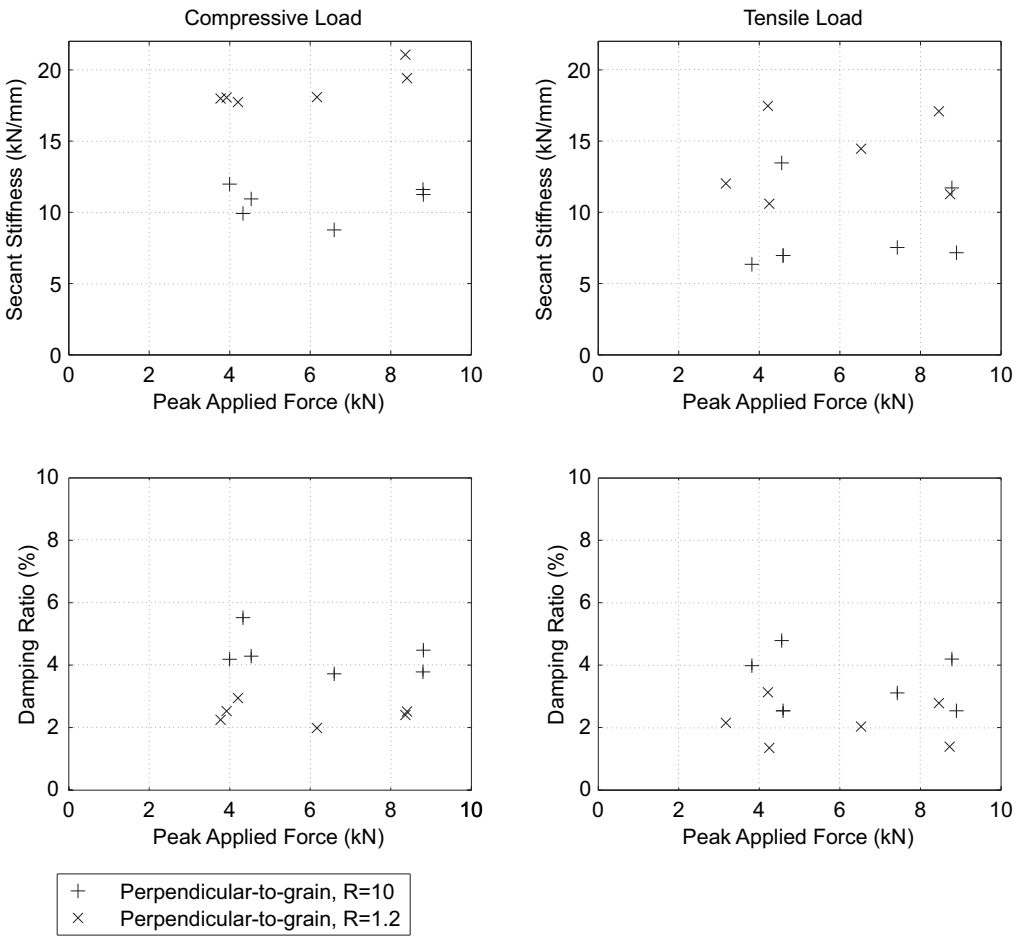

Figure 5-20: Stiffness and energy dissipation for single-dowel connection tests perpendicular to grain

Table 5.8: Student's t-test applied to investigate the effect of variation in peak load on the secant stiffness measured in single-dowel connection tests

	$\overline{d}$	s_x	n	ν	t	p
Tension						
Perpendicular	0.91	1.42	3	2	1.11	0.38
Parallel	4.11	0.73	3	2	9.70	0.01
Compression						
Perpendicular	1.60	1.46	3	2	1.90	0.20
Parallel	8.46	1.33	3	2	10.99	0.01

5.3.3.1 Statistical hypothesis testing

The application of Student's t-test to the variation of stiffness with the amplitude of the peak applied load can be used to quantify the observed increase in stiffness with load in the parallel-to-grain specimens and the relatively consistent stiffness between 20% and 40% loads in the perpendicular-to-grain specimens. The results of the t-test, shown in Table 5.8, show probabilities of 0.38 and 0.2 in tension and compression that the null hypothesis is true and the samples of tests at 20% and 40% of the predicted yield force come from populations with the same mean. In contrast, the parallel-to-grain tests are seen to suggest a variation of stiffness with peak load. The probability of the null hypothesis for the test being true is only 0.01 for those tests.

5.4 Material characterization

In order to compare the experimentally-determined dynamic embedment stiffness with that predicted by the stress function models described in Chapter 6, the material properties of the timber were estimated by testing and literature review.

5.4.1 Elastic moduli

The principal elastic moduli of specimens from both Douglas fir and Norway spruce were determined following the method given in BS EN 408 (BSI; 2011) for the compressive modulus of solid timber. For the Douglas fir tests, the elastic moduli were determined from tests on specimens extracted from some of the dynamic test specimens. For the Norway spruce tests, the dynamic test specimens were too small to extract pieces of the right dimensions, so the elastic moduli were determined using specimens extracted from the single-dowel connection test pieces. The parallel-to-grain Norway spruce specimens were 14mm × 60mm and 80mm in the grain direction, and the perpendicular-to-grain

Table 5.9: Douglas fir dynamic test specimens from which elastic modulus specimens were extracted

Test	Grain Orientation	Peak Force F_{peak} (% of Static Failure)	R-ratio $\frac{F_{peak}}{F_{trough}}$	No. of Specimens
1	Parallel	20%	1.2	2
2	Parallel	20%	10	2
3	Parallel	40%	1.2	3
4	Parallel	40%	10	2
5	Parallel	80%	1.2	3
6	Parallel	80%	10	1
7	Perpendicular	20%	1.2	3
8	Perpendicular	20%	10	2
9	Perpendicular	40%	1.2	2
10	Perpendicular	40%	10	2
11	Perpendicular	80%	1.2	2
12	Perpendicular	80%	10	2

Table 5.10: Mean measured elastic moduli and coefficients of variation (COV)

Species	Parallel-to-grain Elastic Modulus	COV	Perpendicular-to-grain Elastic Modulus	COV
Douglas fir	10569	0.21	322	0.38
Norway spruce	12788	0.22	153	0.30

specimens 40mm deep × 70mm in the grain direction and 90mm in the direction in which the modulus was to be measured.

The Douglas fir specimens for which elastic modulus data were obtained are summarized in Table 5.9. Two specimens were taken from each embedment specimen, one in each grain direction, so 26 elastic moduli were obtained in each grain direction, 52 in total. The cutting pattern is shown in Figure 5-21. In the Norway spruce, 18 specimens were made in each grain orientation, 36 in total.

The tests were carried out using an Instron 20-tonne capacity screw-driven servo loading machine. A spherical bearing was used to ensure the specimens were loaded evenly if the top and bottom surfaces were misaligned in manufacture. The deformation was measured by a pair of extensometers, which ensured that deformation in the contact surface between the loading head and the specimen and other local effects near the point of loading were not included in the displacement measurement. The gauge length of the extensometers was 50mm, and they were located centrally in the height of the specimen.

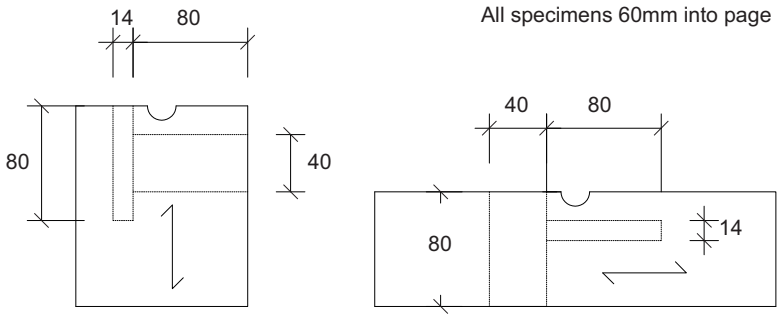

Figure 5-21: Cutting pattern to extract elastic modulus specimens in each grain direction from the Douglas fir embedment specimens, all dimensions are in millimetres

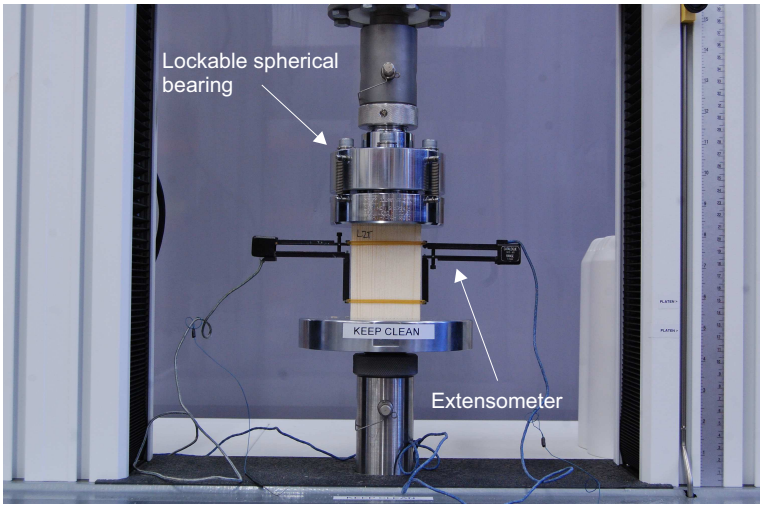

Figure 5-22: Elastic modulus testing according to EN 408 (BSI; 2011) for a parallel-to-grain Norway-spruce specimen

A parallel-to-grain Norway spruce specimen during testing is shown in Figure 5-22.

The elastic moduli for each species are given in Table 5.10. The coefficient of variation is higher for the perpendicular-to-grain moduli in each case, due to the fact that the perpendicular-to-grain specimens included a range of orientations between radial and tangential. The tangential direction was dominant in the solid planks of Douglas fir, while the Norway-spruce specimens, taken from glued-laminated timber beams, contained more specimens with orientations closer to radial.

The measured values of the principal elastic moduli provided two of the four parameters required for two-dimensional analytical model. In addition, the Poisson's ratio and shear modulus are required. The Wood Handbook (Forest Products Laboratory; 2010) provides mechanical properties for various species of timber grown in the USA and Canada, including Douglas fir, and Bodig and Jayne (1993) tabulates elastic prop-

Table 5.11: Mechanical properties for Douglas fir and spruce - all units are N/mm^2, with the exception of the dimensionless Poisson's ratios

	E_L	E_T	E_R	G_{LR}	G_{LT}	G_{RT}	ν_{LR}	ν_{LT}	ν_{RT}
Douglas fir	14740	737	1002	943	1150	103	0.292	0.449	0.390
Spruce	15373	798	503	706	654	36	0.422	0.545	0.470

erties for spruce from three different studies. The values for Douglas fir and Spruce are summarized in Table 5.11.

In the descriptions of the orthotropic elastic properties by Bodig and Jayne (1993) and the Wood Handbook (Forest Products Laboratory; 2010), there are nine independent elastic constants: three elastic moduli corresponding to the longitudinal, radial and tangential orientations with respect to the grain and ring structure; three shear moduli and three Poisson's ratios. In a single plane, only two elastic moduli, one shear modulus and one Poisson's ratio are required.

5.4.2 Estimation of the shear modulus

The mean elastic moduli from the tests on Douglas fir were $10,569$N/mm^2 in the longitudinal direction and 322N/mm^2 in the perpendicular direction, which, for most specimens, was close to tangential. For the Norway spruce, in which the perpendicular direction was usually close to radial, the mean elastic moduli were $12,788$N/mm^2 in the longitudinal direction and 153N/mm^2 in the perpendicular direction. The ratio of the two moduli in each case was, therefore, quite different from that given in the literature, since the measured perpendicular moduli were far lower. It was not, therefore, considered appropriate to obtain the shear modulus as a proportion of the longitudinal elastic modulus, using a ratio from published results. Another rationale was therefore sought to estimate the shear modulus.

Jones (1975) shows that if the elastic compliances of an orthotropic material in plane strain are given by s_{ij}, as in (5.15), then the apparent shear compliance, s'_{66}, for axes at an angle θ to the principal axes, is given by (5.16).

$$s_{11} = \frac{1}{E_1} \quad s_{12} = \frac{-\nu_{12}}{E_1} \quad s_{22} = \frac{1}{G_{12}} \tag{5.15}$$

$$\begin{aligned} s'_{66} =& 4\left(s_{11} + s_{22} - 2s_{12}\right)\sin 2\theta \cos 2\theta \\ &+ s_{66}\left(\sin 2\theta - \cos 2\theta\right)^2 \end{aligned} \tag{5.16}$$

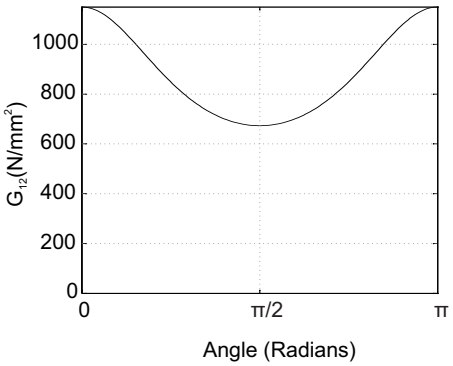

Figure 5-23: Variation of apparent shear modulus with angle from the principal direction for Douglas fir

For Douglas fir, as described in the Wood Handbook (Forest Products Laboratory; 2010), the variation of apparent shear modulus with angle in the longitudinal-tangential plane can be plotted using (5.16). The result is shown in Figure 5-23.

At $\theta = \pi/2$, s'_{66} is independent of s_{66}, and so the apparent shear modulus is independent of the principal shear modulus. Using the elastic moduli obtained from the tests, it was therefore possible to calculate the apparent shear modulus at $\theta = \pi/2$ for each specimen. The ratio of the maximum and minimum shear modulus from Figure 5-23 was then assumed to apply to the Douglas fir used in the tests, and was used to estimate the principal shear modulus for each specimen. The same approach was applied to the Norway spruce.

5.4.3 Friction coefficient

Tests were carried out to estimate the coefficient of friction to use in the analytical models presented in Chapter 6. Figure 5-24 shows the test setup, in which a vertical force was applied to two specimens, with a long dowel between. The vertical load was applied by a servo-hydraulic loading machine, which allowed the load to be held constant despite any vertical settlement. The dowel was pushed horizontally using a hydraulic hand jack, and the force required to do so was continuously recorded through a load cell.

It should be noted that the friction force in this test setup is in a different orientation to the friction force developed during embedment of the dowel into the timber. Tests by McKenzie and Karpovich (1968) showed that the grain orientation had no significant effect on the magnitude of either the static or steady sliding friction coefficients. It was considered reasonable, therefore, to assume that the frictional behaviour will be similar in both orientations, so that this test provides a suitable estimate of the coefficient of

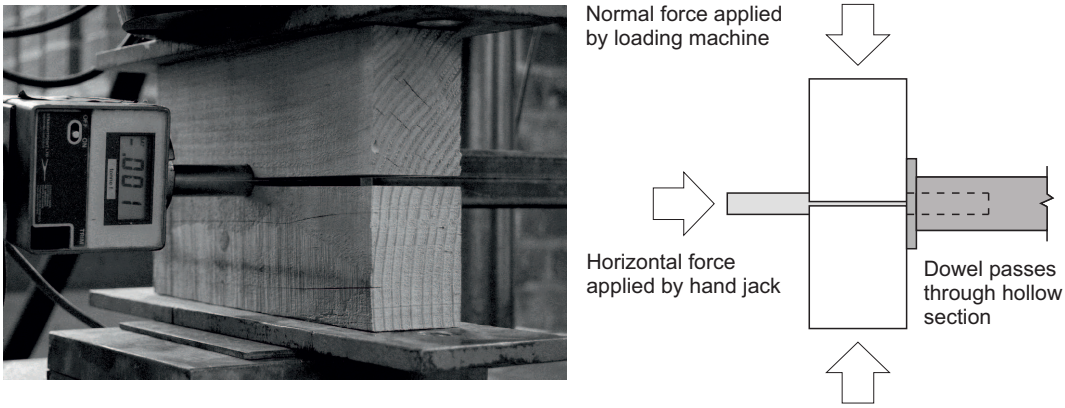

Figure 5-24: Friction test on dynamic test specimens

friction for use in the analytical model. It was noted, however, that the tests on Norway spruce showed some variation of friction coefficient with grain direction.

Six friction tests were carried out for each species: three with the load applied parallel to the grain, and three with the load applied perpendicular to the grain. For the Douglas fir specimens, in each orientation, two specimens were freshly cut, and one was made from two specimens which had been used for a cyclic embedment test for 1000 cycles at 1Hz, in which the peak load was 40% of the predicted yield force. All the Norway spruce tests were carried out on freshly-cut specimens. During each friction test, the normal load was equivalent to 40% of the predicted yield force.

One of the freshly-cut specimens in each grain direction, and in each species, was used for friction tests at three levels of normal force, to investigate the validity of the Coulomb friction approximation, which would suggest that the horizontal force to overcome friction would be proportional to the normal force.

Figure 5-25 shows the plot of applied lateral force against lateral displacement for one of the friction tests. This highlights the influence of the rate of movement of the dowel. In part A of Figure 5-25, the lever of the hand jack was pushed down slowly, which meant that the applied force dropped away before the constant rate of displacement, required for kinetic friction, could develop. The dowel therefore moved a short distance each time and then stopped, a phenomenon known as stick-slip oscillation.

In part B of Figure 5-25, the lever of the hand jack was moved sufficiently quickly that kinetic friction could develop, after overcoming the initial, higher force of static friction. Since there is continuous movement in the dynamic tests, it is considered that the coefficient of kinetic friction is appropriate as the input to the analytical model. The coefficient of friction to be used in the model was therefore estimated based on the kinetic friction in each case.

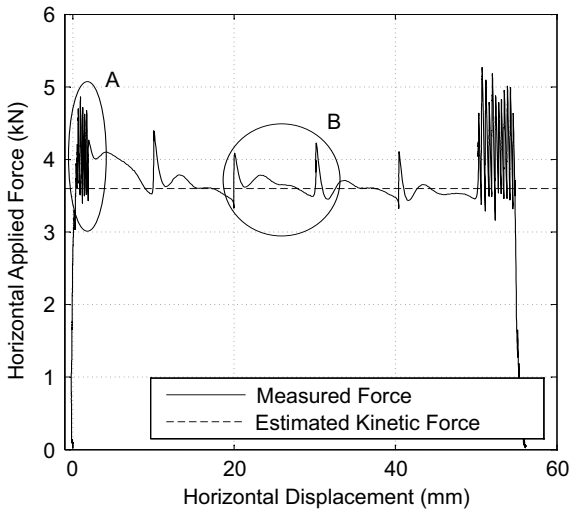

Figure 5-25: Horizontal force-displacement plot for a Douglas fir specimen loaded perpendicular to the grain at 40% of the predicted yield force

In some of the Douglas fir parallel-to-grain friction tests, since a higher vertical load was applied, it was not possible to depress the lever of the hydraulic jack quickly enough to achieve the kinetic friction behaviour as in part B. In these cases, the lower value of force in the stick-slip oscillation, as in part A, was used to estimate the coefficient of friction. Figure 5-25 shows that the lowest force measured in part A is a reasonable estimate of the coefficient of kinetic friction.

The results of the friction tests are shown in Table 5.12. For Douglas fir, the mean ratio of the horizontal kinetic force to the vertical force for all six tests was 0.41, with a coefficient of variation of 0.1, giving an estimate of the coefficient of friction, for use in the analytical models presented in Chapter 6, of 0.21. There was no clear effect of grain orientation on the ratio of normal force to friction force. The parallel-to-grain specimen which had been through the cyclic embedment test exhibited a higher friction coefficient than those which had been freshly cut. This suggests that the polishing effect of the cyclic load may have increased the surface of real contact between dowel and timber, and therefore the friction coefficient by increasing the area of real contact between dowel and timber. Further testing would be required to verify this, however. There was no evidence of the effect of previous loading in the perpendicular-to-grain specimen.

In the Norway spruce specimens, the coefficients were lower, and some variation with grain orientation was observed. The parallel-to-grain tests had a mean coefficient of 0.15, and the perpendicular-to-grain tests a mean of 0.19 for use in the analytical models.

Table 5.12: Friction test results

	Normal force (kN)	Static load (kN)	Static coefficient	Kinetic load (kN)	Kinetic coefficient
Douglas fir					
Para. Unloaded 1	13.8	6.5	0.24	5.4	0.20
Para. Unloaded 2	13.8	6.6	0.24	5.2	0.19
Para. Loaded	13.8	7	0.25	6.8	0.25
Perp. Unloaded 1	8.4	4.2	0.25	3.3	0.20
Perp. Unloaded 2	8.4	4.2	0.25	3.6	0.21
Perp. Loaded	8.4	4.2	0.25	3.3	0.20
Norway spruce					
Para. Unloaded 1	6.3	2.2	0.17	2.0	0.16
Para. Unloaded 2	6.3	2.3	0.18	1.8	0.14
Para. Unloaded 3	6.3	2.0	0.15	1.8	0.14
Perp. Unloaded 1	4.1	1.8	0.22	1.7	0.21
Perp. Unloaded 2	4.1	1.6	0.19	1.5	0.18
Perp. Unloaded 3	4.1	1.6	0.19	1.5	0.18

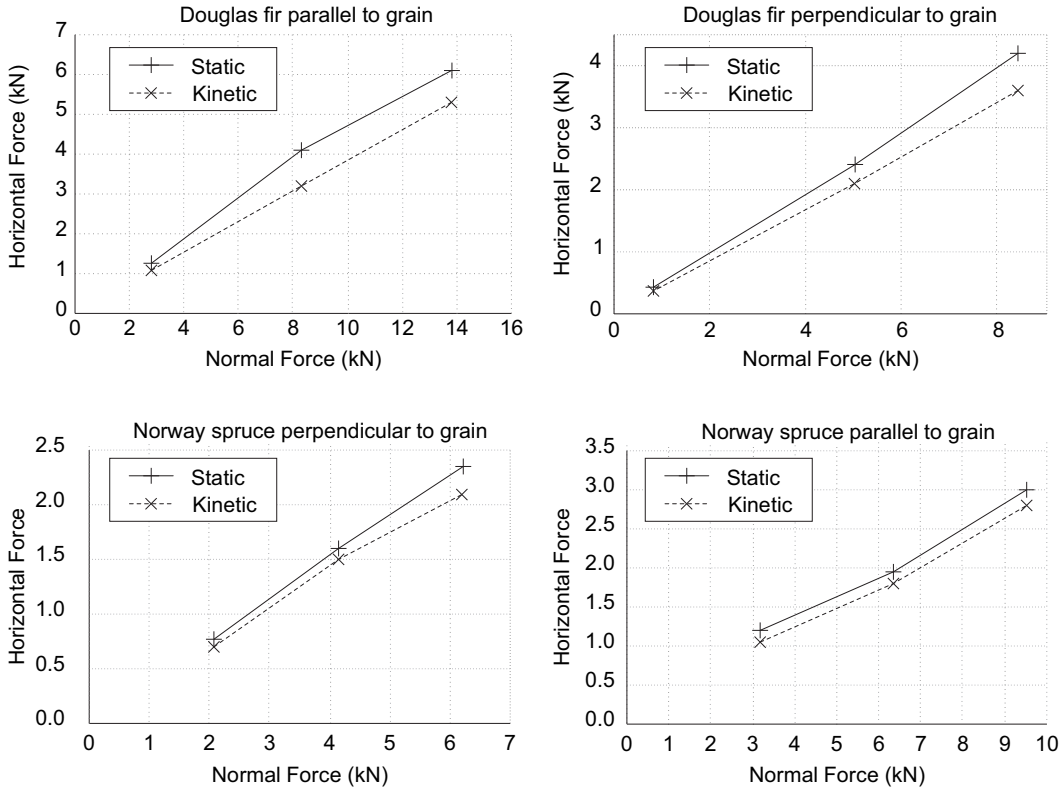

Figure 5-26: Measured normal and horizontal forces for initial slip, labelled as static, and constant movement, labelled as kinetic

The effect of variation in the normal force applied to the specimens is shown in Figure 5-26. It can be seen that the relationship between normal force and horizontal force is close to linear for both the static and kinetic results. In fact, the coefficient of determination R^2, defined as in Section 2.2.2, is above 0.99 for a linear least-squares fit of each of the lines. These results help to justify the use of Coulomb friction theory in the analytical models presented in Chapter 6.

5.5 Microscopy

Microscopy was used to observe the microstructural changes between specimens before and after loading. The specimens for microscopy were therefore taken from the Douglas fir embedment specimens, and the plane in which each specimen was cut is shown in Figure 5-27. The surface of these planes was then viewed under an optical reflected-light microscope, so the view is along the axis of the tracheids for the perpendicular-to-grain specimen and along the dowel axis for the parallel-to-grain specimen.

The specimens for microscopy were prepared by cutting followed by sanding with

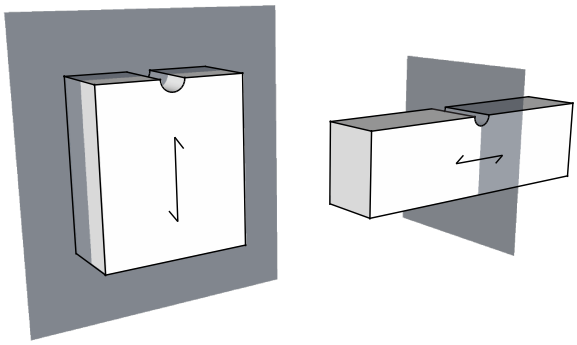

Figure 5-27: Cutting planes for microscopy

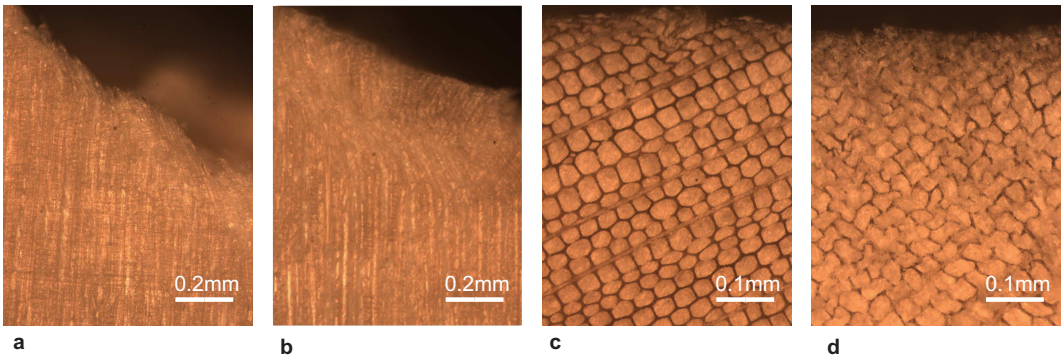

Figure 5-28: Microscope images showing: **a** parallel-to-grain specimen which has not been loaded by a dowel; **b** parallel-to-grain specimen loaded to a peak load of 40% of its predicted yield load; **c** perpendicular-to-grain specimen which has not been loaded; **d** perpendicular-to-grain specimen loaded to a peak load of 40% of its predicted yield load

P600 silicon carbide paper. The surface was then cleared of dust with an air jet. In the case of the perpendicular-to-grain specimen, the air jet did not remove the particles which had filled the pores, and so a plane surface was created by the cell walls and the dust filling each pore.

a and **c** in Figure 5-28 show the microstructure in each orientation for specimens which had remained unloaded. In the perpendicular-to-grain specimen, the cells appear to have been undamaged in this plane by drilling and cutting. In the parallel-to-grain specimens, the tracheids at the edge of the hole curve slightly. This is thought to be a consequence of either drilling during manufacture, or cutting or sanding during preparation for microscopy. The fact that all tracheids were observed to curve tangentially suggests that drilling is the most likely cause.

A similar image for a perpendicular-to-grain specimen which has seen an applied force 40% of its predicted yield force is shown in **d** in Figure 5-28. In this specimen,

the tracheids near the edge of the hole can be seen to have been permanently crushed.

The process of these tracheids being crushed forms part of the irreversible deformation which occurs under initial loading. There are also some areas of intact tracheids around the edge of the hole, which suggests that the crushing of the tracheids acts to allow force to be distributed to these areas, which may initially have been recessed. It is thought that the crushing process, therefore, spreads the applied force over a larger contact area, increasing the stiffness of the connection. Atack and Tabor (1958) noted this closing of the voids of the trachieds whilst investigating the rolling friction of steel balls on timber. They also noted that the voids were observed to snap open very quickly upon addition of a small drop of water. It is considered that it would generally be more desirable in dowel type connections to increase the initial stiffness of the connection by causing the crushing of the trachieds before installation of the dowel. It is possible, however, perhaps for a use in a dedicated energy dissipation device, that it might be desirable to return the crushed trachieds to their original state, in which case the effect of the addition of water might be useful.

In the parallel-to-grain specimen, the force is not applied in the direction which would cause crushing of the tracheids. A similar process of initial irreversible deformation followed by viscoelastic behaviour occurs, however, and the microscope image in **b** in Figure 5-28 shows a possible cause of that initial deformation. In the specimen, previously loaded to 40% of its predicted yield force, some buckling of the tracheid walls can be seen, away from the edge of the hole. This buckling is distinct from the curvature of the tracheids which was observed in the unloaded specimen, in that it does not occur immediately at the edge of the hole. As with the perpendicular-to-grain specimen, some undamaged areas were also visible, suggesting that the irreversible deformation acts to take up unevenness in the contact face between the dowel and the timber.

5.6 Summary

The experimental results in this chapter have shown the prominent features of the behaviour of timber in embedment by a steel dowel under loads representative of in-service vibration. They have also shown that the non-linear features of the response in embedment are also apparent in the response of a single-dowel connection.

It has been found that the stiffness and energy dissipation of a dowel-type connection tend towards a constant value after repeated cycles of load. In the early cycles, a transient contribution to stiffness and energy dissipation was observed, which was thought to be due to the deformation occurring in the contact surface between steel

and timber. The permanent deformation in that contact surface was observed by comparing microscope images from specimens before and after load testing.

In the tests with R=10, substantial non-linear force-displacement behaviour was observed, while at R=1.2, there was little deviation from a linear-elastic response. This was thought, again, to be due to deformation in the uneven contact surface and resulted in a reduced stiffness and an increased energy dissipation at the higher amplitude.

The next chapter will investigate methods of modelling the embedment behaviour which has been described in this chapter, and relate the embedment behaviour to that of the single-dowel connections.

Chapter 6

Models for Embedment

The behaviour of a dowel-type connection can be understood by first considering the embedment of the connector into the timber around it, then the deformation of a single connector along its length, and finally the interaction of groups of connectors under the applied force and moment. The derivation of a model for connection stiffness and energy dissipation under in-service vibration therefore addresses each of those processes.

The results presented in Chapter 5 showed that the nonlinear, time dependent and dissipative behaviour of the connection occurs primarily in embedment. The load-deflection response of a circular dowel embedding into a piece of timber depends on the orthotropic elastic behaviour of the timber, and also on the frictional interaction between the dowel and the timber. An analytical method has been developed to model the stiffness and energy dissipation of the embedding dowel, which takes into account these processes, and that method is described in this chapter.

The method was developed on the assumption that, under small-amplitude vibration significantly below the embedment strength, the behaviour of the timber could be treated as linear, and therefore modelled using an orthotropic linear elastic model. The deformation of the cross-section of the steel dowel was assumed to be negligible, but the friction between the steel and timber determines the distribution of the forces around the face of the timber, so had to be modelled.

Some of the nonlinear and viscoelastic components of the measured embedment behaviour were then represented by a rheological model. This model was used as an inverse-modelling tool to quantify the relative magnitudes of the deformations due to: the plastic behaviour considered to occur in the contact surface; the elastic deformation in the timber and the viscoelastic flow in the timber over time. The viscoelastic model did not form part of the linear elastic method for estimation of connection and frame stiffness under small-amplitude one-sided cyclic loading, but provided some insight into

the field of application of such an elastic model.

Figure 6-1 shows the relationships between all the models developed in this chapter and Chapter 7.

6.1 Elastic foundation models

Two elastic foundation models are presented, and in each the foundation modulus for the timber is estimated using a stress function of the form first proposed by Lekhnitskii (1968). The definition of the stress function then exactly follows the work of Zhang and Ueng (1984) and Hyer and Klang (1985), and the formulae are collated and reproduced here for convenience. The work of those researchers is then extended to assess the deformations in a specimen by superposition of infinite or semi-infinite plate stress functions.

These are linear-elastic models for the timber, but the interaction between dowel and timber is nonlinear not just because of the friction between the two, but also because the timber surface is initially uneven, and this unevenness is compressed under load, improving the contact surface, as seen in microscopy in Section 5.5. This effect is discussed by Dorn et al. (2013), who suggested that the low initial stiffness may be due to the compression of the unevenness in the contact surface, and noted that under unloading and reloading the embedment behaviour is closer to linear elastic, as the surface of the timber remains compressed to its previous level. The effect of unevenness of the contact surface was not taken into account in this elastic model, meaning that it is appropriate only to the secant stiffness under cyclic loading, in which the contact surface is assumed to have been compressed to provide a relatively stiff transfer of load to the timber.

6.1.1 A half hole in a semi-infinite plate

The stress function by Zhang and Ueng (1984) represents the stresses in a semi-infinite orthotropic plate in plane stress with a half-hole in the surface. The following derivation of the model, and its comparison with the results of the Douglas fir embedment tests, were presented in a peer-reviewed publication (Reynolds et al.; 2013a).

The forces applied by the dowel along the surface of the half-hole are defined on the basis of the geometry and the coefficient of friction between the steel and the timber. The geometry and notation are shown in Figure 6-2.

Lekhnitskii (1968) showed that the general form of the stress functions for an infinite orthotropic plate with a hole is as given by (6.2) to (6.6). The solution of a particular problem relies on finding the coefficients a_n and b_n which correspond to the distribution

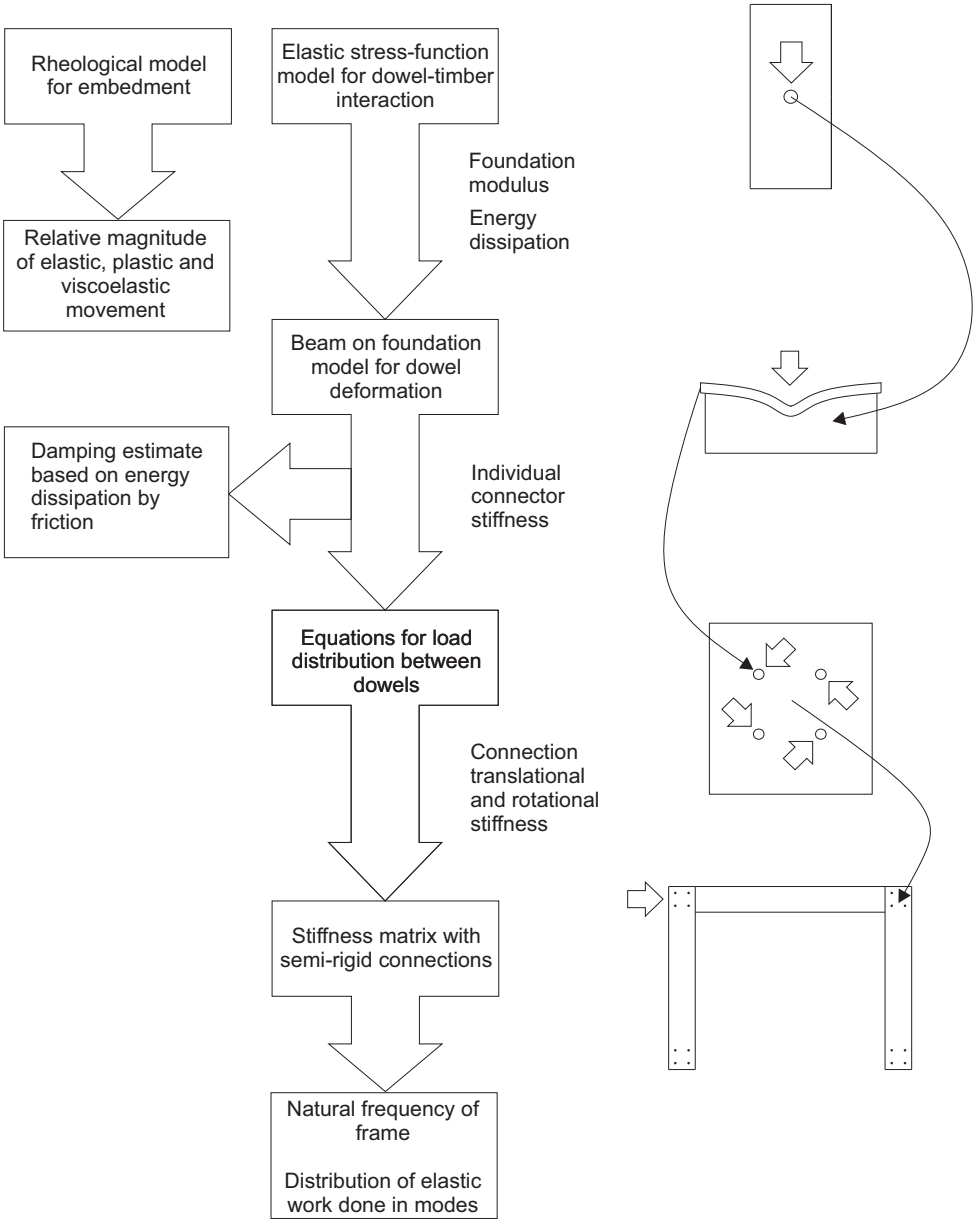

Figure 6-1: Models for embedment, dowel, connection and frame behaviour, showing their relationships to one another

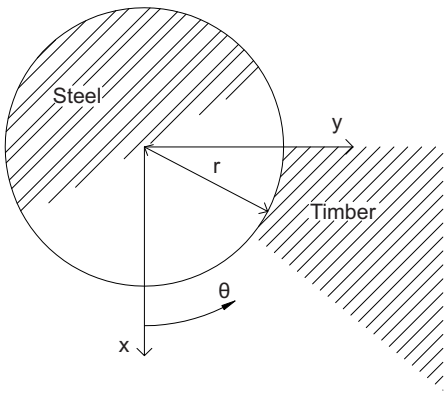

Figure 6-2: Geometry and notation for stress function model for embedment

of the load on the edge of the hole. $\zeta_{1,2}$ are transformed coordinates describing the point on the plate under consideration. The complex stress functions and Φ_1 and Φ_2 are defined so that the displacements u, in the x direction, and v, in the y direction, are given by (6.7) and (6.8). i is the imaginary unit.

Φ_1 and Φ_2 are stress functions defined by their relationship to the direct and shear stresses in the plate: the direct stress in the x direction, for example, is given by (6.1), where Φ_1' is the derivative of Φ_1 with respect to z_1, and Φ_2' the derivative of Φ_2 with respect to z_2. $Re()$ denotes the real part of what is, in general, a complex number in the brackets, and μ_1 and μ_2 are complex constants derived from the material properties of the plate, as in (6.9) and (6.10).

$$\sigma_x = 2Re(\mu_1\Phi_1' + \mu_2\Phi_2') \tag{6.1}$$

This work is not concerned with the stresses in the plate, but rather the relative displacements. The displacements in the plate are given by the integral of the strains, and are therefore proportional to the integral of the stresses. The displacements are therefore calculated using the undifferentiated stress functions Φ_1 and Φ_2. A full derivation of the general form of the stress functions and their relationship to stresses, strains and displacements is given by Lekhnitskii (1968).

$$\Phi_1 = a_0 ln\zeta_1 + \sum_{n=2}^{\infty} \frac{a_n}{\zeta_1^n} \tag{6.2}$$

$$\Phi_2 = b_0 ln\zeta_2 + \sum_{n=2}^{\infty} \frac{b_n}{\zeta_2^n} \tag{6.3}$$

$$\zeta_1 = \frac{z_1 + \sqrt{z_1^2 - \left(1 + \mu_1^2\right)}}{r^2\left(1 - i\mu_1^2\right)} \tag{6.4}$$

$$\zeta_2 = \frac{z_2 + \sqrt{z_2^2 - \left(1 + \mu_2^2\right)}}{r^2\left(1 - i\mu_2^2\right)} \tag{6.5}$$

$$z_1 = x + \mu_1 y \quad z_2 = x + \mu_2 y \tag{6.6}$$

$$u = 2\mathrm{Re}\left(p_1\Phi_1 + p_2\Phi_2\right) + U \tag{6.7}$$

$$v = 2\mathrm{Re}\left(q_1\Phi_1 + q_2\Phi_2\right) \tag{6.8}$$

u is the displacement relative to a particular fixed point, and includes one non-zero constant of integration, U. μ_1, μ_2, p_1, p_2, q_1 and q_2 are derived from the material properties of the plate material, the timber, as in (6.9) to (6.14), where E_1 is the elastic modulus of the plate material in the x direction, E_2 the elastic modulus in the y direction, G is the shear modulus, and ν_{12} the Poisson's ratio in the xy plane.

$$\mu_1^2 = \frac{2\nu_{12} - \frac{E_1}{G} + \sqrt{\left(2\nu_{12} - \frac{E_1}{G}\right)^2 - \frac{4E_1}{E_2}}}{2} \tag{6.9}$$

$$\mu_2^2 = \frac{2\nu_{12} - \frac{E_1}{G} - \sqrt{\left(2\nu_{12} - \frac{E_1}{G}\right)^2 - \frac{4E_1}{E_2}}}{2} \tag{6.10}$$

$$p_1 = \frac{\mu_1^2}{E1} - \frac{\nu_{12}}{E_1} \tag{6.11}$$

$$p_2 = \frac{\mu_2^2}{E1} - \frac{\nu_{12}}{E_1} \tag{6.12}$$

$$q_1 = \frac{1}{\mu_1 E_2} - \frac{\nu_{12}\mu_1}{E_1} \tag{6.13}$$

$$q_2 = \frac{1}{\mu_2 E_2} - \frac{\nu_{12}\mu_2}{E_1} \tag{6.14}$$

Lekhnitskii (1968) presented a method to allow the stress functions to be defined on the basis of the trigonometric series defining the displacements u' and v' on the

hole edge. The general form of those series is as in (6.15) and (6.16). α_m and β_m are coefficients determined by the boundary conditions and $*$ denotes the complex conjugate.

$$u' = \alpha_0 + \sum_{m=1}^{\infty} \left(\alpha_m e^{im\theta} + \alpha_m^* e^{-im\theta} \right) \tag{6.15}$$

$$v' = \beta_0 + \sum_{m=1}^{\infty} \left(\beta_m e^{im\theta} + \beta_m^* e^{-im\theta} \right) \tag{6.16}$$

Once the coefficients are determined, they can be used to generate the stress functions using (6.17) to (6.20), where $D = p_1 q_2 - p_2 q_1$. Note that α_0 and β_0 do not affect the stress distribution in the plate. The overall movement of the hole, caused by a net force P on the hole, is allowed for by A and B.

$$\begin{aligned} \Phi_1(z_1) = & A ln\zeta_1 + \frac{(\alpha_1^* q_2 - \beta_1^* p_2)}{D\zeta_1} \\ & + \frac{1}{D} \sum_{m=2}^{\infty} (\alpha_m^* q_2 - \beta_m^* p_2) \zeta_1^{-m} \end{aligned} \tag{6.17}$$

$$\begin{aligned} \Phi_2(z_2) = & B ln\zeta_2 + \frac{(\alpha_1^* q_1 - \beta_1^* p_1)}{D\zeta_2} \\ & + \frac{1}{D} \sum_{m=2}^{\infty} (\alpha_m^* q_1 - \beta_m^* p_1) \zeta_2^{-m} \end{aligned} \tag{6.18}$$

$$A = \frac{P}{\pi i} \left(\frac{\mu_1 \mu_1^* + \mu_1 \mu_2^* - \frac{a_{12}}{a_{22}} \mu_1 \mu_2 \mu_1^* \mu_2^*}{(\mu_1 - \mu_1^*)(\mu_1 - \mu_2)(\mu_1 - \mu_2^*)} \right) \tag{6.19}$$

$$B = \frac{P}{\pi i} \left(\frac{\mu_2 \mu_2^* + \mu_2 \mu_1^* - \frac{a_{12}}{a_{22}} \mu_2 \mu_1 \mu_2^* \mu_1^*}{(\mu_2 - \mu_2^*)(\mu_2 - \mu_1)(\mu_2 - \mu_1^*)} \right) \tag{6.20}$$

6.1.1.1 Boundary conditions

Zhang and Ueng (1984) used the displacement boundary conditions described in (6.21) to (6.23), for the geometry shown in Figure 6-2, to define the stress functions. In doing so, they assumed that the dowel remained rigidly circular, so that the radial displacement of the timber equals that of the face of the dowel, and that some slip occurs in the tangential direction, at all points except $\theta = 0$.

$$u = \frac{u_0}{c_s} \quad \text{and} \quad v = 0 \quad \text{when} \quad \theta = \pm\frac{\pi}{2} \tag{6.21}$$

$$u = u_0 \quad \text{and} \quad v = 0 \quad \text{when} \quad \theta = 0 \tag{6.22}$$

$$(u_0 - u)\cos\theta = v\sin\theta \quad \text{when} \quad \frac{-\pi}{2} \leq \theta \leq \frac{\pi}{2} \tag{6.23}$$

u_0 is, therefore, the displacement of the dowel in the semi-infinite plate, and c_s represents the extent to which the dowel slips along the surface of the timber. Zhang and Ueng (1984) proposed the trigonometric series in (6.24) to (6.32) to satisfy these boundary conditions. Using these boundary conditions, the standard form of stress function defined by (6.15) and (6.16), the stress functions for this particular case are defined as in (6.33) and (6.34). It can be seen that the friction coefficient μ affects the slip c_s, since it appears in the equations for the constants A_1 and B_1, which also depend on the material properties of the timber.

$$u' = \frac{c-1}{2c_s}u_0\cos 2\theta + \frac{c+1}{2c_s}u_0 cos4\theta \tag{6.24}$$

$$v' = \left(\frac{c_s - 1}{2c_s} + \frac{c_s + 1}{c_s}\right)u_0\sin 2\theta + \frac{c_s+1}{2c_s}u_0 sin4\theta \tag{6.25}$$

$$c_s = \frac{B_1 - A_1}{A_1} \tag{6.26}$$

$$u_0 = \frac{gP}{\pi}\frac{(B_1 - A_1)}{2A_1(\nu_{12} - k - nk) - B_1(\nu_{12} - k - nk)} \tag{6.27}$$

$$\begin{aligned} A_1 = {} & (19n + 11nk + 10k - 10\nu_{12}) \\ & + \mu(11n - 6nk + 15k - 15\nu_{12}) \end{aligned} \tag{6.28}$$

$$B_1 = 10n(1-k) + 10\mu(3k - 3\nu_{12} + 2nk + n) \tag{6.29}$$

$$k = \sqrt{\frac{E_1}{E_2}} \tag{6.30}$$

$$n = \sqrt{2(k - \nu_{12}) + \frac{E_1}{G}} \tag{6.31}$$

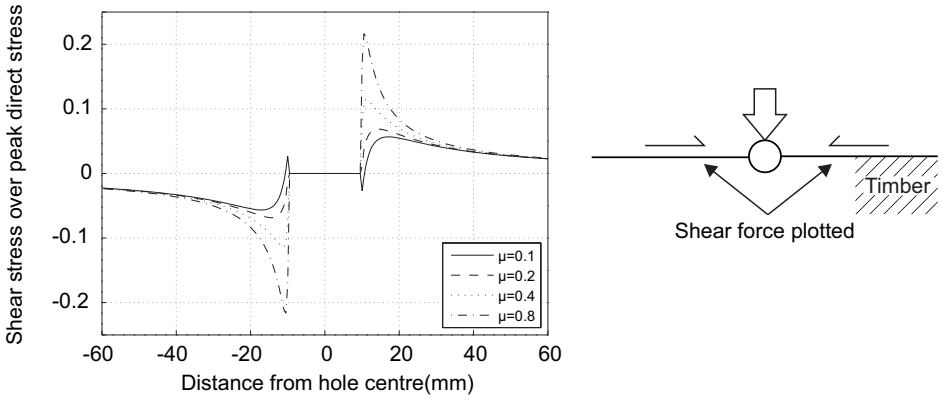

Figure 6-3: Shear on the free surface in the approximate solution for a semi-infinite plate (Zhang and Ueng; 1984)

$$g = \frac{1 - \nu_{12}^2 \frac{E_2}{E_1}}{E_2} + \frac{k}{G} \tag{6.32}$$

$$\Phi_1 = A \ln \zeta_1 + \left(\frac{c_s - 1}{2x} \frac{q_2 - ip_2}{2D} - \frac{c_s + 1}{c_s} \frac{ip_2}{2D} \right) \frac{u_0}{\zeta_1^2} + \frac{c_s + 1}{2c_s} \frac{q_2 - ip_2}{2D} \frac{u_0}{\zeta_1^4} \tag{6.33}$$

$$\Phi_2 = B \ln \zeta_2 + \left(\frac{-(c_s - 1)}{2x} \frac{q_1 - ip_1}{2D} + \frac{c_s + 1}{c_s} \frac{ip_1}{2D} \right) \frac{u_0}{\zeta_2^2} - \frac{c_s + 1}{2c_s} \frac{q_1 - ip_1}{2D} \frac{u_0}{\zeta_2^4} \tag{6.34}$$

Although the general solution by Lekhnitskii (1968) is for a hole in an infinite plate, the form of the stress functions proposed by Zhang and Ueng (1984) means that the vertical component of the resultant force applied to the plate is zero on the y-axis. These functions therefore approximate a semi-infinite plate with a half-hole. It is convenient that this is appropriate for the geometry in the embedment tests described in Section 5.

It should be noted that this is only an approximate solution for a semi-infinite plate with a half-hole, because the shear stress on the y-axis is not zero. Zhang and Ueng (1984) state that this approximation does not affect the stress field significantly for low friction coefficient, and on that basis, it is assumed that it will not significantly affect the vertical deformations. Figure 6-3 plots the shear stress on the free surface for a range of friction coefficients for the mean material properties of the Douglas fir, showing that it exceeds 10% of the peak compressive stress for a friction coefficient of 0.4 or greater.

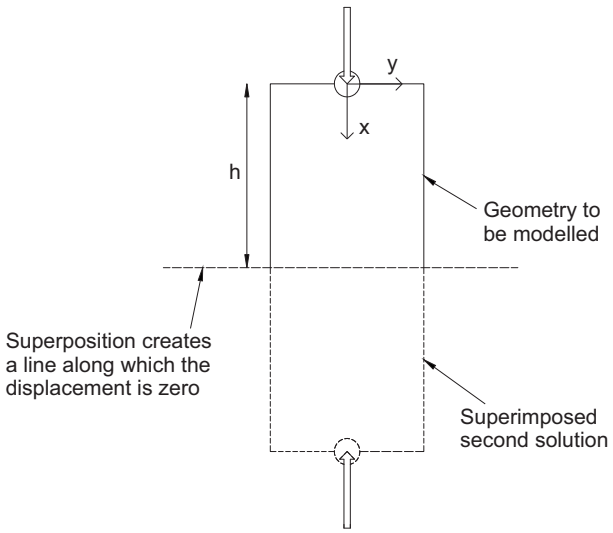

Figure 6-4: Superposition of two infinite-plate solutions to model a supported edge

A further approximation is inherent in the number of terms used in the equations to describe the boundary conditions. Further terms could give a more accurate representation of the offset position of the dowel. The accuracy of the stress function in this form will be considered in comparing analytical and experimental results in Section 6.4.

6.1.1.2 Superposition for displacements

The movement of the dowel for a particular applied load, and particular support conditions, will, in general, be different from the deformation u_0. The strain field is integrated to give the deformations in the plate, resulting, for this case, in one non-zero constant of integration, U in (6.24). For the case of the ASTM embedment test, the constant was eliminated by superimposing the solutions for two holes loaded in opposite directions. By placing the second $2h$ below the first, as shown in Figure 6-4, a line of zero displacement is created at a vertical distance h from the hole. If the holes are sufficiently well separated that there is no significant interaction between the stresses on the edges of each hole, then this is a reasonable representation of a plate supported rigidly along one edge.

In order to calculate the movement of the dowel, the displacement of the timber in the semi-infinite plate is calculated in two positions, u_0 at $y = 0$, $x = r$ and u_1 at $y = 0$, $x = 2h - r$. u_0 can be calculated directly using (6.27). For u_1, the transformed coordinates ζ_1 and ζ_2 are calculated using (6.4) and (6.5). Since the point is on the x-axis, ζ_1 and ζ_2 are equal in both cases. Φ_1 and Φ_2 are then calculated using (6.33)

and (6.34), for a unit applied force P. u_1 is then calculated using (6.7).

The displacement of the dowel relative to the fixed surface at $x = h$ is then given by $\frac{u_1 - u_0}{2}$, and the predicted stiffness of the specimen can be calculated as $\frac{2}{u_1 - u_0}$.

6.1.2 A complete hole in an infinite plate

The complex stress function by Zhang and Ueng (1984) and its extension therefore give a model suitable for the embedment test geometry. Furthermore, it was argued in Section 2.2.1 that the effect of the presence of the timber on the unloaded side of the hole on the foundation modulus measured in these standard embedment tests is small in comparison to the natural variation of the material properties. In certain geometries, however, the semi-infinite plate solution appears to be inappropriate: where a timber member is subject to a tensile force applied by the dowel, for example, or where two or more dowels exert a couple to resist a bending moment.

The Fourier series representing the force or displacement on the hole edge for a complete hole needs to contain more terms than the two used by Zhang and Ueng (1984) to model the half-hole. Hyer and Klang (1985) developed a general solution for the infinite Fourier series to fully represent the distribution of normal and shear forces on the hole edge.

6.1.2.1 Boundary conditions

In contrast to the semi-infinite plate model described in Section 6.1.1, which was defined using only displacement boundary conditions, the calculation for a complete hole in an infinite plate requires both displacement and force boundary conditions. This is particularly due to the fact that on the unloaded face of the hole, the displacement can take any value, while the normal and tangential force on the face of the timber is known to be zero. The boundary conditions are, therefore, defined for three regions around the face of the dowel, referred to as the stick, slip and no-contact regions and shown in Figure 6-5.

In the stick region, the tangential force between timber and dowel is less than the static friction force, so the two move together. A displacement boundary condition is, therefore applied in this region, as in (6.35), where u and v are the deflections of the timber in the x and y directions and u_0 is the displacement of the dowel.

$$u = u_0 \qquad v = 0 \tag{6.35}$$

In the slip region, the faces remain in contact, but the tangential force has overcome the static friction force, so that the two faces have moved relative to one another. As

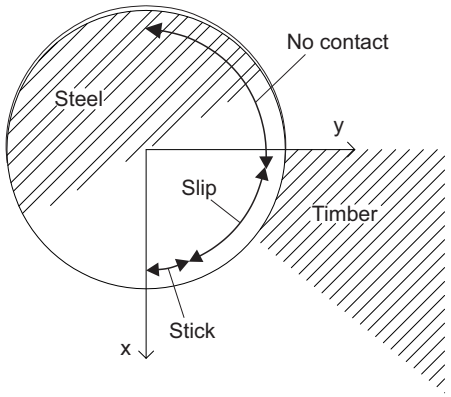

Figure 6-5: The stick, slip and no-contact regions for the boundary conditions around the hole edge

shown in (6.36), displacement and force boundary conditions are applied here, stating that the radial displacement in the timber u_r is equal to that of the dowel, and assuming that the tangential force T is equal to the static limiting friction force, given as the normal force N multiplied by the coefficient of friction μ. The displacement condition here is a simplification which applies for small displacements, and was used by Zhang and Ueng (1984) and Hyer and Klang (1985), though neither acknowledged that it was a simplification. The true relationship between the radial displacement of the timber and the dowel displacement can be derived based on the fact that the final position each timber element must fall on the circle defined by the new position of the dowel, and is given by (6.37).

(6.37), however, since it is not a linear function of u_r and u_θ, does not obey the principle of linear superposition which is necessary for Hyer and Klang's method for determining the forces on the hole edge. Since the same method is used here, the same simplification of the boundary condition, given by (6.36), is used.

$$u_r = u_0 \cos\theta \qquad N + \mu T = 0 \tag{6.36}$$

$$\frac{-(1+u_r)cos(\theta+u_\theta) + \sqrt{(2(1+u_r)cos(\theta+u_\theta))^2 - 4((1+u_r)^2-1)}}{2} = u_0 \tag{6.37}$$

In the final region, representing the rest of the face of the timber, it is assumed that there is no contact between the steel and the timber. Two force boundary conditions are therefore applied here, reflecting the fact that the normal and tangential forces on the timber are zero, as in (6.38).

$$T = 0 \qquad N = 0 \tag{6.38}$$

6.1.2.2 Generating the Fourier series for applied force

The general solution by Lekhnitskii (1968) is a stress function for an infinite orthotropic plate in plane stress, with a hole loaded on its edge. Hyer and Klang (1985) applied the general complex Fourier series (6.39) to the plate, and related the values of the coefficients a_n and b_n in (6.2) to (6.6) to the Fourier coefficients by equating the forces at the hole edge, giving (6.40). $\delta_{1,2}$ and $\gamma_{1,2}$ are material properties defined by (6.41).

$\mu_{1,2}$ in (6.41) are the two roots of the characteristic equation for the stress state in the material (2.5), and so describe the material properties of the plate material. For the elastic constants of timber, the real part of the complex material properties $\mu_{1,2}$ is zero. The imaginary parts of $\delta_{1,2}$ and $\gamma_{1,2}$ are therefore zero.

$$\sum_{n=-\infty}^{n=\infty} A_n e^{in\theta} \tag{6.39}$$

$$\begin{aligned}\sum_{n=-\infty}^{n=\infty} A_n e^{in\theta} = \bar{\delta_1}\left(\bar{a_0}e^{-i\theta} - \sum_{k=1}^{\infty} k\bar{a_n}e^{-i(k+1)\theta}\right) + \bar{\delta_2}\left(\bar{b_0}e^{-i\theta} - \sum_{k=1}^{\infty} k\bar{b_n}e^{-i(k+1)\theta}\right) \\ - \gamma_1\left(a_0 e^{-i\theta} - \sum_{k=1}^{\infty} k a_n e^{i(k-1)\theta}\right) - \gamma_2\left(b_0 e^{-i\theta} - \sum_{k=1}^{\infty} k b_n e^{i(k-1)\theta}\right)\end{aligned} \tag{6.40}$$

$$\delta_1 = \frac{1+i\mu_1}{2} \quad \delta_2 = \frac{1+i\mu_2}{2} \quad \gamma_1 = \frac{1-i\mu_1}{2} \quad \gamma_2 = \frac{1-i\mu_2}{2} \tag{6.41}$$

Hyer and Klang (1985) used the orthogonality of the sinusoidal functions on each side of (6.40) to evaluate the relationship between the A_n coefficients and the a_n and b_n. This process can be carried out for all the coefficients in the complex stress function, a_n and b_n and, in general, the coefficients are as follows: for $c \leq -2$, if $A_c = 1$ and all other $A_n = 0$, the non-zero a_n and b_n are given by (6.42). For $c \geq 0$, if $A_c = 1$ and all other $A_n = 0$, the non-zero a_n and b_n are given by (6.43).

$$\begin{aligned} a_{c+1} &= \frac{1}{c+1}\frac{i-\mu_2}{\mu_1-\mu_2} \\ b_{c+1} &= \frac{1}{c+1}\frac{i-\mu_1}{\mu_2-\mu_1} \end{aligned} \tag{6.42}$$

$$\begin{aligned} a_{c+1} &= \frac{1}{c+1}\frac{i+\mu_2}{\mu_1-\mu_2} \\ b_{c+1} &= \frac{1}{c+1}\frac{i+\mu_1}{\mu_2-\mu_1} \end{aligned} \tag{6.43}$$

The one remaining case, therefore is that of $A_c = 1$ for $c = -1$ and all other $A_n = 0$. This is also an important case, since it is the only term in the Fourier series which represents a net force applied to the hole. Lekhnitskii (1968) shows the solutions a_0 and b_0 for that case are determined by the set of simultaneous equations in (6.44). Lekhnitskii's equations have been modified for load applied along only one of the principal axes.

$$\begin{aligned} a_0 + b_0 - \bar{a}_0 - \bar{b}_0 &= 0 \\ \mu_1 a_0 + \mu_2 b_0 - \bar{\mu}_1\bar{a}_0 - \bar{\mu}_2\bar{b}_0 &= -\frac{P}{2\pi h i} \\ \mu_1^2 a_0 + \mu_2^2 b_0 - \bar{\mu}_1^2\bar{a}_0 - \bar{\mu}_2^2\bar{b}_0 &= 0 \\ \frac{1}{\mu_1} a_0 + \frac{1}{\mu_2} b_0 - \frac{1}{\bar{\mu}_1}\bar{a}_0 - \frac{1}{\bar{\mu}_2}\bar{b}_0 &= -P\frac{\nu_{12}E_2}{E_1} \end{aligned} \tag{6.44}$$

Hyer and Klang (1985) used these results to set up the matrix equation (6.45). **B** is a vector of boundary conditions for force or displacement at a series of points around the hole edge, **A** is a vector of the coefficients of the Fourier series for the applied force A_n in (6.39), and **C** is a matrix formed using (6.42) to (6.44) to calculate the force or displacement at each point in **B** as a result of a unit coefficient A_n.

$$\mathbf{CA} = \mathbf{B} \tag{6.45}$$

Matrix **C** is therefore defined based on the orthotropic elastic behaviour of the plate with a hole under the unknown applied forces **A**. The boundary conditions **B** are derived using an assumed displacement. (6.45) can then be solved numerically to determine the set of Fourier coefficients **A** to meet the given set of boundary conditions, which can then be used to determine the value of the stress function at each point in

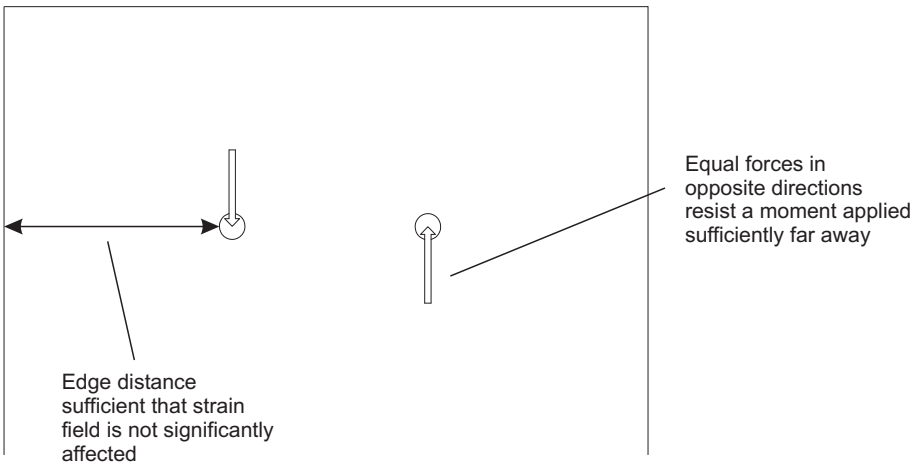

Figure 6-6: Superposition of two infinite-plate solutions to represent two dowels forming a couple

the plate and so the distribution of stress, strain and displacement.

6.1.2.3 Superposition for displacements

The solution can then be translated and superimposed to calculate relative displacements between dowels. This method is effective when, as in the case of the ASTM D5764 (ASTM; 1997) or EN 383 (BSI; 2007) embedment tests, the free edges of the timber do not significantly affect the distribution of stress. This could also be said to be the case for calculation of the rotational stiffness of a moment connection, where the timber subject to significant stress is between the dowels forming the couple. The superposition for two dowels forming a couple is shown in Figure 6-6.

An example of a geometry in which the free edges of the timber affect the stress distribution is the single-dowel connection test, described in Section 5.2.2. In the infinite-plate solution, the stresses tend towards zero far from the dowel. In the single-dowel connection test, the effect of the edges of the timber is to concentrate the stress, so it tends towards a constant value across the section width w of P/tw, where P is the force applied to the dowel, and t is the thickness of the timber.

One way to account for this effect is to superimpose the solution for a stretched plate with a hole onto the pin-loaded plate solution. The infinite plate with a hole loaded along its edge creates a stress field with compressive stresses on the loaded side of the dowel and tensile stresses on the unloaded side, so that, by symmetry, half of the dowel force is resisted in tension and half in compression. By imposing a far-field tensile stress giving half the force on the dowel spread over the cross section, as presented by Echavarría et al. (2007), the stresses on the loaded side of the dowel approximately

cancel out, and the stresses on the unloaded side add to give a tensile force equal to the load on the dowel. Hence the arrangement approximates a dowel transmitting tensile force to a timber beam, and the equivalent situation for a compressive force can be achieved using a compressed, rather than a stretched plate superposition. Echavarría et al. (2007) used the arrangement to investigate the stress around the dowel. The stresses further along the beam will become inaccurate, however, since the integral of the stress over the cross section tends towards only half of the applied load on the dowel.

The general form of the stress function for a pin-loaded stretched plate, subject to a uniform tensile stress of p, is given by (6.46).

$$\begin{aligned}\phi_1 &= a_0 \ln \zeta_1 + \frac{p}{2}\left(\left(\frac{-i}{\mu_1 - \mu_2}\right)\frac{1}{\zeta_1} + \frac{z_1}{\mu_1^2 - \mu_2^2}\right) + \sum_{n=1}^{\infty}\frac{a_n}{\zeta_1^n} \\ \phi_2 &= b_0 \ln \zeta_2 + \frac{p}{2}\left(\left(\frac{-i}{\mu_2 - \mu_1}\right)\frac{1}{\zeta_2} + \frac{z_2}{\mu_2^2 - \mu_1^2}\right) + \sum_{n=1}^{\infty}\frac{b_n}{\zeta_2^n}\end{aligned} \tag{6.46}$$

In contrast to the work by Echavarría et al. (2007), this study is concerned with the movement of the connector relative to other connectors or supports. For that purpose, the stress function in (6.46) can be broken down into three parts:

- the terms in $1/\zeta_{1,2}^n$ represent the change in shape of the hole itself, none of them applying a net force to the hole boundary, so that their effect is confined to the area immediately around the connector;
- the term in $\ln\zeta_{1,2}$ represents the net force applied to the hole edge, causing a concentrated stress in the timber member and the movement of the hole through the timber; and
- the term in p represents the constant value towards which the stress in the member tends, far from the hole.

The edge distances required in timber connections to prevent splitting by Eurocode 5 (BSI; 2009a) ensure that edge effects do not significantly change the local stresses and strains around the hole described by the $1/\zeta_{1,2}^n$ terms, so they present a reasonable model of the deformed shape of the hole. Figure 6-7 shows the direct stresses due to the $1/\zeta_{1,2}^n$ terms, in the direction of the applied load, for a piece of timber loaded parallel to grain with standard C24 material properties according to EN 338 (BSI; 2009b). The extents of the plot are the minimum edge distances according to Eurocode 5 (BSI; 2009a), 7 times the diameter in the along-grain direction and four times the diameter in

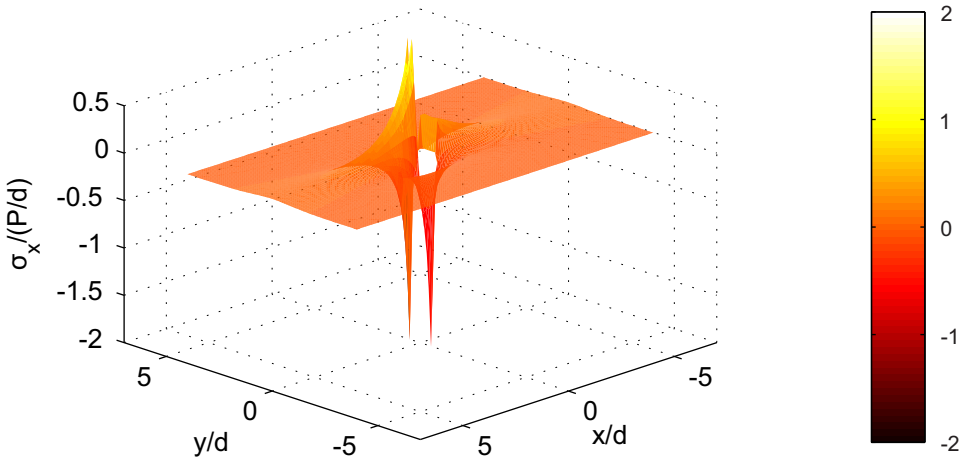

Figure 6-7: Stresses in the timber due to the $1/\zeta_{1,2}^n$ terms, in which the stress has been normalized by the dowel force P divided by the diameter d, x is the coordinate in the loading direction and y is the coordinate perpendicular to the load

the across-grain direction, and it can be seen that the stresses diminish rapidly before the edge of the timber. The highest residual stress at the edge is approximately 1.5% of the peak.

The longitudinal stress in a long member in tension or compression will tend towards being evenly distributed across the cross section, with magnitude $P/(tw)$, where t and w are the dimensions of the beam cross section, and P is the force applied to the dowel. In the infinite plate solution, the force on the dowel is resisted by the stress in the material on the loaded and unloaded sides of the dowel, and the integral of that stress tends towards $P/2$ on each side. As noted by Echavarría et al. (2007), therefore, a stress in the plate of $P/2$ is required to cancel out the stress on one side of the dowel, and approximate a dowel supported on just one side. When two of these infinite plate solutions are superimposed, therefore, the stress between the dowels tends towards $P/(tw)$. This is considered to be a suitable approximation of the stress state between the dowels for calculation of their relative deformations.

The parallel-to-grain single-dowel connection test described in Section 5.2.2 was used as an example. Two infinite-plate solutions, including the stretched-plate terms, were superimposed to give the stress function for the geometry in the test. The resulting deformation field is shown in Figure 6-8.

It should be noted that the calculation illustrated in Figure 6-8 gives a higher stiffness between the two dowels in the case where they transmit a compressive load than in the case where they transmit a tensile load. This is due to the longer load path in the tensile case, in which the load is transmitted in concentrated tension and shear

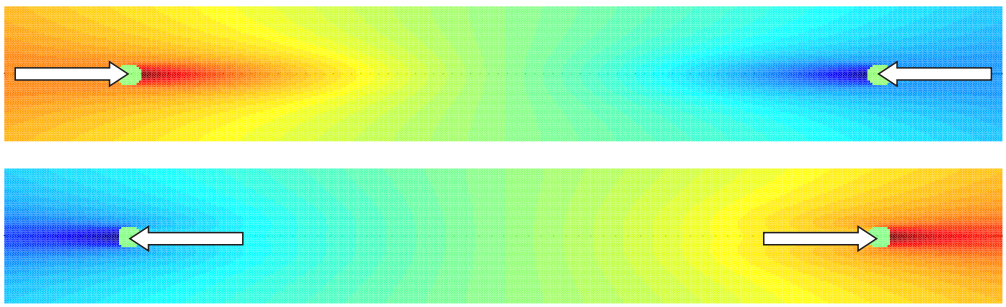

Figure 6-8: Field of deformation in the x direction for single dowel specimens in tension and compression

either side of the hole. The difference is approximately 5% of the total stiffness in this case, but its magnitude will depend on the geometry of the particular connection. It is considered unlikely that a normal structural engineering design process could take this difference into account, but it is notable nonetheless, and reflects the results of the single dowel connection tests reported in Section 5.2.2.

The stiffness between the two dowels calculated from the superposition of stress functions was used as the foundation modulus in a beam-on-elastic-foundation model for the complete dowel. It is pertinent at this point to discuss the assumption of plane stress inherent in the stress function model. The plane stress assumption is appropriate where the body being considered is subject to uniform applied force throughout its thickness, is relatively thin and unconstrained on each face. This geometry meets the requirement of being unconstrained on each face. Its thickness is, however, of the same order of magnitude as the hole diameter, and the applied force is not constant throughout the thickness. The conditions are more suited to the condition of plane stress than plane strain, however, the latter representing a structure very long in the out-of-plane direction, or rigidly restrained at its ends, and commonly applied to structures such as retaining walls.

For the intermediate condition represented by the dowel-type connection, the plane-stress assumption provides an underestimate, and plane strain an overestimate of the true stiffness. The alternative to these simplifying assumptions is a three-dimensional solution which, to the knowledge of the author, could only be carried out numerically, sacrificing the computational simplicity that this analytical solution presents. It is therefore considered that the underestimate, usually conservative in structural engineering design, is the preferable choice.

6.1.2.4 Dimensional analysis

The foundation modulus for the dowel should be expressed in units of force divided by length squared, since it represents a stiffness per unit length of the connector. The solution by Hyer and Klang (1985) is for a hole of unit radius and unit plate thickness, so must be scaled to reflect the real geometry.

To find the foundation modulus given a particular arrangement of dowels, the stress functions for a unit radius are superimposed, and the relative displacements δ are calculated for an applied force F. The displacement has units of length, and the applied force has units of force divided by length, since it is applied to a unit plate thickness. The model should have the correct relative dimensions, i.e. the distance between holes as a multiple of the hole radius should match the full-scale geometry to be modelled.

In order to scale the model to match the full-scale geometry, all the dimensions would be multiplied by the full-scale radius of the hole. Since the plate has unit thickness, the stress σ at each point in the plate is proportional to the force divided by the radius, as in (6.47). As a result, as the radius increases, the stress decreases, and so does the strain ϵ.

$$\sigma \propto \frac{F}{r} \qquad \epsilon \propto \frac{F}{r} \tag{6.47}$$

The displacement, u, of any point relative to another is proportional to the strain times the distance between them. The distance between any two points, since the model matches the full-scale geometry, is proportional to r. This means that the displacement between any two points is independent of r, and therefore does not change as the model is scaled, as given in (6.48).

$$u \propto \epsilon \times r \qquad \therefore \qquad u \propto F \tag{6.48}$$

Since the relative displacement between two points is independent of r, and depends only on F, the displacement under a given force, and therefore the stiffness, can be calculated using the stress function model with unit radius. Given that the model has a unit plate thickness, this stiffness represents the foundation modulus required for a beam-on-elastic-foundation model.

This result has the consequence that an embedment specimen, for example, 40mm high with an 8mm dowel would be expected to have the same stiffness as one 100mm high with a 20mm dowel, if they were to have the same thickness.

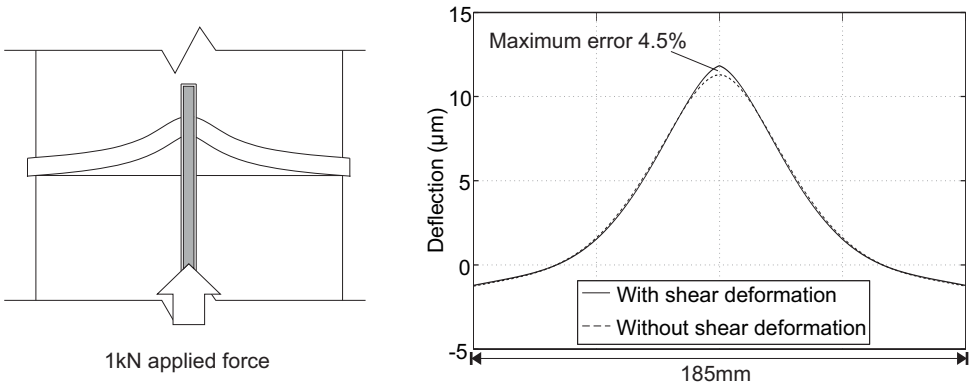

Figure 6-9: Deformed shape of a 12mm steel dowel using a beam-on-elastic-foundation model with 140N/mm^2/mm foundation modulus, with and without shear deformation

6.2 Beam on foundation

All the foregoing discussion and analysis considers only the embedment behaviour of the dowel in the timber, which corresponds to the embedment tests in which the dowel was held rigidly straight as it was pressed into the timber. In any real connection, there is some deformation of the dowel, and this will be represented by a beam-on-foundation model, in which the resistance of the timber to embedment is represented by a foundation modulus and the dowel by a beam to which the appropriate loads are applied. Since the steady-state cyclic embedment behaviour under the smaller-amplitude R=1.2 loads is shown, in Section 6.4.2, to be represented well by a linear elastic model, the foundation provided by the timber will be considered as elastic.

For the connections with a central flitch plate used in this study, the deflection which defines the connection stiffness is at the centre of the beam, where the load is applied. Analytical solutions exist for this geometry, both including and excluding shear deformation. The deformed shape of the dowel for the geometry of the parallel-to-grain single-dowel connection described in Section 5.2.2 is shown in Figure 6-9, illustrating the influence of shear deformation for this case.

6.3 Design method for cyclic stiffness

Both the stress function and the beam-on-elastic foundation calculations introduced in the previous sections reasonably require a computer for their calculation. To be used in structural engineering design, they could be combined into a simple piece of software, but it is considered that they would be more useful and intuitive, and appropriate for integration into design codes, if they were simplified so that they could be used for

hand calculation.

For that purpose, the division of the stress function solution into parts is convenient. The part of the stress function which represents the change in the shape of the hole was seen in Section 6.1.2 to dissipate quickly with distance from the hole. The edge-distances and spacing required to prevent splitting therefore ensure that the finite extent of the timber member does not significantly affect this part of the stress function in parallel-to-grain loading. As a result, this component of the stiffness can be considered to be a property of the timber, in the same way as K_{ser} is in Eurocode 5. The calculation process can therefore be greatly simplified by tabulating this value for each timber grade. This component of deformation will hereafter be referred to as the hole-shape component.

The part of the stress function which represents the far-field stress is only necessary in cases where edge effects lead to the development of a constant stress in the distance between the dowels, such as in the linear single-dowel connection considered in this study. In that case, the effect of this constant stress is simply to produce a constant strain in the member, and this is considered in a normal frame analysis, independently of the connections. In calculating the semi-rigid connection stiffness for frame analysis, therefore, this component of deformation can be omitted.

If the hole-shape component is tabulated, and the far-field stress omitted, then only one term remains in the equation for the stress function. It represents the movement of the circular hole relative to the timber around it, which will hereafter be referred to as the rigid-insert component, since it represents the stress function for the movement of the hole whilst held rigidly circular. The stress functions Φ_1 and Φ_2 for this term are given in (6.49), and are then used to find the displacement in the x-direction by (6.50). l is the distance between the connections as a multiple of the hole diameter. The relative displacement between two dowels separated by a distance l is therefore given by (6.51) to (6.53), which can be combined and simplified to give the approximate solution (6.54).

$$\Phi_1 = a_0 \ln\zeta_1 \qquad \Phi_2 = b_0 \ln\zeta_2 \tag{6.49}$$

$$u = 2\mathrm{Re}\left(p_1\Phi_1 + p_2\Phi_2\right) \tag{6.50}$$

$$u_0 - u_l = -2P\left(p_1 a_0 \ln\frac{\zeta_{1,0}}{\zeta_{1,l}} + p_2 b_0 \ln\frac{\zeta_{2,0}}{\zeta_{2,l}}\right) \tag{6.51}$$

$$\frac{\zeta_{1,0}}{\zeta_{1,l}} = \frac{1+i\mu_1}{2\mu_1 l + \sqrt{4\mu_1 l^2 - 1 + (i\mu_1)^2}} \tag{6.52}$$

$$\frac{\zeta_{2,0}}{\zeta_{2,l}} = \frac{1+i\mu_2}{2\mu_2 l + \sqrt{4\mu_2 l^2 - 1 + (i\mu_2)^2}} \tag{6.53}$$

$$u_0 - u_l = -2P\left(p_1 a_0 \ln\frac{1+i\mu_1}{4l} + p_2 b_0 \ln\frac{1+i\mu_2}{4l}\right) \tag{6.54}$$

In developing a set of equations suitable for hand calculation, it is considered important to avoid the use of complex numbers. Since μ_1 and μ_2 are purely imaginary quantities, $p_1 a_0$, $p_2 b_0$, $i\mu_1$ and $i\mu_2$ are four real-valued material properties which describe the orthotropic elastic behaviour of the timber, and can be calculated from its four independent elastic properties: the two elastic moduli, the shear modulus and the Poissons ratio. Relabeling $p_1 a_0 = \beta_1$, $p_2 b_0 = \beta_2$, $i\mu_1 = \alpha_1$ and $i\mu_2 = \alpha_2$, the four properties are given by (6.55) to (6.58).

$$\alpha_1 = \sqrt{\frac{\frac{E_1}{G} - 2\nu_{12} + \sqrt{(2\nu_{12} - \frac{E_1}{G})^2 - 4\frac{E_1}{E_2}}}{2}} \tag{6.55}$$

$$\alpha_2 = \sqrt{\frac{\frac{E_1}{G} - 2\nu_{12} - \sqrt{(2\nu_{12} - \frac{E_1}{G})^2 - 4\frac{E_1}{E_2}}}{2}} \tag{6.56}$$

$$\beta_1 = \frac{1}{\pi}\frac{\alpha_1(1 + \frac{\nu_{12}E_2}{E_1}\alpha_2^2)}{2(\alpha_1^2 - \alpha_2^2)}\left(\frac{\alpha_1^2}{E_1} + \frac{\nu_{12}}{E_1}\right) \tag{6.57}$$

$$\beta_2 = \frac{1}{\pi}\frac{\alpha_2(1 + \frac{\nu_{12}E_2}{E_1}\alpha_1^2)}{2(\alpha_2^2 - \alpha_1^2)}\left(\frac{\alpha_2^2}{E_1} + \frac{\nu_{12}}{E_1}\right) \tag{6.58}$$

Using these properties, the stiffness associated with the rigid-insert displacement can then be represented as $k_{f,r}$ in (6.59).

$$k_{f,r} = \frac{1}{2\left(\beta_1 \ln\frac{1+\alpha_1}{4l} + \beta_2 \ln\frac{1+\alpha_2}{4l}\right)} \tag{6.59}$$

The same process can be used for a moment connection. In this case, the second superimposed stress function is shifted in the direction perpendicular to the applied load, and so the transformed coordinates $\zeta_{1,l}$ and $\zeta_{2,l}$ change to reflect that. l is now the distance between the two connectors as a multiple of the hole diameter, and the component $k_{f,r}$ of the rigid-insert foundation modulus is given by (6.60).

$$k_{f,r} = \frac{1}{2\left(\beta_1 \ln\frac{1+\alpha_1}{4l\alpha_1} + \beta_2 \ln\frac{1+\alpha_2}{4l\alpha_2}\right)} \tag{6.60}$$

The foundation modulus for use in a beam-on-elastic foundation model can then be calculated by combining the stiffness associated with the hole-shape component $k_{f,s}$, which could be tabulated, with the rigid-insert stiffness $k_{f,r}$, which depends on the geometry of the structure and connection, as in (6.61).

$$k_f = \left(\frac{1}{k_{f,r}} + \frac{1}{k_{f,s}}\right)^{-1} \tag{6.61}$$

The complex stress function model gives an estimate of the stiffness of the timber in embedment in each plane along the length of the dowel. This stiffness was then used as the foundation modulus for a beam-on-elastic-foundation model of the complete dowel. The geometry of the dowel in either a linear or moment connection with a central flitch plate could be simplified to be represented as a beam on elastic foundation with a central point load.

The beam-on-elastic-foundation model can be simplified by neglecting shear deformation, which, for the parallel-to-grain single-dowel connection test, can be seen in Figure 6-9 to represent approximately 5% of the total deflection. This can be considered to be a representative example in that the relative dimensions of the timber member and the dowel have been chosen so that the dowel is just slender enough to give a failure mode with three plastic hinges: failure mode F according to the European Yield Model (BSI; 2009a). Eurocode 5 states that this failure mode is necessary to ensure plasticity of the connection, which suggests that a well-designed connection is likely to have this failure mode, and that connections should not generally have a significantly less slender dowel. It is therefore considered unlikely that the effect of shear deformation will exceed 6 or 7% in practical timber connections.

Another simplification can be made based on the dowel being relatively long and slender, since, for a long beam, the deformation at the centre tends towards u_0 in (6.62), which is a widely stated formula. E_b is the elastic modulus of the dowel, P is the applied force and k_f is the foundation modulus determined from the embedment behaviour of the timber.

$$u_0 = \frac{P}{d\left(\pi E_b k_f^3\right)^{\frac{1}{4}}} \tag{6.62}$$

The design method for connection stiffness under one-sided in-service vibration therefore consists of:

- calculating the transformed material properties from (6.55) to (6.58);
- calculating the rigid-insert stiffness $k_{f,r}$ according to (6.59) for a linear applied force or (6.60) for a moment;
- reading a tabulated value of the hole-shape stiffness $k_{f,s}$ for a particular grade of timber;
- combining these stiffnesses according to (6.61) to obtain the foundation modulus for the beam on elastic foundation; and
- using (6.62) to calculate the stiffness of the individual connector.

Once the stiffness of the individual connector is known, conventional design methods can be used to assess the semi-rigid connection stiffness for use in a frame analysis for modal properties.

6.4 Comparison with experimental results

The predictions of this elastic model were compared with the experimental results of the embedment and single-dowel connection tests presented in Chapter 5 using the material properties given in Section 5.4.

The two elastic moduli were obtained from tests according to EN 408 (BSI; 2011), the Poisson's ratio for the longitudinal-tangential plane was taken from published results (Bodig and Jayne; 1993; Forest Products Laboratory; 2010), and the shear modulus was estimated based on the results of the modulus tests and published values, as described in Section 5.4.2. These properties of the timber were used to create a set of analytical models for the dynamic test specimens. Using these material properties and applying a unit force, the value of the two stress functions could be calculated at each point in the specimen. Using the stress functions, the displacement of every point in the specimen can be calculated. Those displacements are plotted, for illustrative purposes, in Figure 6-10.

No free edge effects are allowed for on the sides of the specimen. The edge distances are considered to be sufficient that the other free edges will not significantly influence the stress or deformation fields. This simplification will not always be appropriate in modelling a connection in a structure, and this issue is addressed in Section 6.1.2.

The friction coefficient influences the unrealistic shear force on the free surface predicted by the stress function, described in Section 6.1.1.1. Based on the measured coefficient of friction of 0.21, the unrealistic shear stress on the free surface will be less than 10% of the peak compressive stress for this model, and the effect of that shear

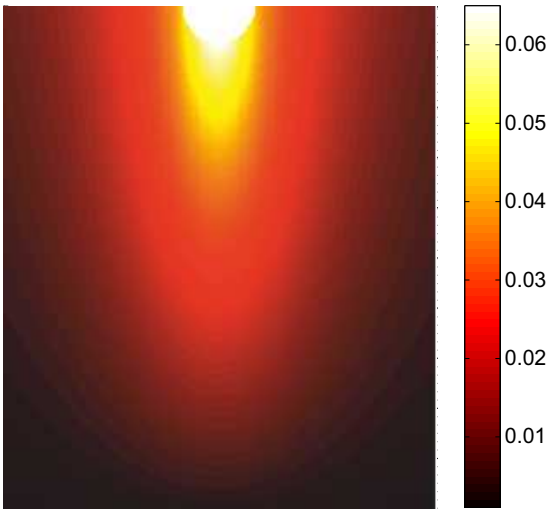

Figure 6-10: Vertical displacements in mm in the timber for a typical Douglas fir specimen in parallel-to-grain loading (1kN applied force)

stress on the vertical deformations in the timber beneath the dowel is expected to be far lower.

The sensitivity of deformation to friction coefficient was assessed by varying the coefficient between the extremes of values published by McKenzie and Karpovich (1968), from their study of friction between steel and timber. For comparison with their work, the rate of movement between the surfaces in these tests corresponds to their classification 'slow', and the surface of the steel dowel falls between his classes of 'rough' and 'smooth'. For all the species of timber tested, the friction coefficient in these classifications ranged from 0.08 to 0.62. Using the material properties for one of the parallel-to-grain Douglas-fir cyclic embedment test specimens, the sensitivity analysis is summarized in Table 6.1, comparing these extreme values to the mean value obtained from the friction tests and used in analysis, 0.21. The resulting variation in stiffness is small in comparison to the variability in material properties in the timber. It is, therefore, considered that the sensitivity of stiffness to friction coefficient is not sufficient to justify a more extensive investigation of friction than has already been carried out.

6.4.1 Statistical hypothesis testing

The modelled stiffness was compared numerically with the experimental results using either a one-sample or two-sample Student's t-test. As described in Section 5.2.4, these tests estimate the probability that two series of tests are two samples taken from the same population of possible test results. In the context of this chapter, the tests

Table 6.1: Effect of friction coefficient on modelled stiffness

Friction Coefficient μ	Stiffness (kN/mm)	% Change from $\mu = 0.21$
0.08	106.2	3.9%
0.21	110.5	-
0.62	120.8	9.3%

represent a measure of the accuracy of the prediction by the theoretical model which allows for both the difference in the mean values of experimental results and prediction and the variance of the measurements.

In order to apply the test, the null hypothesis should first be stated. That is the hypothesis that the mean stiffness predicted by the model is equal to the mean of the population from which the experimental tests are taken. A high probability therefore suggests that the model corresponds well to the experimental results.

For the two-sample t-test, the equations for the test statistic t for independent and paired samples are as given in Section 5.2.4. In the one-sample t-test, the prediction is represented just by its mean value, and not by a variance. The equation for the test statistic t is then given by (6.63), where $\overline{x}$ is the mean of the test results, μ_0 is the predicted mean, s_x is the standard deviation and n the number of tests. The number of degrees of freedom ν, used to generate the probability density function as in Section 5.2.4, is $n - 1$.

$$t = \frac{\overline{x} - \mu_0}{\frac{s_x}{\sqrt{n}}} \tag{6.63}$$

6.4.2 Embedment

For the Douglas fir embedment tests analytical results were compared with the experimental results for each grain orientation, and for each R-value. The predicted values of stiffness are independent of the magnitude of the force applied due to the assumption of elastic behaviour. The results for the three values of peak force were, therefore, combined for this comparison of predicted and measured stiffness. Figure 6-11 plots the stiffness calculated from the experimental results and the analytical model, with the results organized by grain orientation and R-value. Since the specimens for determination of the elastic moduli were taken from the embedment test specimens, a paired two-sample t-test was used. Each experimentally measured stiffness was compared with the analytical prediction based on the moduli measured for the same specimen. The

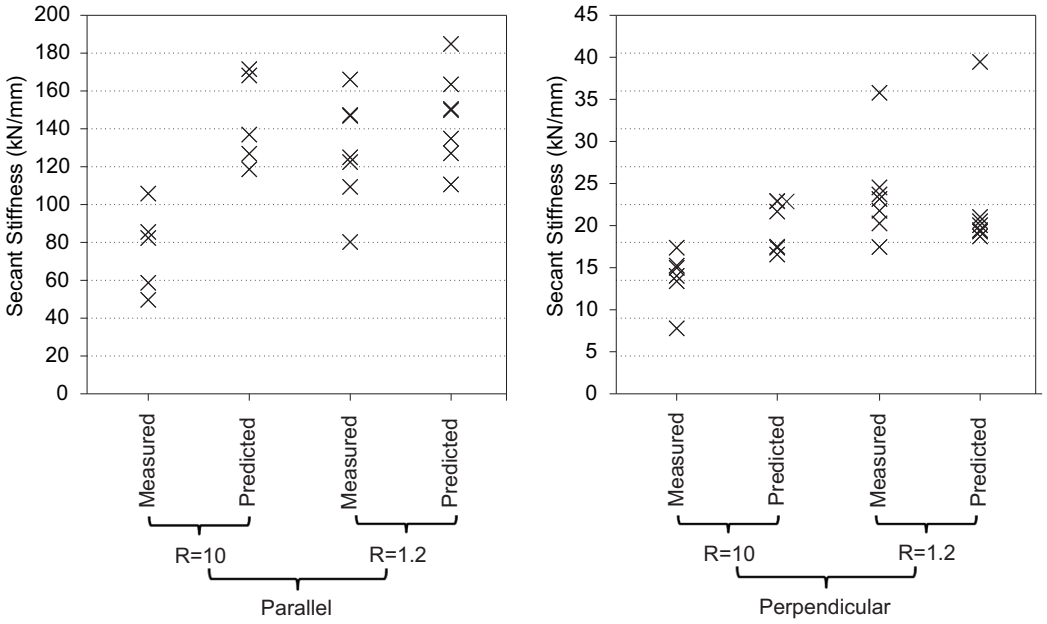

Figure 6-11: Collated parallel- and perpendicular-to-grain results for Douglas fir embedment and predicted values using the analytical model

results of the t-test are shown in Table 6.2.

Table 6.2: Paired two-sample t-test comparing modelled and measured results of Douglas fir embedment tests

	$\overline{x}$	s_x	n	ν	t	p
R=10 Perpendicular	6.02	2.84	6	5	5.19	0.00
R=1.2 Perpendicular	1.16	3.75	7	6	0.82	0.44
R=10 Parallel	68.01	33.17	5	4	4.59	0.01
R=1.2 Parallel	17.73	40.64	7	6	1.15	0.29

Where the amplitude of vibration is smallest, in the tests with $R = 1.2$, the predicted stiffnesses are seen in Figure 6-11 to be similar to the experimental results. For the perpendicular-to-grain tests, the mean predicted stiffness is within 5% of the mean measured stiffness. For the parallel-to-grain tests with $R = 1.2$, the measured values are lower than predicted. The mean measured stiffness is approximately 14% lower than the mean predicted value in these tests. As noted in Section 5.3.2, for some of these tests, a steady-state value of stiffness was not achieved. The measured stiffness in each cycle continued to rise until the end of the test. It is, therefore, possible that, if the test were continued, values of steady-state stiffness closer to the predicted values might be reached.

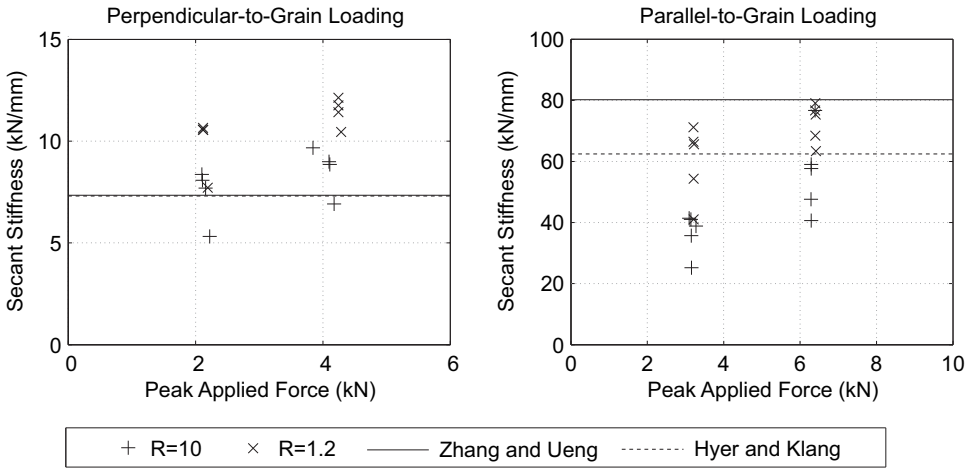

Figure 6-12: Comparison of experimentally measured secant stiffness in embedment with that predicted using the stress function models by Zhang and Ueng (1984) and Hyer and Klang (1985)

This results of the t-test reflect these observations. For the R=1.2 tests, the probabilities of 0.44 and 0.29 in each grain direction suggest that the model is close to the experimental results.

For the greatest amplitude of load, where $R = 10$, the predicted stiffness is significantly higher than the measured stiffness in the dynamic tests both parallel- and perpendicular-to-grain. This can be explained by the reduced secant stiffness in these tests due to nonlinear behaviour at low force caused by the imperfect contact surface between dowel and timber, as described in Section 5.3.2. The t-test results also suggest a large overestimate of stiffness in these cases.

In the Norway spruce tests, the specimens for determination of the elastic moduli were not taken from the dynamic tests specimens. As a result, a separate prediction cannot be made for each specimen. For these tests, therefore, a single prediction of stiffness was made based on the mean of the measured elastic moduli. Those predictions, according to both the stress functions by Zhang and Ueng (1984) and Hyer and Klang (1985) are plotted with the experimental results in Figure 6-12.

It can be seen that the simpler stress function by Zhang and Ueng (1984) results in an overestimate of stiffness in the parallel-to-grain case. This is thought to be due to the extreme variation of elastic moduli in the Norway spruce, so that the three-term representation of the stress distribution cannot accurately represent the concentration of stresses under the dowel. The 200-term representation following the method by Hyer and Klang (1985), however, gives a more representative prediction of the stiffness. It was the 200-term representation which was used in the t-test.

Table 6.3: One-sample t-test comparing the modelled stiffness based on the mean elastic properties of the timber with the secant stiffness measured in the Norway spruce embedment tests

	$\overline{x}$	μ_0	s_x	n	t	s	p
R=10 Perpendicular	7.99	6.51	1.37	8.00	3.05	7.00	0.02
R=1.2 Perpendicular	10.65	6.51	1.35	8.00	8.70	7.00	0.00
R=10 Parallel	46.39	66.05	14.58	10.00	4.27	9.00	0.00
R=1.2 Parallel	66.18	66.05	11.41	10.00	0.03	9.00	0.97

The paired two-sample t-test could not be applied as it was to the Douglas fir embedment tests. Instead, a one-sample t-test was appropriate. The results of the t-test are shown in Table 6.3. They show that the modelled stiffness is very close to the measured values in the parallel-to-grain R=1.2 tests. It is, however, considered that the probability of 0.97 suggests a greater degree of accuracy than is really present. There is some variation in stiffness with the peak value of the applied load, as noted in Section 5.3.2, and the predicted stiffness falls between the mean stiffness of each peak load. The stiffness at the higher peak load would be expected to be closer to the elastic stiffness with a rigid contact surface, and so the model appears to underestimate the elastic stiffness. This is in contrast to the Douglas fir embedment tests, in which the model overestimated the stiffness, and it is considered that this is due to the still-imperfect contact surface. The slight underestimate in the Norway spruce parallel-to-grain tests is thought to be due to the same inaccuracy which results in a more severe underestimate in the perpendicular-to-grain tests, the underestimate of the shear modulus, which will be discussed next.

Perpendicular-to-grain, the stress concentration is not so dramatic and, as a result, the two models predict very similar stiffness. Both stress functions underestimate the embedment stiffness for the R=1.2 tests. The fact that the predictions are close to the R=10 results is considered to be coincidental,since the models do not account in any way for the nonlinear behaviour at low load which is the apparent cause of the reduced stiffness at R=10. The t-test results in Table 6.3 show that the model is inaccurate for the R=1.2 tests, with a probability less than 0.005. It is even an underestimate for the R=10 tests.

These inaccuracies may be due to inaccuracy in the estimates of the shear modulus. The predicted stiffness is sensitive to the shear modulus, which has only been estimated in this study based on the other measured moduli. Based on the method described in Section 5.4.2, the mean shear modulus for the Norway spruce was estimated as 207N/mm^2. This is far lower than the 706N/mm^2 tabulated by Bodig and Jayne

(1993), as a result of the perpendicular elastic modulus, at 153N/mm^2, being lower than the 503N/mm^2 tabulated. A shear modulus of 500N/mm^2, for example, with all the other properties being kept constant, results in a perpendicular-to-grain stiffness of 10.1kN/mm, which is much closer to the measured values. The same effect may be responsible for the slight underestimate of the parallel-to-grain stiffness. Accurate measurement of the true shear modulus would be required to verify the cause of these discrepancies.

6.4.3 Single-dowel connections

Having compared the embedment test results with the predictions of the stress-function models, it was possible to use the foundation modulus derived by the models in a beam-on-elastic-foundation model for the single-dowel connections described in Section 5.2.2. The foundation modulus included the three components of the deformation in embedment described in Section 6.1.2.3: the change in the shape of the hole, the movement of the hole through the timber, and the deformation of the timber due to the far-field stress. The relevant deformation was then the displacement of the centre of the beam under a central point load.

The symmetry of the specimen meant that, if the deformation around each dowel were identical, then there would be a plane of zero displacement half way between the dowels. The foundation modulus was therefore based on the deformation of the timber around the dowel relative to this plane. This deformation occurred in the dowel at each end the single-dowel connection, so the overall stiffness of the specimen, between loading head and test bed, was predicted to be half the stiffness of the beam on foundation.

The predicted stiffness is compared with the experimental results in Figure 6-13. For the parallel-to-grain tests, it can be seen that the elastic model provides a reasonable estimate of the dynamic stiffness of the specimens in tension and compression for the cases where R=1.2. In the case of the perpendicular-to-grain compression tests, the mean predicted stiffness is approximately 50% of the mean measured stiffness.

Part of the underestimate by the theoretical model in the perpendicular-to-grain case was thought to be a result of the simplifications inherent in it, particularly the Winkler foundation in the beam-on-foundation model. The Winkler foundation gives no distribution of load in the direction along the beam axis; the displacement at a point is simply proportional to the pressure applied by the beam at that point. Under the loads described here, a large part of the load is concentrated near the centre of the beam, i.e. near the flitch plate. In reality, and in contrast to the behaviour of the Winkler foundation, this load will spread through the timber supporting the dowel in the direction along the dowel axis, resulting in a stiffer foundation than predicted.

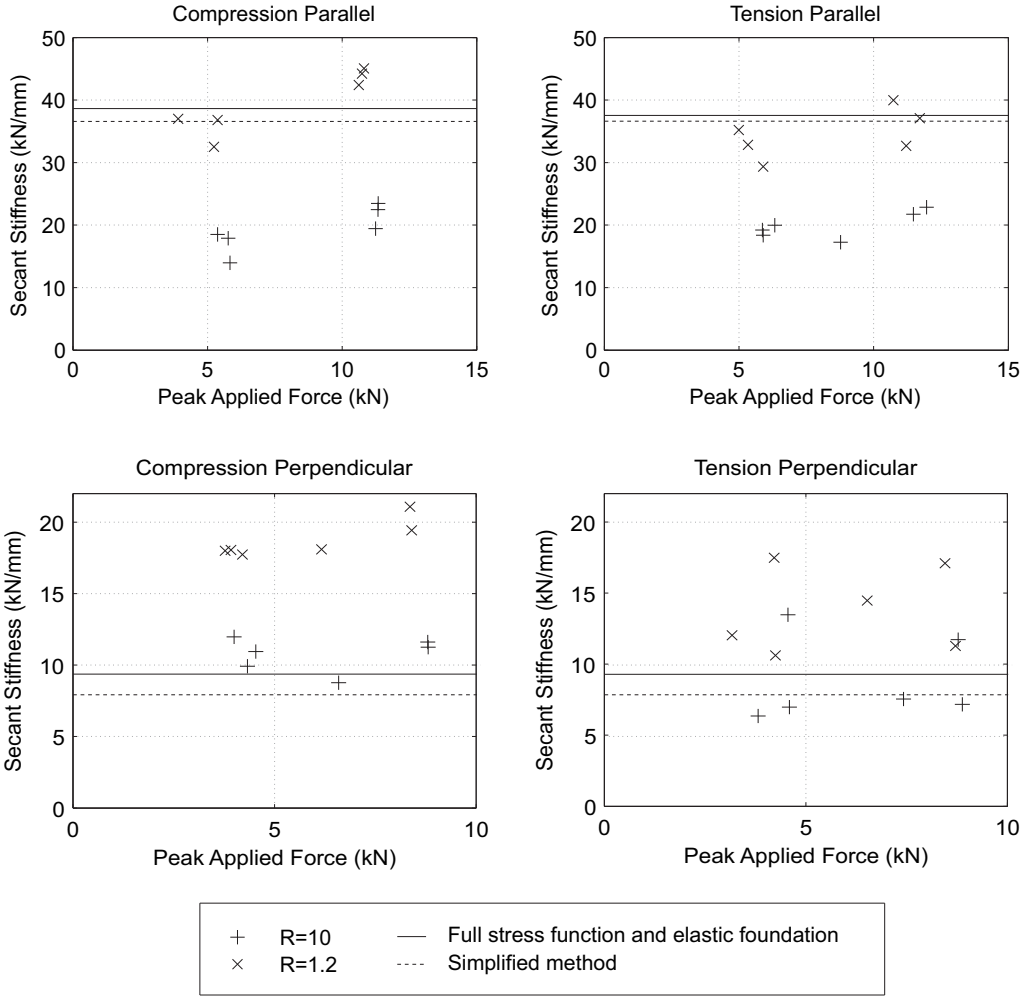

Figure 6-13: Comparison of predicted stiffness using the stress function and beam-on-elastic-foundation method with experimental results for parallel-to-grain single-dowel connection specimens

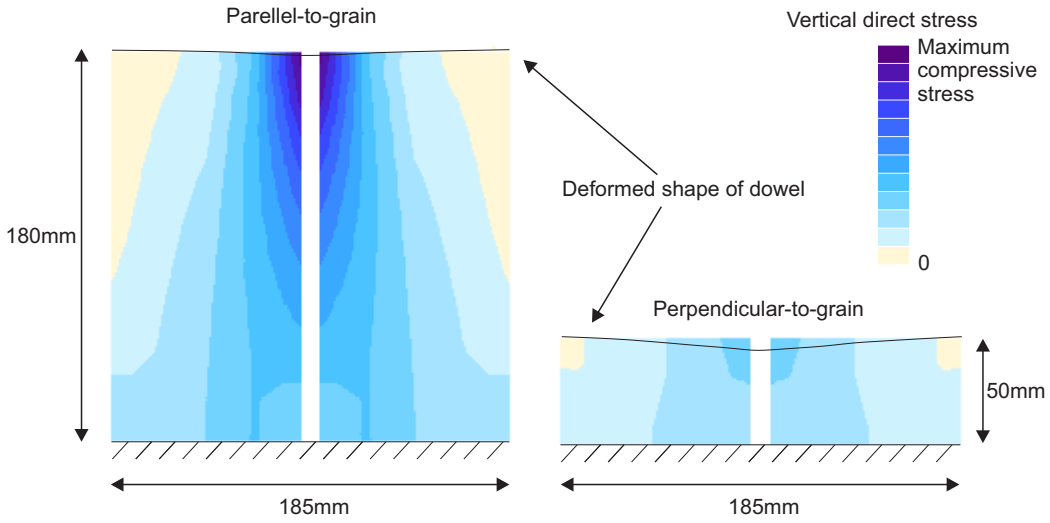

Figure 6-14: Finite element model for single-dowel connection specimens

A two-dimensional finite-element analysis was carried out using the Robot structural analysis program to estimate the magnitude of this effect, by approximating a fully elastic foundation. Symmetry was used to model half of each specimen as shown in Figure 6-14. The dowel was modelled as a linear element supported on a shell, the thickness of which was chosen to give the foundation modulus predicted by the stress function model. This shell was then considered to give a reasonable representation of the timber supporting the dowel, and the way in which the stress in the timber is distributed along the direction of the dowel axis. The resulting prediction of stiffness, plotted in Figure 6-13, shows that the foundation condition accounts for some of the underestimate by the simplified model with the Winkler foundation.

The remainder of the underestimate by the simplified model is considered to be due to the estimate of the shear modulus. The perpendicular-to-grain foundation modulus was seen to be under-predicted in the results in the previous section, and this result was thought to be due to inaccuracy in the estimate of the shear modulus. A combination of the underestimate of the foundation modulus and the distribution of load in the timber along the direction of the dowel axis is considered to be the cause of the underestimate of stiffness by the theoretical model, both of which are influenced by the shear modulus.

It is noted that the stress function calculation gives a higher stiffness between the two dowels in the case where they transmit a compressive load than in the case where they transmit a tensile load. This is due to the longer load path in the tensile case, in which the load is transmitted in concentrated tension and shear either side of the hole. The reduction is approximately 2.5% of the total stiffness in this case, but its magnitude will depend on the geometry of the particular connection.

A paired t-test was carried out to investigate the effect of load direction on stiffness, with the null hypothesis that the mean of the populations for the tensile and compressive tests is the same. This resulted in a probability of 0.01 that the null hypothesis is true based on the experimental results.

For the oscillating loads with R=10, the reduction in stiffness due to nonlinear behaviour at low loads is not allowed for in the purely elastic model, and this is reflected in the overestimate of stiffness in this case in the parallel-to-grain tests. The fact that the predicted stiffness falls close to the measured R=10 stiffnesses in the perpendicular-to-grain tests is considered to be coincidental, since the model does not allow for any nonlinearity in the contact surface.

6.5 Energy dissipation

It is considered that the stress function model for a complete hole gives a sufficiently accurate representation of the stress distribution around the face of the hole to allow calculation of the energy dissipation by friction at the interface between dowel and timber. The calculation is based on the assumption of Coulomb friction around the interface, that is to say, that a tangential friction force is produced in proportion to the force normal to the surface. The constant of proportionality is assumed to be constant around the face, which is consistent with the boundary conditions described in Section 6.1.2.1.

6.5.1 Embedment

The half-hole solution described in Section 6.1.1 is considered to be too simplified in its definition of the distribution of forces around the hole edge to provide a suitable estimate of energy dissipation by friction. Figure 6-15 shows that the full-hole solution, a 200-term Fourier series generated using the method by Hyer and Klang (1985), described in Section 6.1.2, provides a significantly different stress distribution to the 3-term half-hole solution by Zhang and Ueng (1984), described in Section 6.1.1. While the less accurate, but far more concise, 3-term solution has been found to be appropriate for stiffness estimation in certain conditions, the detailed analysis of the friction around the interface required the more accurate solution.

Using the stress function, the final state of the system under a particular load can be calculated, at which all points around the dowel-timber interface in the slip region, as defined in Section 6.1.2, have a tangential stress in balance with the normal stress at the limiting magnitude of the friction force. Furthermore, for the case of a tight-fitting dowel, all the equations defining the stress distribution are linear, so all those stresses

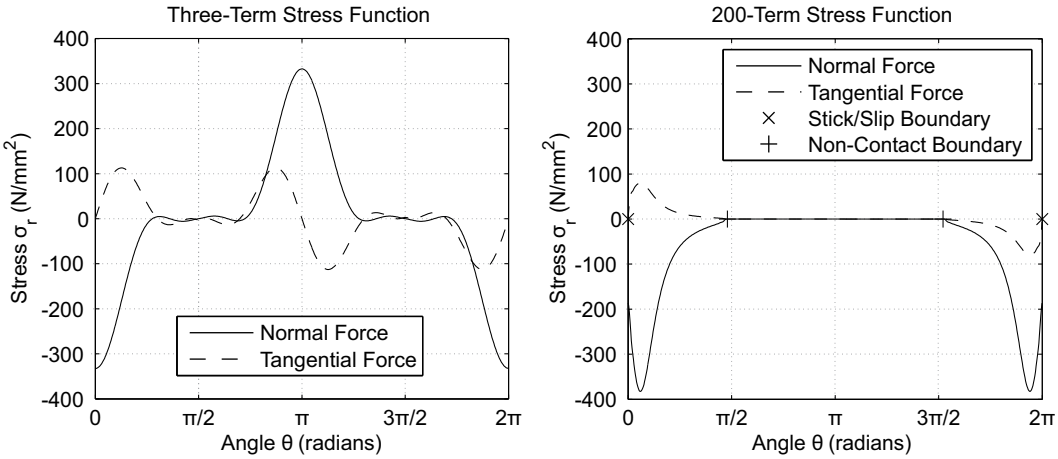

Figure 6-15: Comparison of normal and tangential stresses at the hole edge for a 3-term and a 200-term stress function, using the material properties for Norway spruce from Section 5.4, loaded parallel-to-grain

can be assumed to have grown linearly with displacement as the dowel was moved to that final state.

The energy dissipated as the dowel moved from rest to that position can be found by integration of the tangential stress $\tau_{r\theta}$ multiplied by the relative slip s between the dowel and the timber to give the frictional work done E_d. Since $\tau_{r\theta} = \mu\sigma_r$ in that region, where σ_r is the radial force per unit area, E_d is given by equation (6.64). t is the thickness of the timber along the dowel axis, r is the radius of the dowel and θ the angle measured from the origin and the x-axis. The multipliers of 2 and 0.5 have been shown for clarity: the 2 allows for the work in the symmetrical other half of the dowel and the 0.5 for the linear increase in slip from zero to s.

$$E_d = 2t \int_{\alpha}^{\beta} 0.5\mu\sigma_r s r \mathrm{d}\theta \tag{6.64}$$

The slip between the dowel and the timber at its final position can be calculated, for small dowel displacements, according to (6.65), where u_θ is the tangential displacement of the timber and u_0 the displacement of the dowel. The relative slip between dowel and timber is illustrated in Figure 6-16.

$$s = u_0 \sin\theta - u_\theta \tag{6.65}$$

The energy dissipated can then be calculated using (6.64). A convenient non-dimensional representation of the energy dissipation is the ratio of the energy dissipated to the elastic work done by the applied force. This will be referred to as the work ratio

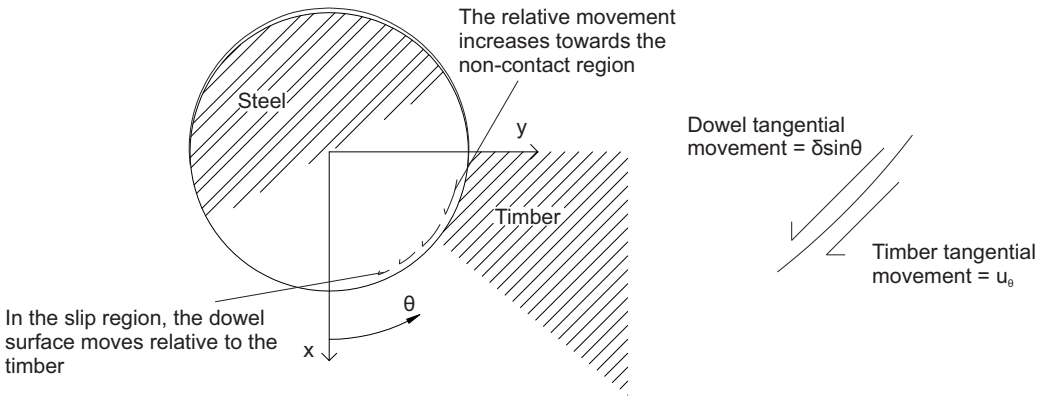

Figure 6-16: Relative slip between dowel and timber at their interface

W, and can be calculated using (6.66), in which P is the applied force. As described in Section (5.2.3), the ratio of stored energy to dissipated energy in a cycle of applied force is related to the contribution to damping made by the element. The energy dissipated by friction during unloading is considered to be equal to that during loading, so the total energy dissipated in a cycle E is equal to $2W$. (5.7) can then be used to express the energy dissipation as a damping ratio for a system oscillating in resonance as (6.67).

$$W = \frac{2E_d}{Pu_0} \tag{6.66}$$

$$\gamma = \frac{W}{\pi} \tag{6.67}$$

The energy dissipated calculated this way is compared with the experimental results for the embedment tests in Figure 6-17. The predicted damping ratio γ is 0.65% for the mean elastic properties of the Norway spruce, and 1.30% for the mean elastic properties of the Douglas fir parallel to grain. The perpendicular-to-grain values are 1.95% for Norway spruce and 2.12% for Douglas fir. The difference between the two is due mainly to their different friction coefficients, which have mean values of 0.15 parallel to grain and 0.19 perpendicular for Norway spruce and 0.21 in both grain directions for Douglas fir, as measured in Section 5.4.3. The results suggest that the energy dissipation by this interface friction form a large part of the total energy dissipation.

The relationship between friction coefficient and energy dissipation for Norway spruce parallel to grain is shown in Figure 6-18, which shows an almost linear relationship between the two over a range of friction coefficients.

This purely theoretical result is presented only tentatively, since the Coulomb friction coefficient is a convenient, but not necessarily accurate, way of representing the

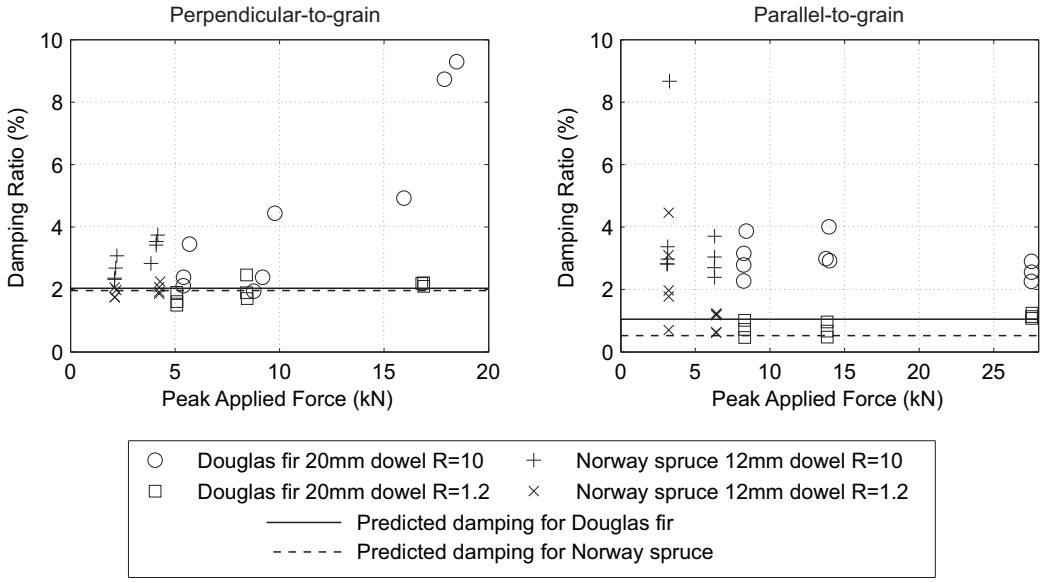

Figure 6-17: Comparison of predicted energy dissipation by interface friction with embedment test results

interaction between the steel and timber at their interface. It is shown in Section 5.5 that there is plastic deformation in the timber immediately around the dowel, and part of the movement between the face of the dowel and the timber is due to this plasticity, rather than frictional slip. This result does suggest, however, that it may be possible to increase the energy dissipation, and therefore the damping, in timber structures by the use of connectors with a higher friction coefficient.

The foregoing discussion shows that the energy dissipated in the connection is most meaningful when considered in conjunction with the elastic work done, and the subsequent stored energy in the structure, as a result of the applied force. The work done by the applied force depends on the distance through which it moves, and so the stiffness of the structure.

In Section 6.1.2.3, the movement of the dowel relative to a support is broken down into: the change of shape of the hole (the hole-shape component); the movement of the hole in the timber (the rigid-insert component); and the deformation of the timber under the overall load. This division is also useful in terms of energy dissipation, since the overall stiffness between the connector and the support can be thought of as the series combination of those three stiffnesses, as illustrated in Figure 6-19, and the overall energy dissipation as the combination of the three energy dissipations.

The total work done by the applied force is equal to the sum of the work done in each of the three springs in the figure, or each of the three mechanisms of deformation. Each mechanism will have an energy dissipation associated with it, represented by the

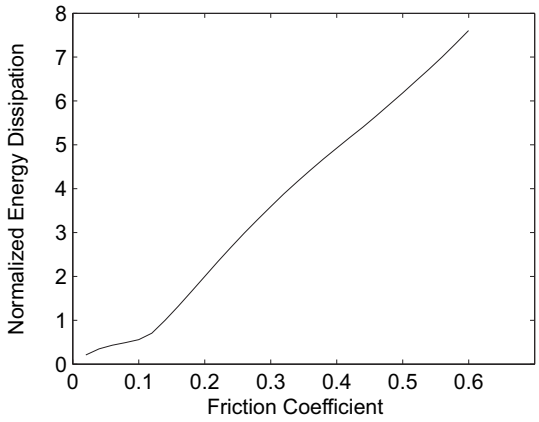

Figure 6-18: Variation of energy dissipation with friction coefficient μ, normalized by the energy dissipation at $\mu = 0.15$

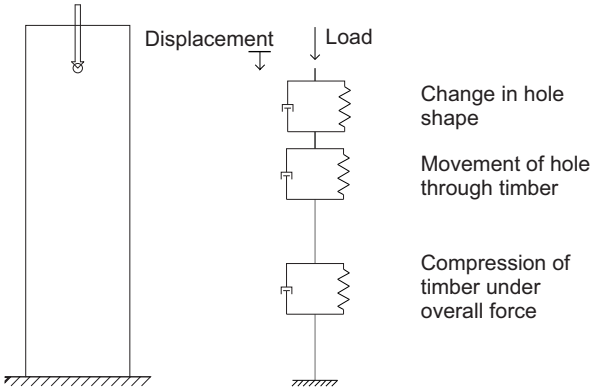

Figure 6-19: A schematic representation of the components of dowel deformation as a series of three springs

damper in parallel with each spring: the frictional energy dissipation due to the change in shape of the hole, as calculated in this section; the energy dissipation due to the movement of the hole through the timber, due to the internal losses in the timber in direct strain and shear; and the energy dissipation due to the deformation of the timber under the overall load, due to the internal losses in the direct compression of the timber. If the energy dissipation in each component can be represented by either linear viscous or hysteretic damping, then the energy dissipated will be proportional to the elastic work done in that component, since the equivalent viscous damping ratio is proportional to the energy dissipated divided by the elastic work. As a result, the combined damping ratio γ is given by (6.68), in which the γ_i are the damping ratios for each element and the W_i are the elastic work done in each.

$$\gamma = \frac{\sum_i \gamma_i W_i}{\sum_i W_i} \tag{6.68}$$

In the Norway spruce parallel-to-grain embedment tests, for example, γ_i was calculated as 1.5%. 39% of the displacement was due to the change of hole shape, so 39% of the work done by the applied force was in the hole-shape component, and the overall contribution to damping by around-the-dowel friction was $0.39 \times 1.5\% = 0.59\%$.

The experimental results showed that the energy dissipation in the embedment tests was often higher than that predicted by the analysis of frictional slip around the face of the dowel alone. It is proposed that the additional energy dissipation is provided by other mechanisms, such as friction within the microstructure of the timber, plastic deformation of small volumes of the timber near the contact surface, and perhaps small volumes of the connector material. The experimental results suggest that these other sources of energy dissipations may be unreliable: present in some connections and reduced or absent in others, perhaps depending on the fine detail of the surface of the hole or the fit of the connector into the hole.

It is therefore considered that the around-the-dowel friction between timber and connector described in this section provides a reliable baseline energy dissipation, to which other less reliable, and more difficult to predict, mechanisms add. The extent to which any of these mechanisms are consistent over the life of the structure cannot be assessed with certainty based on the testing and analysis presented here, primarily because of the short-term nature of the tests. As discussed in Section 5.3.2, the energy dissipation in the tests generally appeared to reach a steady state after 1000s of cyclic load. Whether the behaviour after 1000s is a true representation of the longer-term cyclic response is a subject for further work, but these results suggest that the stiffness

and energy dissipation after 1000s are the result of elastic and frictional behaviour which could be expected to continue through the life of a structure.

6.5.2 Single-dowel connections

In the single-dowel connection tests, the work done by the applied force is distributed between the components of embedment described above and the elastic deformation of the dowel. Given the displacement w of the dowel at each point along its length l, and the foundation modulus k_f, the work W done in embedment can be calculated by integrating the work along the length of the dowel according to (6.69).

$$W = \int_0^l k_f w^2 \mathrm{d}l \tag{6.69}$$

For the parallel-to-grain single dowel connection tests, the work done in the foundation, calculated using (6.69), is 74% of the total work done by the applied force. This enables the damping in that connection to be calculated according to (6.68). Table 6.4 shows that calculation for the parallel- and perpendicular-to-grain single-dowel connection specimens. For the purpose of this calculation, it was assumed that the energy dissipated in the deformation of the timber due to the rigid-insert deformation was zero. In reality, there will be some energy dissipated in the timber itself, as shown in research by Labonnote et al. (2013). The characterization of the timber for this energy dissipation and the study of the direct and shear strain around the dowel required to predict the contribution to damping by internal processes in the timber is beyond the scope of this study, and is therefore neglected.

Table 6.4: Summation of damping in single-dowel connection specimens

	Embedment				Dowel deformation		Total
	Hole shape		Rigid insert				
	W_i	γ_i	W_i	γ_i	W_i	γ_i	γ
Para.	24.0%	1.5%	49.9%	0.0%	26.1%	0.0%	0.36%
Perp.	11.2%	13.2%	65.4%	0.0%	23.4%	0.0%	1.5%

The damping predictions from Table 6.4 are compared with the experimentally measured steady-state damping ratios in Figure 6-20. As in the embedment tests, it can be seen that the predicted energy dissipation by around-the-dowel friction represents a baseline value which is generally exceeded in the tests. The amount by which the predicted value is exceeded is variable, however, and these results further support the hypothesis that this frictional energy dissipation represents a reliable minimum energy dissipation to which other dissipative mechanisms add.

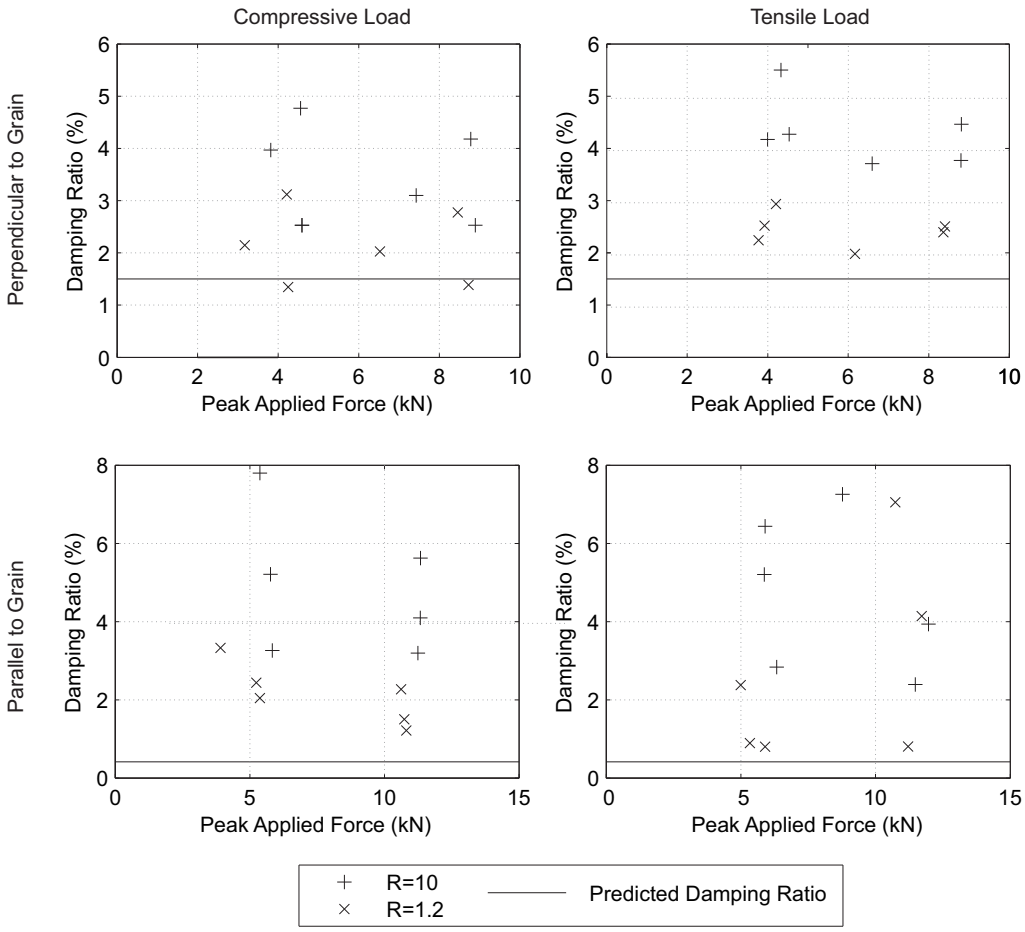

Figure 6-20: Comparison of predicted damping ratio due to around-the-dowel friction alone with experimental results for single-dowel connection tests

It might be suggested that a polishing effect, making the surface of the timber continually smoother, might continually reduce the friction coefficient. This suggestion is at odds with the tribological theory of the interaction of the two surfaces. Atack and Tabor (1958) described the friction between timber and steel as consisting of two main components: the 'ploughing' of the softer timber surface by the harder steel surface, and the adhesion of the two surfaces over areas of 'real' contact. The continual smoothing of the timber surface would not reduce the adhesion term, though the ploughing effect might be reduced as the two surfaces move back and forth along the same path repeatedly. In order to eliminate the energy dissipation associated with deformation of the timber, Atack and Tabor (1958) used tests in which blocks of timber were slid along a steel surface. This resulted in coefficients of friction of 0.6 for wood below 30% moisture content, and 0.5 above 30%. Atack and Tabor (1958) explained the coefficient of friction between steel and timber purely by the adhesion effect, neglecting the small contribution of ploughing. They attribute the adhesion to 'hydrogen bonding between the oxide layer of the metal and the unbound hydroxyl groups in the cellulosic constituents'. The work by Atack and Tabor (1958) therefore suggests that the energy dissipation by friction could be consistent through the life of a dowel-type connection.

6.6 Rheological model

The models for embedment presented so far are elastic approximations of the connection behaviour. The embedment behaviour observed in the tests described in Chapter 5, however, was not linear-elastic. It was concluded that the timber itself behaved in a viscoelastic way, giving time-dependent creep or stress relaxation, even in the time scale considered in this work, relatively short in comparison to conventional creep tests. The models described in Sections 6.1.1 and 6.1.2 have shown that friction between the face of the dowel and the timber also contributes to the force transfer, and dissipates energy under cycles of load. Furthermore, the imperfection of the contact face between dowel and timber means that some initial deformation of the joint is required to achieve full contact, meaning that the joint does not exhibit its full stiffness under small deformations. Finally, stress concentrations due to inaccuracies in construction and unevenness in the contact surfaces can result in regions of plasticity in the timber, even under loads well below the yield strength of the connection. All of these effects take the behaviour away from the linear-elastic approximation.

If an elastic analysis is to be carried out for a timber structure with such connections it must, therefore, use an approximation of the joint stiffness appropriate to a particular applied force. As a result, the stiffness used to calculate the overall deflection due to

a long-term static load must be different to that used for the relative deflection under a short-term, small-amplitude oscillating force, such as might be experienced by a structure vibrating due to wind or footfall. In order to quantify the components of the deflection of a dowel-type connector, a simple rheological model was fitted to the response, which allowed for viscoelasticity and local plastic behaviour.

The analysis and experimental work described in this section produces a foundation model for the timber in embedment. Using this model, the response could be divided into viscoelastic and plastic components, which was then quantified and used to compare the different timbers and connectors which have been tested. This work has been published in a peer-reviewed journal (Reynolds et al.; 2013b).

Before presentation of the model which has been used to represent the embedment behaviour, a qualitative discussion of the behaviour it represents is considered necessary. The displacement of the dowel due to a cyclic applied force is shown in Figure 6-21. First, there is a deformation that occurs simultaneously with the applied force. After the initial deformation, and during the cyclic applied force, there is evidence of a viscoelastic component which responds gradually to the step in applied force over the 1000s duration of the test. When the applied force returns to zero, there is a significant unrecovered deformation.

At this time scale, there is no clear evidence of a tendency towards a constant rate of creep. The viscoelastic creep appears to decay so that the mean displacement in each cycle tends towards a constant value; the creep that would be expected to occur under load applied for a period of hours or days is not evident in these tests.

6.6.1 Model parameters

A rheological model consisting of a combination of Kelvin-Voigt viscoelastic elements introduced in Section 2.1.2 is used to help understand and quantify the time-dependent components of the observed deformation. The basic mechanical model of a Kelvin-Voigt viscoelastic material consists of a linear elastic spring and a linear viscous damper in parallel.

In developing this model, the first step was to examine the near-elastic, or lightly-damped, component of the response. One near-elastic response could be measured as the secant stiffness of each cycle of oscillating load, and another as the initial response to the step in applied load at the start of the test. It was found that the initial stiffness was much lower than the secant stiffness. Since the secant stiffness was relatively constant throughout the test, it was thought that the lower initial stiffness could be explained by transient effects under first loading. This difference in stiffness was therefore represented by a gap element assumed to close under initial loading and remain

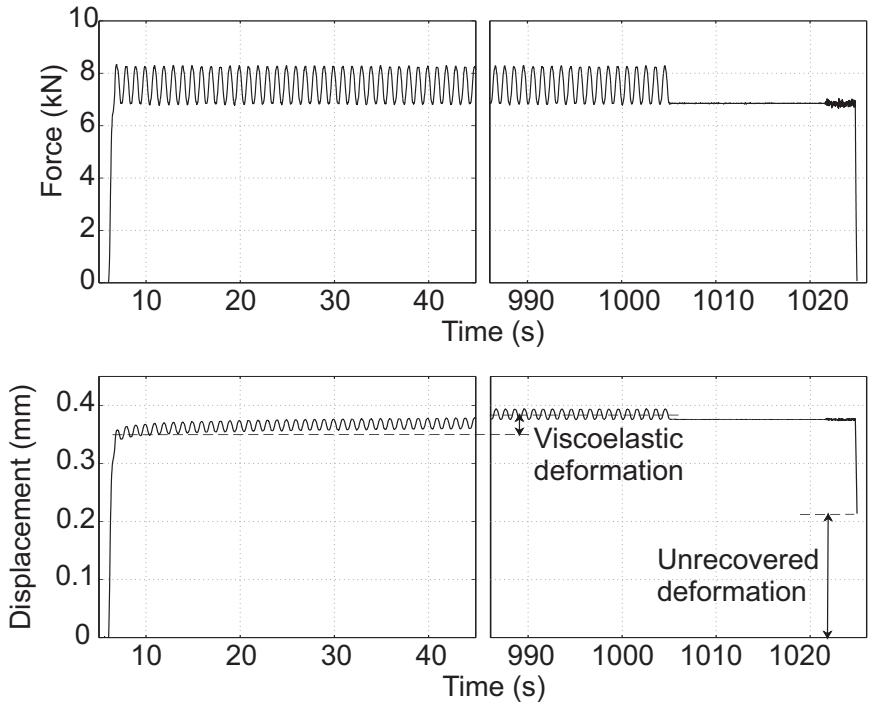

Figure 6-21: Observed displacement under oscillating load

closed under the oscillating load. The nature of this transient effect is further discussed in Section 6.6.3.

The next step was to address the viscoelastic deformation which was observed during the time under oscillating load. A single Kelvin-Voigt element was added, and fitted to match the displacements at the midpoint and the end of the test, at 500 and 1000s. The model with the gap element, near-elastic element and this viscoelastic element reproduced the steady-state stiffness under oscillating load, and followed the displacement response well in the second half of the test. In the first half of the test, the modelled displacement was much lower than the measured displacement, with the peak discrepancy at approximately 40s, as shown in Figure 6-22. A further viscoelastic element was therefore added with a shorter time-constant than the previous one, to match the faster component of the response of the real system. Since the maximum discrepancy was at approximately 40s, the additional viscoelastic element was adjusted to match the displacements at 20 and 40s.

The proposed model therefore consists of three Kelvin-Voigt elements. One Kelvin-Voigt element, which will be referred to as the near-elastic element, has a time constant of the order of 0.01s, stiffness k_0 and damping c_0. This element represents the stiffness and energy dissipation under oscillating load. The second has a time constant of the

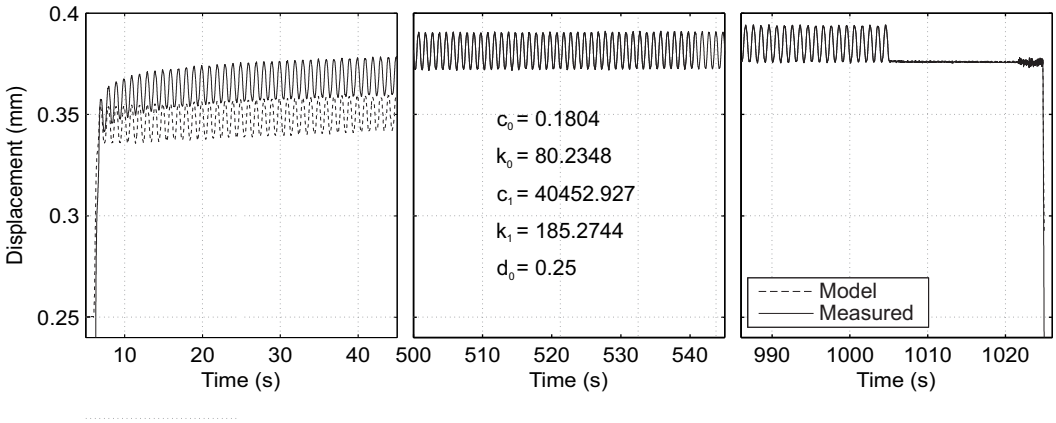

Figure 6-22: Comparison of displacement time-history between measured response and preliminary 5-element rheological model

order of approximately 20s, referred to as the balanced element with stiffness k_1 and damping c_1, and the third has a time constant of approximately 500s, referred to as the near-viscous element with stiffness k_2 and damping c_2. The latter two elements represent the viscoelastic deformation in the duration of the tests.

Under an oscillating load at 1Hz, neither the balanced nor near-viscous elements move significantly due to their relatively high damping, so the majority of the differential movement is in the near-elastic element. The near-elastic element does, however, show hysteresis at this frequency, and so models the hysteretic energy dissipation in the specimen at 1Hz.

A constant deformation of d_0 is added to the deformation in the viscoelastic model, represented by the gap element in the mechanical model. This allows for the displacement associated with the unevenness of the interface between dowel and timber and the imperfect fit of the dowel in the drilled hole. This phenomenon is discussed further in Section 6.6.3.

Part of the deformation represented by d_0 may be recovered upon removal of the load. The scope of this model is, therefore, only to represent the response of the connection to a step in applied load and an oscillating load. It is not intended to differentiate between the reversible and irreversible components of the deformation.

Friction between dowel and timber has been shown by several researchers (Rodd and Leijten; 2003; Sjödin et al.; 2008; Dorn; 2012), as well as the models in Sections 6.1.1 and 6.1.2, to affect the distribution of strain in the timber, and so it is reasonable to assume that the slip between the dowel and the timber may give energy dissipation. The model of the response of the connection, therefore, represents not just the viscoelastic behaviour of the timber parent material, but the frictional interaction between the

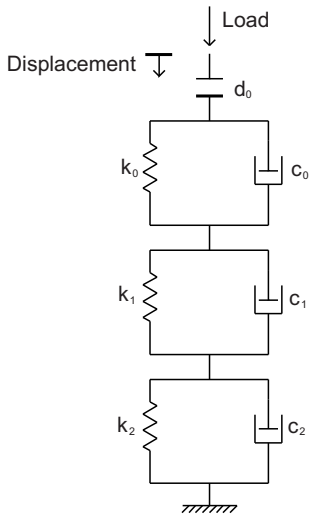

Figure 6-23: Rheological model

dowel and the timber. To preserve the simplicity and linearity of the model, Coulomb friction elements are not included, and the frictional component of the response is therefore allowed for in the stiffness and viscous damping in the viscoelastic elements. A Coulomb friction model predicts no variation of energy dissipation with frequency of loading, while a viscous damper dissipates energy in proportion to frequency. This suggests that the Kelvin-Voigt model may not predict the frequency dependence of damping accurately.

6.6.1.1 Curve fitting procedure

The parameters for the model were derived by considering the response of the specimen to the step in applied load and to the oscillating load. The following process was implemented using MATLAB.

The response of the system to a step in applied load is approximately given by (6.70), the near-elastic element being assumed to respond immediately, contributing to X_0. $X_{1,2}$ and $\tau_{1,2}$ are related to the parameters in the balanced and near-viscous component by (6.71) and (6.72). X_0 represents both d_0 and the displacement due to the near-elastic element, as shown in (6.73). Since neither the balanced nor near-viscous elements move significantly under the oscillating load, the stiffness k_0 can be determined as the secant stiffness in each cycle.

$$x = X_0 + X_1\left(1 - e^{\frac{-t}{\tau_1}}\right) + X_2\left(1 - e^{\frac{-t}{\tau_2}}\right) \tag{6.70}$$

$$X_{1,2} = \frac{1}{k_{1,2}} \tag{6.71}$$

$$\tau_{1,2} = \frac{c_{1,2}}{k_{1,2}} \tag{6.72}$$

$$X_0 = d_0 + \frac{F}{k_0} \tag{6.73}$$

(6.70) contains 5 unknown values: X_0, X_1, X_2, τ_1 and τ_2. 4 points in the measured displacement were used to calculate these parameters for the model: at 20, 40, 500 and 1000 seconds after initial loading. The displacement d_0, which occurs in addition to the viscoelastic behaviour, was estimated and found iteratively.

The curve-fitting procedure was as follows: First, time zero was set to correspond to the midpoint of the application of the force at the start of the test. k_0 was calculated using the average secant stiffness of the specimen under the oscillating load. k_0 and an assumed deflection d_0, which would be revised later, were used to calculate X_0.

The parameters of the balanced element, X_1 and τ_1, were then defined based on the displacement X_0, and the displacement at 20 and 40 seconds, using (6.70). It was assumed that the contribution of the near-viscous element at these times is small.

The deflection due to X_0 and the balanced element was then subtracted from the measured deflection. The remainder of the deflection was assumed to be due to the near-viscous element and the values at zero, 500 and 1000 seconds were used to define X_2 and τ_2. d_0 was then adjusted, and the process repeated iteratively until the appropriate value of d_0 was found, for which the modelled deflection at the initial peak in applied load matched the measured deflection.

The energy dissipated in each cycle of applied force was measured from each cycle in the force-displacement diagram as the area inside the hysteretic loop. The parameter c_0 could then be found using (6.74), where E_d represents the energy dissipated, f the frequency and ΔF the range of the oscillating force. In order to capture the steady-state energy dissipation, the average from the final 300 cycles was used to define the damping in the near-elastic element.

$$E_d = 2\pi^2 f c_0 \left(\frac{\Delta F}{k_0}\right)^2 \tag{6.74}$$

The model was applied to the same time-history of force as applied to the specimen, using an Euler time-stepping method. The experimental measurements were taken at a sampling rate of 100Hz but, in order to ensure the stability of the Euler method, the measured force was interpolated so that the Euler method was applied to a force time

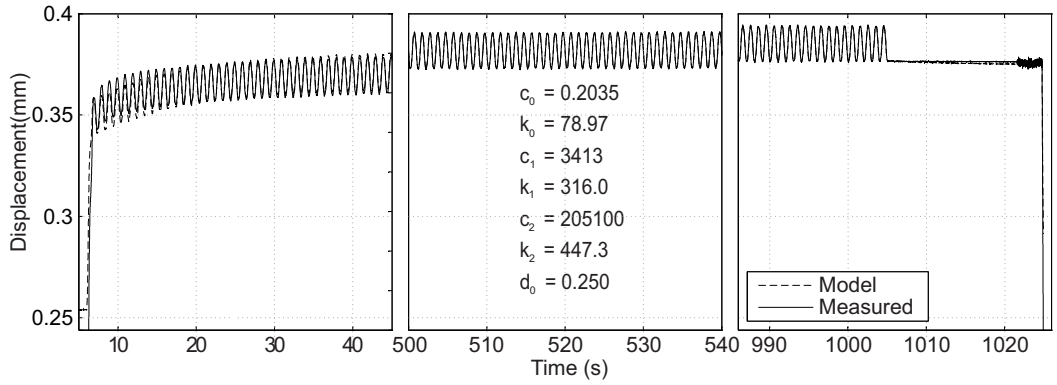

Figure 6-24: Comparison of displacement time-history between measured response and final 7-element rheological model

history with 1000 samples per second.

6.6.1.2 Model accuracy

The measured and modelled values of displacement are plotted against time in Figure 6-24. It can be seen that the modelled response closely follows the response of the specimen, the largest error being during the first 5 to 10 cycles of load. The near-elastic element gives the correct amplitude of displacement due to the oscillating load throughout the test, and the balanced and near-viscous elements follow the creep over the 1000 second duration of the test. In a similar way that, as described in Section 6.6.1.1, the discrepancy between measured and modelled displacement in the first half of the test was reduced by the addition of another viscoelastic element with shorter time constant, the discrepancy in the first 5 to 10 cycles could be reduced by addition of a further viscoelastic element with an even shorter time constant. It is considered, however, that the current model, consisting of three Kelvin-Voigt elements, gives a sufficiently accurate representation for the purpose of the comparisons made between specimens in Section 6.6.2.

Figure 6-25 shows the 15th, 500th and 1000th cycles of applied force, plotted against displacement. It is shown that the rheological model captures the creep between each cycle, shown by the movement of the cycles from left to right. Also captured is the transient contribution that creep makes to energy dissipation, shown by the higher energy dissipation in the 15th cycle. The energy dissipation is given by the area inside the hysteretic loops, and noted as E_d in Figure 6-25. The steady-state energy dissipation, represented by the damping in the near-elastic element of the rheological model, is thought to result from both a consistent hysteresis in the timber, and the friction between the dowel and the timber.

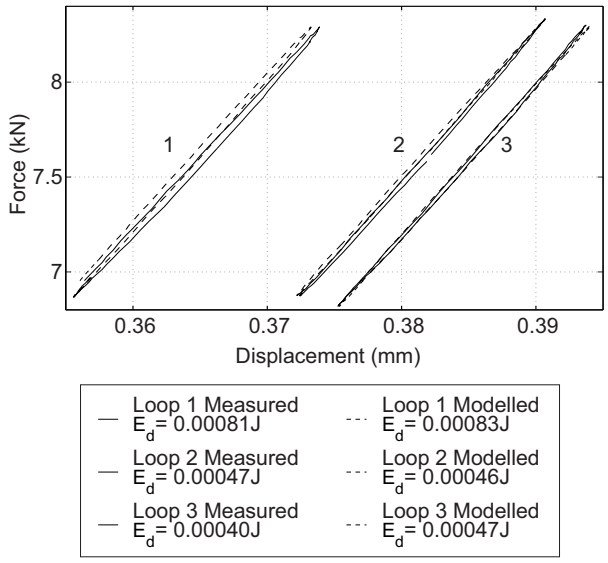

Figure 6-25: The 15th, 500th and 1000th force-displacement cycles - E_d represents the energy dissipated in each cycle

One of the simplifications inherent in this model is that the procedure used to fit the model to the experimental results considers only the time under the mean load, and not the number of cycles of load applied. It is considered that this approach is suitable because of the relatively small magnitude of the oscillating component of the load compared with its mean. A good representation of the overall behaviour has been achieved by considering the viscoelastic response to the mean load, and superimposing upon that the response to the oscillating load as a separate lightly-damped element. The small amplitude and high frequency of the oscillating component means that the heavily-damped parts of the model, the balanced and near-viscous elements, do not have a significant response at the frequency of the oscillating load, and can be considered as responding to a constant load at the mean value.

The fact that the heavily-damped parts of the model are derived based only on the mean of the oscillating load does not mean they do not affect the oscillating response, however, and it is shown, in Figures 6-24 and 6-25, that the model reflects the measured transient effects on displacement and damping. It is noted that this approach may not be suitable for larger amplitudes of oscillating load, but it is considered that this model, and the approach used to fit it to the experimental results, captures several important features of the behaviour of timber in embedment due to the small-amplitude vibration which is regularly experienced by structures in service.

6.6.2 Comparison of specimens

For each specimen, three equivalent stiffnesses are presented, based on the parameters of the fitted rheological model. They are illustrated in Figure 6-26. The first, which will be referred to as the dynamic stiffness k_d, is equal to k_0, the stiffness of the near-elastic element. This is the stiffness which would determine the natural frequency of a structure containing this type of connection, oscillating in the range used in these tests. The second equivalent stiffness is the series combination of k_0, k_1 and k_2, as in (6.75), and represents the stiffness under a static load, once all the viscoelastic elements have relaxed. This is called the viscoelastic stiffness k_v. It only includes the viscoelastic components which are apparent over the 1000 second duration of these tests, so it represents the stiffness appropriate to calculate the relative displacement due to a short-term static load, such as crowd, wind or vehicle loading on a structure.

$$k_v = \left(\frac{1}{k_0} + \frac{1}{k_1} + \frac{1}{k_2} \right)^{-1} \tag{6.75}$$

The third equivalent stiffness is called the total stiffness k_t, and includes the viscoelastic stiffness combined with the effect of d_0. This stiffness would be appropriate to calculate the total deformation of the connection from initial loading due to, for example, the self-weight and imposed loads on a structure. It does not allow for longer-term creep effects which were not apparent in the 1000 second test. The total equivalent stiffness is given by (6.76).

$$k_t = \left(\frac{1}{k_v} + \frac{d_0}{F_{av}} \right)^{-1} \tag{6.76}$$

Figure 6-27 shows the equivalent stiffnesses plotted for each specimen tested. The three equivalent stiffnesses are substantially different in each specimen. For example, over the complete set of tests the dynamic stiffness is, on average, 3.8 times higher than the total stiffness. This difference suggests that each type of behaviour would be best represented in elastic analysis by a different value of stiffness, and shows the importance of considering the nature of the loading in determining an equivalent stiffness for a connection.

Table 6.5 shows the mean of the stiffness for each of the three repetitions of each type of specimen and orientation. The stiffness is also expressed as the foundation modulus K, given by (6.77), where w is the length of the specimen along the dowel axis, and d is the dowel diameter.

$$K = \frac{k}{wd} \tag{6.77}$$

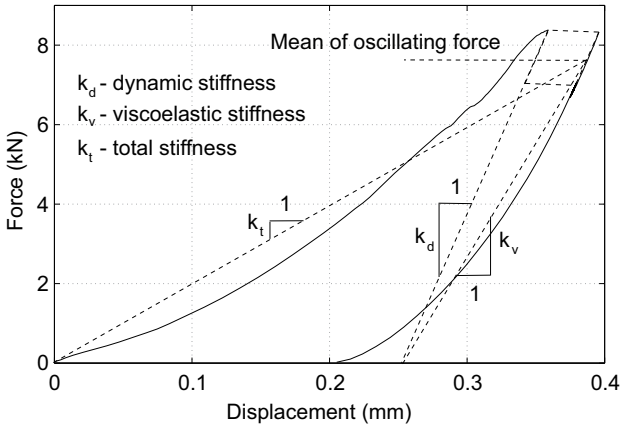

Figure 6-26: The three equivalent stiffnesses used to describe the response of each specimen - the 1000 cycles at 1Hz have been omitted for clarity

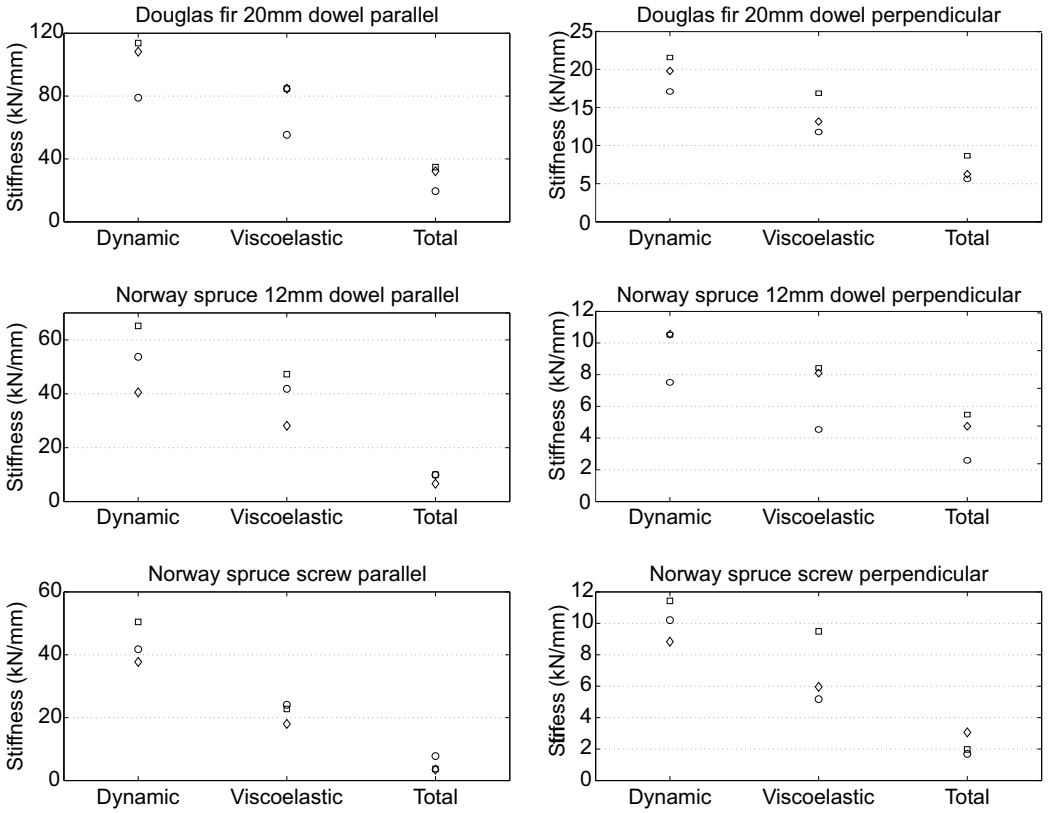

Figure 6-27: Equivalent stiffness calculated using fitted rheological model parameters

The ratio of the viscoelastic stiffness to the dynamic stiffness is consistent between the dowel specimens. This suggests that it may be possible to develop an empirical relationship between these equivalent static stiffnesses, on the basis of further tests, which could be used in design.

The total stiffness depends on the contribution from d_0, which is thought to depend on errors in construction such as oversize of the hole due to movement of the drill bit, and on the quality of the interface between dowel or screw and timber. These parameters are difficult to control, and can be expected to vary between individual specimens. The variation in total stiffness was, therefore, expected.

Table 6.5: Mean stiffness and foundation modulus from rheological model

		Mean dynamic stiffness	Mean dynamic foundation modulus	Viscoelastic	Total
Specimen	Orientation	k_d kN/mm	K_d kN/mm^2/mm	k_v or K_v %	k_t or K_t %
Douglas fir and 20mm dowel	Parallel	100.30	83.58	75%	29%
	Perpendicular	19.48	16.23	72%	35%
Norway spruce and 12mm dowel	Parallel	53.13	110.68	74%	17%
	Perpendicular	9.53	19.85	74%	45%
Norway spruce and screw	Parallel	43.30	144.33	50%	12%
	Perpendicular	10.15	33.84	68%	22%

6.6.3 Initial plastic deformation

Some further discussion of the nature of the displacement d_0 is considered appropriate, since it represents a large proportion of the total deformation of the connection, and appears to be far from linear-elastic.

If the dowel and the half-hole in the timber member do not have exactly the same diameter, then the dowel will initially make contact with the timber along a single line along its length. Any unevenness in the surface of the timber will mean that the line is split into a series of shorter lines or points. As a force is applied to the dowel, the pressure on this, initially very small, bearing area will be very high. It appears that this initial high pressure is sufficient to cause deformation of the timber in small volumes around the dowel, enough that the force is spread over a larger area and the pressure reduced.

The result is that a significant part of the initial deformation of the dowel under first loading is made up of the deformation which accommodates these stress concentrations, which may be plastic in parts of the timber, and elastic in others. Under subsequent dynamic loading, especially when the force remains above the level at which all these imperfections are crushed, the imperfections have little effect on the stiffness of the specimen. It is believed that this behaviour results in the deflection d_0 in the model, which was incorporated so that the viscoelastic model could be fitted to the rest of the response.

On the basis of this explanation, the deformation d_0 would be expected to depend on the magnitude of the applied force, but would be expected to tend toward some value, at which all of the imperfections in the contact surface were taken up.

The magnitude of the initial plastic deformation varies widely between the specimens tested, which is consistent with the hypothesis that it is caused by unevenness in the contact surface between the dowel and the timber and lack of fit between the dowel and the hole. Both of these parameters depend on the accuracy of the manufacturing process.

6.7 Summary

Models have been developed as part of this study to predict the elastic component of the embedment of a dowel into the timber surrounding it, based on an elastic stress function, and to use that information in predicting the stiffness exhibited by a single connector. The mathematical model which takes into account the orthotropy of the timber and the frictional interaction between dowel and timber has been simplified to form a method suitable for hand calculation.

On the basis of this model, the energy dissipation by friction around the dowel in embedment was calculated. It was shown that this energy dissipation could be used to make a prediction of the damping ratio in both the embedment and single-dowel connection tests. The predicted damping ratio appeared to represent a reliable minimum damping, which was exceeded by most of the tests. The measured difference in damping between parallel- and perpendicular-to-grain tests also appeared to be reflected in the theoretical predictions.

It was recognized that the elastic model was only suitable for predicting the steady-state secant stiffness under one-sided vibration where the cyclic load remains well above zero. The discussion and analysis in Chapter 4 showed that this is a common form of loading in in-service vibration, but a model was sought to quantify the relationship between this elastic stiffness and the stiffness exhibited under other forms of loading. For that purpose, a viscoelastic model was used, which enabled a comparison of the stiffness under initial loading, that due to a change in static load, and the cyclic stiffness which can be predicted by the stress-function model.

Chapter 7

Connection and Frame Testing and Analysis

The experimental results in Chapter 5, and the results of the analysis in Chapter 6 have provided information on the way the basic component of the dowel-type connection behaves. Those results indicate various characteristics of the behaviour of individual connectors, which can be expected to affect the behaviour of a complete connection or structure. The testing and analysis described in this chapter was designed in order to investigate how those characteristics influence the response of a complete structure to in-service dynamic loading.

7.1 Materials and methods

Two structures were tested, designed to illustrate the behaviour of connections as part of a complete structure. They were:

- a cantilever beam, supported by a moment connection to the laboratory strong wall with mass imposed by steel blocks at its end; and
- a portal frame with moment connections at each node supported by moment connections on the strong wall with mass imposed by steel blocks at one of the nodes away from the wall.

The portal frame was thus rotated from its normal configuration in a structure, which allowed the self-weight and additional mass to apply a load parallel to the line of the wall. The setup for each test is shown schematically in Figure 7-1.

The purpose of the cantilever and frame tests was to observe the effect of the behaviour of the elements of connections investigated experimentally in Chapter 5 and

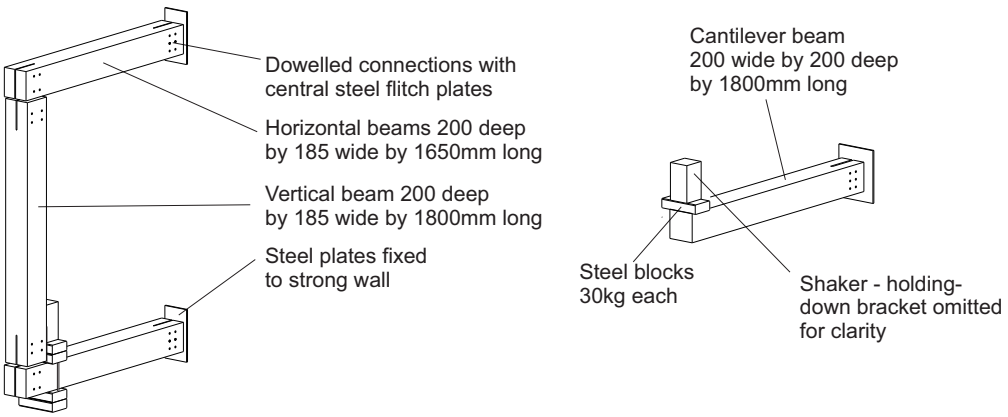

Figure 7-1: Schematic test setup for modal analysis of cantilever and frame structures

modelled in Chapter 6 on the behaviour of a complete connection or structure. The following characteristics were noted in those embedment and single-dowel connection tests, which were expected to influence the behaviour of the complete connection and frame:

- a variation of stiffness with amplitude of applied force due to non-linear force-displacement response at low load;
- a variation of energy dissipation with amplitude of applied force;
- a transient reduction in energy dissipation in the initial cycles of applied load, with energy dissipation tending to become constant after sufficient time; and
- a transient increase in stiffness, for tests under load control, in the initial cycles of applied load, with stiffness tending to become constant after many cycles of load.

The amplitude of the applied load was varied to observe the effect on stiffness and energy dissipation. The tests were designed to measure the steady-state stiffness and damping at each amplitude of applied load, the transient effects being eliminated by applying a static load for a period before the test, and restarting the tests if any significant change in the modal properties or displacement was noted during the application of the oscillating load.

7.1.1 Frames

The size of the frame specimens meant that they could not be loaded by a servo-hydraulic loading machine so, in contrast to the embedment and single-dowel connection tests described in Chapter 5, their dynamic properties were measured using modal

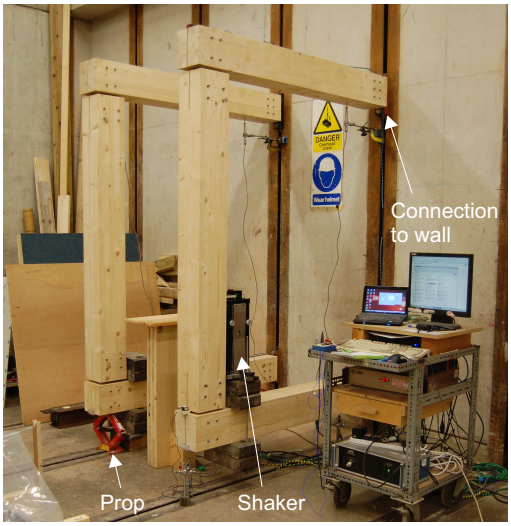

Figure 7-2: Frame specimens during testing

analysis. The structures were excited using an electrodynamic shaker and an instrumented hammer. As a result, the frequency of the oscillating forces in the connections was now determined by the natural frequency of the structure, and the amplitude by the resonant response of the structure to the applied force. This meant that the oscillating force on the connection was not directly controlled, but could be calculated after the tests.

Each frame was constructed from Norway spruce glued-laminated timber beams supplied by Lilleheden. The beams used in the frame tests were 185mm by 200mm, made up of five 40mm laminates and graded GL28h according to BS EN 1194 (BSI; 1999). The beams were used as delivered, which meant that there were examples of knots being present near the holes through which the dowels passed. In Figure 7-2, both frames are shown side by side. The nearer one, Frame B, was being tested, so the shaker and imposed mass can be seen fixed to that frame, while frame A was temporarily propped.

7.1.2 Cantilever beams

Similarly, the complete moment connections were tested by modal analysis of forced vibration. In this case, only the electrodynamic shaker was used to excite the structure. For the cantilever tests, two geometries of moment connection were tested, each fixed to a steel plate inserted into a slot at the end of the beam with 12mm steel dowels. The steel plate was welded to a bracket fixed to the laboratory strong wall. Figure 7-3 shows the geometry of the connection, along with reference numbers for each hole and

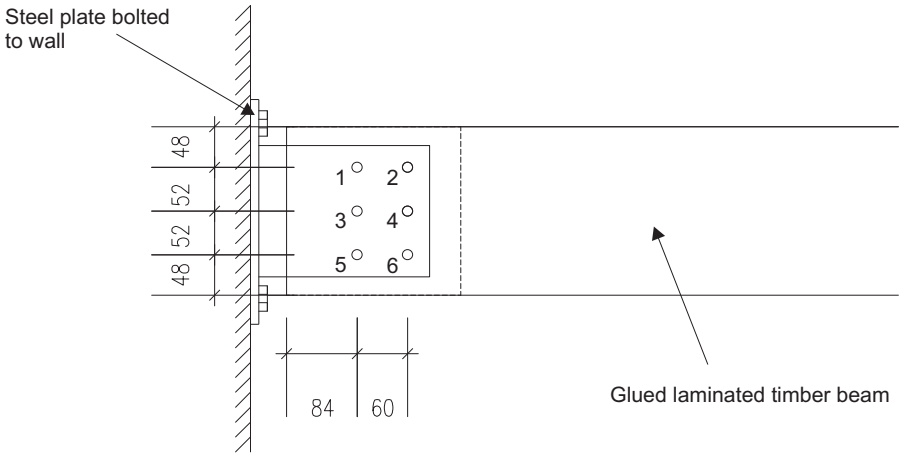

Figure 7-3: Geometry of connections for cantilever beam test and numbering of holes

Table 7.1: Cantilever connection test specimens - see Figure 7-3 for dowel locations

Label	No. of dowels	Dowel locations	Applied mass
A6	6	1 to 6	67kg
A2a	2	1 and 5	37kg
A2b	2	2 and 6	37kg
B6	6	1 to 6	67kg
B2a	2	1 and 5	37kg
B2b	2	2 and 6	37kg

Figure 7-4 shows the connection and the support from the strong wall.

Two-dowel and six-dowel connections were tested. The dowel arrangement is shown in Table 7.1. The two-dowel connection was used since it represented the simplest form of moment connection. The six-dowel connections were tested to represent a more realistic structural connection, and to reflect the connections used in the frame test. All the tests were carried out on the same glued-laminated timber beam, of 1.8m total length. By making connections in either end of the beam, there could be two repetitions of the tests with six-dowel connections, and four repetitions of the tests with two-dowel connections. One end of the beam was labelled A and one end B so, for example, specimen A2a was a test on a two-dowel connection at end A of the beam.

The applied mass was chosen to result in a static load in the connection of approximately 20% of the predicted yield load for the six-dowel connection, and approximately 40% for the two-dowel connection.

The beam used for the cantilever tests was made from glued-laminated timber supplied by Lilleheden, graded GL28h according to BS EN 1194 (BSI; 1999). The cross-section was 200mm by 200mm square, made up of six 33.3mm laminates of Norway

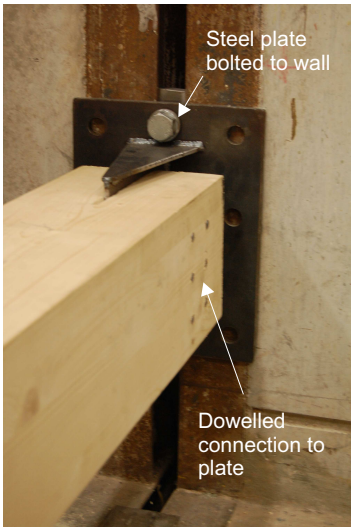

Figure 7-4: Support for cantilever beam tests showing the six-dowel connection

spruce.

7.1.3 Excitation of structures

Three separate methods were used to dynamically excite each structure, each requiring a different analysis method. All were forced vibration tests, exciting the structure at a single point. To preserve the simplicity of analysis in both cases, the excitation was applied at the same point as the imposed mass: at the end of the cantilever and at the right angle of the frame. This also meant that the mass of the shaker, significant at 37kg, could form part of the imposed mass. The excitation methods were:

- a slow sine sweep, in which a sinusoidal force, gradually increasing in frequency, was applied by the shaker and the rate of increase of frequency was sufficiently slow that the steady-state response at each frequency had time to develop;
- a pseudo-random excitation, in which a signal containing a known range of frequency components with random phase was generated and used to drive the shaker; and
- an impulse, applied by an instrumented hammer, was applied at the same point at which the shaker was placed.

Even though the shaker was not used in the impulse tests, it remained in place to maintain the same distribution of mass in each test. The shaker is shown mounted on a frame specimen in Figure 7-5.

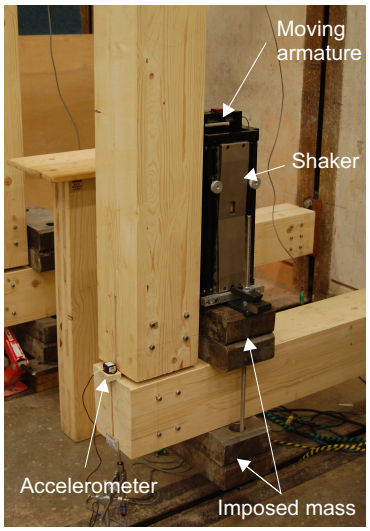

Figure 7-5: Detail of frame test, showing the shaker mounted on the structure, the mass imposed by steel blocks and one of the accelerometers

Before dynamic testing, the structure was assembled, instrumented and propped at the point where the mass was to be placed. The prop was set at a height that made the horizontal members level, as measured with a spirit level. The prop was then removed, and the displacement monitored for a period of 16 hours to allow the transient processes to occur: looseness in the connections to be taken up; surface irregularities at the dowel-timber interface to crush as far as possible; and the initial creep in the connections to occur. The dynamic tests were then carried out, the slow sine sweep and pseudo-random excitation applied at a range of amplitudes.

7.1.3.1 Measurement of input force

The force applied by the instrumented hammer was measured by a high-frequency load cell at its tip. The shaker applied a force to the structure through the inertia of an armature which moved along a single axis as it was driven by an inductive coil. Since the shaker was placed on the structure and otherwise unsupported, the variable force applied to the structure was generated by the inertia of the moving armature, and so was proportional to its acceleration. That acceleration was therefore measured and used to calculate the variable applied force.

The relationship between the measured acceleration of the armature and the force applied to the supporting structure was calibrated using a load cell. The shaker was mounted on the load cell, and the armature caused to oscillate at a frequency of 8Hz, representative of the natural frequency of the cantilever and frame structures. The

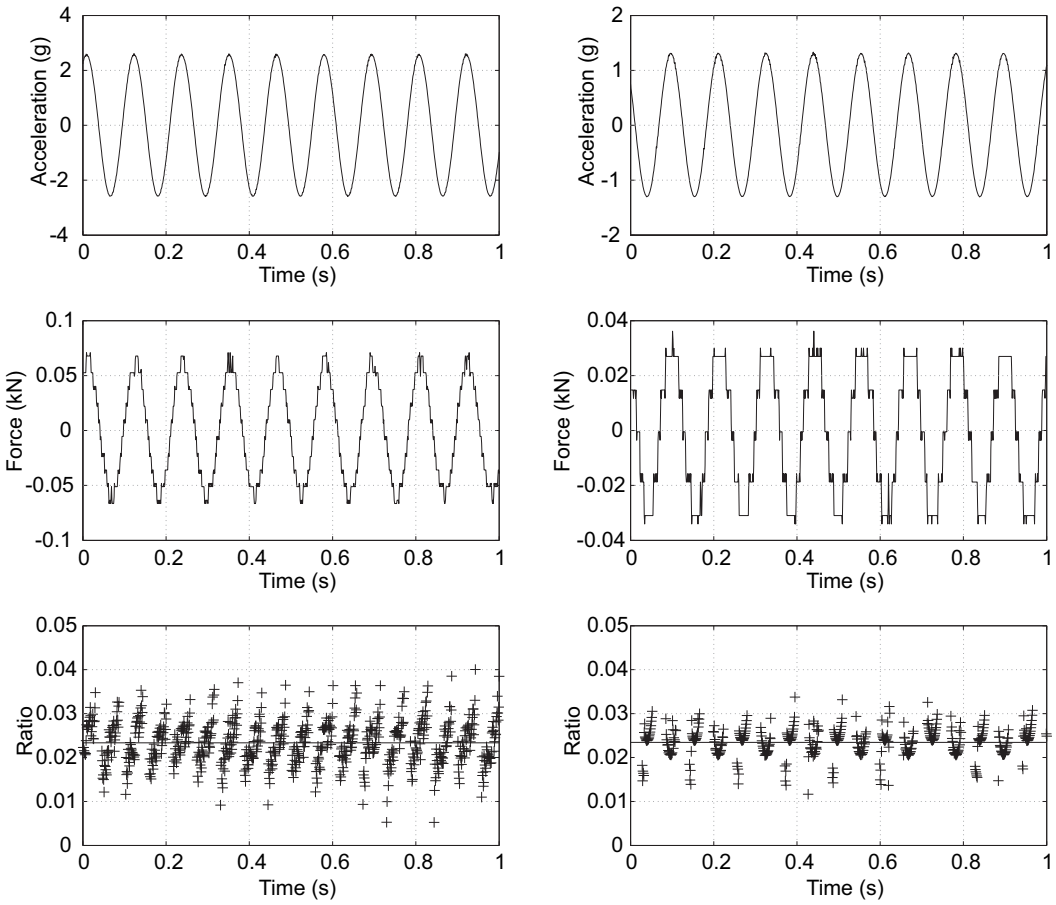

Figure 7-6: Evaluation of the constant of proportionality between the acceleration of the shaker armature, and the inertia force applied to the supporting structure

measured plots of force and acceleration were then compared and used to estimate the constant of proportionality between the two.

The analogue to digital conversion for the load cell did not have sufficient discrete points in the amplitude of the applied force for an accurate representation of the load profile, but the representation was considered sufficiently accurate that, averaged over 200 cycles, a representative value of the ratio of acceleration to force could be estimated. When the force and acceleration were close to zero, the result was sensitive to errors in either, so the average was calculated using only values greater than 9.81m/s^2, or 1g. To verify proportionality, the ratio between the two readings was evaluated at two amplitudes of acceleration. The results are shown in Figure 7-6.

The structures were instrumented so that both displacement and acceleration of various points of the structure could be measured. The location of sensors is shown in

Figures 7-11 and 7-16, later in this chapter. Given the time history of the force applied to the structure, either from the acceleration of the shaker armature or the instrumented hammer, and the time history of displacement and acceleration from these sensors, two transfer functions could be directly calculated: the receptance and the accelerance. The former is the relationship between displacement and applied force over the frequency range, and the latter the relationship between acceleration and applied force. The component of receptance $H_x(\omega)$ at each frequency can be transformed into accelerance $H_a(\omega)$, and vice versa, by the relationship $H_a(\omega) = -\omega^2 H_x(\omega)$, so the two could be compared to verify the accuracy of the measurements.

7.2 Analysis

7.2.1 Modal analysis

The input force spectrum could therefore be obtained from the measured acceleration of the shaker armature, and the response from the accelerometers and displacement transducers around the structure. The concentration of mass in each structure, and the fact that the excitation was applied along a single axis, meant that the response of each was dominated by a single mode of vibration. The purpose of the modal analysis was to identify the natural frequency and modal damping, as well as the presence of any nonlinearity, in that single mode.

For the pseudo-random tests, the precision of the measured transfer function depended on the sampling rate and the length of the measured time-histories of displacement and force. Pilot tests showed that a test of 100s duration sampled at 200Hz provided a sufficiently well-defined transfer function, and these were used on the pseudo-random vibration tests on the cantilever joints and frames.

In the slow sine sweep tests, a sampling rate of 200Hz was again used. The duration of the test had to be chosen so that the rate of sweep was slow enough for the full resonant response to develop at each frequency of applied force.

The amount of time for the full resonant response to develop depends on the natural frequency and damping in the system, since it represents the time at which the energy dissipated by the system in one cycle equals the energy put into the system by the oscillating force in that cycle. In a system with high damping, this condition will be more quickly met compared with a system with low damping, where the amplitude must increase further before the energy balance is satisfied. For a system with a given damping, the balance of input and dissipated energy is achieved over a given number of cycles. For a higher-frequency mode, therefore, the balance of input and dissipated energy is achieved in a shorter time than in a lower-frequency mode.

The natural frequency and damping of the mode in consideration therefore influence the time taken for the system to reach its steady-state response at resonance, and so influence the rate at which the frequency should be increased in a slow sine sweep test. ISO 7626 (ISO; 1990) gives guidance on the appropriate rate of sweep for modal analysis for a model with a given natural frequency and damping. The equation given in that code, adjusted to use the notation used in this study, where f is frequency in Hertz, f_n is the natural frequency of the mode in question, γ is the equivalent viscous damping ratio and t is time, is given in (7.1).

$$\left(\frac{\mathrm{d}f}{\mathrm{d}t}\right)_{max} = 216 f_n^2 \gamma^2 \tag{7.1}$$

The natural frequency of the system was estimated based on pilot tests and a conservatively low estimate of damping, 1.5%, was used to determine the sweep rate for use in the tests.

Once the tests had been conducted, the transfer function, either accelerance or receptance, was plotted from the measured acceleration or displacement. For the slow sine sweep excitation, the accelerance could be calculated by converting the time histories of force and acceleration to their frequency-domain spectra using a discrete Fourier transform, MATLAB's built-in *fft* function, resulting in a complex number at each frequency representing magnitude and phase, and then dividing acceleration by force at each frequency. Using the measured displacement, the receptance could be calculated in a similar way.

For the pseudo-random excitation, even though the pseudo-random signal is generated to contain a range of frequencies, the Fourier transform of the input force is not constant over that range of frequencies, but varies sharply. As a result, slight errors in the measured magnitude and frequency of displacement or acceleration lead to large errors in the transfer function if it is calculated simply by dividing the Fourier transform of the output by that of the input. For the case of pseudo-random excitation, a more accurate measurement of the accelerance H_a can be made by using the relationship between it, the autocorrelation of the input force P_{ff} and the cross correlation between force and acceleration P_{fa} (Ewins; 1986), as given by (7.2). A similar relationship exists for receptance.

$$H_a = \frac{P_{fa}}{P_{ff}} \tag{7.2}$$

For both forms of excitation, the natural frequency and modal damping were initially investigated by the circle fit method. The brief investigation into the frequency dependence of energy dissipation described in Section 5.3.2 concluded that the hys-

teretic damping model was the most appropriate for the observed embedment behaviour. The circle fit method used here therefore uses the fact that the receptance of a single-degree-of-freedom system with hysteretic damping, plotted on the complex plane, forms a circle, as shown in Figure 7-7. The value of the receptance moves around the circle as the frequency is increased, and it can then be shown (Ewins; 1986) that rate of sweep of the receptance function around the circle is a maximum at resonance. The resonant frequency ω_r can therefore be determined using a finite difference method to locate its value between the measured points.

The finite difference method was applied by first calculating the rate of sweep $\mathrm{d}\theta/\mathrm{d}\omega$ for each pair of measured points on the receptance plot. Call this rate of sweep θ'. The maximum rate of sweep could then be seen to lie between two points, θ_2 and θ_3. The location of the maximum rate between those two points could then be estimated using (7.3) to (7.6), a finite difference method which can be derived from the Taylor series, which uses the circular frequency and phase angle at four points, $\omega_{1,2,3,4}$.

Where θ' has its maximum, θ'' will be equal to zero. The second derivatives θ''_2 and θ''_3 are therefore estimated using (7.3) to (7.5). The frequency at which the maximum rate of sweep occurs, ω_r, equal to the natural frequency, is then estimated by interpolation between ω_2 and ω_3, as in (7.6).

$$h = \omega_3 - \omega_2 \tag{7.3}$$

$$\theta''_2 \approx \frac{\theta_3 + \theta_1 - 2\theta_2}{h^2} \tag{7.4}$$

$$\theta''_3 \approx \frac{\theta_4 + \theta_2 - 2\theta_3}{h^2} \tag{7.5}$$

$$\omega_r \approx \omega_2 + h\frac{\theta''_2}{\theta''_2 - \theta''_3} \tag{7.6}$$

The circle fit can also be used to estimate damping, since the equivalent viscous damping γ is given by (7.7), where ω_a and ω_b are arbitrary frequencies either side of ω_r, and θ_a and θ_b are their respective angles measured around the circle from ω_r. Since any pair of data can be used to estimate the damping, it is common to use every possible pair of points in the vicinity of a resonant frequency to calculate the damping, and so to construct a matrix of damping estimates. By plotting this matrix of damping estimates, the accuracy of the measurements, the accuracy of the estimate of ω_r and the linearity of the system being measured can be inferred. This is discussed further later in this section.

$$\gamma = \frac{\omega_a^2 - \omega_b^2}{2\omega_r \left(\omega_a \tan \frac{\theta_a}{2} + \omega_b \tan \frac{\theta_b}{2} \right)} \tag{7.7}$$

Using the accelerance calculated from the test results,the circle-fit method was used to estimate damping and natural frequency as follows:

- the accelerance spectrum was converted to the equivalent receptance spectrum by multiplying by $-\omega^2$, equivalent to integration twice in the time domain;
- a set of receptance values in the vicinity of the resonant peak was selected and plotted on the complex plane;
- a circle was fitted to the points on the complex plane (Bucher; 1991), and the point on the circle corresponding to resonance was estimated using a finite difference method;
- the damping was estimated using (7.7), with each frequency used to create the circle paired with every other frequency used to create the circle; and
- the resulting matrix of damping estimates was plotted.

A flat surface in the plot of damping estimates, corresponding to equal estimates of damping using each pair of frequencies, would indicate a system behaving linearly, measured with sufficient accuracy and a correct estimate of the natural frequency. The MATLAB script written to perform the circle fit method included the option to make fine alterations to the natural frequency estimate to look for a more consistent set of damping estimates.

Figure 7-7 shows the steps in the circle fit method for the response of connection A to pseudo-random excitation. It can be seen that the set of damping estimates forms an approximately flat surface, albeit with some systematic variation due to the nonlinearity in the system, the imperfect fit of the circle and any inaccuracy in the damping estimate. The average of the set of damping estimates is taken to be the measured damping.

If the system behaves in a more nonlinear way, then it is not possible to achieve a consistent set of damping estimates. This was the case for several of the tests carried out as part of this study, and so, for those tests, another approach was developed to estimate the natural frequency and damping, based on a theory of nonlinear vibration.

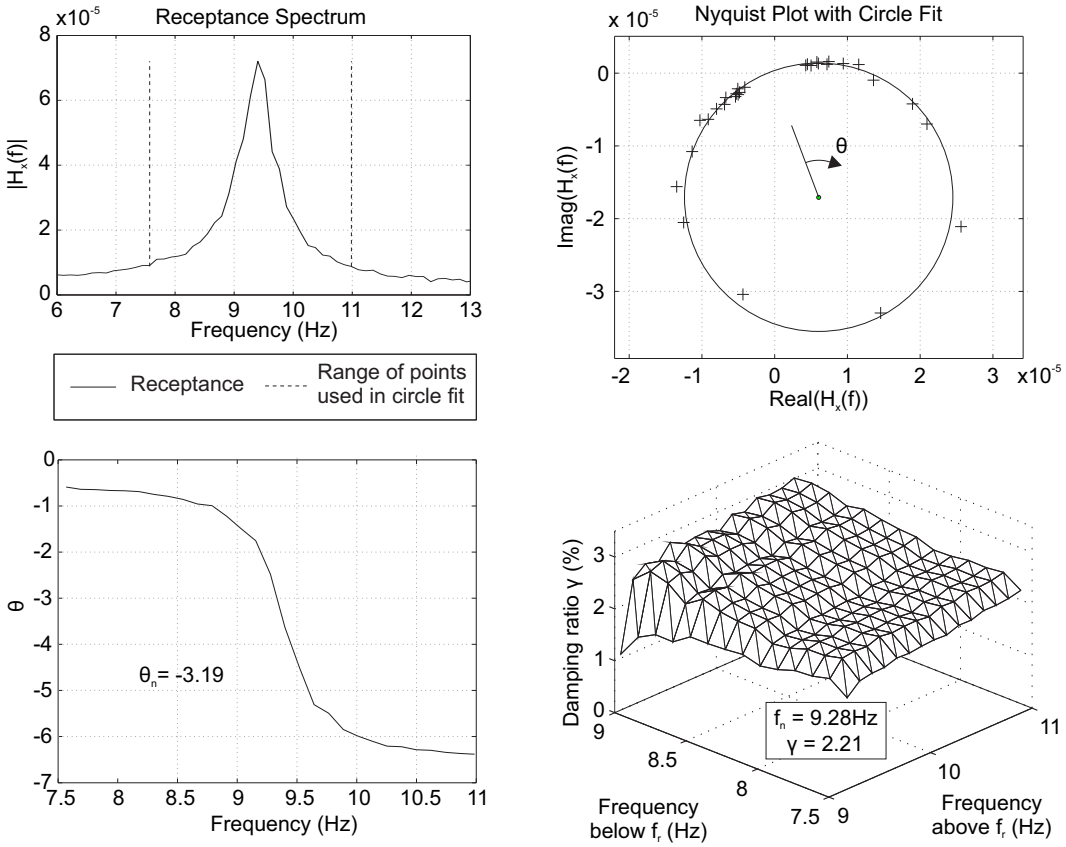

Figure 7-7: Estimates of damping γ and natural frequency f_n using the circle-fit method for connection A under pseudo-random excitation

7.2.2 Nonlinear vibration

It has been seen in the experimental results in Chapter 5 that, for an oscillating force with R=1.2, the force-displacement plot for embedment or for a single-dowel connection appears close to linear. As the amplitude of oscillating force is increased so that R=10, the force-displacement response is noticeably non-linear, and the nonlinearity led to a reduction in the secant stiffness.

In the forced-vibration tests on connections and frames described in this chapter, the applied force on the connection cannot be directly measured, so force-displacement plots cannot be drawn. The reduction in stiffness can be observed as a reduction in natural frequency, but the nonlinearity also has the effect of changing the measured accelerance of the system under harmonic excitation.

The effect of the nonlinearity in the system can be described using a method developed by Duffing (1918). Duffing carried out an extensive study into the equation given in (7.8), which describes the oscillation of a system with undamped natural frequency ω_n and viscous damping ratio γ, under a harmonic force f. The linear restoring force in Duffing's oscillator is generated by the natural frequency squared ω_n^2, equal to the linear stiffness per unit mass k/m, multiplied by the displacement x. There is also a component of the restoring force proportional to x^3, with constant of proportionality μ_3. This will be referred to as the cubic stiffness. Duffing's equation is therefore identical to the equation of motion for a single degree-of-freedom dynamic system, but with an additional cubic component in the restoring force.

$$\ddot{x} + 2\gamma\omega_n\dot{x} + \omega_n^2 x + \mu_3 x^3 = f \tag{7.8}$$

The cubic stiffness term represents a system whose secant stiffness changes with amplitude. A positive value of μ_3 represents a 'hardening' system, whose stiffness increases with amplitude, and a negative value represents a 'softening' system whose stiffness decreases.

Duffing (1918) solved this equation using the method of successive approximation. Given harmonic excitation, it was assumed that the response would also be harmonic, though not necessarily in the same phase. The forcing function is given by $f = F\cos(\omega t + \phi)$, and the response has the form $x = X\cos(\omega t)$.

The first approximation for x was therefore taken as in (7.9), with f rewritten as in (7.10). Substituting this into the equation of motion and rearranging gives (7.11).

$$x_0 = X\cos(\omega t) \tag{7.9}$$

$$f = F_1 \cos(\omega t) + F_2 sin(\omega t) \tag{7.10}$$

$$\begin{aligned}
\ddot{x}_0 &= 2\gamma\omega_n\omega X \sin(\omega t) - \omega_n^2 X \cos(\omega t) - \mu_3 X^3 \cos^3(\omega t) + F_1 \cos(\omega t) + F_2 \sin(\omega t) \\
&= 2\gamma\omega_n\omega X \sin(\omega t) - \omega_n^2 X \cos(\omega t) - \mu_3 X^3 \left(\frac{3}{4}\cos(\omega t) + \frac{1}{4}\cos(3\omega t)\right) \\
&\quad + F_1 \cos(\omega t) + F_2 \sin(\omega t)
\end{aligned} \tag{7.11}$$

In the method of successive approximation, (7.11) is integrated to give a second approximation, x_1, given in (7.12). Assume the steady state response to the forcing function, so that the constants of integration are zero.

$$\begin{aligned}
x_1 &= \iint \left(F_1 - \omega_n^2 X - \mu_3 X^3 \frac{3}{4}\right) \cos(\omega t) - \mu_3 X^3 \frac{1}{4} \cos(3\omega t) \\
&\quad + (F_2 + 2\gamma\omega_n\omega X) \sin(\omega t) \mathrm{d}t \\
&= -\left(F_1 - \omega_n^2 X - \mu_3 X^3 \frac{3}{4}\right) \frac{1}{\omega^2} \cos(\omega t) + \mu_3 X^3 \frac{1}{36\omega^2} \cos(3\omega t) \\
&\quad - \frac{F_2 + 2\gamma\omega_n\omega X}{\omega^2} \sin(\omega t)
\end{aligned} \tag{7.12}$$

The $\cos(3\omega t)$ term arises because of the cubic stiffness, and further iterations would suggest components of the response at higher amplitudes with smaller magnitudes. Based in this first approximation, though, (7.12) suggests a response dominated by the $\cos(\omega t)$ term, which justifies the assumed form of the response given in (7.9). Duffing (1918) proposed that if both x_0 and x_1 are approximations of the true response of the system, then the coefficients of $\cos(\omega t)$ and $\sin(\omega t)$ in each should be equal, so that an approximate solution to the equation of motion is given by equating the two, as in (7.13) and (7.14).

$$X = \frac{\omega_n^2}{\omega^2} X + \frac{3}{4\omega^2} \mu_3 X^3 - \frac{F_1}{\omega^2} \tag{7.13}$$

$$0 = F_2 + 2\gamma\omega_n\omega X \tag{7.14}$$

The magnitude of the forcing function F is given by $F^2 = F_1^2 + F_2^2$, so using (7.13) and (7.14), (7.15) can be written. For a given magnitude of the forcing function, damping and natural frequency, (7.15) becomes a cubic equation in X^2, which can be

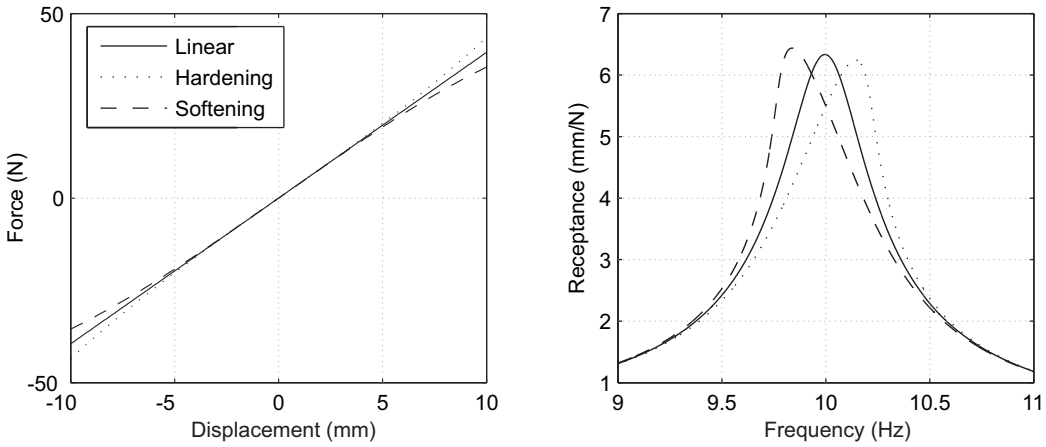

Figure 7-8: Receptance plots for Duffing oscillators with a linear natural frequency of 10Hz, mass of 1kg and a viscous damping ratio of 2%, under an oscillating load with magnitude 1N

solved for a range of frequencies to plot the transfer function for the theoretical system.

$$F^2 = \left(\frac{3}{4}\mu_3 X^3 + (\omega_n^2 - \omega^2)X\right)^2 + (2\gamma\omega_n\omega X)^2 \tag{7.15}$$

Figure 7-8 shows the receptance plots for linear, hardening and softening systems, calculated using (7.15). In each case, all the parameters are kept constant except μ_3, which was $4 \times 10^6 \mathrm{N/m^3}$ for the hardening system and $-4 \times 10^6 \mathrm{N/m^3}$ for the softening system. The effect of the cubic stiffness component on the receptance can be seen. In the softening system, the frequency for the peak response is lower than the linear system, and the magnitude of that peak response higher. The hardening system displays the opposite tendencies.

In the embedment and single-dowel connection tests, the stiffness was observed to decrease with an increasing amplitude of oscillating load. This corresponds to a negative value of μ_3 in Duffing's method.

As shown in Figure 7-9, the gradient of the centreline measured in the embedment tests does not reduce in gradient symmetrically either side of the centre of the oscillating force, as is modelled by the $kx + \mu_3 x^3$, with negative μ_3, in Duffing's equation. The behaviour is, in fact, asymmetrical around the centre of oscillation, with the gradient increasing throughout the upward stroke of the cycle, though at a reducing rate. This asymmetry can be approximated by introducing an $\eta_2 x^2$ term into Duffing's equation (7.16).

$$\ddot{x} + 2\gamma\omega_n\dot{x} + \omega_n^2 x + \eta_2 x^2 + \mu_3 x^3 = f \tag{7.16}$$

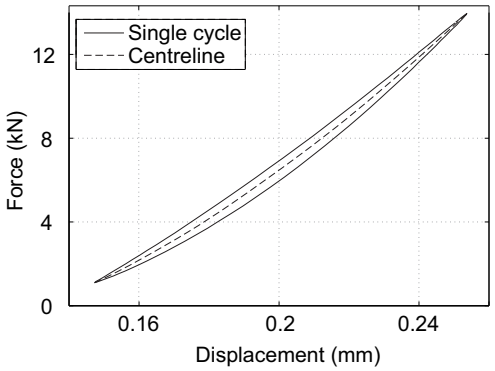

Figure 7-9: The centreline of the force-displacement diagram for a Douglas fir embedment specimen loaded parallel-to-grain to 40% of its predicted yield load with $R = 10$

The effect of the $\eta_2 x^2$ term is to introduce a term in $\cos(2\omega t)$ into the second approximation of the displacement, x_1, as in (7.17). Thus the response at the natural frequency is unaffected, but a further harmonic is introduced by the quadratic stiffness at double the natural frequency.

$$\begin{aligned} x_1 = -\left(F_1 - \omega_n^2 X - \mu_3 X^3 \frac{3}{4}\right) \frac{1}{\omega^2} \cos(\omega t) + \eta_2 X^2 \frac{1}{8\omega^2} \cos(2\omega t) \\ + \mu_3 X^3 \frac{1}{36\omega^2} \cos(3\omega t) - \frac{F_2 + 2\gamma\omega_n\omega X}{\omega^2} \sin(\omega t) \end{aligned} \tag{7.17}$$

Ewins (1986) investigated the effect of cubic stiffness behaviour on the use of the circle-fit method, described in Section 7.2.1, for estimation of natural frequency and damping by using a signal generator to replicate the response of a system with cubic stiffness. He showed that the linearisation inherent in the analysis technique for pseudo-random excitation meant that, for that form of excitation, plotting the matrix of damping estimates still resulted in a flat surface, allowing a damping estimate to be made. In contrast, plotting the matrix of damping estimates resulting from the circle fit of a slow sine sweep test showed a systematic variation of damping, so that a reliable damping estimate could not be made. In this study, therefore, a curve-fitting approach is used to extract modal properties from the measured accelerance, described in Section 7.4.1.

7.3 Theoretical prediction

The stress function model for embedment, presented in Chapter 6, along with a beam-on-elastic-foundation model to allow for the elasticity of the connector, was shown to

predict the stiffness of a single-dowel connection under small-amplitude oscillating load. An increase in amplitude of load resulted in nonlinear behaviour not predicted by the model.

In the structures tested in this chapter, each connection has multiple connectors, loaded at varying angles to the grain and the connections form part of a larger structure. The method was therefore extended to allow for each of these features, by using conventional approaches from timber engineering.

7.3.1 Dowel groups and angle to grain

The stress function approach developed in Chapter 6 was shown to be suitable for estimation of the stiffness due to a single connector loaded either parallel or perpendicular to grain. In this study, where the load is applied neither parallel nor perpendicular to the grain, the calculated stiffness for each case is interpolated using the equation by Hankinson (1921). As discussed in Section 2.2.5, this equation is considered to be a sensible choice for an initial estimate of the effect of angle to grain on stiffness, since it has been widely used to estimate the variation of strength, and has been shown by Schniewind and Barrett (1972) to apply to creep. The true variation of stiffness with angle to grain, however, should be a subject for further analytical and experimental study.

The behaviour of a group of dowels in a moment connection was discussed in Section 2.2.3, with particular reference to work by Noguchi and Komatsu (2004), which suggested that, in order to correctly model an asymmetrical arrangement of dowels in a moment connection, the force in each dowel cannot simply be assumed to be proportional to its distance from the centre of rotation. Instead, Noguchi and Komatsu (2004) presented a design method based on Saint-Venant torsion theory. The basis of Noguchi and Komatsu's calculation was different to that used in this study, in that their calculation was based on a single foundation modulus, independent of the distance of the connector in question from the centre of rotation.

In this study, it has been shown that the dependency of the foundation modulus on the distance of the dowel from the centre of rotation can be modelled. By incorporating that dependency according to the stress-function model from Chapter 6, and the effect of grain orientation on the foundation modulus, the fundamental assertion of Noguchi and Komatsu's work, that the force in each dowel is not, in general, proportional to its distance from the centre of rotation, is considered to be satisfied. The displacement of each dowel relative to the centre of rotation is assumed to be proportional to its distance from the centre of rotation, but the difference in foundation modulus, and therefore in the stiffness of each dowel, ensures that the forces vary. For the purpose

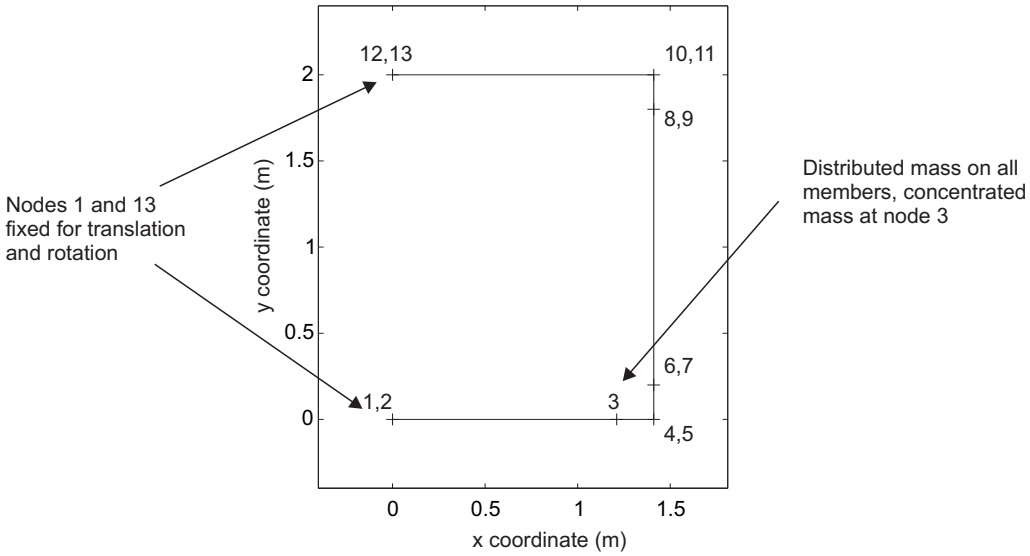

Figure 7-10: Geometry of the frame and node numbering for the stiffness matrix model

of this study, therefore, the conventional equation for the stiffness K_r of a moment connection with n connectors given, for example, by Porteous and Kermani (2007), is modified to allow for the different stiffness in different connectors to give (7.18), where K_{bf} is the stiffness for each connector and l the distance of each connector from the centre of rotation.

$$K_r = \sum_{i=1}^{n} K_{bf,i} l_i^2 \tag{7.18}$$

7.3.2 Stiffness matrix models

The dynamic response of the frame was modelled using the stiffness matrix method. The analysis was therefore purely elastic, but could be used to incorporate the effect of the rotational and translational movement in the connections. It was considered that the cyclic stiffness, measured in Chapter 5, of individual dowels under load with R=1.2 could be adequately represented by a lightly-damped linear-elastic model. An elastic frame with semi-rigid connections was therefore considered appropriate to predict the stiffness properties of the frame, as long as the amplitude of vibration was sufficiently small.

A stiffness matrix was generated for the frame using MATLAB. The geometry and node numbering is shown in Figure 7-10, and the properties of the nodes and the members or connections between them are given in Table 7.2.

Table 7.2: Properties of nodes and members in the stiffness-matrix model for the frame structure

Node	Location	Connection
1	Fixed to wall	
		6-dowel connection
2	On beam	
		200mm by 185mm timber beam
3	On beam	
		200mm by 185mm timber beam
4	On beam	
		4-dowel connection
5	On plate	
		160mm by 6mm steel plate
6	On plate	
		4-dowel connection
7	On beam	
		200mm by 185mm timber beam
8	On beam	
		4-dowel connection
9	On plate	
		160mm by 6mm steel plate
10	On plate	
		4-dowel connection
11	On beam	
		200mm by 185mm timber beam
12	On beam	
		6-dowel connection
13	Fixed to wall	

The dowel-type connections are represented by placing two nodes at the same location, corresponding to the centroid of the connection, and defining the stiffness between them based on the linear and rotational stiffness of the connection. The stiffness of each individual connector was estimated using the complex stress function approach for a dowel through a complete hole described in Section 6.1.2, and the stiffness of each complete connection estimated based on each connector resisting a force in proportion to its distance from the centroid of the connection, thus following the method given by Porteous and Kermani (2007).

In a complete structure with many connections, not all of them would be expected to be highly loaded simultaneously under in-service conditions. In this frame, the applied loads were chosen so that the most loaded connection, the 6-dowel lower connection to the strong wall, would be subject to a peak load of 20% of its predicted failure load for vibration with R=1.2. The upper connection to the strong wall is subject to a peak load of 19% of its predicted failure load in the same condition. The 4-dowel connections between the timber members, however are only loaded to 10% of their predicted failure load in that case. This ratio of applied load to capacity is considered to be a reasonable representation of the loads that a structure would be expected to experience in service.

One of the reasons that it was decided to carry out the stiffness matrix analysis in MATLAB, rather than with proprietary software for the purpose, was to have control over the semi-rigid connection stiffness, and to be able to apply translational as well as rotational stiffness of connections. Another reason was that by using MATLAB, the stiffness matrix could be accessed and manipulated to obtain more information about the behaviour of the structure, such as the distribution of stored energy.

The distribution of stored energy can be used to estimate the damping ratio in the structure. In a similar way that the stiffness in each element is combined to assess the stiffness of the complete frame, the energy dissipation in the complete frame as it vibrates consists of a combination of the energy dissipation in each element. The total energy dissipation is taken to be the sum of the energy dissipation in each element.

The energy dissipation in each element is then related to the damping ratio, which describes the proportion of the elastic stored energy that is dissipated in each cycle. In this work, for consistency and to follow the convention most commonly used in structural dynamics, the equivalent viscous damping ratio has been used throughout. The equivalent viscous damping ratio γ is given by (7.19), where E_d is the dissipated energy per cycle and W is the energy continually alternating between the kinetic form, as the movement of the mass, and the potential form, as the elastic stored energy in the frame.

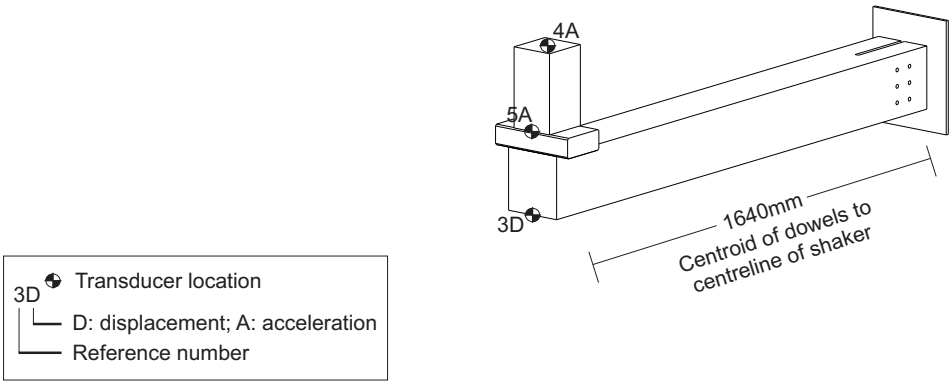

Figure 7-11: Transducer and shaker locations on the cantilever joint structure

$$\gamma = \frac{E_d}{2\pi W} \tag{7.19}$$

Given the damping ratio of an element, therefore, the energy dissipated can only be calculated if the magnitude of the elastic stored energy, otherwise known as the work done on the element, is known. Assuming linear-elastic behaviour, the work done on each part of the system can be readily calculated from the matrices of stiffness, $\mathbf{K}$, and displacement, $\mathbf{X}$, in the stiffness-matrix analysis of the frame.

$$W = \frac{1}{2}\mathbf{X}^T\mathbf{K}\mathbf{X} \tag{7.20}$$

7.4 Results and discussion

7.4.1 Cantilever beams

The location of the transducers on the cantilever joint structure and their numbering system are shown in Figure 7-11. The displacement transducer was used to measure the deformation under the static load applied for 16 hours before testing, and as a check for the readings from the accelerometer mounted at location 5 on the steel block. The accelerometer at location 4 measured the movement of the armature of the shaker to calculate the input force.

The capacity of the connection was calculated according to Eurocode 5 (BSI; 2009a), using the density of the timber measured using the weight and volume of the beam. For the six-dowel connections, the applied static loads resulted in a force per shear plane of 2.34kN in the highest-loaded connector, which was found to be equivalent to 18% of the capacity of the connection according to Eurocode 5. The static load applied to the two-dowel connection was equivalent to 39% of the capacity.

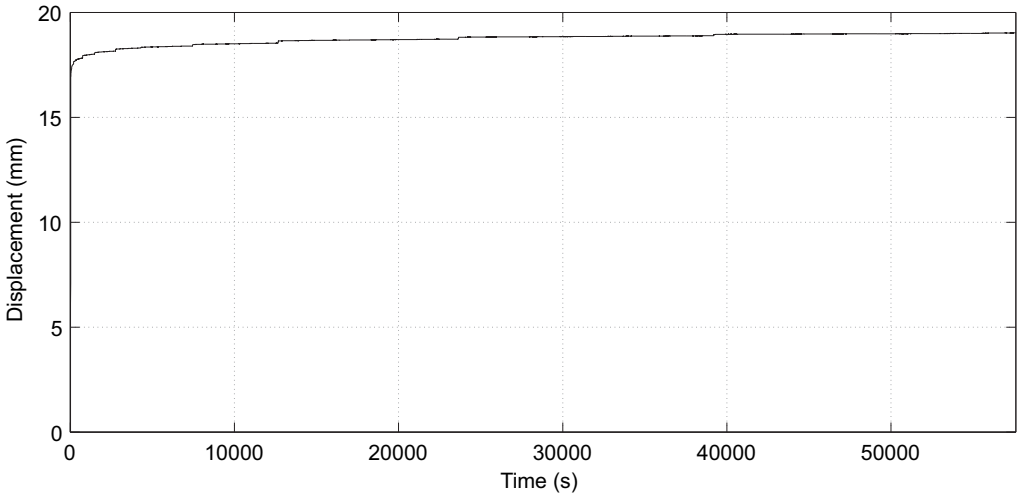

Figure 7-12: Deflection of cantilever beam A under its self weight and an imposed load of 657N at its end over a 16-hour period

The first part of the test process was to apply a static load to the connection for a period to eliminate part of the expected transient behaviour. For the six-dowel connections, the load was applied for 16 hours, and for the two-dowel connections, since the same dowels had already been subject to the 16-hour loading, 15 minutes. The dynamic tests were then carried out over an extended period of time after preloading, which included leaving the static load in place overnight between dynamic tests. The displacement of connection A6 during 16 hours under the static load of its self-weight, the weight of the shaker and that of the steel block is shown in Figure 7-12. The deformation was measured at the tip of the cantilever at location 3 in Figure 7-11.

It can be seen in Figure 7-12 that the immediate deformation forms a large part of the total deformation of the connection. The bending and shear deformation of the timber cantilever beam was calculated to represent less than 1mm of deflection at the tip, and so less than 5% of the total measured deflection. The remainder was due to the rotation and vertical movement in the connection. The deformation can be seen to follow a curve indicative of viscoelastic behaviour under constant load, with the addition of several rapid steps in displacement, of the order of 0.1mm at the tip of the beam. When one of these steps occurred, there was an audible creak, which was thought to be a sign of frictional slip.

A possible explanation for these steps in displacement is that, due to the unintentional misalignment of the holes in the timber and the steel plate, the contact force between the dowel and the steel plate is asymmetrical, with the force transferred at a point of contact which is not at the apex of the hole in the plate, as shown in Figure

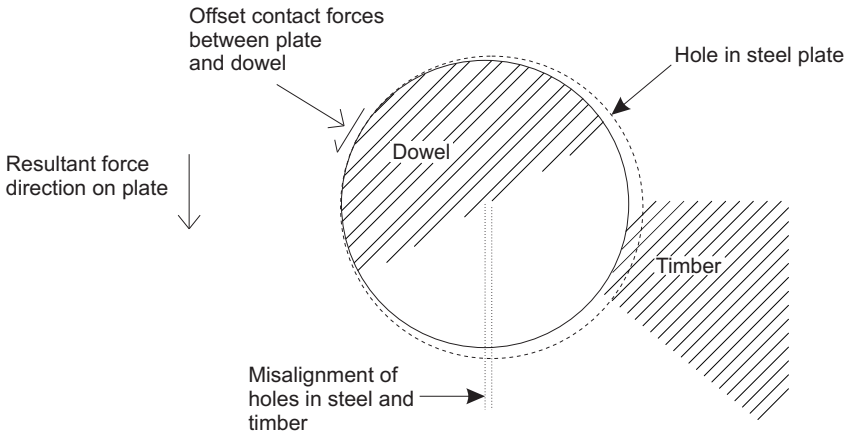

Figure 7-13: The affect of misalignment of the hole in the steel flitch plate with the dowel on force transfer

7-13. This position is unstable, in that as the timber deforms, the dowel can move closer to the apex of the hole, perhaps as a rapid slip as the stress relaxation in the timber reduces friction forces supporting the asymmetrical load. This behaviour would be extremely difficult to predict, since it results from inaccuracies in construction, but with time under load, as creep occurs in the timber, each dowel would be expected to slip towards the stable state in which the dowel was loaded at the apex of the hole.

After the time under static loading was complete, dynamic loads were applied using the shaker, which had been attached to the beam forming part of the static load. The displacement measured at location 3 in Figure 7-11 was observed during each test, and a further step in displacement was occasionally observed under dynamic load. If this occurred, it generally had a subsequent effect on the resonant frequency, due to the change in stiffness, and so the series of dynamic tests was restarted. The results presented here, therefore, are for a series of tests for which the final static displacement was not significantly different from the initial resting displacement, and this set of results is considered to be representative of the steady-state behaviour of the system.

7.4.1.1 Six-dowel connections

First, the analysis of the results of the six-dowel connection tests, on connections A6 and B6, will be presented and discussed, since they were carried out first, and it was on the basis of these results that the procedures for analysis of nonlinear vibration were developed. For the slow sine sweep tests, the modal properties were estimated by curve fitting the receptance for the fundamental mode of vibration using the theoretical receptance function, from Section 7.2.2, for a system with cubic nonlinearity. The curve fitting was carried out using the MATLAB function *fminsearch* to minimize the sum

Table 7.3: Modal mass of the fundamental mode of vibration of the cantilever beam, calculated using the circle-fit method on the pseudo-random vibration response of cantilever B6

Test	Root Mean Square Amplitude (N)	Estimated Modal Mass (kg)
BN0.5	8.9	78.3
BN0.75	13.2	77.1
BN1	17.6	82.3

of the square of the difference between the experimental and theoretical curves at each point.

The curve-fitting procedure allows estimation of the natural frequency, the linear stiffness component, the cubic stiffness component and the damping in the system. For the pseudo-random excitation, the same parameters could be identified using the circle-fit method, described in Section 7.2.1, with the exception of the cubic stiffness component, since the linearlization inherent in the use of auto- and cross-correlation functions used to generate the measured receptance function resulted in a symmetrical receptance plot.

The known variable was the modal mass of the system, calculated by the application of the circle-fit method to the pseudo-random vibration test results for connection B6. Since the connections were at either end of the same beam, the modal mass was expected to be very similar for connection A6. The modal mass calculated from each of the three pseudo-random vibration tests is given in Table 7.3, and the mean value, 79kg, was used for curve fitting.

The three unknown variables, the damping and the linear and cubic components of the stiffness, were then obtained by fitting a receptance function for a system with cubic stiffness to the measured receptance.

The cubic nonlinearity was chosen because of its mathematical convenience, and because the receptance function for cubic nonlinearity had been defined by Duffing (1918). The extent to which the stiffness reduced with amplitude was not expected to be precisely represented by a cubic function, since the use of the cubic function had no basis in the behaviour of the connection. As a result, the cubic-stiffness receptance function could not be expected to precisely fit the measured behaviour of the connection at all amplitudes. It was therefore decided to fit the function to the measured response in the near vicinity of resonance, since it is in that region that the majority of the response occurs.

A range of measured points either side of the peak response were used for curve

fitting. For consistency across the tests, the range was expressed in terms of the magnitude of the response: the curve fitting encompassed all the points with a magnitude greater than a given proportion of the peak value. A brief sensitivity analysis was carried out to investigate the influence of the chosen value of that proportion on the fitted values of stiffness and damping.

Figure 7-14 shows curves fitted to the measured receptance of a slow sine sweep test on connection A6 using different ranges of points. It can be seen that if too wide a range of points is used for the curve fitting, the cubic function does not fit the behaviour at high and low amplitudes closely enough, resulting in a poor representation of the measured receptance, as in the lower plot in Figure 7-14, where all receptance measurements higher than a quarter of the peak value were used to fit the curve.

The values of the parameters estimated by the curve-fitting process are noted in Figure 7-14. The natural frequency of the linear system is the frequency towards which the system would be expected to tend as the amplitude of vibration reduces, and the contribution of the cubic component of stiffness becomes negligible. This corresponds, according to the interpretation of the models and results in Section 6.4, to the linear elastic stiffness of the connection in which the contact there is a rigid contact surface between dowel and timber. The cubic stiffness represents the reduction in stiffness as the amplitude of vibration increases. The damping ratio was observed to be relatively insensitive to the change in the points used for curve fitting, which gave confidence that a reasonable estimate of modal damping could be achieved this way.

The upper plot in Figure 7-14 shows a much closer fit of the measured receptance over a smaller range of values. It was considered, however, that the middle plot in Figure 7-14 provided a suitable balance between including sufficient measured data to accurately represent the measured behaviour in the fitted model, and allowing for the fact that cubic function could only be expected to represent the real behaviour over a limited range of amplitudes. In fitting the receptance function for cubic stiffness to the measured data from the slow sine sweep tests, therefore, a range of data was used incorporating all the points with a receptance greater than half the peak value.

Figure 7-15 shows the variation of the underlying linear natural frequency, cubic stiffness and damping as the amplitude of the applied cyclic force increased. The upper plot in Figure 7-15 shows that the natural frequency of the elastic system is similar for the two connections. Both show a slight reduction as the excitation amplitude is increased. This reduction is more prominent in connection A6. In a system with cubic stiffness, this frequency would be expected to remain constant as the excitation increased, with the reduction in the frequency of the peak response accounted for by the cubic component. The fact that the 'softening' in the system is not perfectly represented

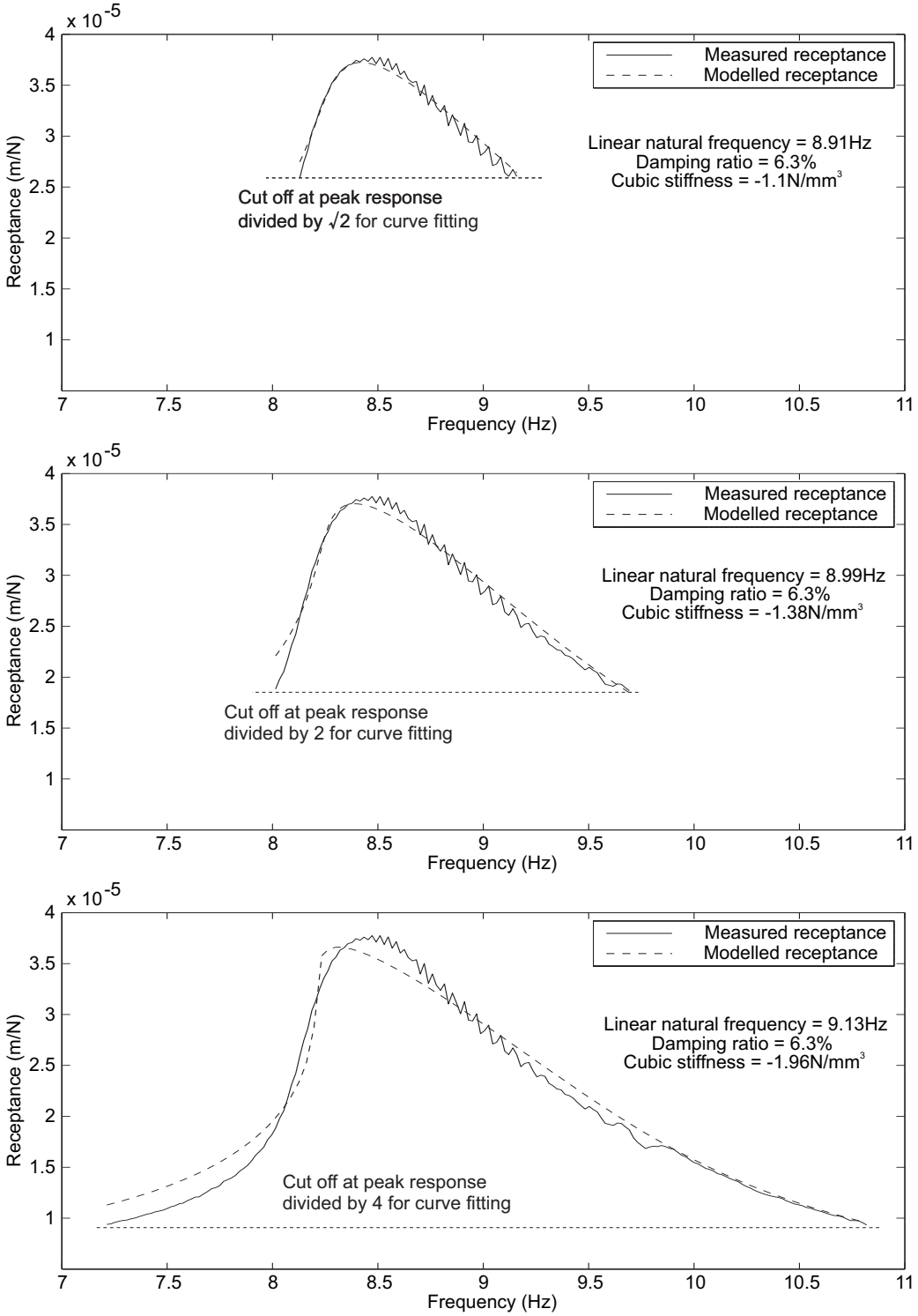

Figure 7-14: Curves fitted using the receptance function for cubic stiffness to receptance data measured in a slow sine sweep test of a cantilever beam

by the cubic function is indicated by the different natural frequencies estimated using the different amplitudes of vibration.

The shortcomings of the cubic stiffness model are further identified in the lower plot, which shows that the cubic stiffness component calculated at each amplitude is different. The plot does, however, give an impression of the magnitude of the nonlinearity in each connection, and shows that the receptance of connection B6 is far closer to that for a system with linear stiffness than the receptance of connection A6.

The middle plot in Figure 7-15 shows the damping calculated at each amplitude using the cubic-stiffness curve fit. It can be seen that the damping in connection A6 is approximately double that in connection B6. Figure 7-15 is suggestive, therefore, of a pair of connections with similar linear components of stiffness, but of one connection exhibiting a much more prevalent reduction in stiffness with amplitude of applied force, and a much higher energy dissipation.

The receptance plots, and the calculations of natural frequency and damping calculated from them were, therefore, compared between each of the connections tested and each of the amplitudes of excitation in each test. The magnitude of the vibration in each test can be classified either by the magnitude of the input force from the shaker, as above, or by the magnitude of the output displacement or acceleration. Since each connection has, in general, a different receptance, these classifications will affect the way tests on different connections are compared.

The force applied to each connector in the vibrating system depends both on the input force from the shaker and the inertial force on the vibrating mass. At resonance, the inertial force is far higher than the shaker force, as the shaker adds more energy to the system with each cycle. It is therefore considered that the amplitude of the output displacement or vibration gives an indication of the force applied to the connection.

The measured acceleration can be used for an additional comparison with the experimental work described in Chapter 5, since a 1g vertical acceleration of the concentrated mass on the end of the cantilever represents an inertial force equal to the static weight of the mass. If the magnitude of the oscillating acceleration is 1g, therefore, the force applied to the connection oscillates between twice the static value and zero. This is equivalent to an R-ratio of ∞. The magnitude of the oscillating acceleration A can, in general, be expressed as an R-ratio using (7.21).

$$R \approx \frac{g + A}{g - A} \tag{7.21}$$

It should be noted that, although the static force is approximately 20% of the yield force in the connection, this is the mean value of the oscillating force, and so differs

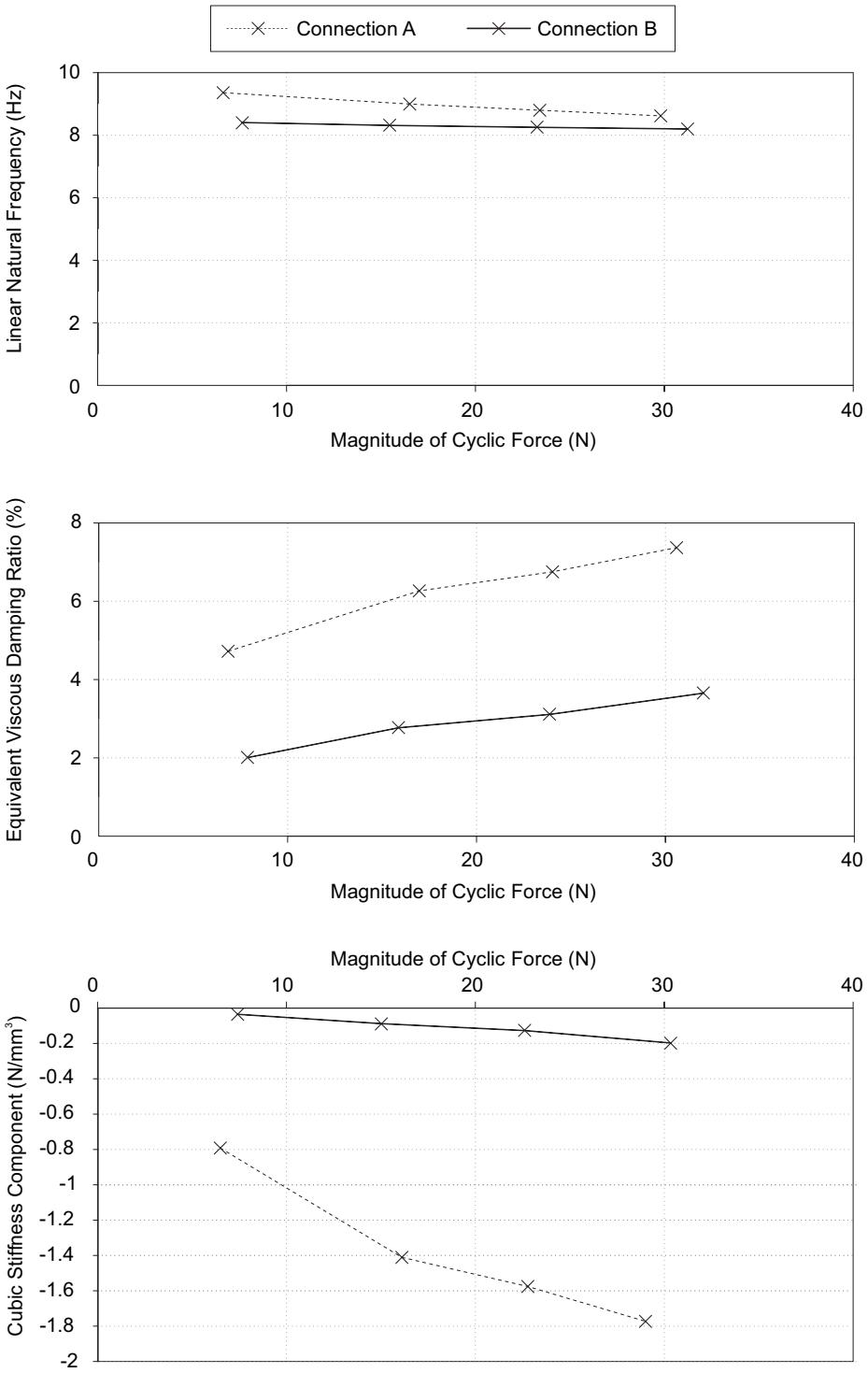

Figure 7-15: Variation of linear stiffness, cubic stiffness and damping with the magnitude of the applied cyclic force

from the oscillating force applied in Chapter 5, which used a peak force of 20% of the yield force.

The R-ratio of the loads experienced by the connections in the slow sine sweep tests on the cantilever beams ranged from 1.2 to 1.8 for connection A6 and 1.8 to 3.8 for connection B6. The primary reason the connections experienced cyclic load of different R-values, despite the cantilever being subject to the same cyclic applied force, was the higher damping in connection A6, which resulted in a far lower amplitude of vibration at resonance. The embedment and single-dowel connection tests would suggest that a higher R-ratio results in a greater reduction in stiffness and a higher energy dissipation. This pattern is followed by each individual connection under increased loading, but does not explain the difference between the response of the two connections.

The most likely cause of the additional energy dissipation in connection A6 is considered to be the tightness of fit of the steel plate into the slot. In connection B6, the beam slid freely on and off the steel plate, with a clear gap between the timber and steel. The connections at end A, in contrast, fitted snugly around the steel plate. The force required to pull it off the steel plate was measured after the dynamic tests as having a peak value of 0.16kN. This frictional resistance is thought to have contributed significantly to the more nonlinear stiffness, and higher energy dissipation in connection A6.

Other processes may also contribute to the additional energy dissipation. Imperfections in the contact surface between dowel and timber could produce additional energy dissipation, and may be responsible for the nonlinear component of stiffness, as discussed in Section 6.6.3. Any misalignment of the dowel and the hole in the steel plate, as shown in Figure 7-13, could lead to an increase in energy dissipation by frictional slip, since the tangential component of the contact force between the dowel and the steel plate, and the dowel and the timber, would be increased.

It was primarily the much higher damping in connection A6 which resulted in its lower amplitude of vibration, and so it is important to note the profound effect of the subtle difference in the structure, the snug fit of the steel plate into the slot in the timber beam, on its response to vibration at this amplitude. This difference would not be expected to have any significant effect on the strength of the connection, or even its response under large-amplitude vibration, but under vibration representative of in-service conditions, the forces and movements involved were sufficiently small that the force and energy dissipation generated by this friction reduced the magnitude of the receptance by approximately 50%.

Table 7.4: Modal properties of two-dowel connections by pseudo-random (P-R) and slow sine sweep excitation, RMS stands for root mean square

Connection	Test	Excitation	RMS force (N)	R-ratio at resonance	Natural frequency Hz	Equivalent viscous damping (% of critical)
A2a	A2aS0_25	Sweep	10.53	1.65	11.11	7.07
	A2aS0_5	Sweep	21.28	2.22	10.78	9.00
A2b	A2b0_25	Sweep	10.65	1.67	10.66	7.08
	A2b0_5	Sweep	21.48	2.40	10.18	8.49
B2a	B2aN0_25	P-R	4.48	-	8.55	6.39
	B2aS0_25	Sweep	10.73	2.14	8.38	5.11
	B2aS0_5	Sweep	22.12	3.53	8.00	6.07
B2b	B2bN0_25	P-R	4.43	-	8.67	2.40
	B2bS0_25	Sweep	10.89	2.27	8.62	4.40

7.4.1.2 Two-dowel connections

The same analysis can be applied to the two-dowel connections. Since they have a lower tip mass, the same applied force results in a higher R-ratio. As a result, the behaviour of the two-dowel connections was more non-linear. Table 7.4 shows the results of the pseudo-random and slow sine sweep tests carried out on the two-dowel connections.

There were several tests from which modal parameters were not successfully extracted. Pseudo-random excitation, for example, was applied at two amplitudes to each connection, but for connection A2a and A2b, the damping matrix did not form a level surface with superimposed noise, as in Figure 7-20. Instead, there was a systematic variation of damping with the frequencies chosen for damping estimation. This meant that no damping estimate could be made, and so the estimate of the natural frequency could not be verified. This was thought to be a consequence of the increased nonlinearity in the structure at higher amplitudes, meaning that the linearisation inherent in the modal analysis for pseudo-random vibration was no longer applicable.

The difference in the response of connections A and B is again noticeable in the two-dowel connection tests. Connections A2a and A2b again have the higher stiffness and damping ratio, which further suggests that the tightness of fit of the steel plate into the slot at that end of the beam contributes significantly to stiffness and damping.

7.4.2 Frames

The location of the transducers on each frame structure and their numbering system are shown in Figure 7-16. The results from the displacement transducers 3 and 4 could be compared with those of accelerometers 9 and 10 as a check, while the other transducers measured movement in other parts of the structure. Since the imposed mass was concentrated at one point on the structure, and was large compared with the self-weight of the structure, it was expected that the response in the vertical direction would be dominated by one mode of vibration. The data from the transducers around the structure therefore served not to distinguish between different modes of vibration, but to verify that the dominant mode did excite all parts of the structure as expected.

A receptance spectrum for each frame is shown in Figure 7-17, based on the acceleration measured by accelerometer 9 for frame A and accelerometer 10 for frame B. Both are calculated from slow sine sweep excitation where the magnitude of the applied force was approximately 28N across the frequency range.

Figure 7-18 shows the spectra of acceleration for the two frames, covering frequencies up to 50Hz. The greatest response, by several orders of magnitude, is in the range of excitation, between 6 and 12Hz. The logarithmic vertical scale, however, enables some features of the response to be seen at higher frequencies: frame A shows a small response at 20Hz, 28Hz and 35Hz and frame B has a small response at approximately 17Hz and approximately 26Hz. These additional components of the spectrum correspond to the responses at 2 and 3 times the natural frequency predicted by the nonlinear stiffness model described in Section 7.2.2. The component at 3 times the natural frequency corresponds to the cubic stiffness component, and the component at 2 times the natural frequency to the quadratic stiffness component frame B. This observation supports the hypothesis that the asymmetry of the receptance plot is due to softening behaviour, i.e. a reduction in stiffness with amplitude of displacement.

Figure 7-19 shows four receptance spectra at increasing amplitudes of applied force, measured using the slow sine sweep and pseudo-random excitation. The spectra measured using pseudo-random excitation were smoothed by 3-point averaging for clarity, though it should be noted that the receptance was not smoothed for estimation of natural frequency and damping, since the smoothing would introduce a phase lag into the spectrum, which would result in an artificial increase in damping.

Both graphs show the tendency for the frequency of the peak response to reduce with amplitude. This suggests a reduction in the stiffness of the system with increasing amplitude of applied force. The reduction in stiffness would also lead to an increase in the magnitude of the receptance if the damping remained constant, but the increase in damping with amplitude can be seen to outweigh the reduction in stiffness, reducing

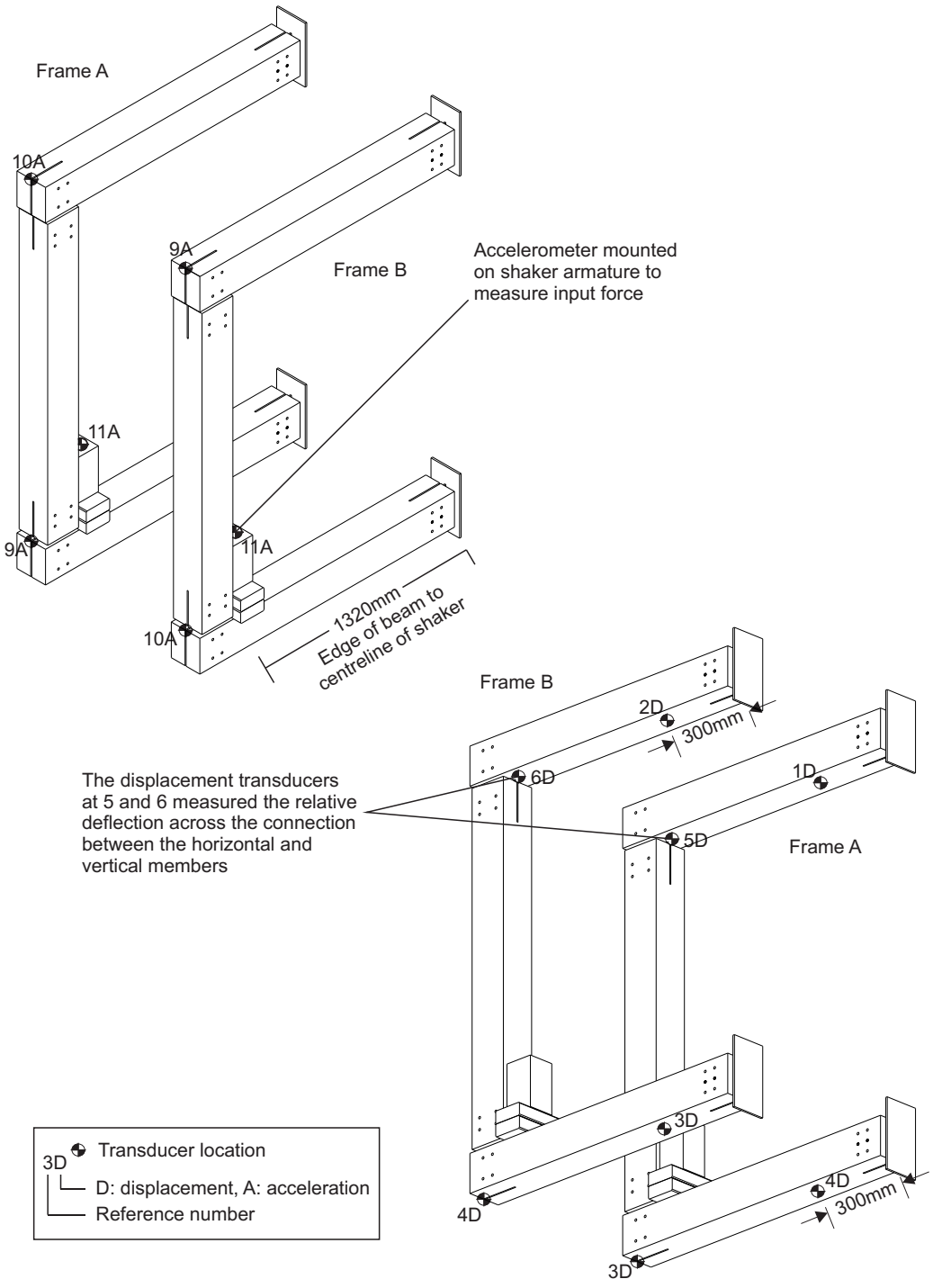

Figure 7-16: Both test frames showing transducer and shaker locations

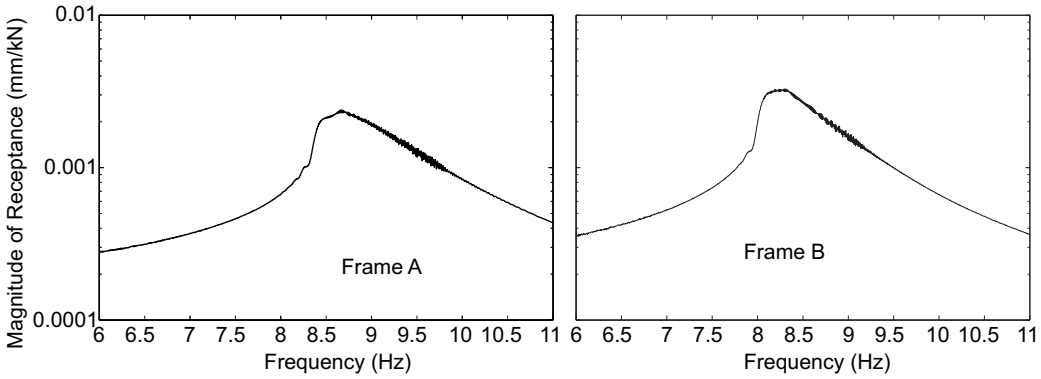

Figure 7-17: Receptance spectra for each frame measured by the accelerometers at points 9 and 10 in Figure 7-16

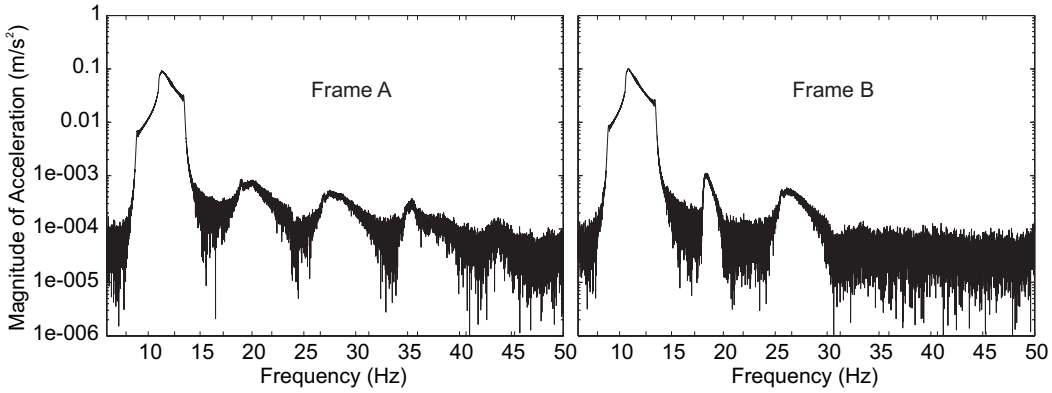

Figure 7-18: Fourier transform of acceleration for each frame for slow sine sweep excitation

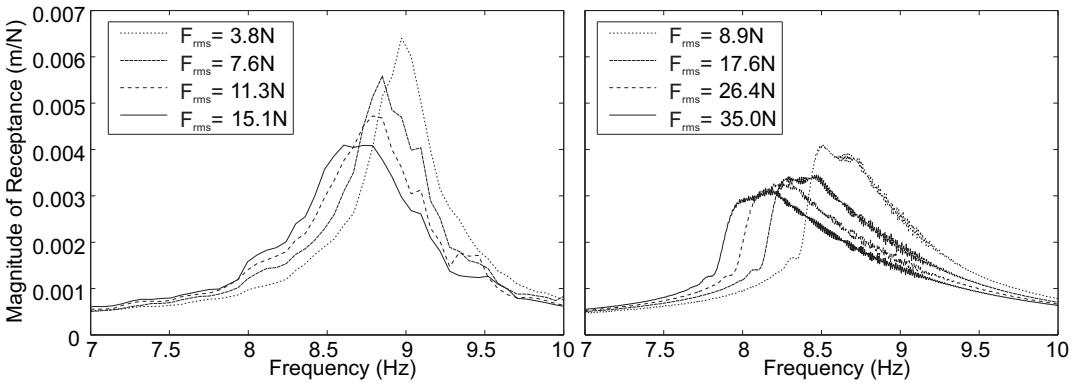

Figure 7-19: Receptance spectra for frame B measured by the accelerometer at point 10 in Figure 7-16, showing the variation of receptance with amplitude of applied force - the left hand graph is for pseudo-random excitation and the right hand graph for slow sine sweep

the magnitude of the receptance. It should be noted that the fact that the receptance reduced with amplitude of applied force did not mean that the amplitude of vibration reduced, merely that it did not increase in proportion with the applied force.

The results of modal analysis of the frame system therefore corresponded qualitatively to the single dowel connection tests, in that stiffness was observed to reduce with increasing amplitude of applied force, with a simultaneous increase in damping.

In the same way as for the cantilever beam specimens, the circle-fit method could be used to estimate the natural frequency and damping in each of the tests with pseudo-random excitation. Figure 7-20 shows the process. The noise in the receptance, calculated according to the method in Section 7.2.1, is thought to be due to the nonlinearity in the frame, rather than an inadequate averaging time. Since the pseudo-random excitation continually causes the structure to vibrate at a range of amplitudes, the receptance of the system will continually change, which may explain the unevenness of the calculated receptance. Despite this noise, a reasonably consistent range of damping estimates can be made, as shown in **d** in Figure 7-20, with the exception of the values very close to the natural frequency, where the noise has a disproportionate effect on the estimate. This suggests that the natural frequency estimate is accurate, and gives a reliable estimate of the damping in the frame.

The slow sine sweep, pseudo-random and impulse excitation methods covered a range of amplitudes of applied force, and therefore of acceleration in the structure. Table 7.5 combines the results from the three forms of excitation, for the tests in which it was possible to extract modal parameters.

Pseudo-random excitation was applied at four amplitudes for each frame, but, as

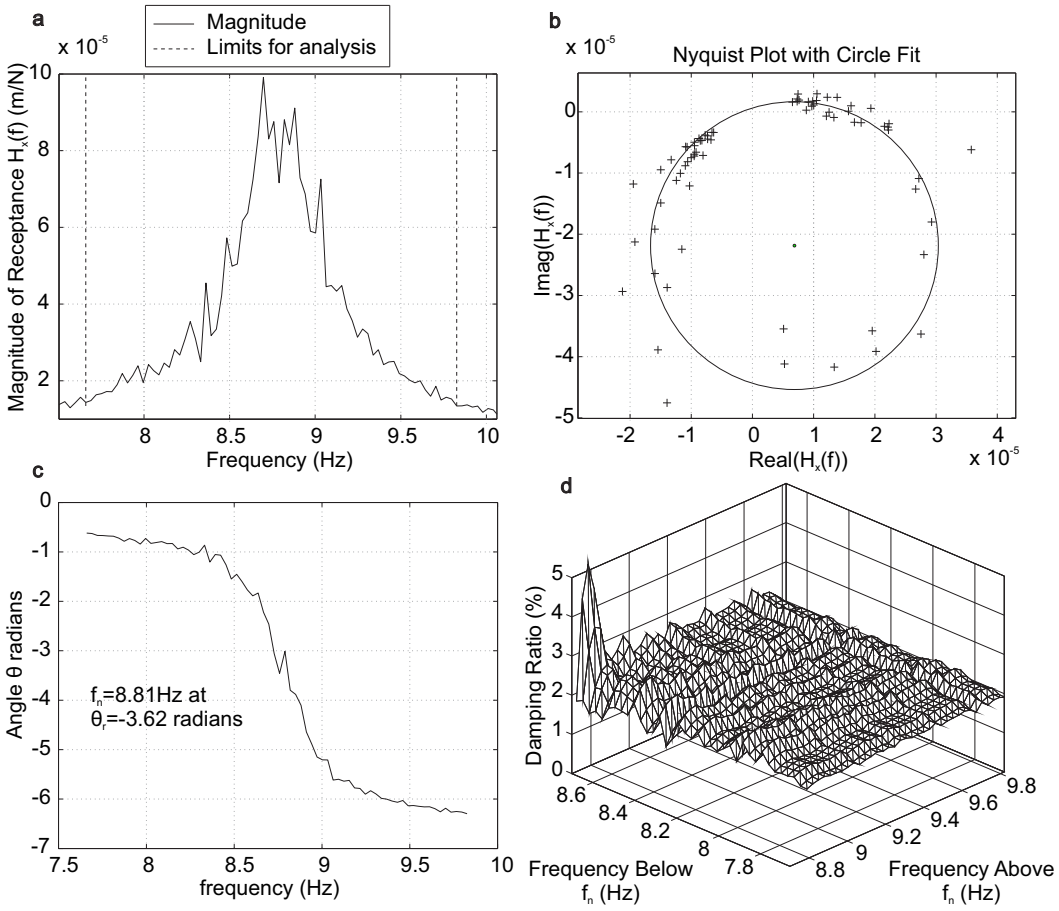

Figure 7-20: Modal analysis of frame B, under pseudo-random excitation, by the circle-fit method, using the input force calculated using the accelerometer at point 11 and the acceleration measured at point 9: **a** shows the receptance, **b** the circle-fit to that receptance data, **c** the variation of angle around the circle with frequency and the resulting estimate of natural frequency and **d** the plot of damping estimates using that natural frequency

Table 7.5: Modal properties of frames by impulse, pseudo-random (P-R) and slow-sine-sweep excitation, RMS stands for root mean square

	Test	Excitation	RMS force (N)	R-ratio at resonance	Natural frequency (Hz)	Equivalent viscous damping (% of critical)
Frame A	AI3	Impulse	2.2	-	10.0	0.5
	AN0_5a	P-R	3.8	-	9.4	2.1
	AN1	P-R	7.6	-	9.2	2.4
	AS0_25a	Sweep	10.8	1.38	9.5	3.0
	AS0_5	Sweep	21.6	1.65	9.3	3.7
	AS0_75	Sweep	32.7	1.90	9.2	4.3
	AS1	Sweep	43.2	2.23	9.1	4.5
Frame B	BI5	Impulse	2.6	-	9.1	1.2
	BN0_5a	P-R	3.8	-	8.8	2.1
	BN1	P-R	7.6	-	8.7	2.2
	BS0_25a	Sweep	10.8	1.42	8.9	2.5
	BS0_5	Sweep	21.7	1.69	8.9	3.0
	BS0_75	Sweep	32.6	2.16	8.7	3.2
	BS1	Sweep	43.3	2.66	8.6	3.6

was the case for the two-dowel cantilever beams, it was not possible to extract modal parameters from all of these tests. In the case of the frames, the higher two amplitudes of applied force resulted in a systematic variation in the damping estimate across the range of frequencies tested, so that neither a damping estimate nor an accurate estimate of natural frequency could be made.

Similarly, in several of the impulse tests, a systematic variation was found in the damping matrix. This was thought to be a result of the quality of the impulse applied, rather than a high degree of nonlinearity, since it was possible to extract modal information from one of the impulse tests on each frame, and they are presented in Table 7.5.

The common reference used to compare the three methods of excitation in Table 7.5 is the root-mean-square (RMS) of the time-series of force applied to the structure. The excitation and response for each form of excitation is inherently different, so it is not considered that a pseudo-random and a slow-sine-sweep test, for example, with the same RMS amplitude of force should give exactly the same modal properties for the non-linear system. It is, however, considered to be a suitable approximate measure of the magnitude of each test. The three excitation modes cover a range of RMS force

from just over 2N to just over 43N.

For the slow-sine-sweep tests, since the full resonance is allowed time to develop, it is possible to measure the peak acceleration at resonance and assign an R-ratio according to (7.21). The natural frequency of the frame varies from 10.0Hz to 9.1Hz for frame A, and from 9.1Hz to 8.6Hz for frame B, though it should be noted that the magnitude of the excitation force has been increased by approximately twenty times for this change to occur.

As in the cantilever beam tests, the frame with the higher stiffness also had the higher damping, though the difference between the two frames was not as great as the difference between the two cantilever beams. In the frames, all of the steel plates slid freely into the slot during assembly; none of them required any force to insert as in the case of connection A. The results do suggest, however, that a similar process of friction between the steel plate and the timber may be responsible for the higher stiffness in frame A, and it is certainly likely that the plates were forced to one side of the slot during installation of the dowels, and this could generate the normal force required for this friction to develop.

7.5 Comparison with theoretical predictions

The stress function approach for the stiffness of a moment connection, as presented in Section 6.3, was used to assign a stiffness to each dowel in each connection. The orientation of the load on each connector was assumed to be at right angles to the radial line between the connector and the centroid of the connection. This meant that dowels in the the two-dowel cantilever connections were assumed to be loaded parallel to the grain, while in the four-dowel connections in the frames, the dowels were all loaded at 30° to the grain direction, and the additional two dowels in the six-dowel connection were loaded perpendicular to the grain. For those dowels loaded at 30° to the grain, Hankinson's formula (Hankinson; 1921) was applied to interpolate between the calculated foundation moduli parallel and perpendicular to grain. The appropriateness of this formula for the task was discussed in Section 2.2.5.

The material properties used were based on the material characterization tests for Norway spruce described in Section 5.4. The specimens for determination of the elastic modulus were therefore taken from the same batch of glued-laminated timber used for construction of the cantilever and frame specimens, but were not taken from the cantilever and frame specimens themselves. The density of the timber for self-weight was determined by weighing the cantilever beam specimen.

The modal analysis was carried out using the stiffness-matrix model described in

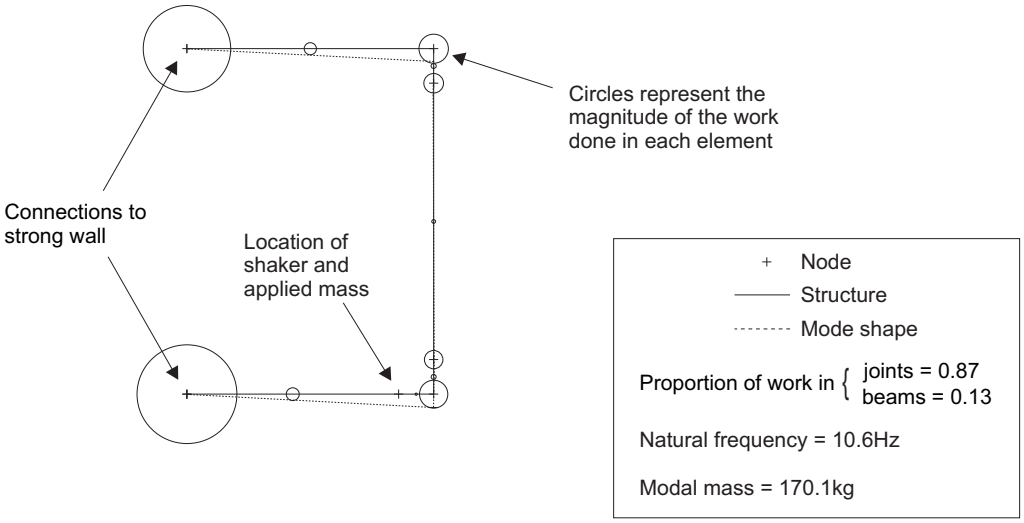

Figure 7-21: Mode shape of the fundamental mode of vibration for the frame, with circles indicating the magnitude of the work done in each element of the structure as it vibrates

Section 7.3.2, which calculated the mode shape, natural frequency, and the distribution of elastic work done in the structure for each mode of vibration.

Figure 7-21 shows the mode shape for the fundamental mode for the frame, along with the modal properties. Circles are drawn half way between each pair of nodes to represent the magnitude of the work done in the element or connection between the nodes. In total, for this frame, 87% of the total work done on the structure by the vibrating mass was predicted to be transferred into strain energy in the connections. As a result, the energy dissipation in the connections was expected to provide the majority of the energy dissipation in the structure as a whole, and the damping ratio in the structure as a whole was expected to be similar to that for an individual connection. In the cantilever joint, 85% of the work was done in the connection, with the remainder done in bending the beam, for the case of the six-dowel connections. This rises to 87% for the two-dowel connections. The contribution of the connections to damping in each structure was therefore expected to be similar, and this was reflected in the similar range of damping ratios observed in all the cantilever beam and frame tests, with the exception of the low damping in the impulse tests on the frames, though to be the result of the extremely low amplitude of vibration, and the high damping in connections A2a, A2b and A6, thought to be due to the higher friction between the steel plate and the timber around it.

Having carried out the same theoretical modal analysis for each of the structures, the predicted natural frequency could be compared with the range of natural frequencies

Table 7.6: Comparison of predicted natural frequency with the range of natural frequencies measured in tests on each cantilever and frame structure

Structure	Predicted frequency (Hz)	Label	Measured frequency range (Hz)
Cantilever beams	8.7	A2a	10.8-11.1
		A2b	10.2-10.7
		B2a	8.0-8.6
		B2b	8.6-8.7
	7.7	A6	8.6-9.4
		B6	8.2-8.4
Frame	10.6	A	9.1-10
		B	8.6-9.1

measured during the tests. The results are shown in Table 7.6.

If the connectors were perfectly aligned with the centre of each hole and there was no significant normal force, and therefore no significant friction between the steel plate and the timber, then it would be expected that the predicted frequency would be at the upper part of the range of measured frequencies. This is because the prediction is based on an elastic analysis, and the results in previous chapters have shown that the secant stiffness is predicted well by an elastic analysis for small-amplitude oscillation, but reduces as the amplitude of oscillation increases. This is seen in the results for the two-dowel moment connections B2a and B2b. The much higher frequencies in A2a and A2b, as discussed in Section 7.4.1, are thought to be a result of the tightness of fit between the steel plate and the slot in the timber and the resulting friction. This unintentional outcome of the cantilever beam tests is of relevance to structural engineering design, in that it suggests that systems, such as prestressed bolts, which could provide reliable friction of this form, could be used to improve the performance of dowel-type connections under in-service vibration.

The two-dowel connections with a loose fit between the steel plate and the slot therefore perform approximately as predicted. The six-dowel connections do not behave as predicted. Again, the frequency of connection A is higher than that of connection B, but in this case even the frequency of connection B is significantly higher than predicted. The result is sensitive to the angle to grain at which the outer connectors are loaded or, in the same sense, to the interpolation between the known parallel- and perpendicular-to-grain stiffnesses: using an angle of 20°, for example, instead of 30°, results in a predicted frequency of 8.4Hz. It is acknowledged that a more rigorous

approach to predicting the variation of stiffness with angle to grain is required.

In the predicted stiffness of the six-dowel connection, the outer four dowels contribute 95% of the stiffness of the connection. The fact that the measured stiffness is higher than the predicted value therefore suggests that at least these outer four dowels are contributing fully to the moment resistance of the connection. The process of preloading, therefore, appears to have allowed any misalignment of the dowels, which would result in some remaining unloaded or less loaded than the simple analysis predicts, to be taken up, distributing the force evenly between the dowels.

Comparison of the predicted and measured stiffness of the frames given in Table 7.6 shows that the measured frequency of the frame is slightly lower than predicted in each case. This may be a result of the lower initial loading as a proportion of the capacity of the connection. The results in Chapter 5 show that the stiffness of connectors loaded to 20% of their predicted yield strength fell below the elastic value. In the frame, as described in Section 7.3.2, while the connections to the laboratory wall were loaded to approximately 20% of their predicted yield force, the connections between members were only loaded to approximately 10%. It is therefore considered reasonable that their stiffness would be lower as a result.

As a simple comparison, the connection stiffness given by Eurocode 5 (BSI; 2009a) in the form of the slip modulus K_{ser}, when applied to generate the semi-rigid connection stiffness for the frame, predicts a natural frequency of slightly over 6Hz. This substantial underprediction is due to the fact that the slip modulus allows for all of the components of deflection from initial loading, including the initial deflection due to plastic behaviour in the contact surface between dowel and timber, which was shown in Section 6.6.2 to lead to a stiffness 3.8 times lower than the stiffness under oscillating load with R=1.2, as an average of the tests presented in that section.

7.5.1 Energy dissipation

It was shown in Section 6.5 that an insight into the equivalent viscous damping ratio for the single-dowel connection test specimens could be gained by calculating the energy dissipation due to friction around the face of the dowel. It was found that the energy dissipation through that mechanism contributed a large proportion of the damping measured in many of the tests, although there was also evidence of energy dissipation due to other processes which were not modelled.

Using the same method presented in Section 6.5, it was possible to predict the damping ratio expected to result from around-the-dowel friction, and this was done for the two-dowel moment connections. The calculation, as shown in Table 7.7, resulted in a predicted damping ratio of 0.6%. Table 7.4 shows that the measured damping ratios

Table 7.7: Predicted damping by around-the-dowel friction for two-dowel connection

		W_i	γ_i
Embedment	Hole shape	18.9%	2.9%
	Rigid insert	49.0%	0.0%
Dowel deformation		22.1%	0.0%
Beam deformation		10.0%	0.0%
Total		γ	0.6%

for the two-dowel connections ranged from 2.40% to 9.00%, which suggests that other processes are responsible for the majority of the energy dissipation in those connections.

The difference in damping between the connections in which the steel plate fitted tightly into the slot and those in which there was a looser fit suggests that friction between the steel plate and the timber around it may be responsible for at least part of the additional damping which was observed. In this study, there was insufficient experimental evidence to test any prediction of energy dissipation by this mechanism, since the force between the timber and the steel plate was not quantified. The analysis of the energy dissipation in the connection and frame structures was therefore limited to qualitative discussion.

The damping ratios measured in the frames and cantilever beams are higher than those in the embedment and single-dowel connection tests. This is considered likely to be due to friction between the steel plate and the timber. In the single-dowel connection tests, the loading machine held the steel plate vertically and applied a purely vertical load through the plate to the dowel. In the frame and cantilever-beam tests, the structures were unrestrained in the horizontal direction, and so the restraint against lateral movement was provided by contact between the steel plate and the timber, consequently leading to the friction forces which were thought to contribute to the additional measured energy dissipation. It is uncertain whether this friction would develop in a complete, fully-braced structure.

7.6 Summary

Experimental modal analysis of simple structures with dowel-type connections has shown that their stiffness and energy dissipation follows a similar pattern to that of the embedment specimens and single-dowel connections considered in previous chapters. An additional contribution to both stiffness and energy dissipation has been suggested, which is the friction between the steel flitch plate and the sides of the timber slot into which it is inserted. In a connection with a snug fit between the plate and the slot,

this effect has been seen to approximately double the energy dissipation, and increase the stiffness by approximately a fifth.

This source of energy dissipation appeared to be far more substantial than the around-the-dowel friction predicted according to the method described in the previous chapter, and a predictive model for this additional form of energy dissipation was considered to be beyond the scope of this study. The apparent influence of this interface friction on energy dissipation is a potential topic for further research, however, and it may be possible to produce highly dissipative connections for in-service conditions by creating the appropriate conditions for friction between those two surfaces.

An established formulation by Duffing (1918) was used to develop a curve-fitting approach to analyse the nonlinear response of the cantilever beams and frames to slow-sine-sweep excitation. Duffing's formulation was for a particular form of nonlinearity, cubic stiffness, which was seen to describe parts of the receptance of the systems, but could not be fitted to the response over its full range of excitation. Nonetheless, by fitting the cubic stiffness response to the measured receptance, modal parameters such as the underlying linear natural frequency and the damping could be estimated, where approaches designed for linear systems failed to provide estimates.

The method used to predict the natural frequencies of the structures took the stiffness calculated according to the stress-function and beam-on-elastic-foundation model from Chapter 6 and applied the conventional approach to modelling the stiffness of moment connections and frames. The predicted natural frequency matched the measured natural frequency well for the smallest amplitude of applied dynamic load, and for the simplest form of connection, the two-dowel moment connection. Based on the behaviour of the six-dowel moment connection, it appeared that either the simple approach to determination of the embedment angle for each connector, or the interpolation between parallel- and perpendicular-to-grain stiffness, may be inappropriate. A reliable calculation for the effect of angle to grain requires further analytical and experimental study.

The same effect is assumed to be present in the frame specimens, but their measured natural frequency is, in fact, slightly lower than the predicted value. This is thought to be due to the low loads, as a proportion of their yield strength, on some of the connectors in the frames. Despite these inaccuracies, the elastic model gives a reasonable prediction of the natural frequency of both the cantilever and frame structures, based on the elastic properties of the timber and the steel, the geometry of the structure and its mass distribution.

The process of modelling and analysing these structures therefore shows that a nonlinear variation of stiffness with amplitude of load in each connector appears to be

superimposed on an underlying elastic behaviour which can be predicted by the elastic stress-function model for embedment in conjunction with conventional connection design methods.

Chapter 8

Application to Example Structure

In this study, the structural processes which determine the dynamic stiffness of dowel-type connections have been observed and modelled, starting with the basic component of a dowel type connection, the embedment of a circular dowel into a piece of timber, and building up to a complete frame with moment connections formed of four and six dowels. The analytical methods which have been found to give a good prediction of the stiffness under certain conditions have been simplified to form a design method suitable for the calculation, without specialist software, of the natural frequency, under one-sided in-service vibration, of frames joined by steel dowels.

In this chapter, that design method will be documented and applied to the tall timber building example used in Chapter 4. In that chapter, the method given in Eurocode 5 (BSI; 2009a) was used to predict the connection stiffness for analysis of the along-wind vibration response of the structure. It has been shown in this study that the Eurocode 5 method greatly underestimates the stiffness of a connection under this form of vibration.

8.1 Summary of design method

Separate parts of a design method to calculate this stiffness have been presented in Chapters 6 and 7. They can be combined to give a method for calculating the stiffness of a complete connection based on its geometry and the material properties of the steel and timber, which is as follows.

- The local deformation due to the change in the hole shape under load, referred to as the hole-shape deformation, is estimated. This is done using the stress function

Table 8.1: Hole-shape stiffnesses for the GL28h class given in EN 1194 (BSI; 1999)

Load orientation	Stiffness for local deformation (N/mm)
Parallel to grain	6581
Perpendicular to grain	2190

in Section 6.1.2 but, since it is independent from the geometry of the connection, could be tabulated for standardized timber properties such as those in EN 338 (BSI; 2009b) for solid timber or EN 1194 (BSI; 1999) for glued-laminated timber.

- The deformation due to the movement of the dowel through the timber, referred to as the rigid-insert deformation, can be calculated using the simplified method given in Section 6.3, using (6.59) for a linear applied force and (6.60) for a moment.
- The total stiffness calculated from (6.61) is then used as the foundation modulus for a beam-on-elastic-foundation calculation representing a single connector under the given loads.
- The stiffness of a single connector is multiplied by the number of connectors for a linear applied force, or combined according to (7.18) for a moment.
- The resulting linear and rotational stiffness is applied as a semi-rigid connection stiffness in the appropriate degrees of freedom of a stiffness-matrix model for the complete structure, which can be used for modal analysis.

8.2 Calculations

8.2.0.1 Hole shape deformation

It is assumed that the structure will be made from glued-laminated timber complying with the GL28h classification in EN 1194 (BSI; 1999). The material properties can therefore be taken to be those given in that standard. The deformation due to change in hole shape can therefore be calculated for parallel- and perpendicular-to-grain embedment, and the results are shown in Table 8.1.

8.2.0.2 Rigid-insert deformation

In contrast to the hole-shape stiffness, the rigid-insert deformation depends on the geometry of the connection and the structure. For the translational stiffness of the connection, the rigid-insert stiffness depends on the length of the member between

Table 8.2: Translational rigid-insert stiffness for each dowel in the braced frame of the example structure

Length	Stiffness Parallel N/mm	Perpendicular N/mm
14m	62773	17360
16m	62014	17154

Table 8.3: Geometry for the example connection: c_x is the horizontal distance of the dowel from the centroid in mm, c_y the vertical distance in mm and the table shows the radial distance in mm

		c_x				
		120	60	0	60	120
c_y	200	233	209	200	209	233
	100	156	117	100	117	156
	0	120	60	0	60	120
	100	156	117	100	117	156
	200	233	209	200	209	233

connections. The length of the members in the braced frame of the example structure is 16m for the vertical members and 14m for the diagonals. The calculated stiffness is shown in Table 8.2, showing that the difference in length makes a negligible difference to the translational stiffness of the connection.

While the lateral loads are resisted primarily by truss action in the frame, the rotational stiffness of the connections is included for completeness, and to illustrate the method for their calculation. For the rotational stiffness of the connection, the rigid-insert stiffness of each dowel depends on its distance from the centroid of the connection. The geometry of the connection is summarized in Table 8.3, in which each of the 25 dowels is assigned c_x and c_y coordinates relative to the centroid, and the radial distance from the centroid is tabulated for each. c_x is the distance from the centroid in the parallel-to-grain direction, and c_y the distance in the perpendicular-to-grain direction.

Using these radial distances, rigid-insert stiffness can be calculated according to the simplified method in Section 6.3.

The foundation modulus for calculation of the stiffness of a single connector can then be found. The stiffness associated with the rigid-insert deformation of each dowel for this rotational movement can then be added to the stiffness associated with the hole-shape deformation, and corrected for the angle to the grain given by $tan^{-1}(c_x/c_y)$.

Table 8.4: Foundation moduli, corrected for angle to grain, for each dowel in N/mm/mm

		c_x				
		120	60	0	60	120
c_y	200	746	1125	1446	1125	746
	100	513	857	1635	857	513
	0	374	447	0	447	374
	100	513	857	1635	857	513
	200	746	1125	1446	1125	746

Table 8.5: Stiffness for movement of each dowel relative to the centroid of the connection

		c_x				
		120	60	0	60	120
c_y	200	50664	67590	79219	67590	50664
	100	37720	56122	86869	56122	37720
	0	28719	32821	0	32821	28719
	100	37720	56122	86869	56122	37720
	200	50664	67590	79219	67590	50664

The resulting matrix of foundation moduli is shown in Table 8.4, where the foundation modulus for each dowel is appropriate to its distance from the centroid and the angle to the grain at which it is loaded. The variation of the foundation modulus with grain orientation and distance from the centroid can be seen.

The same process for the translational movement of each dowel results in a foundation modulus of 1060N/mm^2 in the parallel-to-grain direction and 191N/mm^2 in the perpendicular-to-grain direction. The stiffness is, therefore, dominated by the rigid-insert deformation, as can be seen by comparing these values to those in Table 8.1.

8.2.0.3 Beam on elastic foundation

A beam-on-elastic-foundation calculation can then be carried out for each dowel based on its foundation modulus, to calculate its overall stiffness. For translational movement, this results in a stiffness of 62773N/mm^2 parallel and 17360N/mm^2 perpendicular to grain. For rotational movement, the stiffness for each dowel is given in Table 8.5.

These stiffnesses have been calculated for a single flitch plate, using (6.62). The connection in the example structure contains four flitch plates, and therefore exhibits approximately four times this stiffness. This approximation corresponds to current design guidance for the calculation of the slip modulus for a connection according to Eurocode 5 (BSI; 2009a).

Table 8.6: Semi-rigid connection stiffness for use in the stiffness-matrix model

	Stiffness	
Translation along the grain	7846595	kN/m
Translation across the grain	2169994	kN/m
Rotation	136074	kNm/radian

8.2.0.4 Combination

For translational movement, all 25 connectors are assumed to exhibit the same stiffness, which can be summed to give the total stiffness of the connection.

The combined rotational stiffness of the connectors can be calculated according to (7.18) from Section 7.3.2, reproduced as (8.1). Thus, the translational and rotational stiffness of the connections in the example structure has been estimated as shown in Table 8.6.

$$K_r = \sum_{i=1}^{n} k_{c,i} r_i^2 \tag{8.1}$$

8.2.0.5 Stiffness matrix

Using the semi-rigid connection stiffnesses in Table 8.6, the structural analysis could be carried out in the same way in Section 4.1.3, resulting in a mode shape for the fundamental mode of vibration as shown in Figure 8-1. The analysis in Section 4.1.3 investigated the wind-induced vibration of a 20-storey braced-frame timber structure, and found that the effect of connection stiffness, modelled according to the Eurocode 5 method, reduced the natural frequency of the first mode of vibration from 0.52Hz to 0.37Hz, with a consequent effect on the amplitude of vibration in the structure due to turbulent wind load. Table 4.3, from Section 4.1.3, can now be extended to include the natural frequency calculated using the method developed in this study to give Table 8.7.

The underestimation of stiffness, and therefore natural frequency, by the Eurocode 5 method BSI (2009a) for this structure is less dramatic than in the case of the portal frame described in Chapter 7. This is because the connections in this structure are relatively stiff, even according to the Eurocode 5 method, in comparison to the members themselves, due to their four steel plates and 25 fasteners per connection. Looking at a typical 700mm by 700mm glulam corner column, the combined translational stiffness of the connections at either end, as calculated in this section, is approximately 9 times higher than the axial stiffness of the member itself.

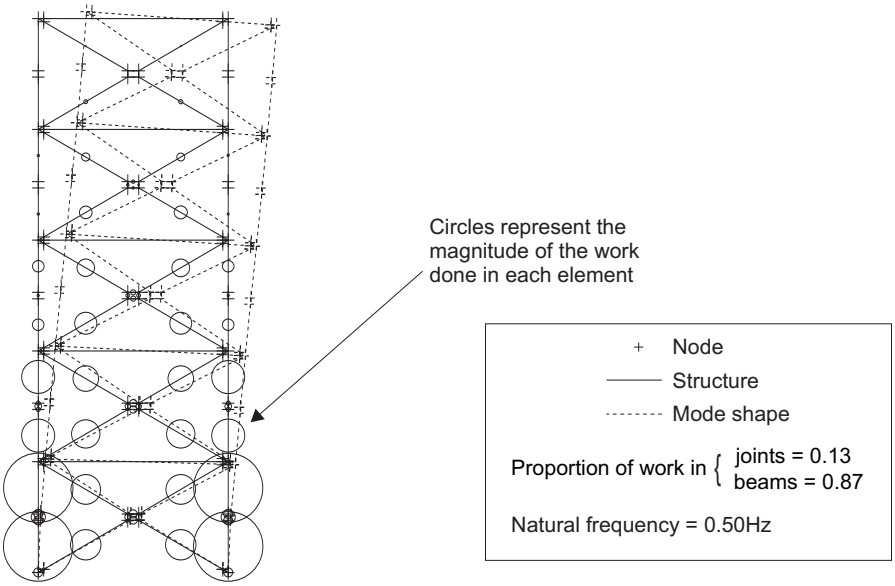

Figure 8-1: Mode shape for the fundamental mode of vibration with the connection stiffness determined according to the method developed in this study

Table 8.7: Natural frequency of the first mode of vibration for the 20-storey glued-laminated timber structure

Truss connection	1st/2nd mode natural frequency (Hz)
Fixed	0.54
Semi-rigid (Eurocode 5)	0.39
Semi-rigid (This method)	0.50

The connection stiffness predicted by the method developed in this study is, in fact, approximately 8 times higher than the stiffness according to the Eurocode 5 method parallel to grain and 2 times higher perpendicular, but the effect on natural frequency is far less pronounced, because of the relatively small contribution of the connections to the overall stiffness.

8.2.1 Energy dissipation

The analysis shows that, for the connection stiffness calculated according to the method presented in this study, the work done in the connections is 13% of the total work done in the structure in the fundamental mode of vibration. As a result, the weighted contribution of the connections to the damping ratio of the complete structure will be small. If the connections have an independent damping ratio γ_i of 1.3%, as predicted in Section 6.5 for single-dowel connections carrying a linear load, then their contribution to the overall damping of the structure would be only 0.17%. On this basis, the material damping in the timber and the contribution of non-structural elements would be expected to form the majority of the damping in the structure. It is not therefore possible to make a more informed estimation of damping than the range from 0.95% to 1.9% used in the sensitivity analysis in Section 4.1.3.2. It can be stated that, if the structure is to exhibit damping in this range, then the contribution of energy dissipation in embedment to that damping would be expected to be small compared to other sources of energy dissipation.

It is noted, however, that this structure represents only a single example, and there may be many other structural forms in which the connections store a greater proportion of the potential energy in the vibrating structure, and so may contribute more to the overall damping. The experimental and theoretical work on energy dissipation in this study has also given rise to tentative suggestions of methods of increasing energy dissipation in connections for in-service vibration, by using high-friction dowels or by inducing friction between the steel flitch plates and the timber. If methods such as these could produce much higher energy dissipation in the connections, then they could make a significant contribution to the overall damping, even in structures such as this example, where only 13% of the elastic work is done in the connections.

8.3 Summary

The method developed in Chapters 6 and 7 for calculating stiffness in dowel-type connections under in-service vibration has been applied to an example structure, a 20-storey braced-frame. The structure, as described in Section 4.1.3, was the result of

a preliminary design by Norwegian engineers Sweco (Reid; 2009), who published the member sizes for the main members. The form of the connections, though not their geometry, was taken from a bridge designed by the same engineers (Abrahamsen; 2008), using dowel-type connectors with multiple steel flitch plates.

The results showed that the connections were relatively stiff in comparison to the members they connected, but that the method developed in this study still resulted in a substantial difference in the calculated natural frequency of the building, compared with the only method currently open to an engineer designing according to Eurocode 5 (BSI; 2009a), the slip modulus K_{ser}.

There remain some simplifications in this example calculation, which are not considered to affect these conclusions, but should be noted nonetheless. One is that the four-plate connection will not, in general, exhibit four times the stiffness of the connection with a single plate. The true stiffness will depend on the spacing of the plates and the dimension of the member into which the connector is inserted. By representing the connector as a beam on elastic foundation, the method presented here allows this geometry to be taken into account.

In a multiple-dowel connection, all the dowels may not exhibit their full stiffness according to the infinite-plate solution which underlies the stress function used here. Interaction between the deformation fields around each dowel may result in a lower stiffness for a group of dowels. This is considered to be an area for further study.

The analysis in this chapter has demonstrated that the results of this study can have a significant influence on the design of cutting-edge timber structures which use dowel-type connections, such as a 20-storey building with a glued-laminated timber frame. The result is to show that, for in-service vibration, the connections exhibit far higher stiffness than existing empirical design methods allow for.

Chapter 9

Conclusion

This study has addressed a shortfall in the understanding of the load-deformation behaviour of dowel-type connections in timber structures under cyclic loads. It has focussed on their response to loads representative of in-service vibration, which is taken to mean vibration as a result of loads which a structure experiences regularly under normal use. Under this type of dynamic load, the structure should behave in such a way that ensures the comfort of the occupants, and allows all the systems housed in the building to perform their function unhindered by any structural movement.

The published performance criteria defining acceptable levels of structural vibration have been reviewed, and compared against published results of vibration tests on timber structures and a theoretical analysis of a proposed multi-storey timber structure. These results showed the sensitivity of timber structures to this form of vibration, highlighted the lack of knowledge of the behaviour of their connections under such conditions, and allowed the design of dynamic load tests to mimic the form of load applied to the connections of structures vibrating in service.

Cyclic load tests and modal analysis were carried out on embedment specimens, single-dowel connections, moment connections and complete frames. Most of the tests applied one-sided loading, with no load reversal, in order to represent a common form of in-service vibration. Their amplitude was represented by the ratio of the maximum to the minimum load, the R-ratio.

The larger-amplitude R=10 tests generally exhibited lower secant stiffness and higher energy dissipation than the R=1.2 tests. The reduced stiffness was observed to be due to nonlinear load-deformation behaviour, in which the stiffness was lower at lower applied loads, so as the amplitude increased and the minimum of the cyclic component was closer to zero, the secant stiffness was reduced. This was considered to be a result of the imperfect contact surface between dowel and timber, being responsible for

a component of deformation under low loads. The higher energy dissipation was also considered to be due to this contact surface, and the dissipative crushing and buckling of the microstructure of the timber inherent in its deformation.

It was shown that the stiffness of the timber in embedment by a dowel at R=1.2 could be predicted with reasonable accuracy using an elastic orthotropic stress-function model, the results of which could then be used to predict the stiffness of single-dowel connections, where the deformation of the connector was modelled as a beam on elastic foundation.

Two forms of the stress function, developed by other researchers for investigation of the stress distribution around pin-loaded holes in orthotropic plates, were reviewed with the aim of using them to calculate deformations in the material around the hole. As part of this study, it was shown that by translating and superimposing the stress function on itself, the geometries of connections subject to linear forces and moments could be represented. The relative displacements of connectors could then be calculated, which could be used as the foundation modulus in the beam-on-elastic-foundation model for the complete connector.

It was noted that such an analytical model would be most useful in the context of timber engineering if it could be used to derive equations which could be used in design. It was shown that, using certain simplifying assumptions about the physical behaviour of the connection and some mathematical approximations, the equations defining the stress function could be expressed as a concise set of formulae for the relative deformation of connectors.

The analytical model for embedment was also used for investigation of the mechanisms by which energy was dissipated under cyclic load. It was shown that a particular dissipative process, that of friction around the dowel as it embeds into the timber, could be predicted, and appeared to represent a significant part of the total energy dissipation in the embedment specimens, and in the single-dowel connections. In the multiple-dowel moment connections in the cantilever beams and frames, other dissipative mechanisms appeared to be more prevalent.

The contact surface between dowel and timber was seen to have a great influence on the stiffness of the connection. In Chapter 6, by breaking down the deformation in embedment into its elastic, viscoelastic and plastic components, it was shown that the stiffness under initial loading was 38% of that for subsequent cyclic load, as an average of 54 embedment tests for dowels and screws. The reduced stiffness was thought to be due to the plastic behaviour of small volumes of timber at the interface between dowel and timber, micro-buckling and crushing irreversibly under initial loading and then forming a more rigid contact surface under subsequent cycles of load. This hypothesis

was justified by microscope images of the timber immediately around the edge of the hole, which showed micro-buckling of fibres where the timber had been subject to load parallel to the grain and crushing of trachieds as a result of perpendicular-to-grain load. The quality of this contact surface would have depended on variables such as the type of drill bit used and its speed of rotation, which would make it difficult to predict.

Under the small-amplitude movements associated with in-service vibration, the contribution of viscoelastic and plastic behaviour in the timber to the stiffness of the connection was observed to become small in comparison to the elastic component. In those conditions, the method developed in this study, which predicts the magnitude of the elastic component based on the material properties of the timber and connector, can therefore be used to predict the stiffness of a single connector.

Having derived the stiffness of a single connector, it was shown that conventional design methods could be used to express the behaviour of a group of connectors, albeit with some modification to allow for the fact that the stiffness of each connector may vary depending on their position in the geometry of the connection. It was therefore possible to predict the stiffness of a multiple-dowel connection, and then, using a stiffness-matrix method, a complete frame.

The nonlinear effect of the contact surface between dowel and timber was observed throughout the experimental investigation, and was evident in the modal analysis of two simple structural forms, a cantilever and a portal frame, with dowelled connections. The nonlinear stiffness in the connections resulted in an amplitude-dependence of stiffness in the cantilever and frame. A curve-fitting approach was developed, based on the theory of an oscillator with cubic stiffness, which allowed assessment of the damping in these structures. It was shown that the assumption of cubic stiffness did not fit the response of the structures well over a range of amplitudes, but could be used on a selected portion of the measured receptance for estimation of the modal properties.

This study has therefore traced the behaviour of dowel-type connections under cyclic loads from the embedment of the dowel into the surrounding timber to the behaviour of a complete frame. Methods have been developed to analyse and quantify the experimental results at each scale, and a calculation process has been derived to predict the linear part of the response of a connection based on the elastic properties of the timber and connector.

This nonlinear response has consequences for design, in-situ testing and analysis of timber structures for vibration, since it means that the natural frequency and damping in a structure can be expected to vary with the amplitude of vibration. In the investigation into in-service vibration described in Chapter 4, it was shown that in-service vibration in structures often consists of a resonant response resulting in oscillating loads

on connections with an R-ratio between 1 and 1.2. It was then shown that an elastic model predicted the stiffness of the connections well for that range of R-ratios. The elastic design would not be appropriate, however, for vibration at a higher amplitude, or with load reversal, and it has been shown that the stiffness in dowel-type connections under such conditions is much lower, and is accompanied by an increase in damping. This is also a consideration for modal testing of structures, since it means tests carried out at a certain amplitude of vibration would not necessarily be representative of the response at other amplitudes.

A design procedure was developed to allow calculation of this elastic stiffness, and the calculation was carried out for an example structure, a 20-storey building with a frame of glued-laminated timber. This example highlighted the effect that connection stiffness can have on the response of a full-scale building structure to in-service dynamic loads such as wind, and showed that the design procedure could be used to predict that amplitude of the additional forces imposed on structural components by vibration, and the amplitude of acceleration which would be imposed on the building's occupants.

9.1 Potential further work

Given a reliable theory for prediction of the elastic component of deformation in a connection, there is also potential to predict the deformation including viscoelastic and plastic components based on fundamental properties of the material rather than empirical relationships. This is an area for further research, and is considered to be a tractable problem, given that, under loads below the yield strength of the connection, the majority of plastic deformation is thought to be in the compaction of the contact surface between dowel and timber. Further study could include measurement of properties of the contact surface prepared by different drilling techniques and their effect on that component of the deformation in the connection.

The viscoelastic component of deformation has been addressed in this study, producing a rheological model applicable to a particular range of movement, but further research could develop a more generally applicable model. If the three components of the dowel deformation: elastic, plastic and viscoelastic, could be separately predicted, this would lead to a method which could be applied at a range of serviceability limit states in design, including vibration in-service, as in this study, but also differential movement under variable loads and total deformation. This would result in more efficient design of connections in timber structures, and therefore in more efficient design of complete structures.

This study uses plain dowels and screws made of steel, but it is considered that

the experimental and theoretical methods developed could be applied, with further research to determine appropriate parameters, to other materials. The materials and forms of connector could be chosen to enhance energy dissipation or reduce initial slip.

The results presented in Section 6.6 broke down the deformation in embedment over a 16-minute period into its elastic, viscoelastic and plastic components, and found that a large part of the initial deformation was likely due to local plastic compression of the contact surface between dowel and timber. This result suggests that there is potential to greatly increase the stiffness of such connections by improving the surface of the timber with which the dowel makes contact. The drilling process has been seen to leave a rough surface which compresses irreversibly under initial loading. An improved drilling method could therefore reduce this deformation. Another possibility would be a process in which the hole was drilled to a smaller diameter, and the contact surface pre-compressed to reduce the residual plastic deformation. On the structural scale, pre-stressing could be used to ensure that load reversal does not occur, and the contact surface remains compressed in the range of in-service forces and displacements.

The theoretical investigation of energy dissipation in Section 6.5 showed the potential for the friction around the dowel as it embeds into the timber to strongly influence the energy dissipation in embedment. This suggests that a high-friction interface between dowel and timber could improve energy dissipation in the connection and therefore damping in the structure as a whole. Experimental investigation would be necessary to validate this theoretical prediction, and to find the dowel material or surface preparation which could have a suitable interaction with the timber at the hole edge.

Similarly, in the cantilever beams and frames tested, friction between the steel connecting plate and the timber was considered to provide a substantial amount of energy dissipation. It therefore seems reasonable that an appropriate compressive force between the plate and the timber, perhaps applied by bolts tightened to a specified level, could result in a highly dissipative connection.

Bibliography

Abrahamsen, R. (2008). Bridge across Rena River - "World's strongest timber bridge", *World Conference of Timber Engineering*, Miyazaki, Japan.

Adalian, C. and Morlier, P. (2002). "Wood Model" for the dynamic behaviour of wood in multiaxial compression, *Holz als Roh- und Werkstoff* **60**(6): 433–439.

Airy, G. B. (1863). On the strains in the interior of beams, *Philosophical Transactions of the Royal Society* **153**: 49–80.

Aluko, O. and Whitworth, H. A. (2008). Analysis of stress distribution around pin loaded holes in orthotropic plates, *Composite Structures* **86**(4): 308–313.

Armstrong, L. D. and Kingston, R. S. T. (1960). Effect of moisture changes on creep in wood, *Nature* **185**(4716): 862–863.

ASTM (1997). Standard test method for evaluating dowel-bearing strength of wood and wood-based products (reapproved 2002), *Technical Report D5764-97a*, ASTM.

Atack, D. and Tabor, D. (1958). The friction of wood, *Proceedings of the Royal Society of London. Series A, Mathematical and Physical Sciences* **246**(1247): 539–555.

Baber, T. T. and Noori, M. N. (1986). Modeling general hysteresis behavior and random vibration application, *Journal of Vibration Acoustics Stress and Reliability in Design* **108**(4): 411–420.

Bachmann, H. (1992). Case studies of structures with man-induced vibrations, *Journal of Structural Engineering* **118**(3): 631–647.

Bachmann, H. and Ammann, W. (1987). *Vibrations in structures: induced by man and machines*, International Association of Bridge and Structural Engineering, Zurich.

Birkinshaw, C., Buggy, M. and Henn, G. G. (1986). Dynamic mechanical analysis of wood, *Journal of Materials Science Letters* **5**(9): 898–900.

Bodig, J. and Jayne, B. (1993). *Mechanics of wood and wood composites*, Krieger Publishing Company, Malabar, FL, USA.

Bouc, R. (1967). Forced vibration of mechanical systems with hysteresis, *Preceedings of the 4th International Conference on Nonlinear Oscillations*, Prague, Czechoslovakia.

BSI (1991). Timber structures. joints made with mechanical fasteners. general principles for the determination of strength and deformation characteristics, *Technical Report BS EN 26891:1991*, BSI.

BSI (1999). Timber structures - glued laminated timber, *Technical Report BS EN 1194:1999*, BSI.

BSI (2002a). Eurocode 0 - basis of structural design, *Technical Report BS EN 1990:2002*, BSI.

BSI (2002b). Moisture content of a piece of sawn timber, *Technical Report BS EN 13183:2002*, BSI.

BSI (2005). Eurocode 1 actions on structures part 1-4: General actions - wind actions, *Technical Report BS EN 1991-1-4:2005*, BSI.

BSI (2007). Timber structures. test methods. determination of embedment strength and foundation values for dowel type fasteners, *Technical Report BS EN 383:2007*, BSI.

BSI (2008a). Guide to evaluation of human exposure to vibration in buildings, *Technical Report BS 6472-1:2008*, BSI.

BSI (2008b). UK National Annex to Eurocode 3: Design of steel structures Part 1-1: General rules and rules for buildings, *Technical Report NA to BS EN 1993-1-1:2005*, BSI.

BSI (2009a). Eurocode 5 design of timber structures part 1-1: General - common rules and rules for buildings, *Technical Report BS EN 1995-1-1:2004+A1:2008*, BSI.

BSI (2009b). Structural timber. strength classes, *Technical Report BS EN 338: 2009*, BSI.

BSI (2011). Timber structures. structural timber and glued laminated timber. determination of some physical and mechanical properties, *Technical Report BS EN 408:2010*, BSI.

Bucher, I. (1991). circfit MATLAB function, `http://www.mathworks.co.uk/matlabcentral/fileexchange/5557-circle-fit/content/circfit.m`.

Buffon, G. L. L. D. (1740). Experiences sur la force du bois, *L'Academie Royale des Sciences - Histoire et Memoires* pp. 453–467.

Bulíĉek, M., Málek, J. and Rajagopal, K. (2012). On kelvin-voigt model and its generalizations, *Evolution Equations and Control Theory* **1**(1): 17–42.

Burgers, J. M. (1939). Mechanical considerations - model systems - phenomenological theories of relaxation and of viscosity, *First Report on Viscosity and Plasticity*, 2nd edn, N.V. Noord-Hollandsche Uitgevers Maatschappij, Amsterdam, pp. 27–30.

Casado, C. M., Díaz, I. M., de Sebastián, J., Poncela, A. V. and Lorenzana, A. (2013). Implementation of passive and active vibration control on an in-service footbridge, *Structural Control and Health Monitoring* **20**(1): 70–87.

Ceccotti, A. (2008). New technologies for construction of medium-rise buildings in seismic regions: The XLAM case, *Structural Engineering International* **18**(2): 156–165.

Charney, F. A. (1990). Wind drift serviceability limit state design of multistory buildings, *Journal of Wind Engineering and Industrial Aerodynamics* **36, Part 1**(0): 203–212.

Chen, J. T. and You, D. W. (1997). Hysteretic damping revisited, *Advances in Engineering Software* **28**(3): 165–171.

Chui, Y. H. and Li, Y. (2005). Modeling timber moment connection under reversed cyclic loading, *Journal of Structural Engineering* **131**(11): 1757–1763.

Chui, Y. H., Ni, C. and Jiang, L. (1998). Finite-element model for nailed wood joints under reversed cyclic load, *Journal of Structural Engineering* **124**(1): 96–103.

Chui, Y. and Ni, C. (1997). Load-embedment response of timber to reversed cyclic load, *Wood and Fiber Science* **29**(2): 148–160.

Clouser, W. S. (1959). Creep of small wood beams under constant bending load, *Technical Report 2150*, Department of Agriculture, Forest Service, Forest Products Laboratory, Madison, WI.

Cobb, F. (2009). *Structural Engineer's Pocket Book*, 2nd edn, Butterworth-Heinemann, Oxford.

Coulomb, C. A. (1821). *Théorie des machines simples*, nouvelle édicion edn, Huzard courcier, Paris.

Crandall, S. H. (1991). The hysteretic damping model in vibration theory, *Journal of Mechanical Engineering Science* **205**(13): 23–28.

Daudeville, L., Davenne, L. and Yasumura, M. (1999). Prediction of the load carrying capacity of bolted timber joints, *Wood Science and Technology* **33**(1): 15–29.

Davenport, A. G. (1961). The application of statistical concepts to the wind loading of structures, *Proceedings of the Institution of Civil Engineers* **19**(4): 449–472.

De Jong, T. (1977). Stresses around pin-loaded holes in elastically orthotropic or isotropic plates, *Journal of Composite Materials* **11**(3): 313.

Derdas, C. and Kostopoulos, V. (2011). On the bearing failure of laminated composite pin-loaded joints: exploitation of semi-analytical solutions for the determination of the stress state, *Strain* **47**: 320–332.

Dinwoodie, J. M. (2000). *Timber its nature and behaviour*, 2nd edn, Spon, London.

Dorn, M. (2012). *Investigations on the serviceability limit state of dowel-type timber connections*, PhD thesis, Faculty of Civil Engineering, Vienna University of Technology.

Dorn, M., de Borst, K. and Eberhardsteiner, J. (2013). Experiments on dowel-type timber connections, *Engineering Structures* **47**(0): 67–80.

Duffing, G. (1918). *Erzwungene schwingungen bei veränderlicher eigenfrequenz und ihre technische bedeutung*, F. Vieweg & Sohn, Braunschweig.

Echavarría, C., Haller, P. and Salenikovich, A. (2007). Analytical study of a pinloaded hole in elastic orthotropic plates, *Composite Structures* **79**(1): 107–112.

Ehlbeck, J. and Larsen, H. J. (1993). Eurocode 5 - design of timber structures: Joints, *International workshop on wood connectors*, Forest Products Society, Madison, WI, USA, pp. 9–23.

Ellis, B. R. and Bougard, A. J. (2001). Dynamic testing and stiffness evaluation of a six-storey timber framed building during construction, *Engineering Structures* **23**(10): 1232–1242.

Eriksson, P.-E. (1994). *Vibration of low-frequency floors-dynamic forces and response prediction*, PhD thesis, Department of Civil Engineering, Chalmers University of Technology.

Ewins, D. J. (1986). *Modal testing: theory and practice*, Research Studies Press Ltd., Baldock, Hertfordshire, England.

Filiatrault, A., Christovasilis, I. P., Wanitkorkul, A. and Lindt, J. W. v. d. (2010). Experimental seismic response of a full-scale light-frame wood building, *Journal of Structural Engineering* **136**(3): 246–254.

Filiatrault, A., Isoda, H. and Folz, B. (2003). Hysteretic damping of wood framed buildings, *Engineering Structures* **25**(4): 461–471.

Foliente, G. C. (1995). Hysteresis modeling of wood joints and structural systems, *Journal of Structural Engineering* **121**(6): 1013–1022.

Folz, B. and Filiatrault, A. (2001). Cyclic analysis of wood shear walls, *Journal of Structural Engineering* **127**(4): 433–441.

Forest Products Laboratory (2010). The wood handbook, *Technical Report FPLGTR190*, Department of Agriculture, Forest Service, Forest Products Laboratory, Madison, WI.

Foschi, R. (2000). Modeling the hysteretic response of mechanical connections for wood structures, *World Conference of Timber Engineering*, Whistler, B.C., Canada.

Foschi, R., Yao, F. and Rogerson, D. (2000). Determining embedment response parameters from connector tests, *World Conference on Timber engineering*, Whistler, B.C., Canada.

Goodier, J. N. (1942). An extension of Saint-Venant's principle, with applications, *Journal of Applied Physics* **13**(3): 167–171.

Gressel, P. (1984). Zur vorhersage des langfristigen formnderungsverhaltens aus kurzkriechversuchen, *Holz als Roh- und Werkstoff* **42**(8): 293–301.

Hankinson, R. (1921). Investigation of crushing strength of spruce at varying angles of grain, **3**(259).

Hearmon, R. F. S. (1961). *An introduction to applied anisotropic elasticity*, 1st edn, Oxford University Press, London.

Heiduschke, A. (2006a). Analysis of wood-composite laminated frames under dynamic loads - analytical models and model validation. part i: Connection model, *Progress in Structural Engineering and Materials* **8**(3): 103–110.

Heiduschke, A. (2006b). Analysis of wood-composite laminated frames under dynamic loads - analytical models and model validation. part ii: Frame model, *Progress in Structural Engineering and Materials* **8**(3): 111–119.

Hooke, R. L. (1678). Lectures de potentia restitutiva.

Hunt, D. G. (1999). A unified approach to creep of wood, *Proceedings: Mathematical, Physical and Engineering Sciences* **455**(1991): 4077–4095.

Hunt, D. G. (2004). The prediction of long-time viscoelastic creep from short-time data, *Wood Science and Technology* **38**(7): 479–492.

Hwang, K. and Komatsu, K. (2002). Bearing properties of engineered wood products I: effects of dowel diameter and loading direction, *Journal of Wood Science* **48**(4): 295–301.

Hyer, M. and Klang, E. (1985). Contact stresses in pin-loaded orthotropic plates, *International Journal of Solids and Structures* **21**(9): 957–975.

Ingólfsson, E. T., Georgakis, C. T. and Jönsson, J. (2012). Pedestrian-induced lateral vibrations of footbridges: A literature review, *Engineering Structures* **45**(0): 21–52.

Irwin, A. W. (1978). Human response to dynamic motion of structures, *The Structural Engineer* **56**(9): 237–244.

Irwin, P. A. and Breukelman, B. (2001). Recent applications of damping systems for wind response, *Proceedings of the Council on Tall Buildings and Urban Habitat, World Congress*, Melbourne, Australia.

ISO (1984). Guidelines for the evaluation of the response of occupants of fixed structures, especially buildings and offshore structures, to low-frequency horizontal motion (0.063 to 1.0 hz), *Technical Report ISO 6897: 1984*, International Organization for Standardization.

ISO (1990). Method for experimental determination of mechanical mobility - Part 2: Measurements using single-point translation excitation with an attached vibration exciter, *Technical Report ISO 7626-2:1990*, International Organization for Standardization.

ISO (2007). Bases for design of structures - Serviceability of buildings and walkways against vibrations, *Technical Report ISO 10137:2007*, International Organization for Standardization.

Jiali, J. and Jianxiong, L. (2009). Anisotropic characteristics of wood dynamic viscoelastic properties, *Forest Products Journal* **59**(7/8): 59–64.

Johansen, K. W. (1949). Theory of timber connections, *International Association of Bridge and Structural Engineering* **9**: 249–262.

Jones, R. M. (1975). *Mechanics of Composite Materials*, Scripta Book Company, Washington D. C.

Jorissen, A. (1999). Double shear timber connections with dowel type fasteners, *Heron* **44**(3): 131–161.

Kharouf, N., McClure, G. and Smith, I. (2003). Elasto-plastic modeling of wood bolted connections, *Computers & Structures* **81**(811): 747–754.

Kimball, A. L. and Lovell, D. E. (1927). Internal friction in solids, *Physical Review* **30**(6): 948–959.

Kuenzi, E. W. (1955). Theoretical design of a nailed or bolted joint under lateral load, *Technical Report D1951*, US Department of Agriculture, Forest Service, Forest Products Laboratory.

Kwok, K. C. S., Hitchcock, P. A. and Burton, M. D. (2009). Perception of vibration and occupant comfort in wind-excited tall buildings, *Journal of Wind Engineering and Industrial Aerodynamics* **97**(7-8): 368–380.

Labonnote, N., Rønnquist, A. and Malo, K. A. (2012). Experimental study on material damping in timber beams, *World Conference of Timber Engineering*, Auckland, New Zealand.

Labonnote, N., Rønnquist, A. and Malo, K. A. (2013). Modified hysteretic damping model applied to Timoshenko timber beams, *Computers & Structures* **121**(0): 22–31.

Leijten, A. J. M., Ruxton, S., Prion, H. and Lam, F. (2006). Reversed-cyclic behavior of a novel heavy timber tube connection, *Journal of Structural Engineering* **132**(8): 1314–1319.

Lekhnitskii, S. G. (1968). *Anisotropic Plates*, 2nd edn, Gordon and Breach, New York.

Liang, H., Wen, Y.-K. and Foliente, G. C. (2011). Damage modeling and damage limit state criterion for wood-frame buildings subjected to seismic loads, *Journal of Structural Engineering* **137**(1): 41–48.

Maxwell, J. C. (1868). On the dynamical theory of gases, *Philosophical Magazine* **35**: 134.

McKenzie, W. M. and Karpovich, H. (1968). The frictional behaviour of wood, *Wood Science and Technology* **2**(2): 139–152.

Noguchi, M. and Komatsu, K. (2004). A new method for estimating stiffness and strength in bolted timber-to-timber joints and its verification by experiments (ii): bolted cross-lapped beam to column joints, *Journal of Wood Science* **50**(5): 391–399.

Polensek, A. and Schimel, B. D. (1991). Dynamic properties of light-frame wood subsystems, *Journal of Structural Engineering* **117**(4): 1079–1095.

Porteous, J. and Kermani, A. (2007). *Structural Timber Design to Eurocode 5*, Blackwell, Oxford.

Proen ca, J. M. S. F. M. and Branco, F. A. B. (2005). Case studies of vibrations in structures, *Revue Européenne de Génie Civil* **9**(1-2): 159–186.

Rainer, J., Pernica, G. and Allen, D. E. (1988). Dynamic loading and response of footbridges, *Canadian Journal of Civil Engineering* **15**(1): 66–71.

Reid, R. L. (2009). Norwegian team designs world's tallest timber building, *Civil Engineering* **80**(8): 26–28.

Resch, E. and Kaliske, M. (2010). Three-dimensional numerical analyses of load-bearing behavior and failure of multiple double-shear dowel-type connections in timber engineering, *Computers & Structures* **88**(34): 165–177.

Reynolds, T., Harris, R. and Chang, W.-S. (2013a). An analytical model for embedment stiffness of a dowel in timber under cyclic load, *European Journal of Wood and Wood Products* **71**(5): 609–622.

Reynolds, T., Harris, R. and Chang, W.-S. (2013b). Viscoelastic embedment behaviour of dowels and screws in timber under in-service vibration, *European Journal of Wood and Wood Products* **71**(5): 623–634.

Rodd, P. D. and Leijten, A. J. M. (2003). High-performance dowel-type joints for timber structures, *Progress in Structural Engineering and Materials* **5**(2): 77–89.

Rönnquist, A., Wollebæk, L. and Bell, K. (2006). Dynamic behavior and analysis of a slender timber footbridge, *World Conference on Timber Engineering*, Portland, Oregon.

Santos, C. L., De Jesus, A. M. P., Morais, J. J. L. and Lousada, J. L. P. C. (2009). Quasi-static mechanical behaviour of a double-shear single dowel wood connection, *Construction and Building Materials* **23**(1): 171–182.

Santos, C. L., De Jesus, A. M. P., Morais, J. J. L. and Lousada, J. L. P. C. (2010). A comparison between the EN 383 and ASTM D5764 test methods for dowel-bearing strength assessment of wood: experimental and numerical investigations, *Strain* **46**(2): 159–174.

Sawata, K. and Yasumura, M. (2002). Determination of embedding strength of wood for dowel-type fasteners, *Journal of Wood Science* **48**(2): 138–146.

Sawata, K. and Yasumura, M. (2003). Estimation of yield and ultimate strengths of bolted timber joints by nonlinear analysis and yield theory, *Journal of Wood Science* **49**(5): 383–391.

Schniewind, A. P. and Barrett, J. D. (1972). Wood as a linear orthotropic viscoelastic material, *Wood Science and Technology* **6**(1): 43–57.

Simiu, E. and Scanlan, R. H. (1986). *Wind effects on structures: an introduction to wind engineering*, 2nd edn, Wiley, New York ; Chichester.

Sjödin, J., Enquist, B. and Serrano, E. (2006). Contact-free measurements and numerical analyses of the strain distribution in the joint area of steel-to-timber dowel joints, *European Journal of Wood and Wood Products* **64**(6): 497–506.

Sjödin, J., Serrano, E. and Enquist, B. (2008). An experimental and numerical study of the effect of friction in single dowel joints, *European Journal of Wood and Wood Products* **66**(5): 363–372.

Smith, A. L., Hicks, S. J. and Devine, P. J. (2009). Design of floors for vibration: a new approach, *Technical Report P354*, The Steel Construction Institute, Ascot, Berkshire, UK.

Song, J. and Der Kiureghian, A. (2006). Generalized Bouc-Wen model for highly asymmetric hysteresis, *Journal of Engineering Mechanics* **132**(6): 610–618.

Stevenson, R. (1821). Description of bridges of suspension, *The Edinburgh Philosophical Journal* **5**: 237–256.

Student (1908). The probable error of a mean, *Biometrika* **6**(1): 1–25.

Sun, N., Das, S. and Frazier, C. E. (2007). Dynamic mechanical analysis of dry wood: linear viscoelastic response region and effects of minor moisture changes, *Holzforschung* **61**(1): 28–33.

Thomson, W. (1865). On the elasticity and viscosity of metals, *Proceedings of the Royal Society of London* **14**: 289–297.

Thorby, D. (2008). *Structural dynamics and vibration in practice*, Materials & Mechanical, Butterworth-Heinemann, Amsterdam.

Voigt, W. (1892). Ueber innere Reibung fester Körper, insbesondere der Metalle, *Annalen der Physik* **283**(12): 671–693.

von Karman, T. and Rubach, H. (1912). On the mechanisms of fluid resistance, *Physikalische Zeitschrift* **13**: 49–59.

Vural, M. and Ravichandran, G. (2003). Dynamic response and energy dissipation characteristics of balsa wood: experiment and analysis, *International Journal of Solids and Structures* **40**(9): 2147–2170.

Wen, Y.-K. (1976). Method for random vibration of hysteretic systems, *Journal of the Engineering Mechanics Division* **102**(2): 249–263.

Willford, M. R. and Young, P. (2006). A design guide for footfall induced vibration of structures, *Technical Report CCIP-016*, The Concrete Centre, Camberley, Surrey, UK.

Winkler, E. (1867). *Die Lehre von der Elasticitaet und Festigkeit mit besonderer Rcksicht auf ihre Anwendung in der Technik, für polytechnische Schulen, Bauakademien, Ingenieure, Maschinenbauer, Architekten, etc.*, H Dominicus, Prague.

Zhang, H., Foliente, G. C., Yang, Y. and Ma, F. (2002). Parameter identification of inelastic structures under dynamic loads, *Earthquake Engineering & Structural Dynamics* **31**(5): 1113–1130.

Zhang, K.-D. and Ueng, C. E. (1984). Stresses around a pin-loaded hole in orthotropic plates, *Journal of Composite Materials* **18**(5): 432–446.

Živanović, S., Pavic, A. and Reynolds, P. (2005). Vibration serviceability of footbridges under human-induced excitation: a literature review, *Journal of Sound and Vibration* **279**(12): 1–74.

List of Publications

Chapman, J., Reynolds, T. P. S. and Harris, R. (2012). A 30 level cross laminated timber building system and anlaysis of the Eurocode dynamic wind loads, *World Conference on Timber Engineering*, Auckland, New Zealand.

Reynolds, T., Harris, R. and Chang, W.-S. (2013a). An analytical model for embedment stiffness of a dowel in timber under cyclic load, *European Journal of Wood and Wood Products* **71**(5): 609–622.

Reynolds, T., Harris, R. and Chang, W.-S. (2013b). Viscoelastic embedment behaviour of dowels and screws in timber under in-service vibration, *European Journal of Wood and Wood Products* **71**(5): 623–634.

Reynolds, T. P. S. (2012). Vibration of timber structures with dowel-type connections, *Young Researchers' Meeting of COST Action FP1004*, Zagreb, Croatia.

Reynolds, T. P. S., Harris, R. and Chang, W.-S. (2011). Dynamic response of tall timber buildings to wind load, *IABSE-IASS Symposium*, London, UK.

Reynolds, T. P. S., Harris, R. and Chang, W.-S. (2012). Dynamic stiffness and damping of dowel-type connections for timber structures under service conditions, *World Conference on Timber Engineering*, Auckland, New Zealand.

Reynolds, T. P. S., Harris, R. and Chang, W.-S. (2013c). In-service dynamic stiffness of dowel-type connections, *Meeting of CIB-W18 on Timber Structures*, Vancouver, Canada.